Matthias Pesch

Formation and properties of a discrete family of dissipative solitons in a nonlinear optical system

2006

Experimentelle Physik

Formation and properties of a discrete family of dissipative solitons in a nonlinear optical system

Inaugural-Dissertation
zur Erlangung des Doktorgrades
der Naturwissenschaften im Fachbereich Physik
der Mathematisch-Naturwissenschaftlichen Fakultät
der Westfälischen Wilhelms-Universität Münster

vorgelegt von
Matthias Pesch
aus Köln

— 2006 —

Dekan:	Prof. Dr. J. P. Wessels
Erster Gutachter:	Prof. Dr. W. Lange
Zweiter Gutachter:	Prof. Dr. R. Friedrich
Tag der mündlichen Prüfung:	05.02.2007
Tag der Promotion:	05.02.2007

Abstract

One of the central concepts of nonlinear physics is the soliton. It is about localized structures in conservative systems which exhibit particle-like characteristics. Over the last years, the analysis of similar localized structures existing in dissipative systems, so-called dissipative solitons, has developed into one of the core issues of research on the formation of structures in spatially extended dissipative systems. An analytically exact description of these strongly nonlinear structures is impossible in general. Nevertheless, well-accepted models have been developed that explain the formation of dissipative solitons. However, the magnitude of theoretical works faces a much smaller number of experiments. In addition, the latter are often not accessible to a detailed theoretical analysis.

In this work, spatial dissipative solitons are analyzed in a conceptually simple optical system which has proven its suitability for the experimental and theoretical analysis of structure formation on various occasions. Solitons are observed as localized polarization states in the transverse field distribution of a laser beam which passes through an optically nonlinear system.

In contrast to previous experimental observations of dissipative solitons, for the first time a sequence of higher-order solitons which differ in their inner structure is observed in the present system. The existence of such a discrete family of solitons was predicted in a multitude of theoretical works. The structures can be selectively ignited and erased by means of a laser pulse. Using a novel technique to measure the spatially resolved states of polarization of a light field, the experimental observations could be directly compared to numerical simulations of a well-established microscopic model of the system. A very good agreement between the experimental findings and numerical simulations has been achieved.

A main part of this work is devoted to the identification and characterization of the mechanisms that lead to the formation of stable solitons. It turns out that the stability properties of the solitons are closely linked with the dynamics of switching fronts that connect two stable spatially extended states of the system. These bistable extended states result from a polarization instability and are equivalent or nearly equivalent due to the type of that bifurcation. The switching front constitutes a continuous connection

between the two states which differ in their polarization properties.
The dynamics of switching fronts is determined by two main effects. On the one hand, a motion of fronts in the two-dimensional plane is observed that originates from the curvature of the fronts. For the first time, this curvature-driven motion is experimentally analyzed in a quantitative way by the example of circular domains. The obtained growth law is in agreement with general theoretical predictions and numerical simulations. On the other hand, fronts move due to an inequality of the involved extended states which can be introduced by a well-controlled parameter. If a circular domain is appropriately prepared, the compensation of these two effects can lead to significantly reduced front velocities. In such a situation, solitons can emerge due to the short-range interaction of fronts which lead to a stabilization of the circular domain. This interaction is mediated by oscillatory tails of the front, which emerge due to a nearby modulational instability in the system considered here. Solitons are observed both on a homogeneous and on a weakly modulated background.
The dissipative solitons are interpreted as a spatially localized excursion of the system from one extended state towards the vicinity of the other one. The region of existence of the individual solitons is experimentally and numerically determined with respect to the most important parameters, and large regions of coexistence of solitons of different order are obtained. By means of a numerical analysis, the connection of the different solitons is shown in the context of the global bifurcation scenario.
The interactions of the solitons exhibits the typical particle-like properties, and a multitude of stable configurations of solitons of the same and of different order is observed. Furthermore, structures are observed that are interpreted as tightly bound states of solitons.

Kurzfassung

Eines der zentralen Konzepte in der nichtlinearen Physik ist das Soliton. Hierbei handelt es sich um lokalisierte Strukturen in konservativen Systemen, die einen teilchenartigen Charakter besitzen. In den letzten Jahren hat sich die Untersuchung ähnlicher lokalisierter Strukturen in dissipativen Systemen, so genannter dissipativer Solitonen, zu einem der Kernthemen des großen Forschungsgebiets entwickelt, das sich mit der Strukturbildung in räumlich ausgedehnten dissipativen Systemen beschäftigt. Eine analytisch exakte Beschreibung dieser stark nichtlinearen Strukturen ist im Allgemeinen unmöglich. Es wurden jedoch inzwischen wohlakzeptierte Modellvorstellungen entwickelt, welche die Mechanismen der Entstehung von dissipativen Solitonen erklären. Der Vielzahl theoretischer Arbeiten steht allerdings eine deutlich geringere Zahl an Experimenten gegenüber. Diese sind darüber hinaus nicht immer einer detaillierten theoretischen Analyse zugänglich.
In dieser Arbeit werden räumliche dissipative Solitonen in einem konzeptionell einfachen optischen System untersucht, das sich schon vielfach zur experimentellen und theoretischen Untersuchung von Strukturbildungsphänomenen bewährt hat. Die Solitonen werden als lokalisierte Polarisationszustände in der transversalen Feldverteilung eines Laserstrahls beobachtet, der ein optisch nichtlineares System durchläuft.
Im Gegensatz zu bisherigen experimentellen Beobachtungen dissipativer Solitonen wird im hier untersuchten System zum ersten Mal eine Sequenz von Solitonen höherer Ordnung beobachtet, die sich in ihrer inneren Struktur unterscheiden. Die Existenz einer solchen diskreten Familie von Solitonen war in einer Vielzahl theoretischer Arbeiten vorhergesagt worden. Die Strukturen lassen sich mit Hilfe eines Laserpulses gezielt erzeugen und vernichten. Mittels einer neuartigen experimentellen Technik zur räumlich aufgelösten Untersuchung von Polarisationszuständen eines Lichtfeldes konnten die experimentellen Befunde direkt mit den Resultaten numerischer Simulationen eines wohletablierten mikroskopischen Modells des Systems verglichen werden. Es wird ein hohes Maß an Übereinstimmung zwischen Experiment und Theorie beobachtet.
Ein Schwerpunkt der Arbeit liegt in der Identifikation und Charakterisierung der Mechanismen, die zur Bildung der Solitonen beitragen. Es zeigt sich, dass die Stabilitätseigenschaften der Solitonen eng mit der Dynamik von Schaltfronten verknüpft sind, die

zwei stabile räumlich ausgedehnte Zustände des Systems verbinden. Diese bistabilen ausgedehnten Zustände entstehen durch eine Polarisationsinstabilität und sind aufgrund des Typs der Bifurkation äquivalent oder nahezu äquivalent. Die Schaltfront stellt eine kontinuierliche Verbindung dieser beiden in ihren Polarisationseigenschaften unterschiedlichen Zustände dar.
Die Dynamik von Schaltfronten wird im Wesentlichen durch zwei Effekte bestimmt. Zum einen wird eine Bewegung der Fronten in der zweidimensionalen Ebene beobachtet, die ihre Ursache in der Krümmung der Fronten hat. Diese krümmungsgetriebene Bewegung wird am Beispiel kreisrunder Domänen zum ersten Mal experimentell quantitativ untersucht. Das beobachtete Wachstumsgesetz zeigt eine Übereinstimmung mit generellen theoretischen Vorhersagen und numerischen Simulationen. Zum anderen bewegen sich die Fronten aufgrund einer Nichtäquivalenz der beiden beteiligten ausgedehnten Zustände, die durch einen gut kontrollierbaren Parameter eingeführt werden kann. Bei geeigneter Präparation einer runden Domäne können die genannten Effekte gegenläufig sein, was zu deutlich reduzierten Frontgeschwindigkeiten führt. In einer solchen Situation können Solitonen durch die kurzreichweitige Wechselwirkung von Fronten entstehen, die zu einer Stabilisierung der Domäne führt. Diese Wechselwirkung wird über oszillatorische Ausläufer der Fronten vermittelt, wie sie im hier untersuchten System durch die Nähe einer Modulationsinstabilität entstehen. Solitonen werden sowohl auf homogenem als auch auf einem schwach modulierten Hintergrund beobachtet.
Die dissipativen Solitonen werden als räumlich lokalisierte Exkursion des Systems von einem ausgedehnten Zustand in die Nähe des anderen Zustands interpretiert. Der Existenzbereich der einzelnen Strukturen wird hinsichtlich der wichtigsten Parameter experimentell und numerisch untersucht, und es finden sich große Bereiche, in denen Solitonen unterschiedlicher Ordnung koexistieren können. Mit Hilfe einer numerische Analyse wird der Zusammenhang der einzelnen Solitonen im Rahmen des zu Grunde liegenden globalen Bifurkationsszenarios gezeigt.
Bei der Wechselwirkung der Solitonen zeigen sich die typischen Teilcheneigenschaften, und es wird eine Vielzahl von stabilen Konfigurationen von Solitonen gleicher oder unterschiedlicher Ordnung beobachtet. Darüber hinaus werden Strukturen beobachtet, die als stark gebundene Zustände von Solitonen interpretiert werden.

Contents

Chapter 1

Introduction

The formation of self-organized structures in spatially extended dissipative nonlinear systems that are driven far from the thermodynamical equilibrium is a universal phenomenon that is observed in many disciplines of science including biology, chemistry and physics [CH93]. In such systems, structures are formed due to the interaction between a nonlinear process and spatial coupling. In many cases, regular structures that extend over the whole considered area emerge from a homogeneous state if the system is driven beyond a certain threshold. These modulational instabilities leading to simple periodic patterns with small amplitudes can often be treated by perturbative methods and are well-understood in many cases [CH93].

Another class of structures that have gained a lot of interest in recent years are dissipative solitary structures [Rie99, AA05]. These structures extend only over a small area and exhibit a kind of particle-like behavior. In analogy to the solitons in conservative systems, which are localized wave phenomena with similar properties, the solitary states in dissipative systems are often called 'dissipative solitons'. Prominent examples are current density filaments in gas discharges and semiconductors [BP95] as well as localized excitations, so-called oscillons, that are observed in a thin layer of vertically oscillating granular media [UMS96] or fluid [LAF96].

The dissipative soliton is an attractor of the dynamics of the considered system, and in contrast to solitons in conservative systems, its amplitude and size are fixed by the parameters and do not depend on the initial conditions [KO94]. It has been shown in different model systems, however, that the dissipative soliton is not necessarily unique, but that a sequence of higher-order solitons might exist that differ in their inner structure [RK90, PMEL98, OSF99]. An analytical description of dissipative solitons is complicated in general, since they are high-amplitude, thus strongly nonlinear, structures that cannot be treated by perturbative methods.

Much progress in the field of dissipative solitons has been made in optics, where localized light spots are observed in the transverse plane of a laser beam that passes through an optically nonlinear system. As a main advantage of optical systems, the interaction between light and matter is well-understood in many cases, and a theoretical description of the nonlinear system can be derived from first principles.

Different approaches have been proposed in order to understand the mechanisms that lead to the formation of dissipative solitons. They describe solitons in systems that display bistability between two extended homogeneous or patterned states. In most cases, solitons are predicted to occur in systems where a homogeneous and a patterned state coexist due to a subcritical bifurcation [TF88, FT90, TML94, FS96]. Also, most of experimentally observed solitons were found in such a situation [SFAL00, SKTT97, BTB$^+$02].

Another approach describes the occurrence of solitons as a result of the motion and interaction of fronts that connect two homogeneous states of a system [RK90]. An interesting situation arises if the two extended states are equivalent or nearly equivalent. In this situation, the front velocities are expected to be low, which should favor the existence of solitons. Indeed, systems with two equivalent extended states are frequently encountered in nonlinear optics, and the formation of solitons has been widely studied in theoretical models describing these systems [Lon97, SSM98a, PMEL98, GMT00, TSW98]. Only in one case, however, solitons were observed experimentally [TSW98].

The subject of this thesis is the experimental and theoretical investigation of the formation of spatial solitons in an optical system that exhibits a pitchfork bifurcation. This system is a modification of the well-known single-mirror feedback scheme [Fir90, DF91, DF92], which consists of a laser beam that passes through an optically nonlinear medium and is fed back into the medium by a mirror after having propagated over a certain distance. In this work, sodium vapor is used as the nonlinear medium. The single-mirror feedback system with sodium vapor has proven to be one of the most versatile structure-forming experiments in many preceding works [LA98, LAA$^+$99, AL01, SFAL00]. Its significance as a model system for the analysis of spatial structures is particularly enhanced by the availability of a well-established microscopic model for the light-matter interaction [MDLM86], which enables an extensive theoretical treatment of the experimental system. In the present setup of the experiment, a polarization instability has been observed which has been interpreted as a symmetry-breaking pitchfork bifurcation [YOKO84, GWKL$^+$00].

In this work, special emphasis is laid on the identification and characterization of the mechanisms that lead to the formation of stable solitons. It will turn out, that front motion plays a central role. In this context, the prediction of recent theoretical works that the extension of one-dimensional models to two spatial dimensions is not trivial, will be taken into account [GCOM01]. Experimental results in two-dimensional systems have

been limited to a rough qualitative description yet [TSW98, TZWW99]. The lack of a quantitative experimental description is going to be addressed in this work.
It will turn out that not only the fundamental single-peaked soliton can be observed, but also a set of stable higher-order solitons exists, whose existence has been predicted in many theoretical works. The family of solitons will be characterized with respect to their basic properties and to their regions of existence in parameter space. A numerical treatment of the system will give further insight into its bifurcation structure. Following the detailed characterization of the soliton family, an overview of the interaction properties of solitons as well as of more complex structures will conclude the work.

Chapter 2

Dissipative optical solitons

2.1 The soliton concept

The concept of solitons is one of the central issues of nonlinear physics. In a rather strict definition, a soliton is *a large-amplitude coherent pulse or very stable solitary wave, the exact solution of a wave equation, whose shape and speed are not altered by a collision with other solitary waves* [1]. Solitons in that sense can be obtained as localized solutions of integrable systems that are described by conservative nonlinear partial differential equations, the most prominent ones being the Korteweg-de Vries equation, the nonlinear Schrödinger equation, and the Sine-Gordon equation [Rem99]. In many other cases, exact soliton solutions cannot be obtained. However, the qualitative phenomenon of a soliton *representing a balance between the effect of dispersion and that of nonlinearity*[1] is quite common. Hence, these solitary waves are often also referred to as solitons.

A more phenomenological definition associates the term soliton *with any solution of a nonlinear equation (or system) which (i) represents a wave of permanent form; (ii) is localised, so that it decays or approaches a constant at infinity; (iii) can interact strongly with other solitons and retain its identity*[2].

As an extension of the solitons in conservative systems, localized structures in dissipative nonlinear systems are called 'autosolitons' [KO94] or 'dissipative solitons' [AA05]. *An autosoliton is a steady solitary intrinsic state (eigenstate) of a nonequilibrium system*[3]. Similarly to the conservative case, the dissipative soliton originates from an equilibrium between a nonlinear effect and a process that inhibits localization. In contrast to the conservative case, *a localized structure in a dissipative system requires a continuous en-*

[1] in [Rem99], page 11
[2] in [DJ96], page 15
[3] in [KO94], page 2

ergy flow into the system, and, in particular into the localized structure, in order to keep it "alive"[4]. Hence, a second balance, namely that between the energy input and output, has to be fulfilled. As a result, the *parameters of autosolitons [...] depend entirely on the parameters of the system, and do not depend on the properties of the initial perturbation which gave rise to this particular autosoliton in the first place*[5]. Hence, *autosolitons [...] may be viewed as attractors characterized by a certain range of attraction. [...] An autosoliton corresponds to an attractor in the configuration space - that is, in a space each point whereof is associated with certain functions which describe one of the possible distributions of the system with respect to coordinates. A system may be characterized by several attractors in this complex configuration space, and may therefore host autosolitons of different types and shapes. [...] Accordingly, the initial perturbation must bring the system into the range of that attractor which corresponds to the autosoliton of the desired type, which will then form spontaneously after the initial perturbation is switched off*[6]. This is in strong contrast to the conservative soliton, where continuous families of solutions are formed.

Dissipative solitons have found considerable interest in a vast variety of systems [Rie99, AA05]. Among these are hydrodynamic systems [LAF96], granular media [UMS96], gas discharges [SSBP98] and nonlinear optics. The fact that dissipative solitons are observed in physically completely different systems suggests that the underlying mechanisms have large similarities.

In the following section, a short review will be given on the field of dissipative optical solitons. The qualitative mechanisms and theoretical descriptions that have served as a good model for the understanding of the formation of solitons as well as the experimental systems that have given evidence of the existence of solitons are presented in terms of their relevance for the conception of this work.

2.2 Dissipative optical solitons

Historically, optical solitons were considered in conservative systems. One type of conservative soliton is a soliton that is localized in time ('temporal soliton'). A typical example is a light pulse that is propagating along an optical fiber. Normally such a wave packet would spread during propagation due to the dispersion of the medium. This spreading is counteracted by the action of a nonlinearity (in the simplest case, a focusing Kerr nonlinearity, where the refractive index of the material increases linearly with increasing

[4] in [AA05], preface
[5] in [KO94], page 2
[6] in [KO94], page 3

light intensity), which leads to a self-phase modulation of the pulse. In terms of applications, these temporally confined light pulses are interesting for the improvement of the bandwidth of long transmission lines of optical data communication networks.
The other type of soliton in the conservative limit is the spatial soliton, which is a light beam that is spatially confined in the transverse direction during the propagation in bulk media [KA03]. Here, the focusing nonlinearity compensates for the diffractive spreading that would normally occur. Since the first observation of such a spatial soliton [BA74] a wide field has evolved. Especially due to the availability of new media in the last ten years, many types of (far more general) spatial solitons have been discovered and are widely discussed in terms of their application in all-optical information systems. A comprehensive overview on conservative optical solitons can be found e.g. in [KA03].
The conventional spatial soliton propagates in an essentially lossless medium. A different type of spatial solitons with its own characteristic features is observed in the dissipative regime, where gain and losses play an essential role in the formation of transverse structures. The basic idea in the development of the field of dissipative optical solitons was to trap the spatial optical soliton between two mirrors, i.e. in an optical cavity, filled with a nonlinear medium. These 'cavity solitons' are self-localized due to the nonlinearity of the medium like classical spatial solitons. However, the losses that generally appear in optical cavities need to be compensated by either gain within the nonlinear medium or an external pump field. Actually, even one of the cavity mirrors can be completely removed in such a situation. The solitons arising in such single-mirror feedback schemes are often called 'feedback solitons'. Due to the need of an energy balance, the dissipative soliton has a fixed shape and amplitude for the given parameters, being an attractor of the dynamics. Nevertheless, a discrete sequence of different dissipative solitons might exist. This is in strong contrast to the conservative case, where continuous families of solitons are observed. Dissipative spatial solitons are interesting in terms of information processing for two reasons: one the one hand they can be ignited and erased by means of a short light pulse, which makes them a candidate for an all-optical memory. On the other hand, their position in the transverse plane can be manipulated, e.g. by external gradients, which enables data buffering in a shift register.

2.2.1 Mechanisms leading to soliton formation

From a theoretical point of view, the phenomenon of self-localization of dissipative spatial structures has been treated using different approaches. They are based on the assumption of a bistability of two spatially extended states. Those states might be homogeneous states or patterns. The two most prominent cases will be presented in the following. However, these two approaches are not mutually contradictive, though their relation is

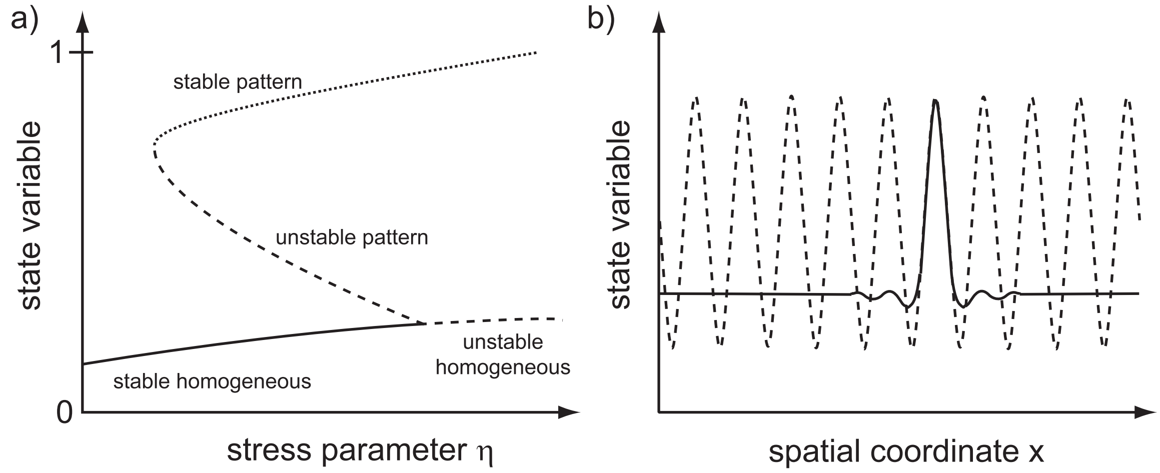

Figure 2.1: Solitons in the presence of a subcritical modulational instability. a) Schematic bifurcation diagram. b) Soliton (full line) as a constituent of an extended pattern (dashed line).

not completely understood. An overview of the field can be found in various review articles and books [FW02, Lug03, PMW03, MT04, DHV04, AA05].

Solitons in the presence of a subcritical modulational instability

The first approach describes the formation of solitons in a situation where a homogeneous state becomes unstable against the formation of patterns [TF88, FT90]. If the bifurcation is subcritical, there is a range of the stress parameter where the homogeneous solution and the pattern coexist (see schematic bifurcation diagram in Fig. 2.1a). Depending on the initial conditions, the system typically approaches one or the other solution in such a bistable situation. However, in a spatially extended system, both solutions can coexist at the same time. And this finally leads to the observation of solitons. The soliton typically is very similar to a single constituent of the patterned solution that is embedded into the homogeneous solution (see Fig. 2.1b). Hence, starting from the homogeneous solution, the system is locally switched to the patterned solution. This ignition can be achieved by a local increase of the control parameter beyond the point where the homogeneous state becomes unstable. In optics, this is achieved by means of a short light pulse. Using an (out of phase) light pulse that lowers the control parameter, a soliton can similarly be erased.

Solitons in nonlinear optics that exist in the presence of a subcritical modulational instability have been reported to occur in generic equations of the Swift-Hohenberg type [TML94], in cavities filled with a Kerr medium [SFM$^+$94], optical parametric oscillators [TM99, Lon97, SSM97], semiconductor microresonators [BLP+97, MPL97, STB+98, TSB+99b], cavities filled with a saturable absorber [FS96, BLS96] and in single-mirror feedback arrangements using sodium vapor [SFAL00] or an electrooptical device [NOTT95] as the nonlinearity (to name just the pioneering works). In many cases where solitons are predicted, the subcritical modulational instability is accompanied by a situation of nascent optical bistability between homogeneous solutions. This situation is characterized by a large dependency of the homogeneous solution on the control parameter. In fact, most of the experimentally observed solitons are observed in such a situation (see below).

One or more solitons can be ignited at arbitrary positions, which makes the system highly multistable. A single soliton is often surrounded by small-amplitude oscillatory tails. If the distance between two solitons is small enough, they can interact via these oscillatory tails. As a result, one or more preferred distances between solitons are observed [BLS96, TSB+99a, SFAL00, GNKT03, BRB05]. If the system is switched to the patterned state over a larger area, i.e. a cluster of densely packed solitons, this structure is called 'localized pattern' [TML94, CRT00b].

Solitons move in the presence of spatial (amplitude and/or phase) gradients [RK90, FS96, STB+98, SJMO05, BRB05]. On the one hand, this is welcome in terms of possible applications. Solitons can be arranged by will using external gradients. On the other hand, spatial gradients are omnipresent in experimental systems due to the always limited size of the driving field and inhomogeneities within the experimental system.

The existence of a discrete soliton family, whose members differ in the number of radial oscillations, is studied in a model of semiconductor microresonators [MPL97]. The family of solitons coexists with multiple simple periodic patterns. The solitons are surrounded by oscillating tails.

Fronts and solitons in the presence of optical bistability

The second approach leading to the formation of solitons is connected to the very general phenomenon of moving domain boundaries that separate two different states of the considered system. The motion of domain boundaries is considered, e.g. in reaction-diffusion systems, hydrodynamical systems, population dynamics, bacterial growth and many other systems. A review on these systems can be found in [vS03].

Front motion has been widely discussed in terms of thermodynamical first order phase transitions. Typically a system is considered that is prepared in an unstable state which then relaxes to a thermodynamical equilibrium. In such systems, the motion of domain walls is well-understood [GMS83]. Generally, growth laws that describe the evolution of the size $R(t) \propto t^x$ of a domain can be obtained. The growth coefficient x depends on the physical system that is considered.

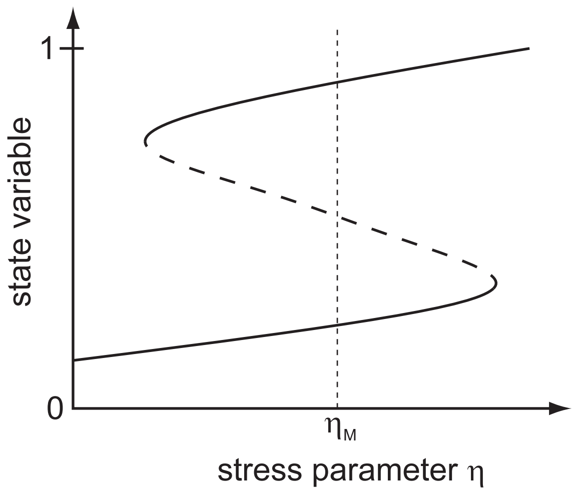

Figure 2.2: Optical bistability between two homogeneous solutions

Systems that do not reach a thermodynamical equilibrium after a transient has passed can be divided into systems where a potential similar to a free energy can be derived (potential systems) and systems where such a potential cannot be obtained (nonpotential systems). In both cases, the analysis of such systems is much more complicated, and there is only a partial understanding of the involved mechanisms [Mer92, CM95, JR97, GSMT98]. Much effort has been made in models describing nonlinear optical systems. These will be discussed below. In some cases, qualitative results can be transferred from the case of systems that reach a thermal equilibrium.

In potential systems, an interface connecting two states will generally move. In a one-dimensional system, the direction of motion is given by the relative stability of the two states. The less stable (often called metastable) state is invaded by the more stable state. The velocity of the front is determined by the energy difference of the two states. If the two states are energetically equivalent (at the Maxwell point η_M), the front will not move. In nonpotential systems, the relative stability of the two states cannot be related to an energy difference. However, still many phenomena are qualitatively similar to the potential dynamics. A Maxwell point can be defined as the unique parameter value where a front is at rest [Pom86]. If two-dimensional systems are considered, a further analysis relies on the dynamics of curved domain walls (see below).

A mechanism based on front motion that leads to the formation of so-called 'diffractive autosolitons' in optical systems was considered first in the pioneering works of Rosanov [RK90, Ros91, Ros02]. A model of an externally driven ring resonator that is filled

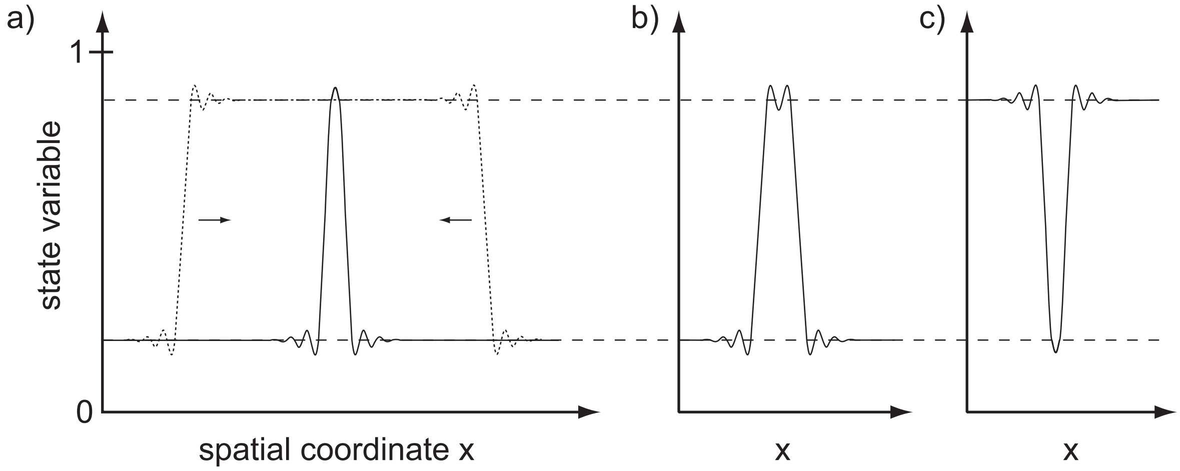

Figure 2.3: Solitons in the presence of optical bistability. a) Front motion (dotted line) and stabilization of solitons (full line) due to locking fronts. b) Second order soliton. c) dark soliton

with a nonlinear medium which is modelled as a two-level system is considered. This dissipative system shows bistability between two homogeneous states that differ from each other in their intensity and show an S-shaped characteristic curve (see schematic curve in Fig.2.2). In a spatially extended system, those two states can be connected by a 'switching front' within the bistability range. In a one-dimensional system, the switching front will generally move due to the nonequivalence of the two homogeneous states (dotted line in Fig. 2.3a). If two switching fronts approach each other, they will typically annihilate and leave the system in the homogeneous state that is more stable for the given parameters. However, in optical systems, different points in the transverse plane are coupled via diffraction. Due to this diffraction, the switching front will typically be surrounded by oscillatory tails. Solitons can emerge if, in a one-dimensional picture, two switching fronts approach and start to interact via the nonmonotonic tails. Due to this interaction, the motion of the fronts may stop and lead to a stable localized structure (full line in Fig. 2.3a). This 'locking' mechanism is most probable for low front velocities, i.e. near the Maxwell point of the system (Fig. 2.2). Hence, the driving intensity range where stable solitons are observed includes the Maxwell value. The oscillatory tails often include more than one oscillation period. Hence, the locking process can take place at different spatial separations of the fronts, which leads to the observation of so called 'excited' or 'higher-order' solitons (see second-order soliton in Fig. 2.3b). Together with the single peaked fundamental soliton that has been discussed up to now, a discrete family of solitons emerges. The stability regions of the higher order-solitons are still located around the Maxwell point. However, they are smaller due to the decay of the oscillatory tails with increasing distance from the front. There are two types of solitons in systems that have two nonequivalent homogeneous solutions. A bright soliton is characterized by a high-intensity peak on a low-intensity background, while a dark soliton is a dark spot surrounded by an intense light field (Fig. 2.3c). Those two types of solitons have different properties due to the nonequivalence of the two homogeneous states.

Dissipative solitons are also predicted to occur in bistable active systems like lasers with a saturable absorber. A review on those structures can be found in [Ros02]. These laser solitons are often characterized by a point in the transverse plane where the intensity vanishes and the phase has a singularity. The phase variation along a closed path around this point is given by multiples of 2π. These 'topologically charged' solitons show a different interaction behavior than their uncharged counterparts but will not be considered further.

In more recent theoretical papers by Coullet et al. [CRT00b, CRT00a, CRT04], also the solitons that exist in the presence of a subcritical modulational instability (which were discussed in the preceding section) have been interpreted in terms of front dynamics. A front that connects the homogeneous state with the patterned state is considered . Within the bistable range, also this front will generally move. However, due to the high-amplitude oscillations within the pattern, the addition or removal of a single constituent of the pattern requires a certain amount of energy. As a result, a locking phenomenon is observed [Pom86]. There is a finite range of the control parameter, where single solitons and clusters of solitons (that can also be interpreted as localized patterns) are stable. Around this locking range, single constituents are added or removed from the cluster. In strict terms, the results of Coullet apply only in one spatial dimension. However, to a certain extent, they are also valid in two-dimensional systems. The resulting sequence of n-peaked localized states has been numerically confirmed in 1D and extended to two dimensional systems in [MFOH02]. These results show that a relation between one and the other interpretation of solitons exists.

2.2.2 Fronts, domains and solitons in the presence of two (nearly) equivalent states

An interesting situation that has attracted a lot of interest in recent years is the situation where two (nearly) equivalent homogeneous states exist due to a symmetry-breaking pitchfork bifurcation (see Fig. 2.4a). Depending on the considered system, the two states differ in their phase or polarization properties. However, they are equivalent from an 'energetic' point of view. As a result of this equivalence, the system is always at the Maxwell point independently of the control parameter. Hence, straight fronts that connect the two states will not move. It can be expected that soliton formation is simplified in such

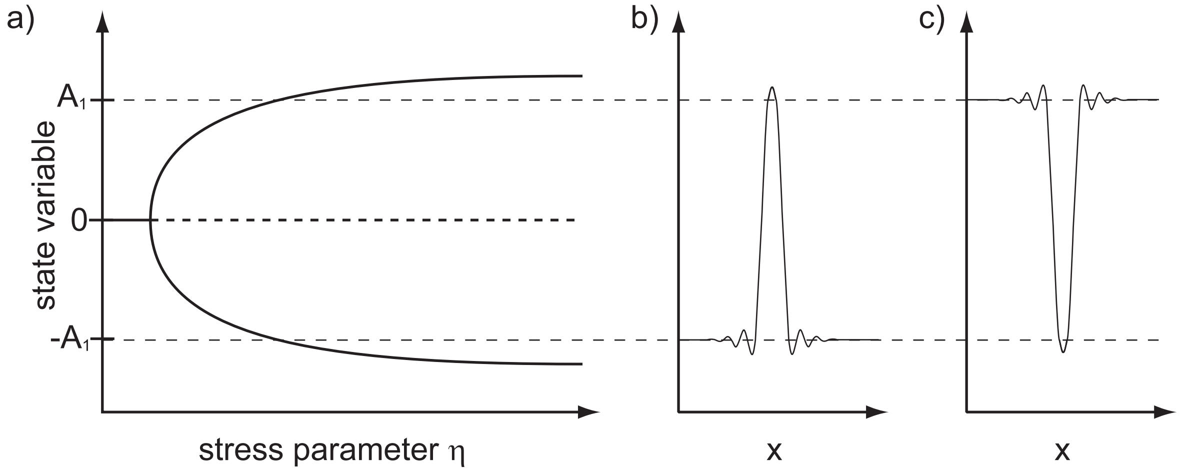

Figure 2.4: Solitons in the presence of a pitchfork bifurcation. a) schematic bifurcation diagram. b) 'positive soliton'. c) 'negative soliton'

a situation.
Pitchfork bifurcations are frequently encountered in different theoretical models connected to transverse nonlinear optics. This includes unspecific model equations like the Swift-Hohenberg equation [SMS97, OF96, SSM98b] and the parametrically driven complex Ginzburg-Landau equation[GCOM01, TM98, GCOSM04]. Another class of widely studied prototype systems are mean field models of a degenerate optical parametrical oscillator [THS97, Lon97, SSM98a, OSF99, OSSB00, OSF01, TMLB$^+$00, GCSM$^+$03], also non-mean-field models have been studied [BRT00]. In these models, a pitchfork bifurcation of the signal field is observed which is due to a phase indetermination. The bifurcation leads to two equivalent solutions that differ in phase by π. A similar phenomenon is observed in intra-cavity second harmonic generation [PMEL98]. Another system that exhibits a pitchfork bifurcation is a cavity that is filled with a vectorial generalization of a Kerr medium [GMT00, GCSM$^+$03]. Here, bistability is due to a polarization instability that leads to two equivalent homogeneous states that differ in the helicity of the polarization.
Though a front connecting two equivalent states will not move in one-dimensional models [THS97], this is not true in two-dimensional systems. In a two-dimensional system, a front typically has a certain curvature $\kappa = 1/R$. The curvature of a front will lead to a motion of the front, where the velocity increases with the curvature. This mechanism is often interpreted to be similar to a line-tension which is the two-dimensional equivalent of a surface-tension. Curvature-driven front motion is described in [SSM98a, SSM98b, OSF99, OSF01, GMT00, GCOM01, GAGW$^+$03, GCOSM04, BRT00, TMLB$^+$00]. In

many systems [OSF99, GMT00, GCOM01, GAGW$^+$03, GCOSM04], the normal velocity of the front is given by its local curvature: $v = -\gamma_c \kappa$, where γ_c is a coefficient that depends on the parameters. Often the dynamics of a large circular domain of radius R of one solution embedded into the other one is considered. The resulting dynamics is given by $dR(t)/dt = -\gamma_c/R$ and a growth law is obtained : $R(t) \propto t^{0.5}$. It has been shown that this exponent, originally valid for systems that reach a thermodynamical equilibrium with nonconserved order parameters [GMS83], applies to a very general class of systems out of the thermodynamic equilibrium [GCOM01]. It has been argued that different growth exponents that have been reported [BRT00, TMLB$^+$00] are non-asymptotic [GCOM01, Gom03]. Depending on the sign of γ, a circular domain will either contract and disappear ($\gamma > 0$) or expand ($\gamma < 0$), which leads to the observation of labyrinthine patterns [SSM98a, GMT00, GAGW$^+$03].

In many cases, a contracting circular domain will disappear due to the pronounced curvature-driven motion. This contraction might be stopped by the interaction of oscillatory tails that surround the front, which are omnipresent in optics due to the diffractive spatial coupling. As a result of this interaction, solitons are observed in parameter regions where curvature effects are small (small γ_c [GMT00]) or spatial oscillations are very pronounced. Another proposal [Cou02, GCOSM04] to stabilize solitons is to compensate for the curvature-driven contraction by the introduction of a small asymmetry of the underlying pitchfork bifurcation. Due to the resulting imbalance of the homogeneous states, the preferred state will have a tendency to expand, which might slow down or even stop the curvature-driven motion at a certain domain radius. The domain dynamics should then be governed by $dR(t)/dt = -\gamma_c/R + \gamma_i$, where γ_i depends on the asymmetry of the bifurcation and denotes the velocity of a straight front.

The fundamental soliton in systems with pitchfork bifurcation are often referred to as 'dark ring cavity solitons', which is due to the appearance of the soliton in the total intensity distribution of the light field. In many of the studied cases the fundamental soliton is accompanied by higher order solitons [SSM98a, PMEL98, OSF99, OSF01, GAGW$^+$03]. A type of soliton whose stability relies purely on curvature effects has been predicted and named 'stable droplet' [GCOM01, GAGW$^+$03, GCOSM04]. Due to the symmetry properties of the system, every soliton is accompanied by an inverse counterpart with equal properties. Only the roles of background and target state are interchanged. Hence, one might call them 'positive' (Fig. 2.4b) and 'negative' (Fig. 2.4c) solitons in contrast to the bright and dark solitons in systems with nonequivalent homogeneous states that differ from each other significantly.

Up to now, the discussion has been restricted to systems where the state variable of a front connecting the two equivalent states vanishes at a certain point ('Ising front'). In recent years, a phenomenon called 'nonequilibrium Ising-Bloch transition' has gained a lot of interest. If the state variable of the considered system is complex-valued, a front that connects two equivalent solutions does not necessarily include a point where both, real and imaginary part vanish, but might have a chirality ('Bloch front') [CLHL90, MPL+01]. While an Ising front is at rest if the two states it connects are equivalent, a Bloch front will move into a direction that is determined by the chirality of the front. A criterion for the onset of a transition from an Ising to a Bloch front was formulated and demonstrated in a model of intracavity second-harmonic generation in [MPL+01]. An Ising-Bloch transition was also found in optical parametric oscillation [VPAR02] and the control and steering of domain walls has been discussed [PASRV04].

2.2.3 Experiments on fronts and solitons in nonlinear optics

Though the large amount of theoretical studies has shown that the occurrence of spatial dissipative solitons is a quite general phenomenon in nonlinear optics, the number of experiments that have given evidence of the existence of these structures is rather limited. The next section is dedicated to giving a short overview of these experiments.

Laser with saturable absorber

Taranenko et al. describe the existence of a localized state in a laser cavity with saturable absorber [BTV92, TSW97]. Due to a global coupling mechanism only one localized state exists at a time. If another localized state is ignited, the first one disappears. The motion of a localized state in an external gradient is demonstrated. The solitons are interpreted to be due to the bistability between two homogeneous states.

Semiconductor microresonators

In passive resonators consisting of multiple quantum wells enclosed in a Bragg resonator, the existence of bright and dark solitons has been demonstrated [TGKW00, TGKW01, TW02]. Depending on the parameters, solitons exist either on a homogeneous or a patterned background. In both cases, the stability of the solitons is interpreted to be due to the locking of fronts. In addition, the individual switching of single constituents of a hexagonal pattern is demonstrated. Ignition and erasure of localized structures by means of a coherent addressing beam is shown. Even incoherent switching is possible. However, the erasure process relies on thermal effects that are undesired. The aspect ratio of the experiments was quite limited. Hence, the observed structures are slightly boundary dependent.

The generation of cavity solitons in broad-area vertical-cavity surface-emitting lasers (VCSELs) is very appealing for possible applications. Due to the large aspect ratio of these devices, a large number of cavity solitons could be obtained in principle. However, inhomogeneities within the devices complicate the observation of cavity solitons. The first proof of cavity solitons in VCSELs described the controlled ignition and erasure of two cavity solitons [BTB+02]. They are observed in a device that is electrically pumped close to but below the lasing threshold. A holding beam is injected, and switching is provided by coherent superposition with a focused addressing beam. The observed cavity solitons are interpreted to be related to a subcritical modulational instability. They exhibit independence and mobility despite the imperfection of the devices [HBF+04]. Currently promising attempts are being made towards the realization of a 'cavity soliton laser' that does not require external optical driving [Ack06].

Single-mirror feedback with sodium vapor

Schäpers et al. analyzed solitons in a single-mirror feedback arrangement using sodium vapor as the nonlinear medium [SFAL00, SAL01, Sch01, SAL02, SAL03]. The experimental setup is similar to the one that is considered in this work. However, due to the variability of the nonlinearity of sodium vapor, the solitons observed by Schäpers are entirely different from the ones reported here, as will be shown. The sodium vapor is irradiated by circularly polarized light and is exposed to an external oblique magnetic field. Under these conditions, a nonmonotonic response of the vapor is observed when the input intensity is increased [SAL02]. Localized states appear in parameter regions where a subcritical modulational instability leading from a homogenous state to hexagonal patterns is observed. At the same time, the system is in the situation of nascent optical bistability. Due to the nonlinear properties of the sodium vapor, robust incoherent switching of solitons by means of a circularly polarized addressing beam is possible [SAL02]. In neighboring parameter ranges, solitons are spontaneously generated. Solitons arrange in clusters that incorporate several preferred distances between the single entities [SFAL00]. The shape of the solitons coincides well with a single constituent of the coexisting hexagonal patterns, whose wave number corresponds well with the different preferred distances between the solitons [SAL03]. The solitons are shown to be stable due to a self-induced lens that warrants positive localized feedback [SFAL00, SAL03]. External gradients as they are induced by the Gaussian input beam lead to a motion of the solitons which come to rest at a certain distance from the beam center. By imprinting artificial gradients on the system, proof-of concept is given to applications like an all-optical memory and a buffer register [SAL01].

Single-mirror feedback in an electrooptic system

An intensively analyzed system exhibiting localized structures uses an electrooptic device as the nonlinearity [KST96, SKTT97, KTT98, RDBA00, Res05, BCF+06]. This Liquid Crystal Light Valve (LCLV) is composed of a liquid crystal layer, a dielectric mirror and a photoconductor that is sandwiched between two transparent electrodes [NOTT95]. It acts as a converter from spatial intensity distributions to spatial phase modulations.
In the experiment, the input light field is first reflected at the 'read side' of the device, thereby being modulated in phase. Then the light field propagates along a certain distance and is then directed onto the 'write side', thereby closing a feedback loop. This setup can be interpreted as a realization of the single-mirror feedback scheme [Fir90, DF91, DF92] that is also the basis of the experiment presented in this work.
Solitons appear as intensity peaks on a homogeneous background. They are interpreted as a constituent of a coexisting hexagonal pattern. Switching of individual solitons and a large variety of control and forcing mechanisms which use parameter gradients or filtering techniques have been demonstrated [RBB+02, GKNT02, GNKT03, GZD+05].
In a recent experiment, the bistability of two different localized structures has been reported [BPR+04]. In addition to the standard single peaked soliton a stable triangular localized state is observed. These solitons are interpreted to occur as patches of two different patterns evolving from two coexisting branches. In another experiment, the spontaneous nucleation of localized peaks is shown in a situation where bistability between two patterns that have different amplitudes is present [BRR05].
Clerc et al. [CNP+04] study the dynamics of fronts in a LCLV in the situation where the characteristic curve is S-shaped and connects two nearly homogenous, bright and dark, states. Qualitative evidence is given that a two-dimensional bright domain shrinks below a kind of Maxwell point and increases above that point. However, the dynamics is influenced by curvature effects. To minimize these effects, a quasi one-dimensional system is prepared and the front velocity is determined, delivering the Maxwell point.

Intracavity four-wave mixing

The only optical experiment that considers the case of two equivalent homogeneous states that emerge from a pitchfork bifurcation is a degenerate intracavity four-wave mixing experiment that uses a photorefractive crystal ($BaTiO_3$) as the nonlinear medium. As the four-wave-mixing process is phase sensitive, the two homogeneous states differ in phase and are separated by a phase difference of π. The authors of the first paper considering this experiment [TSW98, WVS+99] describe the appearance of domain boundaries connecting these two homogenous states. Depending on the detuning of the resonator,

different spatial structures are observed experimentally and numerically. For small detuning, domain dynamics is observed and the domains shrink and disappear. At large detunings, the domains grow. Asymptotically this leads to the formation of labyrinthine patterns. At intermediate detunings, the shrinkage of domains leads to the formation of stable localized spots that are interpreted as spatial solitons. The temporal evolution of the boundary length of arbitrarily shaped domains is characterized and domain contraction as well as time-independent solitary solutions are presented [TZWW99]. The stabilization of solitons is interpreted to be due to the locking of oscillatory tails. The overall change of the properties of the system with the control parameter confirms the predictions in [SSM98a, SSM98b] and shows similarities to the situation in [GMT00].
In recent experiments, the dynamics of domain walls was studied. Special emphasis was laid on the characterization of an Ising-Bloch transition. Larionova et al. [LPEM+04] gave evidence of the existence of Ising and Bloch fronts and showed that a relation between the curvature, the type and the velocity of a front exists. An experiment by Esteban-Martin et al. [EMTG+05] shows a controlled Ising-Bloch transition in a quasi one-dimensional system where curvature effects are suppressed by means of a Fourier filtering technique. In this experiment, domain walls can be injected, erased and positioned in a controlled manner by means of an addressing beam [EMTRV05].

2.3 The single-mirror feedback arrangement with sodium vapor

2.3.1 Motivation of this work

In the past years, knowledge of spatial dissipative solitons has rapidly increased. Nevertheless there are some very central questions that remain open from the experimental point of view. Despite of the large number of theoretical works that predict the existence of a discrete family of dissipative solitons, only the fundamental soliton has been observed experimentally. The first goal of this work is to prove the existence of such a soliton family experimentally. It can be expected, that the occurrence of a soliton family is more probable in systems that can be described in the framework of locking fronts that exist in the presence of two (nearly) homogeneous solutions than in systems where solitons are observed in the presence of a subcritical modulational instability. An especially promising situation is the one where front velocities are low over a wide range of parameters. As it has been described, such a situation is quite naturally given in systems that display a pitchfork bifurcation to two equivalent states. A straight front should rest in such a situation. In two-dimensional systems, the curvature of the front is expected to have an

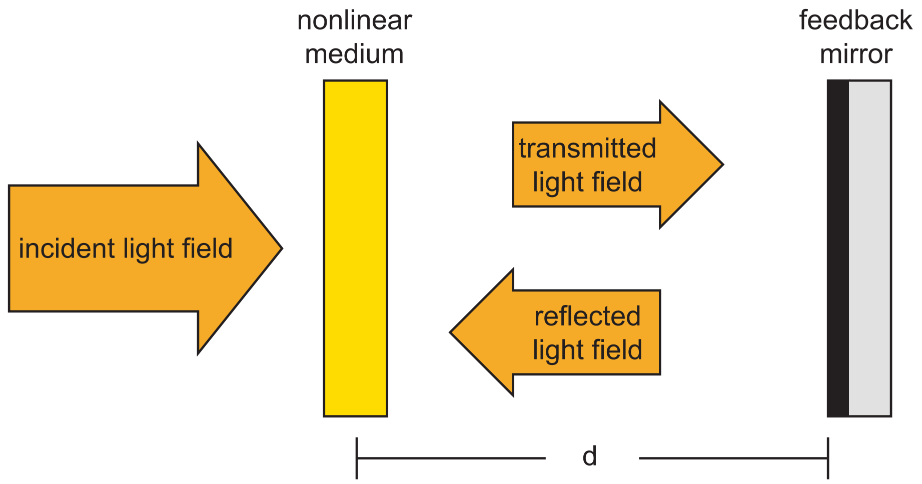

Figure 2.5: Schematic view of the single-mirror feedback arrangement

influence on the front dynamics. However, curvature-driven dynamics has not been experimentally analyzed in detail yet. Therefor, a comprehensive characterization of front dynamics in two-dimensional systems, including the phenomenon of locking fronts, is the second main goal of this work.
Though in principle optical systems with pitchfork bifurcation are promising candidates for the analysis of front motion and soliton formation, their experimental realization is often not practicable. Up to now, only the described four-wave mixing experiment has given evidence of a (fundamental) soliton and domain dynamics in general. Thus, more experimental work on systems with pitchfork bifurcation would be desirable.
In this section, the basic concept of an experiment will be presented which seems to be an appealing candidate for a systematic analysis of the open questions. First, the theoretical concept behind the single-mirror feedback arrangement will be illustrated. Afterwards, the choice of the nonlinear medium and modifications of the standard scheme will be elucidated, and an overview of the previous results obtained in this experiment will be given.

2.3.2 Basic concept

The single mirror feedback arrangement was introduced by d'Alessandro and Firth [Fir90] as a model system for optical pattern formation whose theoretical description is conceptually simple. Originally designed for the observation of simple periodic patterns

[DF91, DF92], it has developed to a workhorse for the investigation of optical structures. Especially the most systematic experiments on dissipative solitons were conducted in realizations of the single-mirror feedback configuration (see previous section). The basic scheme of the single-mirror feedback arrangement is depicted in Fig. 2.5. It consists of a thin slice of an optically nonlinear medium and a plane feedback mirror at a distance d. A light field that is assumed to be a plane wave is injected into the medium. The portion of light that is transmitted by the medium then propagates towards the feedback mirror and is fed back into the medium after having propagated over the distance $2d$.
Dissipative spatial structures originate from the interplay of a nonlinearity with some kind of spatial coupling. The main advantage of the single-mirror feedback arrangement that leads to a significant simplification of the theoretical description is the spatial separation of nonlinear interaction and spatial coupling. The thickness of the medium in the direction of light propagation L is assumed to be small. Under this assumption, the diffraction of light within the medium can be neglected, and only the nonlinear interaction between light field and medium has to be taken into account. Contrary to the situation within the medium, no nonlinearities occur during the propagation of the light field towards the mirror and back. Here only diffraction has to be taken into account.
A further simplification is given by the assumption of instantaneous feedback which neglects the delay induced by the finite speed of light. This assumption is fulfilled by the choice of a nonlinear medium that relaxes on a significantly slower timescale than the round trip time. Furthermore, a diffusive spatial coupling within the medium is assumed that washes out the standing wave pattern that is induced by the interference of the forward and backwards propagating light fields.
D'Alessandro and Firth analyze a single-mirror feedback arrangement with a Kerr-type nonlinearity. This is a medium without absorption whose refractive index varies linearly with increasing light intensity. In the following, a focusing nonlinearity is assumed, where the refractive index increases with the light intensity. If the input intensity is increased, at a certain threshold intensity a spatially extended pattern with hexagonal symmetry emerges spontaneously. The occurrence of periodic patterns in a single-mirror feedback arrangement can be explained by means of the Talbot effect [Tal36]. This linear optical effect describes the periodical conversion of a light field that is transversally modulated in phase into a light field that is amplitude modulated and back due to diffraction. The distance where the light field is recovered in its original state is called Talbot length and is given by

$$z_T = \frac{4\pi k_0}{q^2}, \tag{2.1}$$

where k_0 is the wave number of the light field in the direction of propagation and q the wave number of the transverse modulation. After a propagation distance of $t_T/4$, a conversion between phase and amplitude modulation is accomplished, whereas the modulations in planes that are separated by $z_T/2$ are transversally shifted in phase by a half wavelength. In the single-mirror feedback arrangement, fluctuations within the medium induce broadband spatial modulations of the refractive index. The light field that is transmitted by the medium will be modulated in phase. During the following propagation, due to the Talbot effect, the phase modulation will by transferred into an amplitude modulation. For certain Fourier components of the transverse spatial modulation, the corresponding propagation distance matches $2d$. If the spatial phase of the intensity modulation of that Fourier component matches the one of the corresponding original modulation of the refractive index, the latter can grow due to the nonlinearity of the medium. Thus, starting from an infinitesimal fluctuation within the medium, this mechanism leads to a growth of a macroscopic transverse refractive index profile. Due to the diffusive damping within the medium, the structure that evolves will have the lowest resonant wave number. The shape of the evolving pattern cannot be predicted by the Talbot effect. It will be determined by the nonlinear interaction of the evolving Fourier modes.

If different nonlinearities are considered, the conditions for a positive feedback are changed. The corresponding wave numbers are given by

$$q_n^2 = \left((n-1) + \frac{l}{4}\right) \frac{2\pi k_0}{d} \quad \text{with} \quad n \in \mathbb{N}. \tag{2.2}$$

If purely dispersive media are considered positive feedback for a focusing medium is provided for $l = 1$, while a defocusing medium (refractive index decreases with increasing intensity) requires $l = 3$. In the case of absorptive media, a saturable absorber (absorption coefficient decreases with increasing intensity) gets positive feedback for $l = 4$, while a limiting absorber (absorption coefficient increases with increasing intensity) requires $l = 2$. In general, nonlinear media exhibit a mixed nonlinearity. Therefor the Talbot effect gives only a rough estimate of the length scale to be observed.

2.3.3 Sodium vapor as the nonlinear medium

The single-mirror feedback arrangement does not only represent a conceptually simple structure-forming system from the theoretical point of view. Also the setup of experiments that can be taken as a realization of a single-mirror feedback scheme is comparatively simple. Over the last fifteen years, single-mirror arrangements using very different types of nonlinear media have been realized [Hon93, TBWS93, TNT93, PRA93, GMP94, AL94, DSS+98]. Each of them has its advantages, like e.g. low threshold intensities, nearly

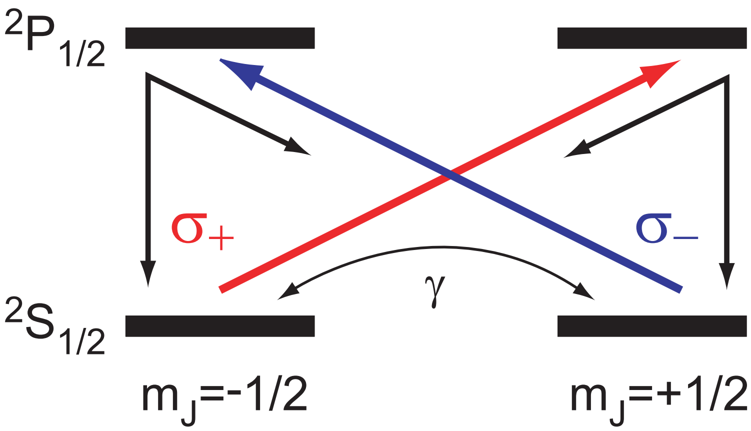

Figure 2.6: Kastler diagram of the sodium D_1 transition.

Kerr-type nonlinearity or convenient timescales. In this work, sodium vapor is used as the nonlinear medium.

The nonlinearity of sodium vapor is significantly different from the Kerr-type media discussed in the preceding section. It is provided by optical pumping [Kas50]. The nonlinearity has both a dispersive as well as an absorptive character. The dominating effect is chosen by the parameters. From the experimental side, the use of sodium vapor has the big advantage that atomic vapors can be prepared with a high optical quality. Furthermore, the nonlinear optical properties of the vapor can be manipulated in various ways by well-controlled external parameters. From the theoretical side, the use of sodium vapor offers the advantage that a well-established microscopic model for the light-matter interaction exists that has been derived by the density matrix formalism from quantum mechanics [MDLM86]. For the D_1 lines of alkali metal vapors the corresponding equations reduce to a simple form and allow for an analytical and numerical treatment.

The sodium vapor is prepared in a buffer gas atmosphere of nitrogen, which leads to a homogeneous broadening of the D_1 line that is significantly larger than the hyperfine splitting and the Doppler broadening. Under these conditions, the D_1 transition can be treated as a homogeneously broadened $J = \frac{1}{2} \to J' = \frac{1}{2}$ transition. This approach has proven successful in many preceding works that consider transverse effects [LA98, LAA$^+$99, AL01, LAAB98, Ack96, Gah96, Aum99, Sch01, GW02, Hun06].

Optical pumping [Kas50] is illustrated in a Kastler diagram of the transition in Fig. 2.6. Without the presence of a light field, the Zeeman substates will be equally populated.

If a σ_+ polarized light field is applied, it will couple only to the Zeeman substate with $m_J = -\frac{1}{2}$ due to selection rules. Transitions to the $m_J = \frac{1}{2}$ excited state will take place. From this state, the system relaxes into both substates of the ground state (though not with equal probabilities). As a net effect, a population difference between the Zeeman substates is induced. The normalized population difference (ranging from -1 to +1) is called *orientation* w. This orientation determines the nonlinear optical properties of the vapor, i.e. its nonlinear susceptibility χ for σ_+ (+) and σ_- (-) polarized light:

$$\chi_\pm(w) = \chi_{lin}(1 \mp w) \tag{2.3}$$

Here, χ_{lin} is the linear susceptibility. For any nonvanishing orientation, the susceptibilities for the circularly polarized light fields differ from each other. Since the collision-induced relaxation rate γ of the Zeeman substates of the ground state towards the thermal equilibrium is small, optical pumping is very efficient and can completely empty the substate that couples to the light field at very low light intensities. In this situation, the vapor becomes transparent for the light field, i.e. the nonlinearity of the vapor is saturable. It is known, however, that spatial structures do not appear in a saturated medium [Ack96]. Therefor a mechanism has to be induced that prevents the medium from being saturated. In many preceding works, an external transverse magnetic field has been used, which induces transitions between the Zeeman sublevels and acts like a damping mechanism [ALHL95, SFAL00, HAL04]. Another possibility is the introduction of a second circular polarization component with opposite helicity (σ_- light). It will couple to the substate of the ground state with $m_J = \frac{1}{2}$ only and provide optical pumping into the opposite direction (see Fig. 2.6). In the single-mirror feedback arrangement, the second polarization component can be included in the input field by the use of either elliptically or linearly polarized light. If the light field is chosen to be linearly polarized, it contains equal portions of σ_+ and σ_- light. No net pumping occurs in this situation, the orientation stays zero. However, a so-called polarization instability can take place, where the linear polarization becomes unstable against the generation of new polarization components. In such a situation, square patterns were observed at threshold [ABL+97]. If an elliptically polarized light field is used, the system loses its symmetry due to the preference of one circular polarization component and a transition to hexagons is observed [ABL+97].

A second circular polarization component can also be introduced into the system by placing a polarization-changing element in the feedback loop of the single-mirror feedback arrangement. In an experiment with linear input polarization and a quarter-wave-plate in the feedback loop, eightfold quasipatterns were observed [AAGWL02]. If a circularly polarized input is used in combination with a quarter-wave plate in the feedback loop, secondary bifurcations leading from hexagonal patterns to twelvefold quasipatterns

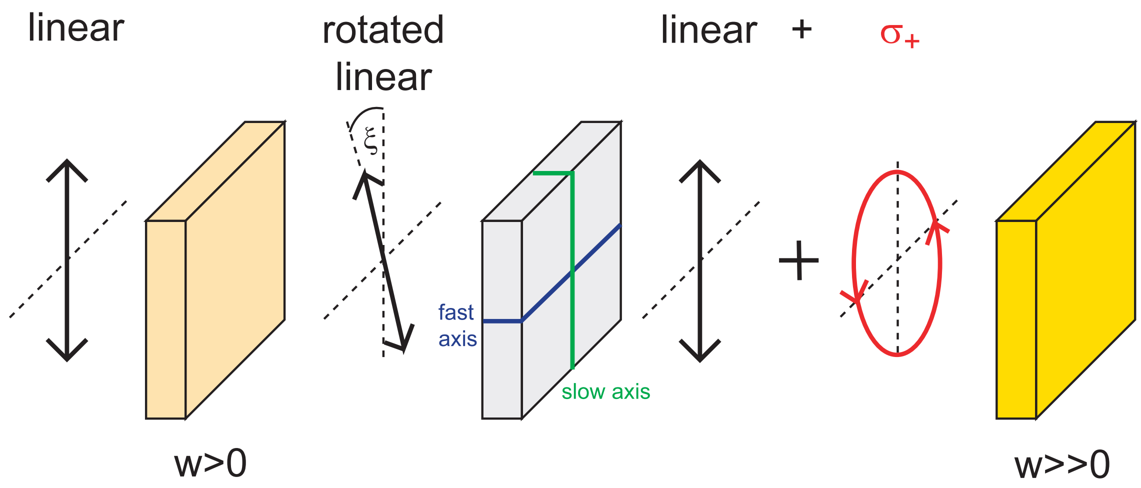

Figure 2.7: Mechanism of the polarization instability. See text for explanation.

[HGWA+99] and superlattice [GWHAL03] patterns are observed.

2.3.4 Single-mirror feedback with $\lambda/8$ retardation plate

Already in 1984, a single-mirror feedback arrangement with sodium vapor and a $\lambda/8$ retardation plate in the feedback loop has been analyzed by Yabuzaki et al. [YOKO84]. In this work, the transverse spatial dimensions have been neglected. Recently, this system has been reconsidered by Große Westhoff et al. [GWKL+00] with respect to transverse effects. These experiments provide the basis of the experiment in this work.

Both works consider a linear input polarization. After the beam is transmitted through the cell, it passes the $\lambda/8$ plate, propagates towards the feedback mirror and is reflected back into the medium, again passing $\lambda/8$ plate. The double transmission of the $\lambda/8$ plate is equivalent to a single pass through a quarter-wave plate. Hence, as long as the linear polarization is not aligned with one of the optical axes of the wave plate, the light field that is fed back into the medium will be elliptically polarized. The imbalance of the circularly polarized components of that light field will lead to optical pumping within the medium.

Yabuzaki et al. studied the observation of optical bistability due to a symmetry-breaking pitchfork bifurcation. The mechanism that leads to the polarization instability is depicted in Fig. 2.7. For simplicity, a pure dispersive nonlinearity of the sodium vapor is assumed. The slow optical axis of the wave plate is assumed to be aligned with the direction of polarization of the linearly polarized input light field. Hence, no optical pumping occurs if the orientation is zero. If, however, a small perturbation of the orientation is assumed (a positive perturbation is considered here), the circularly polarized components of the input light field experience a nonlinear phase shift that is of opposite sign for the different helicities. In the picture of linear polarizations, the polarization vector of the light field that is transmitted by the vapor is rotated by a (positive) angle ξ. At this point, the action of the quarter-wave plate comes into play. Since the polarization vector is not aligned with the optical axis of the wave plate anymore, the light field that is reflected into the medium will be elliptically polarized. This light field can be divided into a component of linearly polarized light (which does not lead to optical pumping within the medium) and a component of circularly polarized light. In the case considered here, an excess of σ_+ light is produced, which leads to an optical pumping process that enhances the initial perturbation of the orientation distribution. The orientation as well as the polarization rotation angle increases further. In the same manner, a negative perturbation of the orientation is amplified, which results in a macroscopic negative orientation and a negative polarization rotation angle ξ. The mechanism is completely symmetrical to the case with positive orientation.

At $|\xi| = 45°$, the feedback field is purely circular, which results in an optimal optical pumping. If the polarization angle exceeds rotation angle of $|\xi| = 45°$, optical pumping is reduced again which leads to a saturation of the polarization rotation.

If the input power is increased from zero, the linear input polarization becomes unstable due to the described mechanism at a certain threshold, which is essentially given by the losses within the medium. The bifurcation of the system leads to the observation of two equivalent states with positive and negative orientation. A similar bifurcation diagram is shown in Fig. 2.4a. The observed bifurcation has been interpreted as a pitchfork bifurcation [YOKO84, GWKL$^+$00]. In principle, both branches should be chosen with equal probabilities if the threshold is crossed. In the experiment, the perfect symmetry-breaking bifurcation is observed only in a close approximation. This is due to the structural instability of this type of bifurcation. A disturbed pitchfork bifurcation is observed if the optical axis of the wave plate is not perfectly aligned with the input polarization [YOKO84]. In this situation, one of the two states is preferred and is always chosen by the system if the input power is increased from zero. The branch can be changed by rotating the wave plate back and forth about an angle of 90°. Also a change of branches by means of a circularly polarized second laser beam that overcompensates the optical pumping process is theoretically considered [YOKO84].

If transverse spatial effects are considered, it turns out that the pitchfork bifurcation leads to two spatially homogeneous solutions. If the input power is increased by two orders of magnitude, a modulational instability is observed on both branches of the pitchfork bifurcation [GWKL+00]. At a certain threshold power, the system displays hexagonal patterns which are again equivalent and differ only in the sign of the orientation distribution. The appearance of hexagons is due to the broken inversion symmetry of the system when the pitchfork bifurcation has already occurred. In switch-on experiments, where the input power is increased from zero to a value above the threshold for pattern formation, typically one of the hexagonal patterns is observed. In some cases, a pattern is observed which consists of a polarization front that connects two domains of opposite elliptical polarization.

Große Westhoff et al. also analyze the situation where the fast axis of the wave plate is aligned with the input polarization. In this case, the input polarization is stable, since fluctuations of the orientation experience negative feedback. The inversion symmetry of the system is maintained. Also in this situation, a modulational instability is observed that leads to the observation of triangular or rhombic patterns. The experimental findings are well reproduced by an analytical as well as a numerical treatment of the microscopic model.

In conclusion, the single-mirror feedback scheme with sodium vapor and $\lambda/8$ wave plate seems to be appropriate for a systematic analysis of the open questions that were given in the beginning of this subsection. The previous works [YOKO84, GWKL+00] as well as preliminary numerical simulations [GW03] have indicated that this system fulfills many of the prerequisites that are expected to play a fundamental role in the formation of such structures. First, the system displays a symmetry-breaking pitchfork bifurcation to two equivalent homogeneous states. An imperfection of this bifurcation that is considered useful for the modification of front dynamics can be introduced in a well-controlled way. Furthermore, it has been shown in previous works that the possibility to use an incoherent addressing beam in the sodium system results in robust switching between bistable states. This should simplify the preparation of domains and solitons. The occurrence of a modulational instability within the accessible parameters range is a further phenomenon that may help to provide front locking due to spatial oscillations. In addition, the observed experimental phenomena can be compared to theoretical results that can be obtained thanks to the availability of a well-established microscopic model.

Chapter 3

Experimental setup

3.1 Overview

An overview of the experimental setup is shown in Fig. 3.1. It consists of three building blocks that have to meet certain requirements resulting from the aim of the experiment:

- Beam preparation

  For the observation of solitary structures, it is necessary to have two laser beams. The 'holding beam' contains most of the input power and drives the nonlinearities of the vapor in a spatially extended region, whereas the 'addressing beam' is used to increase the laser power locally to ignite and erase solitary structures. Both beams need to be controlled in their power, polarization, frequency and beam profile individually.

- Single-mirror feedback arrangement

  The single-mirror feedback arrangement is the center part of this experiment. It consists of a nonlinear medium, in this case sodium vapor in a nitrogen buffer gas

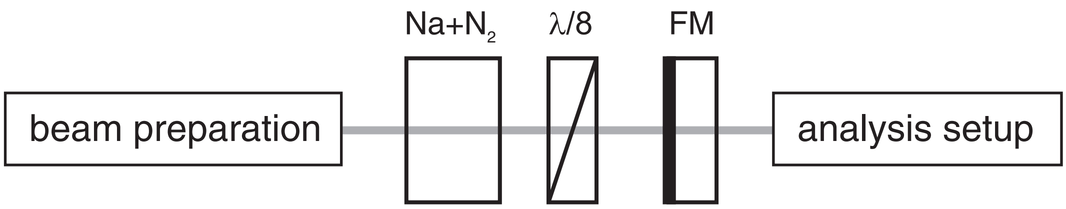

Figure 3.1: Overview of the experimental setup.

atmosphere, a $\lambda/8$ retardation plate and a plane feedback mirror. The sodium vapor needs to be prepared in a way that the assumptions made in the derivation of the microscopic model are fulfilled as exactly as possible.

- Analysis setup

  The light that is transmitted by the feedback mirror is used for the analysis of the structures emerging from the single-mirror feedback arrangement. The polarization of the light field will play an important role in understanding the mechanisms involved. Camera systems in general are not sensitive to polarization. Therefor the light field has to be analyzed in its polarization properties before imaging it onto cameras. The capabilities of the imaging system have to be adapted to the phenomenon to be observed. For the observation of stationary structures the images have to have a high resolution in space and intensity levels, while for the observation of dynamical processes an imaging system with a high temporal resolution is required.

The different parts of the setup will be discussed below. Many parts of the experimental setup have already been used and described in previous works [Ack96, Aum99, Sch01, GW02, Hun06]. These parts will be only briefly described.

3.2 Beam preparation

3.2.1 Light source

The preparation of the laser beams used in the experiment is shown schematically in Fig. 3.2. The laser beam is created by a cw dye laser (Spectra-Physics 380D) using Rhodamine 6G solved in ethylene glycol as the dye. It is pumped by a diode-pumped frequency-doubled solid state laser (Spectra-Physics Millennia Xs) operating at 532 nm. In the first experimental sessions an argon ion laser (Spectra-Physics 2030T-15) operating on the 514 nm line has been used. From a pump input power of 6 to 6.5 W the dye laser produces an output power of up to 950 mW at the desired wavelength.
The frequency of the dye laser can be continuously tuned in the vicinity of the sodium D_1 line (λ=589.6 nm). The laser is equipped with an active control loop (Stabilok, Spectra-Physics 388), which stabilizes the laser frequency to the slope of a transmission peak of a temperature stabilized reference Fabry-Perot interferometer (FPI). By means of this stabilization, short-term frequency fluctuations are reduced to ± 5 MHz within one second. A second temperature stabilized FPI with a larger free spectral range is used to detect and correct frequency jumps of one or more free spectral ranges of the reference FPI.

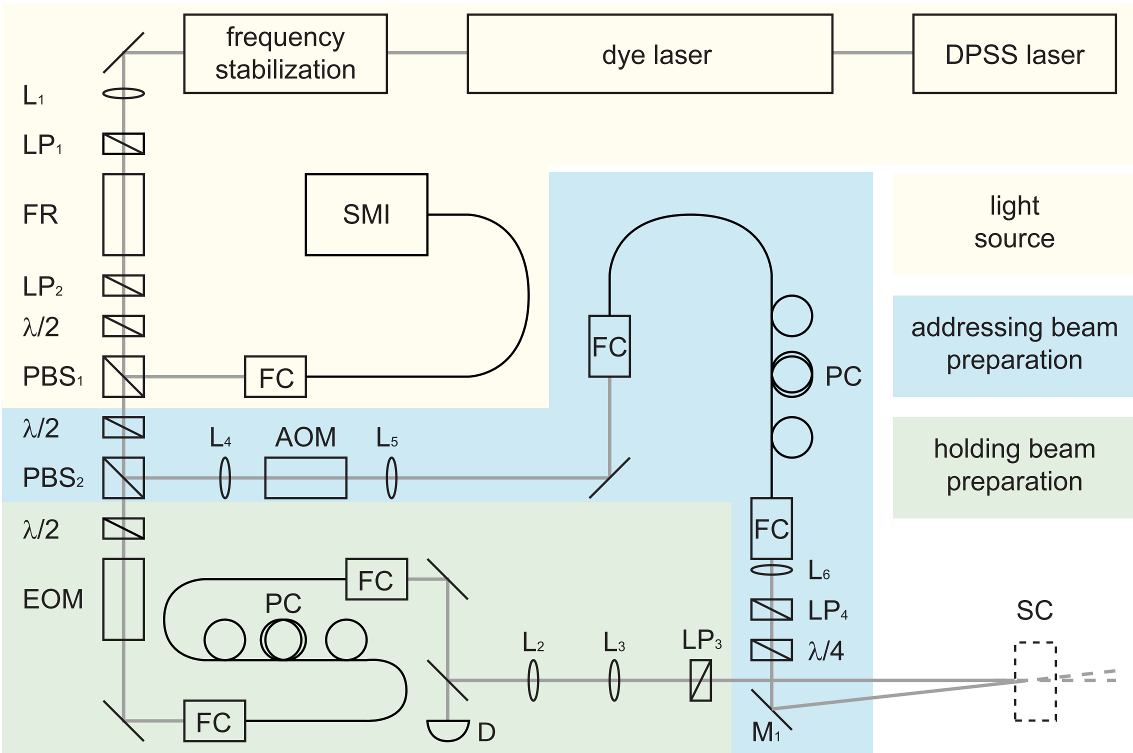

Figure 3.2: Schematic view of the beam preparation setup. L: lens, LP: linear polarizer, FR: Faraday rotator, $\lambda/2$: half-wave plate, $\lambda/4$: quarter-wave plate, PBS: polarizing beam splitter, EOM: electro-optical modulator, AOM: acousto-optical modulator, FC: fiber coupler, PC: polarization controller, SMI: scanning Michelson interferometer, D: photodetector, SC: sodium cell.

The stabilization fails if the frequency jump is larger than the free spectral range of the second FPI. Such frequency jumps, as well as frequency drifts on large time scales, can be detected by a frequency measurement.

The dye laser is very sensitive to light fed back into the resonator by back reflections. In this experiment there is a high amount of light travelling backwards due to the feedback mirror in the single-mirror feedback arrangement. To avoid the resulting frequency and power fluctuations of the dye laser an optical diode consisting of a Faraday rotator preceded (LP_1) and followed (LP_2) by a linear polarizer is inserted into the beam path (specified suppression: -38 dB).

The laser frequency is measured with a wavemeter, which is a modified scanning Michelson interferometer (SMI). A small fraction of light is coupled out of the laser beam by means of a half-wave plate and a polarizing beam splitter. It is coupled into a single mode fiber and led to the SMI. This device determines the unknown laser frequency by comparing it to the known frequency of a HeNe laser. Relative changes in the dye laser frequency can be detected with an accuracy of about 200 MHz [Ohl87]. The absolute accuracy is lower due to dependencies of the measurement on the beam parameters inside the SMI. By calibrating the SMI with a small signal absorption profile of the sodium D_1 line, an absolute accuracy of about 1 GHz is achieved.

3.2.2 Preparation of the holding beam

The holding beam is the intense laser beam, which is needed for the observation of dissipative structures in this experiment. Its power needs to be adjusted and the beam profile and polarization have to be prepared.

Input power

The laser beam coming from the laser system is focused onto the crystal of an electro-optical modulator (EOM) by lens L_1. The EOM (Gsänger LM020P) is used to control the power of the holding beam P_{in}. The last mirror before the beam is injected into the sodium cell transmits about 0.1 % of the laser power onto a photodiode. By calibration with a bolometer (Spectra-Physics 407) that is placed directly in front of the sodium cell, the input power can be determined with an absolute accuracy of 10 %. Changes of the input power are detected with an accuracy which is estimated to be of the order of 1 mW. The maximum holding beam power in front of the cell is 350 mW.

Beam profile

The intensity profile of the holding beam is controlled by spatial filtering by means of a single mode optical fiber (Thorlabs SN3224). In the fiber, light can only propagate in the $LP_{0,1}$ mode which resembles the $TEM_{0,0}$ mode. The output fiber coupler contains a microscope objective (f=16.85 mm), that is movable in three directions in space. It is adjusted to produce a collimated beam with a beam radius of 1.5 mm. This beam is expanded by means of a telescope consisting of two plano-convex lenses L_2 (f=150 mm) and L_3 (f=200 mm). The resulting beam that is injected into the sodium cell has a beam radius of 1.89 mm. The beam waist is chosen to be positioned within the sodium cell with an accuracy of 50 cm. This is small compared to the Rayleigh length of the beam ($z_R \approx 20\,\mathrm{m}$).

Polarization

The laser beam is linearly polarized when it leaves the output face of the EOM. The single mode fiber is not polarization maintaining, but it maintains the degree of polarization. The output polarization can be adjusted by means of a polarization controller [Lef80]. This device consists of a sequence of a single, a double and a single loop of the fiber. Due to bending-induced birefringence of the fiber [URE80] this sequence is equivalent to a sequence of a quarter-wave, a half-wave and a quarter-wave retarder. By means of this polarization controller the output beam is preadjusted to be linearly polarized with the axis of polarization aligned with the direction perpendicular to the optical table and with the linear polarizer LP_3. That polarizer (B. Halle Nachfl. PGT 2.12) is the last optical element before the beam is injected into the cell. The extinction ratio of the polarizer is specified to be better than 10^{-6}.

3.2.3 Preparation of the addressing beam

Input power

A variable fraction of light is coupled out of the holding beam by means of a half-wave plate and a polarizing beam splitter (PBS_2) to build the addressing beam. The beam is focused into an acousto-optical modulator (AOM, NEC OD-8813A) to allow for fast switching. The rise time of the transmitted intensity lies below 200 ns which is fast enough compared to the typical timescale of the dynamical phenomena in the experiment ($\approx 20\,\mu$s).
Holding and addressing beam propagate individually over a certain distance and are both coupled into an optical fiber. Therefor it is impossible to keep the relative phase between these two beams constant. Without an other action taken, the result of the reunification of the two beams in the sodium cell is an interference pattern fluctuating in time. This behavior strongly perturbs the process of igniting and erasing localized structures in the experiment. But due to the nonlinearity of the sodium vapor the addressing beam does not have to be coherent with the holding beam. Therefor the frequency of the addressing beam is shifted by means of the AOM. If the first order of diffraction of the AOM is used as the addressing beam, its frequency is shifted by $\Delta\nu = 140$ MHz.

Beam profile

As in the holding beam, a single mode optical fiber is used to control the transverse intensity profile of the addressing beam. A homogeneous Gaussian profile allows for a good focusability of the beam. The output coupler consists of a lens that can be moved

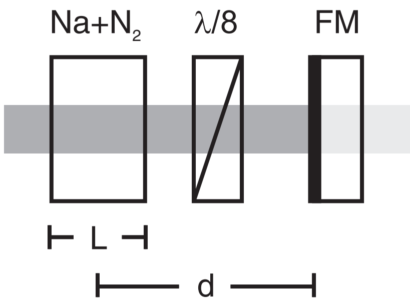

Figure 3.3: Schematic view of the single-mirror feedback arrangement.

in three directions in space. Its distance from the fiber in combination with lens L_6 determines the radius of the beam in the sodium cell. It can be adjusted from 180 µm to 1.5 mm. The position of the addressing beam in the cell is adjusted by means of mirror M_1 which superimposes addressing and holding beam in the sodium cell. Both beams include an angle of approx. 1°.

Polarization

The polarization of the addressing beam is adjusted analog to the holding beam. A fiber polarization controller is used to generate a linearly polarized beam whose polarization axis is aligned with linear polarizer LP_4. The addressing beam needs to be circularly polarized in this experiment. This is achieved by inserting a quarter-wave retardation plate behind LP_4. The helicity of the circular polarization can then be chosen by adjusting the rotation angle of the quarter-wave plate to ±45° with respect to the axis of linear polarization introduced by LP_4.

3.3 Single-mirror feedback arrangement

The single mirror feedback arrangement consists of the sodium cell, an eighth-wave retardation plate and a feedback mirror (see Fig. 3.3).
The core piece of the experiment is the sodium cell. It consists of a Duran glass tube of length 7 cm and diameter 12 mm. This tube can be evacuated and filled with nitrogen as the buffer gas. A buffer gas pressure of 300 hPa has proven to be appropriate to fulfill the requirements of the microscopic model. It has therefor been used throughout the experiments.

The center part of the tube (length $L = 15\,\mathrm{mm}$) is surrounded by a copper block that is heated by four DC driven heat modules. A piece of solid sodium is placed in this heated area of the tube. It is contained in a tantalum shuttle to simplify handling.
The outer parts of the tube are connected to a water cooling loop. This creates a steep temperature gradient within the gas, which limits the area of high sodium particle densities to the heated zone. In the presence of a buffer gas, a deposition of sodium particles on the cell windows that close the ends of the tube is prevented. The cell windows were chosen to be thicker (5 mm) than in previous experiments in order to reduce stress-induced birefringence and depolarization. They are antireflection coated to reduce interferences.
The cell temperature is measured inside the copper block near the tube. Heating the cell to a temperature of 280°C to 360°C results in a sodium particle density in the range of $10^{19}\mathrm{m}^{-3}$ to $10^{20}\mathrm{m}^{-3}$. The dependence of the particle density on the temperature has been determined experimentally by the measurement of a small signal absorption profiles [Aum99].
The sodium cell is surrounded by three pairs of Helmholtz coils, that produce a homogeneous magnetic field in the heated area of the cell. A magnetic field significantly influences the optical pumping process in sodium vapor. This has been used as a parameter in previous works [ALHL95, SFAL00, HAL04]. In this work, the magnetic field is kept fixed. It is adjusted to compensate for the earth magnetic field. Additionally, a static magnetic field is applied, that is oriented parallel to the direction of the laser beam. The magnetic field component in the direction of the laser beam is adjusted to $|B_z| = 200 - 400\,\mu\mathrm{T}$, which is large compared to the residual transverse magnetic field components $|B_{x,y}| < 1\,\mu\mathrm{T}$.
The $\lambda/8$ plate in the feedback loop (VLOC WM30.0-0.125-589-C) is antireflection coated and fixed in a rotation mount. The rotation angle can be determined with an accuracy of $\pm 2\,'$. This accuracy applies for all rotation mounts in the setup.
The feedback mirror is plane and has a reflectivity of R=0.99. The substrate is wedged with an angle of 2° to minimize interferences. It is kept in a three-point mount, all of which are adjustable by means of a micrometer screw. Additionally, the controls of the two tilt axes are equipped with piezoelectric transducers which allow for a precise alignment of the feedback mirror tilt. The mirror distance d is chosen to be approx. 10 cm.

3.4 Analysis setup

The light that is transmitted by the feedback mirror is used for the analysis of the system. The distribution of the light field that is transmitted by the sodium cell is imaged onto charge-coupled device (CCD) cameras. These are only sensitive to light intensities and not to the polarization of light. However, the polarization properties of the light field

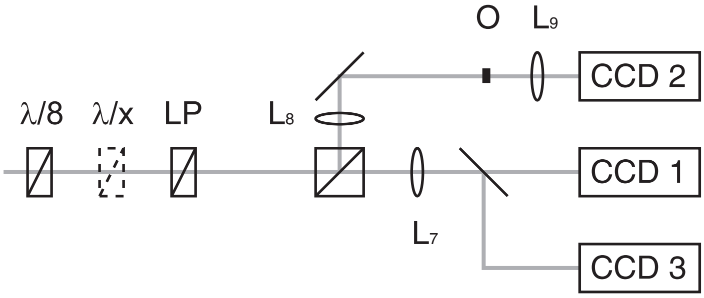

Figure 3.4: Schematic view of the analysis setup.

change during the transmission through the sodium cell and this gives important information about the state of the nonlinear medium. Therefor the analysis setup consists of a polarization analysis unit and an imaging unit.

3.4.1 Polarization analysis

To analyze the polarization of the light field that is transmitted by the sodium cell, it is important to compensate for the effect the $\lambda/8$ plate in the feedback loop has on the polarization. This is accomplished by inserting a second eighth-wave plate behind the feedback mirror. Its optical axes are oriented perpendicular to the optical axes of the first $\lambda/8$ plate. After transmission through this second $\lambda/8$ plate the state of polarization behind the sodium cell is reestablished.
A very simple way to gain information on the polarization of the light field is the use of a linear polarizer that is installed into a rotation mount. The transmitted light field is a projection onto a linear polarization component, whose axis is chosen by the optical axis of the polarizer. By rotating the linear polarizer arbitrary linear polarization components can be analyzed. Alternatively the linear polarizer is kept at a chosen reference axis and a half-wave retardation plate in a rotation mount is inserted in front of the polarizer. To measure the circularly polarized components of the light field, a quarter-wave plate is inserted in front of the linear polarizer. Its fast axis includes an angle of $\pm 45°$ with the reference axis to measure the right and left circularly polarized components of the light field.
In order to gain full information on the polarization of a light field a spatially resolved measurement of the Stokes parameters can be accomplished by combining four of the described measurements. The Stokes parameters S_1, S_2 and S_3 characterize the state of

polarization of an electromagnetic field. The first parameter S_1 gives the relative fraction of radiation that is linearly polarized with respect to a chosen reference axis. It can be determined by measuring the intensities in the two linear polarization components parallel ($I_{||}$) and orthogonal ($I_{\perp}$) to the reference axis. S_2 gives the relative fraction of linearly polarized light that is polarized at an angle of 45° with respect to the reference axis, which is measured at a rotation angle of 22.5° of the $\lambda/2$ plate. S_3 gives the relative fraction of circularly polarized light. Here the $\lambda/2$ plate is replaced by a $\lambda/4$ plate and its fast axis includes an angle of 45° with the reference axis. The normalized Stokes parameters can be calculated from the measured intensities:

$$S_1 = \frac{I_{||} - I_{\perp}}{I_{||} + I_{\perp}} \qquad (3.1)$$

$$S_2 = \frac{2 \cdot I_{45}}{I_{||} + I_{\perp}} - 1 \qquad (3.2)$$

$$S_3 = \frac{2 \cdot I_{circ}}{I_{||} + I_{\perp}} - 1. \qquad (3.3)$$

The total degree of polarization of the light field is given by the fractional polarization:

$$D_{pol} = \sqrt{S_1^2 + S_2^2 + S_3^2}$$

From the measured Stokes parameters the ellipticity ϵ and the orientation of the main axis ξ of the polarization ellipsoid can be calculated:

$$S_1 = \cos(2\epsilon) \cdot \cos(2\xi) \qquad (3.4)$$

$$S_2 = \cos(2\epsilon) \cdot \sin(2\xi) \qquad (3.5)$$

$$S_3 = \sin(2\epsilon). \qquad (3.6)$$

3.4.2 Imaging system

The imaging system records the near and far field intensity distribution of the light field component that is transmitted by the sodium vapor and the polarization analyzer.

The near field, which is the light field transmitted by the sodium cell, is imaged onto a camera (CCD 1) by means of a lens (L7). The choice of the CCD camera to image the near field depends on the phenomenon to observe. Most of the images in this work show stationary or quasistationary states. These are imaged onto a digital CCD camera (Vosskühler CCD-1300LN). This camera has a high spatial resolution (1024×1024 pixels), a high dynamic range (12 bit) and an exposure time of 100 µs. The high dynamic range is essential for the measurement of Stokes parameters.

A videosampling method is used for imaging dynamical processes [Bru94, MB95, MSA+99]. This method is capable of imaging processes that are either periodic themselves or can be periodically reproduced. In this work, the dynamical processes are the response of the system to a perturbation induced by the addressing beam. A trigger signal is derived from the signal that is periodically driving the AOM, thereby repeatedly triggering the dynamical process. The CCD camera has a trigger input with programmable exposure delay. By repeatedly capturing an image with increasing exposure delay, a sequence of the dynamical process is obtained. The camera (Proxitronic HF4 S 5N) is equipped with a gated photomultiplier that allows for short exposure times. Throughout this work the exposure time is chosen to be 1 µs. The delay increment between two subsequent images is typically in the order of 10–100 µs.

The far field is the optical Fourier transform of the light field that is transmitted by the sodium vapor. It is present in the back focal plane of lens L8 and is imaged onto camera CCD 2 by means of lens L9. Since the (often very intense) zero order of refraction is insignificant in the analysis of spatial structures it is blocked by an opaque obstacle to increase the dynamic range that is available for recording higher spectral components.

Chapter 4

Experimental results

4.1 Symmetry-breaking pitchfork bifurcation

Yabuzaki et al. [YOKO84] and Große Westhoff et al. [GWKL$^+$00] have described the occurrence of a symmetry-breaking pitchfork bifurcation for the system under consideration here. In this section these results will be reproduced, characterized and enhanced for the experimental parameters used in this work.

In the input power range considered here, the system does not exhibit any structured state, the intensity profile transmitted by the vapor is always homogeneous.

Figure 4.1 shows the polarization rotation angle ξ of the light field transmitted through the sodium cell in dependency on the input power of the holding beam. The slow axis of the $\lambda/8$-plate is aligned with the holding beam polarization. The polarization rotation angle ξ is determined by adjusting a linear polarizer in the polarization analysis such that the transmitted intensity is minimal. For very low input powers ($P_{\mathrm{in}} \lesssim 1.3\,\mathrm{mW}$) the main axis of polarization is not rotated ($\xi \approx 0\,^{\circ}$). Increasing the input power beyond 1.3 mW results in a pronounced change of ξ, and the polarization axis starts to rotate clockwise. The rotation of the polarization plane is continuous, intensity jumps are not observed at the detector. Above an input power of $P_{\mathrm{in}} \approx 5\,\mathrm{mW}$ the rotation of the polarization plane saturates up to a saturation angle $\xi = -65\,^{\circ}$ at $P_{\mathrm{in}} = 25\,\mathrm{mW}$.

A second steady state solution, which is expected from the previous works [YOKO84, GWKL$^+$00] can be prepared in the following manner: The holding beam is blocked. Then a σ_+ polarized ignition beam is injected into the cell and induces a positive orientation within the sodium vapor. If the holding beam is unblocked and afterwards the ignition beam is turned off, the main axis of polarization is rotated counterclockwise with respect to the input polarization at an angle of $\xi = 65\,^{\circ}$. If the input power is reduced down to 10 mW, ξ slightly decreases. Reducing the input power further, the reduction of ξ

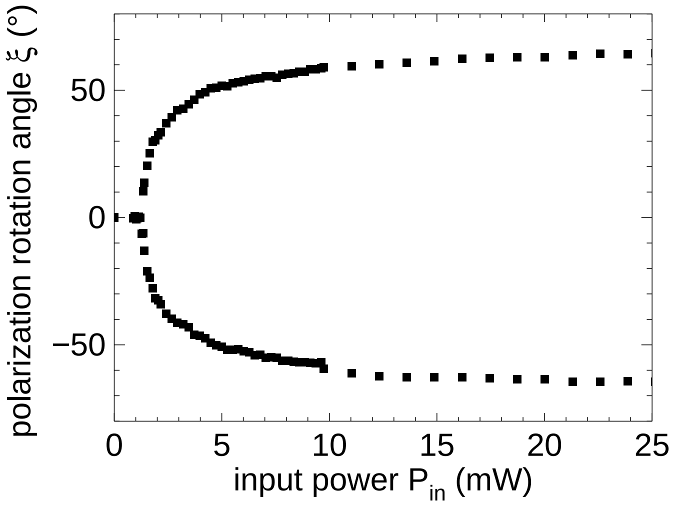

Figure 4.1: Rotation of the main axis of polarization in dependency on the input power. The slow axis of the $\lambda/8$-plate is aligned with the input polarization ($\rho = 0\,^\circ\,0'$). Parameters: $d = 105\,\mathrm{mm}$, $\Delta = 16.8\,\mathrm{GHz}$, $T = 342.5\,^\circ\mathrm{C}$.

becomes more pronounced, and the rotation angle decreases continuously down to $10\,^\circ$ at $P_{in} = 1.34\,\mathrm{mW}$. At this point, there is a jump in the power transmitted through the analyzer. An adjustment of the analyzer shows that the main axis of rotation has jumped to a slightly negative angle of rotation. This solution belongs to the solution branch described first. The system changes from a bistable to a monostable situation.

The observed behavior corresponds to a weakly perturbed pitchfork bifurcation [Nic95] and has been accordingly interpreted by Yabuzaki and Große Westhoff. In the following, the power at which ξ starts to change rapidly will be called critical power. The power at which the second solution sets in will be called bistability power. In the case of a perfect pitchfork bifurcation, the two powers coincide. Due to the structural instability of the pitchfork bifurcation [Str94] this is not expected to be observed in an experiment in its pure form.

The degree of perturbation is very low, however. If the holding beam is blocked again, the vapor relaxes to its equilibrium situation where the orientation is zero. If the holding beam is switched on to a power above the bistability power, the system spontaneously chooses one of the two stable branches. If this experiment is repeated, a switching to both branches is observed.

Rotating the slow axis of the $\lambda/8$-plate by an angle ρ with respect to the input polarization

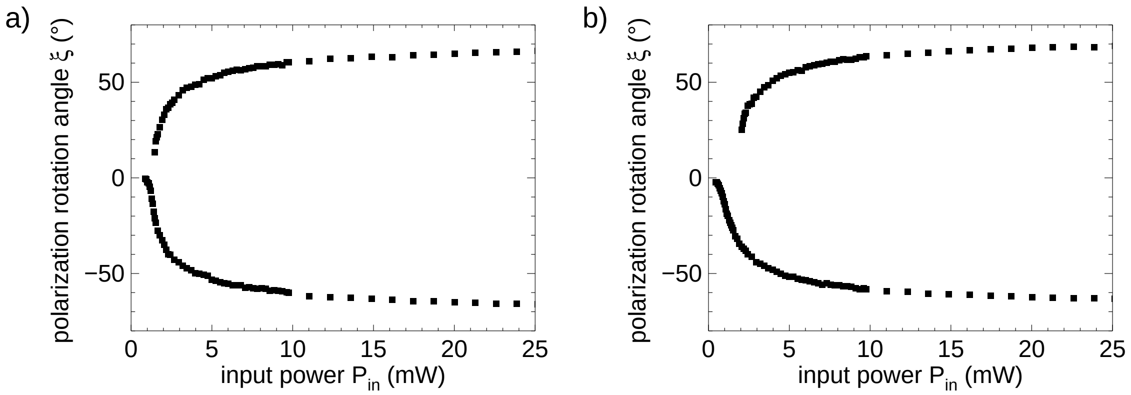

Figure 4.2: Rotation of the main axis of polarization in dependency on the input power for positive wave plate rotation angles ρ. Parameters: See Fig. 4.1 except a) $\rho = 0\,^{\circ}\,30\,'$, b) $\rho = 5\,^{\circ}\,0\,'$.

introduces a perturbation of the pitchfork bifurcation. If ρ exceeds $\pm 10\,'$, switching to only one branch is observed in switch-on experiments. This branch will be called the *favored* branch. The branch that is not observed in switch-on experiments will be called the *disfavored* one.

Fig. 4.2a shows the bifurcation diagram for a small positive wave plate rotation angle ($\rho = 30\,'$), which is measured in a similar way to Fig. 4.1. The critical power is less defined because the polarization softly starts to rotate when the input power is increased. The branch that exhibits a negative (positive) polarization rotation is the favored (disfavored) one for positive wave plate rotation angles ξ. The bistability power increases to 1.46 mW. The degree of imperfection of the pitchfork bifurcation is significantly increased.

In Fig. 4.2b, the bifurcation diagram for a larger positive wave plate rotation angle is shown ($\rho = 5\,^{\circ}$). The bistability point is at 2.1 mW, and the disfavored branch is separated from the input polarization direction by at least $\xi = 25\,^{\circ}$. There is a significant difference in the absolute value of the saturation angles of the polarization rotation $|\xi|$. At $P_{in} = 25\,\mathrm{mW}$, it is $\xi = 63.3\,^{\circ}$ for the favored branch and $\xi = -69.0\,^{\circ}$ for the disfavored branch. If the direction of rotation of the $\lambda/8$-plate is changed, the asymmetric behavior of the system is reversed. This is shown in Fig. 4.3 for two different negative rotation angles ρ. The branch with positive polarization rotation angles ξ now is continuously connected with the zero solution, i.e. it is the favored branch. The branch characterized by negative ξ values is disfavored. It can now be reached by means of a σ_- polarized ignition beam. For $\rho = -30\,'$ (Fig. 4.3a) the imperfection of the bifurcation is weak, and the measured values correspond well to those of (Fig. 4.2a) with reversed signs for ξ. The bistability power is 1.53 mW. If the wave plate rotation angle is increased (see Fig. 4.3b), the degree

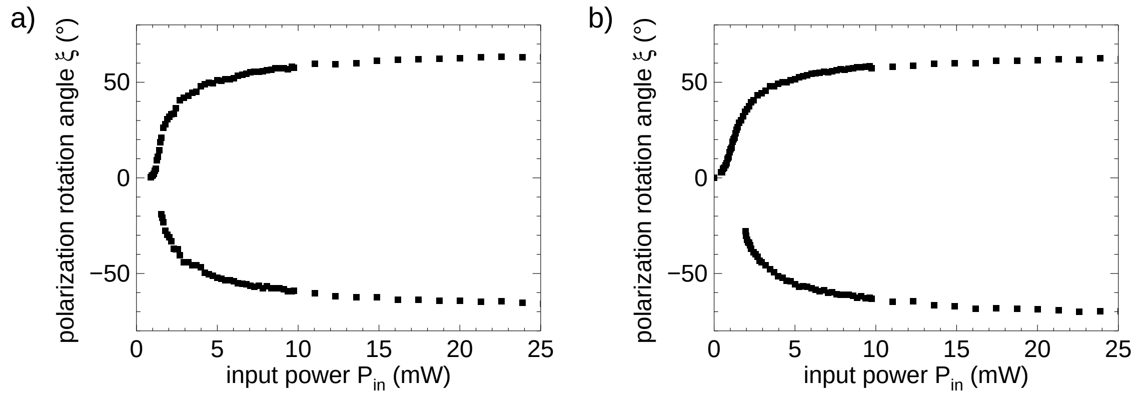

Figure 4.3: Rotation of the main axis of polarization in dependency on the input power for positive wave plate rotation angles ρ. Parameters: See Fig. 4.1 except a) $\rho = 0^\circ - 30'$, b) $\rho = -5^\circ\, 0'$.

of imperfection increases similarly to Fig. 4.2b. The bistability power is 1.95 mW. The maximum rotation angles amount to $\xi = 62.2^\circ$ for the favored branch and $\xi = -69.8^\circ$ for the disfavored branch.

Figure 4.4a shows the bistability power in dependency on the rotation angle ρ of the $\lambda/8$-plate. It is measured by bringing the system onto the disfavored branch at maximum input power and then reducing the power stepwise until there is a jump in the intensity transmitted by the linear polarizer. This indicates that the disfavored branch has disappeared and the system has jumped to the favored branch. Above the curve built up by the measured points, the system is bistable. For $\rho = 0^\circ$, the threshold for the onset of bistability is lowest. If $|\rho|$ is increased, the threshold power increases monotonically. Above angles of 30° the laser power necessary for a bistability of the system increases drastically. Above angles of $|\rho| = 35^\circ$, no bistability is observed in the given input power range.

The polarization rotation angle of the unstructured states in dependency on the wave plate rotation angle ρ is shown in Fig. 4.4b. The measurement is started at a wave plate rotation angle $\rho = -90^\circ$, which due to the π periodicity of the wave plate is equivalent to $\rho = 90^\circ$. At this point, the input polarization stays stable. If ρ is increased, the polarization axis starts to rotate in positive direction. At $\rho \approx 21^\circ$, ξ reaches a maximum of 67°. It then slightly decreases, and at $\rho = 27^\circ$, a discontinuous jump of the polarization axis is detected. The branch with positive polarization rotation disappears, and the system jumps to a stable homogeneous state with negative polarization rotation.

If the system is prepared in the initial state $\rho = 90^\circ$ and ρ is decreased, the polarization

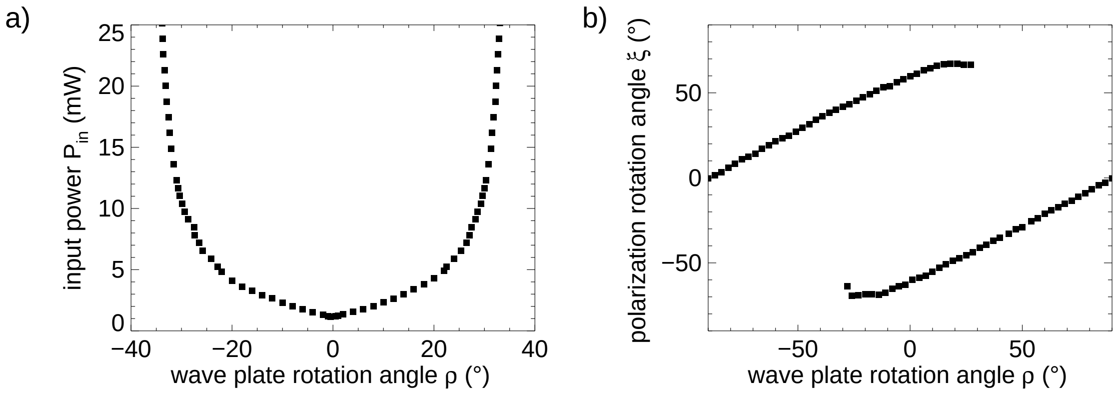

Figure 4.4: a) Threshold input power for the existence of two stable homogeneous states. b) Rotation of the main axis of polarization in dependency on the wave plate rotation angle ρ. Parameters: $d = 105\,\mathrm{mm}$, $\Delta = 16.8\,\mathrm{GHz}$, a) $T = 346.3\,°\mathrm{C}$, b) $T = 346.8\,°\mathrm{C}$, $P_{in} = 6.8\,\mathrm{mW}$.

axis rotates towards negative angles. The maximum rotation angle of $\xi = -69\,°$ is observed at $\rho = -27\,°$, and the state loses stability at $\rho = -28\,°$. In a good approximation, the diagram is point-symmetric with respect to the origin.

The described behavior provides another way to change between the two stable states without the use of the ignition beam. In order to change from the state with positive (negative) polarization rotation to the state with negative (positive) polarization rotation, ρ is increased (decreased) until the branch loses its stability and then rotated back to the desired position within the bistable region.

4.2 Modulational instability

At input powers that lie beyond the level discussed in the previous section ($P_{in} \leq 25\,\mathrm{mW}$), the system does not significantly change its properties over a wide power range. Depending on the rotation angle of the wave plate, there are one or two stable unstructured states. The intensity distribution is smooth and the Gaussian shape of the input beam is not distorted. The whole beam can be suppressed well in the polarization analysis by setting the linear polarizer to an angle $\xi + 90\,°$, i.e. the polarization is homogeneous over the whole beam (see Fig. 4.5a).

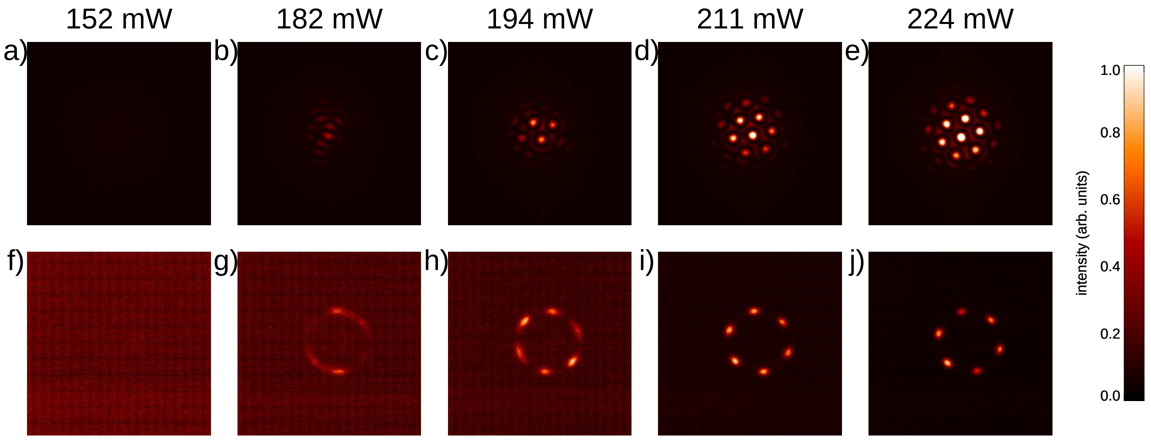

Figure 4.5: Modulational instability. Intensities in the near field images are equally scaled, far field images are individually intensified for contrast enhancement. Color table leading from black to white via red will be used for intensity images throughout this work. Parameters: $d = 112\,\text{mm}$, $\Delta = 15.1\,\text{GHz}$, $T = 359.5\,°\text{C}$, $\rho = 0\,°$.

4.2.1 Hexagonal patterns

The system is prepared to be on the branch that exhibits a positive polarization rotation for the case of a (nearly) perfect pitchfork bifurcation ($\rho = 0\,°$). The linear polarizer is adjusted to suppress the unstructured beam.

A change in the properties of the system occurs at input powers above typically 150 mW. If the input power is increased beyond that level, inhomogeneities occur in the light field transmitted by the linear polarizer. The unstructured state becomes unstable, and the instability is connected to the generation of new polarization components.

The upper row of Fig. 4.5 shows the near field intensity distributions that are transmitted by the linear polarizer for increasing input power. The lower row shows the corresponding far field images (with suppressed zero order). At $P_{\text{in}} = 152.0\,\text{mW}$, there is no modulation, the unstructured state is stable. Correspondingly, there are no higher Fourier components. If the input power is increased to 182 mW, modulations of the near field occur that have no defined symmetry. However, the far field image (Fig 4.5g) indicates that the modulations have a well-defined length scale ($q = 16.3\,\text{rad mm}^{-1}$). There is a band of excited wavevectors, that lie on a circle around the (suppressed) zero order.

If the input power is increased further, the modulations become more intense, and the near field images show bright spots on a dark background that are arranged in a hexagonal order. With increasing input power, the number of constituents increases, i.e. the patterned area grows. The hexagonal symmetry also becomes manifest in the far field (Fig. 4.5h,i,j), where six well-defined spots are present.

The same phenomenon is observed, if the system is prepared to be in the state with negative polarization rotation.

4.2.2 Patterns in dependency on the wave plate rotation angle

As described in section 4.1, the bifurcation scenario at low input powers changes in dependency on the wave plate rotation angle ρ. Depending on ρ, there is either a (nearly) perfect pitchfork bifurcation ($\rho = 0\,^\circ$), a perturbed pitchfork bifurcation ($|\rho| \lesssim 35\,^\circ$) or monostability ($|\rho| \gtrsim 35\,^\circ$). For all angles ρ a modulational instability on all unstructured branches that exist at this position is observed within the available laser power range. Fig. 4.6 shows an overview of the dominating patterns that evolve beyond the threshold for pattern formation in dependency on ρ. The first two columns show the evolving near and far field patterns on the branch that exhibits a rotation of the polarization plane in positive direction. Again, the linear polarizer in the analysis is adjusted to suppress the unstructured background. For $\rho = 0\,^\circ$, a hexagonal pattern is observed as described in section 4.2.1. Hexagons are also dominantly observed, if the wave plate is rotated in positive direction. In this case, the discussed branch is the disfavored one. Hexagonal patterns persist, until the branch disappears at $\rho \approx 40\,^\circ$. In tendency, the number of constituents of the pattern, i.e. the patterned area decreases with increasing ρ. The opposite is true, if ρ is decreased. This is the situation where the discussed branch is the favored one. Hexagons dominate pattern formation up to an angle of $\rho \approx -40\,^\circ$. At $\rho \approx -60\,^\circ$, hexagons still appear, but the dominant pattern is a rhombic pattern. In the far field, it consists of four intensity peaks that have the same wave number ($q = 16.7\,\mathrm{rad\ mm}^{-1}$) and enclose angles of 55° and 125°. The near field shows a rhombic pattern with D2 symmetry.

A very peculiar pattern can be observed at wave plate rotation angles around $\rho \approx -90\,^\circ$. While rhombic patterns can also be observed, the dominant pattern is composed of six Fourier modes arranged in a hexagonal symmetry. However, the near field image shows that the pattern is not a simple hexagon (circular intensity maxima arranged in a hexagonal order) nor is it a honeycomb pattern (intensity minima arranged in hexagonal order, 'negative hexagons'). Due to the triangular shape of its constituents, the pattern has been interpreted as a triangular pattern [GWKL+00].

A similar behavior is observed, if the system is prepared in the state with negative polarization rotation $\xi < 0$. This state is favored for $\rho > 0$, and therefor the transition to triangular patterns via a rhombic pattern is observed for positive angles ρ. Of course, the first and last row of Fig. 4.6 show the very same state. Again, the system proves to be symmetric with respect to $\rho \approx 0\,^\circ$.

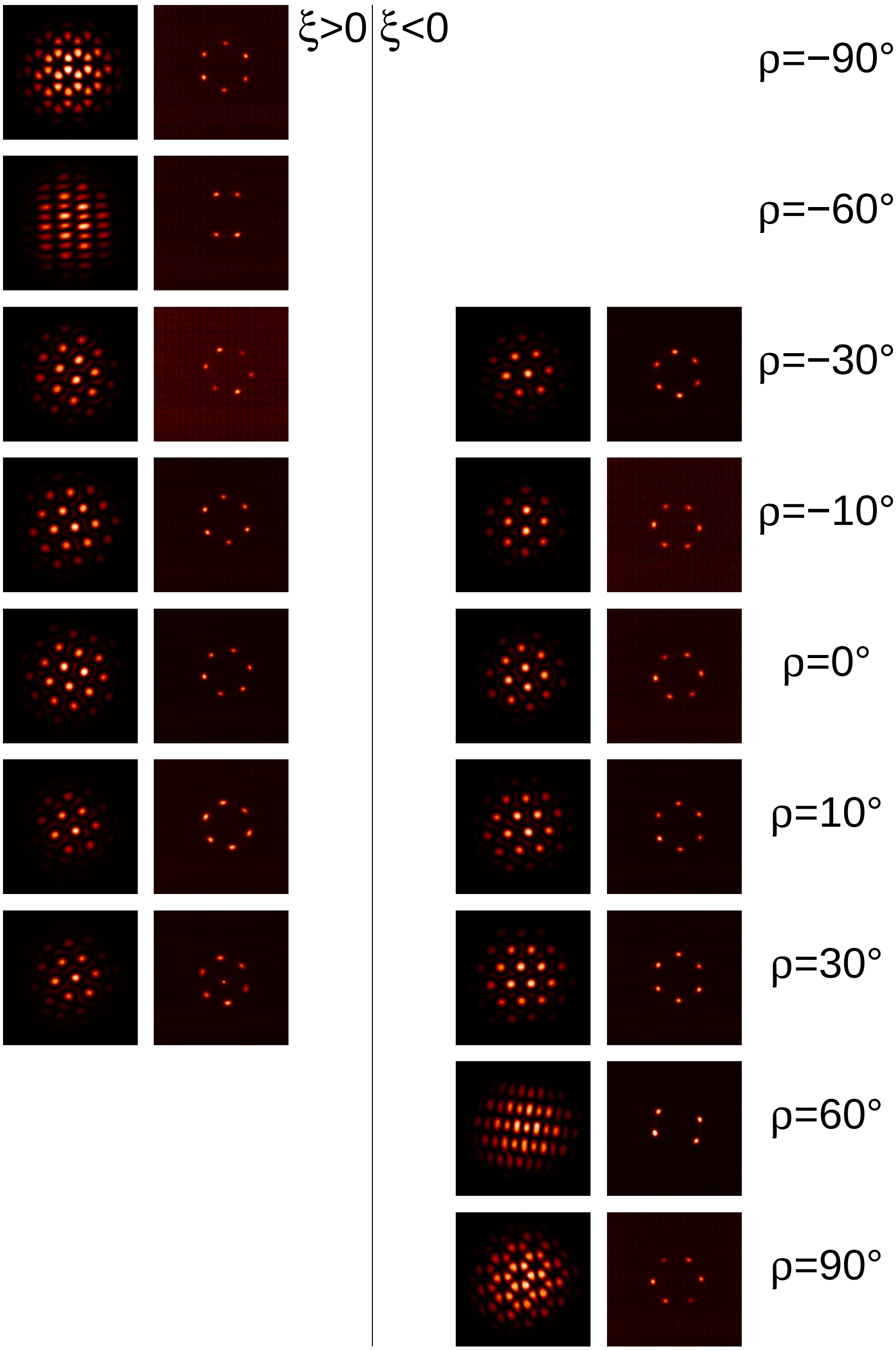

Figure 4.6: Dominant patterns in dependency on the wave plate rotation angle ρ. First and second column: Near and far field images of patterns emerging from the unstructured branch with positive polarization rotation. Third and fourth column: Near and far field images of patterns emerging from the unstructured branch with negative polarization rotation. The linear polarizer is adjusted to suppress the unstructured background. Parameters: $d = 112\,\mathrm{mm}$, $\Delta = 15.1\,\mathrm{GHz}$, $T = 359.5\,°\mathrm{C}$, $P_{in} = 244.0\,\mathrm{mW}$.

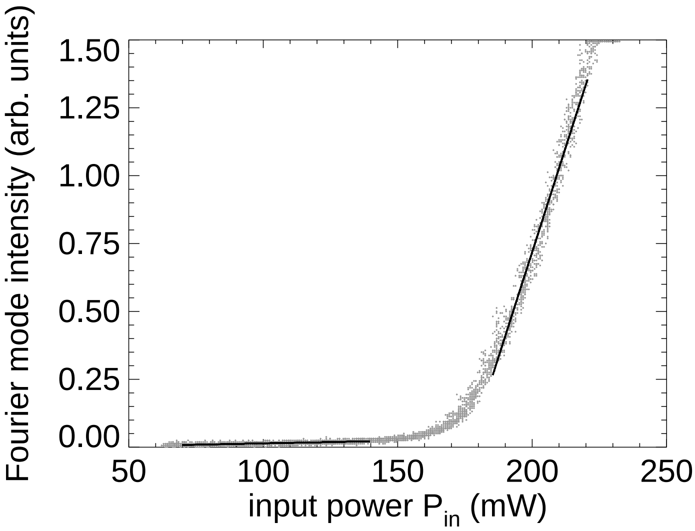

Figure 4.7: Determination of the threshold for pattern formation. Parameters: $d = 120\,\mathrm{mm}$, $\Delta = 17.8\,\mathrm{GHz}$, $T = 347.0\,°\mathrm{C}$, $\rho = 0\,°$.

4.2.3 Threshold for pattern formation

The previous section has shown that the size of the patterned area (weakly) depends on ρ for a constant input power. It is known that the size of a pattern in a Gaussian beam is amongst others determined by the distance to the threshold of pattern formation, which is also clearly visible in Fig. 4.5. This suggests, that the threshold for pattern formation depends on the rotation angle of the wave plate ρ.

To obtain a more exact measurement of the pattern formation threshold, the far field CCD camera was removed and the far field with removed low spatial frequencies was focused onto a photodetector.

Fig. 4.7 shows a typical diagram of 5 up- and down scans of the input power. The intensity in the higher spatial modes is near zero well below the threshold. The fact that there is a slight increase in the intensity with increasing input power is related to residual stray light that cannot be totally eliminated as well as to the observation that the metal film blocking the low spatial frequencies is not totally opaque.

At $P_{in} \approx 150\,\mathrm{mW}$, the intensity in the Fourier spectrum starts to increase significantly. Within the experimental resolution, there is no observation of a jump in the intensity curve. Thus the increase of the Fourier mode intensity is continuous. In that region, also the increase of the slope of the curve is continuous. After the threshold has passed, the slope of the curve doesn't change further, and in a good approximation, there is a linear

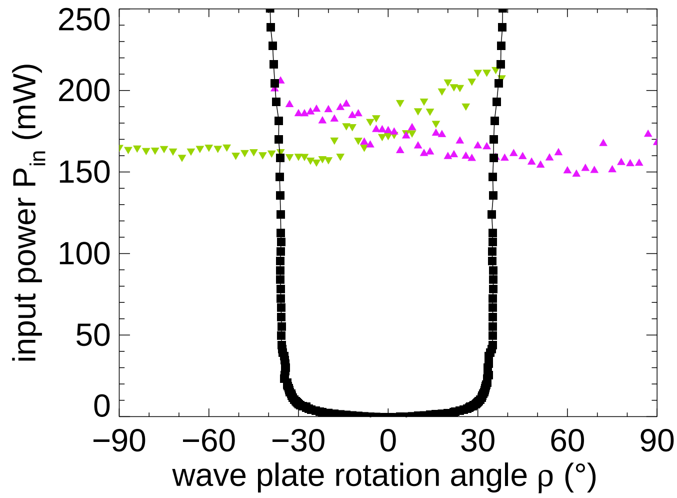

Figure 4.8: Bifurcation diagram. ■: threshold for bistability; ▲: threshold for pattern formation for $\xi < 0$; ▼: threshold for pattern formation for $\xi > 0$. Parameters: see Fig. 4.7.

dependency of the Fourier mode intensity on the input power.

The smoothness of the curve can be interpreted by considering spatial noise that is always present in the system. Near but below the threshold for pattern formation, spatial fluctuations that have the critical wave number of the pattern that is about to evolve are only weakly damped. This spectral component persists in the system with a certain amplitude that is defined by the distance to the threshold point in the system without noise. This phenomenon is generally referred to as a 'noisy precursor' of the pattern. Bifurcations of this type are also often discussed in experiments considering the lasing threshold of semiconductor lasers. Following the usual approach, the threshold of the bifurcation is defined by the intersection point of two linear approximations of the curve well below and above the threshold as indicated in Fig. 4.7.

This bifurcation behavior is observed for all of the discussed patterns and all angles ρ, respectively. Typically, the transition to hexagonal patterns in a system with broken inversion symmetry is expected to be subcritical [CH93]. This behavior is not observed here. Numerical simulations show, however, that a very small hysteresis cycle exists (see section 5.2.3). It is interpreted to be covered by fluctuations in the experiment.

Figure 4.8 shows the threshold for pattern formation in dependency on ρ. The region where the system is bistable is indicated by squares connected by an line. Above the curve the system is bistable, below it is monostable. As stated in the beginning of this section, the system remains basically unchanged concerning this property above an input power of 25 mW. The threshold for pattern formation on the branch exhibiting a positive polarization rotation is nearly constant within the monostable range, i.e. where triangles and rhombs are the dominating patterns. In the bistable region, hexagons are the dominating pattern. For negative ρ, the unstructured state the modulational instability originates from is the favored one. In case of positive ρ, it is the disfavored one. Obviously the threshold for pattern formation increases the more disfavored the underlying unstructured state is. A similar behavior is observed with reversed angles ρ if the branch exhibiting a negative polarization rotation is considered. Within the bistable range, the modulational instability is a secondary bifurcation. Remarkably, its threshold power is separated from the threshold of the pitchfork bifurcation by two orders of magnitude.

4.3 Fronts and domain dynamics in a bistable situation

It has been shown in the previous section, that the system exhibits a bistable behavior within a large parameter region. In a spatially extended system, in principle, the coexistence of both states emerging from the pitchfork bifurcation is possible. However, this phenomenon is rarely observed, if the system is running freely without an external perturbation. A spontaneously appearing structure where the two states coexist has been observed by Große Westhoff [GWKL$^+$00] and will be covered in the first subsection. The following subsections will investigate the behavior of the system under the influence of large-amplitude perturbations that can be introduced by means of the addressing beam.

4.3.1 Spontaneous appearance of polarization fronts at high input powers

If the input power is switched from a value below the onset of bistability to a value above the bistability threshold, the system spontaneously chooses the branch that is favored in that situation. This behavior is also observed, if the target input power is beyond the threshold for pattern formation. In this case, the favored hexagonal pattern is observed. If the system is prepared to have nearly equivalent states ($\rho \approx 0$), the system typically chooses one of the hexagonal patterns. However, in subsequent switch-on experiments sometimes another type of pattern – that has already been described in [GWKL$^+$00]– is observed (see Fig. 4.9). It consists of two different domains. If the linear polarizer is adjusted to suppress a polarization rotation angle $\xi = 70°$, the upper left part of the beam is bright while the lower right part is dark (Fig. 4.9a). If, on the other hand, the polarizer

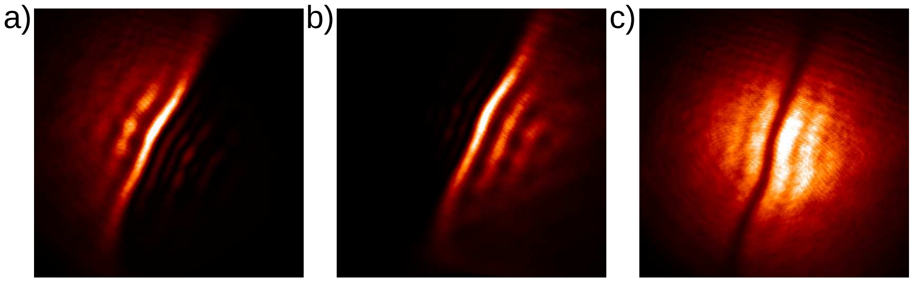

Figure 4.9: Polarization front a) linear polarizer adjusted for suppression of state with positive polarization rotation; b) linear polarizer adjusted for suppression of state with negative polarization rotation; c) total intensity. Parameters: $d = 120\,\mathrm{mm}$, $\Delta = 16.4\,\mathrm{GHz}$, $T = 329.2\,^\circ\mathrm{C}$, $P_{\mathrm{in}} = 216\,\mathrm{mW}$, $\rho = 1\,^\circ\,40'$.

is adjusted to suppress $\xi = -70°$, the lower right part is bright and the upper left part is dark. The beam is divided into two different states of polarization both of which originate from the pitchfork bifurcation. The boundary is interpreted as a polarization front that continuously connects the two polarization states. It is visible as a dark line in the total intensity distribution (Fig.4.9c). This is due to the higher absorption that is present if the orientation of the vapor is small. Hence, the orientation of the vapor crosses zero at the domain boundary which is an important information with respect to the classification of the front (see section 5.3.1). Both spatially extended states exhibit a stripe pattern that is oriented parallel to the polarization front. A slight modulation along the stripes can only be anticipated. It is interpreted as a remains of the hexagonal symmetry of the coexisting hexagonal patterns that is suppressed by the perturbation induced by the front. However, the modulational instability seems to play a role in the stabilization of this pattern, since it only exists at or above the threshold for pattern formation. Below this threshold, the front moves towards the border of the Gaussian beam and disappears. A further characterization of stable fronts will be given in section 4.6.1.

4.3.2 Domain dynamics: basic observation

The system is prepared in a state with negative polarization rotation in a situation where both unstructured states are nearly equivalent ($\rho \approx 0\,^\circ$). Then the addressing beam, which is σ_+ polarized, is switched on. It is positioned in the center of the holding beam and has a radius of approx. 1.5 mm. By optical pumping, it locally creates a transition from the state with negative polarization rotation to the state with positive polarization rotation. A domain of one of the bistable unstructured states embedded into a background

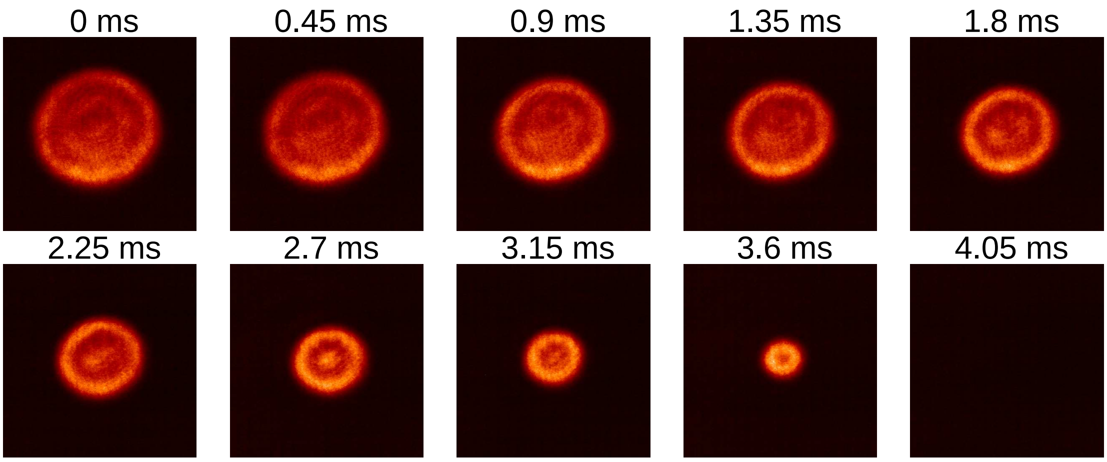

Figure 4.10: Video sampling sequence of a contracting domain. The background state is suppressed by means of the linear polarizer. Parameters: $d = 120\,\mathrm{mm}$, $\Delta = 17.6\,\mathrm{GHz}$, $T = 340.7\,^\circ\mathrm{C}$, $P_{\mathrm{i}n} = 90.0\,\mathrm{mW}$, $\rho = 0\,^\circ$.

of the other state is created. As long as the addressing beam is switched on, the domain remains unchanged after an equilibrium has been reached.

If the addressing beam is switched off, the system becomes dynamic. The domain shrinks and finally disappears within a time period that can not be resolved by standard video equipment. However, this dynamic behavior can be analyzed by means of the video sampling technique. Therefor the acousto-optic modulator that is used for switching the addressing beam is driven with a square pulse signal having a repetition rate of 100 Hz. This square signal serves as the periodic signal needed for the application of the video sampling method. The falling edge of the square pulse, i.e. the point in time where the addressing beam is switched off, is taken as the beginning of the sampling sequence. The increment by which the exposure of the camera is delayed in consecutive images is chosen in a way to capture a smooth sequence of 50-100 images that covers the essential timescale of the process (typically 10-100 μs).

Figure 4.10 shows an excerpt of such a sampling sequence. It shows that the initial domain is of a circular shape and has some slight radial oscillations. Immediately after the addressing beam is turned off, the domain starts to contract symmetrically, i.e. the circular shape is maintained. The continuous shrinkage of the domain finally leads to the disappearance of the domain within a time period of 4 ms. The initial background state is recovered.

From each image of the video sampling sequence, a domain radius can be determined. It is defined as the half width at half maximum (HWHM) of a radially averaged profile

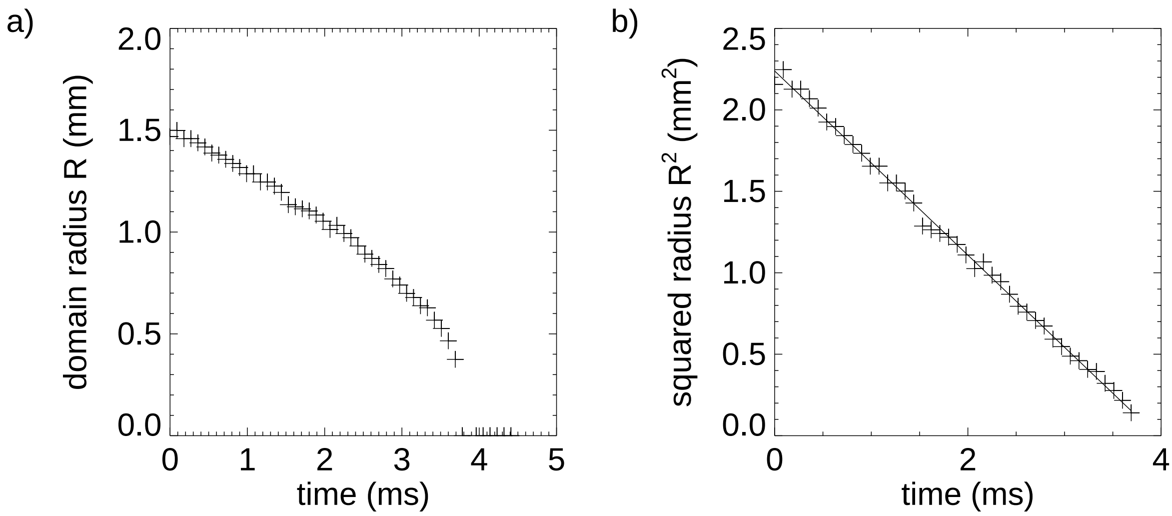

Figure 4.11: Contraction of a circular domain. a) domain radius against time; b) squared domain radius against time and linear fit. Parameters: see Fig. 4.10.

of the intensity distribution centered at the center of the domain. The domain radius in dependency on time of the described sequence is shown in Fig.4.11a.
From general considerations (cf. section 2.2.2), the contraction or expansion of a circular domain of a homogeneous state embedded in a background of another equivalent homogeneous state is not unexpected. It is attributed to the curvature of the domain boundary. Theoretical considerations predict that the front dynamics of a circular domain of one homogeneous solution embedded into a background of another equivalent homogeneous solution is governed by the following equation for the domain radius R:

$$\frac{dR}{dt} = -\frac{\gamma_c}{R}$$

It describes a curvature-driven dynamics, where the coefficient γ_c determines the strength and direction of motion of the circularly shaped front connecting the two homogeneous states. For $\gamma_c > 0$, the domain will contract and disappear. If $\gamma_c < 0$, the domain will expand. Setting $R(0) = R_0$, an equation for the temporal evolution of the domain radius can be derived:

$$R(t) = \sqrt{{R_0}^2 - 2\gamma_c t} \tag{4.1}$$

The domain contracts or expands following a $\sqrt{t}$ law. In a plot, where R^2 is plotted against t, the halve negative slope of a linear fit through the experimental values will give

γ_c. The representation of the experimental time series is shown in Fig. 4.11b. Apparently the dynamics of the domain is described very well by the assumption of a curvature-driven dynamics. The linear fit yields a coefficient $\gamma_c = 0.283\,\mathrm{mm^2ms^{-1}}$.
As already shown, the most important parameters in this experiment are the input power P_{in} and the wave plate rotation angle ρ that determines the degree of imperfection of the pitchfork bifurcation. In the following two sections, the dynamics of circular domains is studied under variation of these parameters.

4.3.3 Variation of input power

The system is bistable over a wide range of input powers, as shown in section 4.2.3. At a certain point, the two unstructured states become unstable against pattern formation. However, the bistable behavior persists. Within the whole power range where bistability is present, domains can be ignited. This applies for domains where a domain of the state that exhibits a positive polarization rotation is embedded in a background that has a negative polarization rotation (*positive domains*) as well as for the opposite case (*negative domains*).
Fig. 4.12 shows the temporal evolution of a circular domain under variation of the input power of the holding beam. Within the whole power range, only contracting domains are observed. The curves show that up to an input power of approximately 150 mW the dynamics can very well be described in the framework of curvature-driven contraction as discussed in the previous subsection. All data points lie on a straight line in a very good approximation, and therefor the coefficient γ_c can be determined easily.
Above an input power of 150 mW, there is a qualitative change in the dynamical behavior of the domains. While the monotonic contraction of the domain persists, the time series show that the curve is not a straight line anymore, but it becomes modulated. The degree of modulation obviously seems to depend on the input power. Also, there seem to be certain fixed radii, where the dynamics slows down. However, a linear fit through the data points can still approximate the time scale of the contraction. Fig. 4.12 shows the temporal evolution of negative domains. The experiment was repeated with positive domains and yields qualitatively similar results.
The coefficients γ_c resulting from the linear fits of the curves in dependency on the input power are plotted in Fig. 4.13. Squares indicate the coefficients belonging to positive domains, while circles represent negative domains. For completely equivalent states, the coefficients for positive and negative domains are expected to coincide. In the experiment, there is a certain deviation between the dynamics of positive and negative domains. This might, on the one hand, be attributed to a slight parameter drift which slightly changes the overall behavior of the system. On the other hand, systematic imperfections like

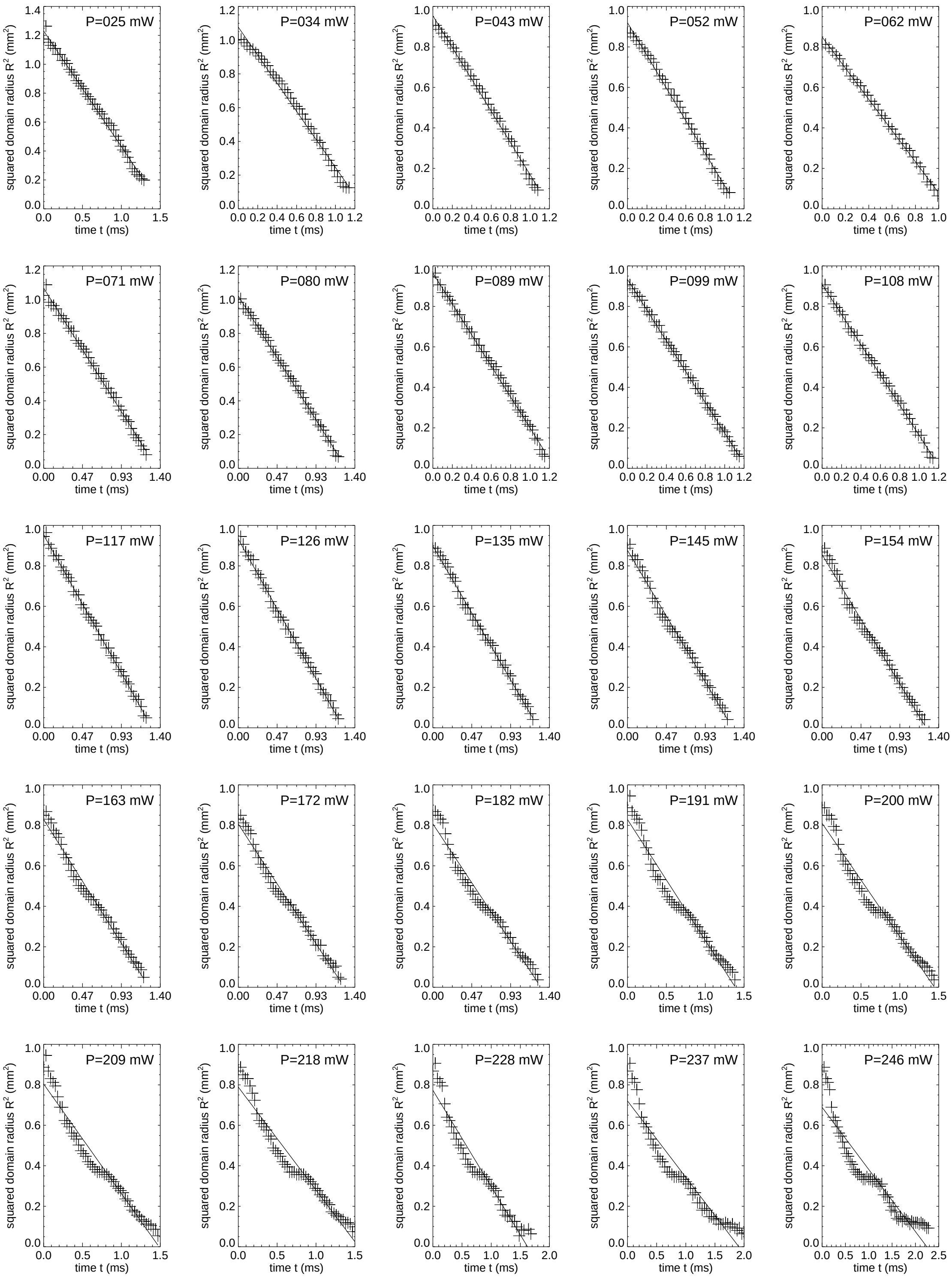

Figure 4.12: Contraction sequences of negative domains under variation of the input power P_{in}. Parameters: $d = 112\,\mathrm{mm}$, $\Delta = 17.5\,\mathrm{GHz}$, $T = 354.7\,^\circ\mathrm{C}$, $\rho = 0\,^\circ$

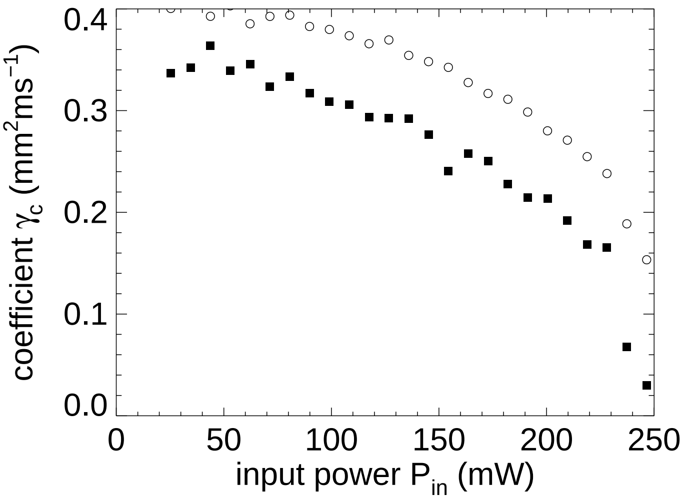

Figure 4.13: Coefficient γ_c in dependency on input power P_{in} for positive (■) and negative (○) domains. Parameters: see Fig. 4.12.

depolarization of the light field may play a role. However, the qualitative behavior of positive and negative domains is very similar. Therefor the dynamics will be discussed together.

The curves show a monotonic decrease of γ_c with increasing input power, i.e. the dynamics of the domains slows down. The deceleration is relatively weak up to an input power of approx. 180 mW. Above this input power, γ_c decreases drastically. This pronounced slowdown seems to be related to the strength of the modulations within the contraction curves.

A hint to the origin of these modulations can be derived from Fig. 4.14. It shows the images of the domain at the starting point (t=0) of the contraction sequence for varying input power. The appearance of this initial domain significantly changes within the considered power range. For low input powers, the domain is very smooth and there are virtually no radial oscillations. With increasing input power, the edges of the domain become sharper, and a certain amount of radial oscillations within the domain appears. The appearance of oscillatory tails near domain boundaries is a well-known phenomenon (see section 2.2.2). Here, the domain boundary has a circular shape, and consequently also the oscillations obey a circular symmetry. These oscillations become more and more pronounced with increasing input power. At the highest input powers, even a modulation of the background state is observed. The modulations seem to correspond to a certain

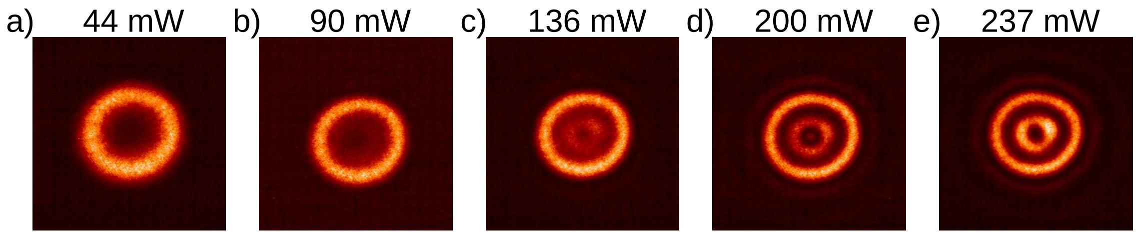

Figure 4.14: Images of the initial domain immediately after switch-off of the addressing beam for different input powers P_{in}. Parameters: see Fig. 4.12.

spatial frequency. As shown in section 4.2.3, the homogenous states become modulationally unstable in the considered power range. It can be conjectured, that the modulational instability can facilitate the appearance of spatial modulations with a certain length scale even below the threshold for pattern formation.

Figure 4.15 shows the temporal evolution of a domain at high input powers in an overlay of three video sampling sequences at equal parameters. The contraction curve shows a large amount of modulations. In fact, the modulations result in two plateaus where the slope of the curve nearly vanishes. The insets in the figure show images of the domains at the radii of the plateaus. These structures display pronounced radial oscillations and seem to be a metastable configuration. The interaction of oscillatory tails of domain boundaries has often been considered to warrant the stabilization of domains in one-dimensional systems. The oscillations show a *locking* phenomenon. The extension of such a locking phenomenon to two spatial dimensions is nontrivial. However, it seems to play a certain role here in the change of the behavior of the system. If the input power is increased beyond a certain level, stable structures are observed that will be discussed in section 4.4.

4.3.4 Variation of wave plate rotation angle

By varying the rotation angle of the wave plate ρ and thereby the imperfection of the pitchfork bifurcation, a domain that is ignited is either in the favored or in the disfavored state. This has a significant influence on its dynamics. A series of contraction curves of positive domains taken under variation of ρ is shown in Fig. 4.16. The input power was adjusted to be well below the appearance of the locking phenomenon described above. For $\rho < 0$ ($\rho > 0$) the domain is in the favored (disfavored) state. Throughout the whole measurement, the parameters of the ignition beam have been kept constant. As a first observation, the initial domain radius resulting from the ignition depends significantly on ρ. The size of the initial domain increases with increasing preference of the domain.

If the domain is in the disfavored state, it always contracts. With increasing ρ, the

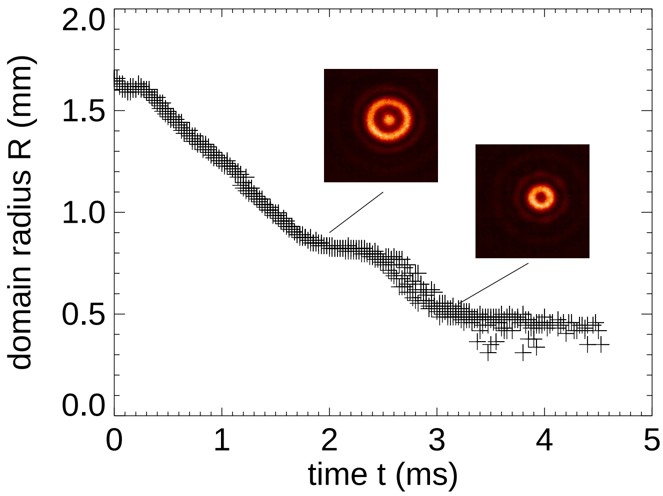

Figure 4.15: Contraction sequence of a domain at high input power. Insets show the images corresponding to the locking regions. Parameters: $d = 112\,\mathrm{mm}$, $\Delta = 15.8\,\mathrm{GHz}$, $T = 346.0\,^\circ\mathrm{C}$, $P_{\mathrm{in}} = 189.9\,\mathrm{mW}$, $\rho = 0\,^\circ$.

initial domain size as well as the duration until the domain disappears gets smaller. The dynamics seems to be well approximated by a linear fit in the R^2 vs. t diagram. If the domain is prepared to be in the favored state, the behavior of the system changes. For small angles $|\rho|$, the initial domain size as well as the time until the disappearance of the domain increases. The contraction slows down significantly for $\rho < -5°$. Still, the basic time scale of the dynamics can be described by a linear fit in the diagram. However, there seem to be systematic deviations. At angles $\rho < -9°$ the behavior of the system changes qualitatively. The domain no longer contracts but expands until the whole beam is switched to the unstructured favored state. Obviously the introduction of a preference for the domain can compensate the curvature-driven contraction. As the system does not recover its initial state after the dynamics has come to an end, the expansion of domains cannot be covered by the described video sampling method.

Figure 4.17a shows the coefficients resulting from a linear fit of the time traces of the squared radius for positive (squares) and negative (circles) domains. Qualitatively the dynamics of positive and negative domains is the same. In both cases the dynamics slows down with increasing preference of the domain until at approx. 10°, γ vanishes and the domain expands. The curves intersect at approx. 2°. This might be induced by the slight asymmetry that has already been observed in section 4.3.3. The measurement can

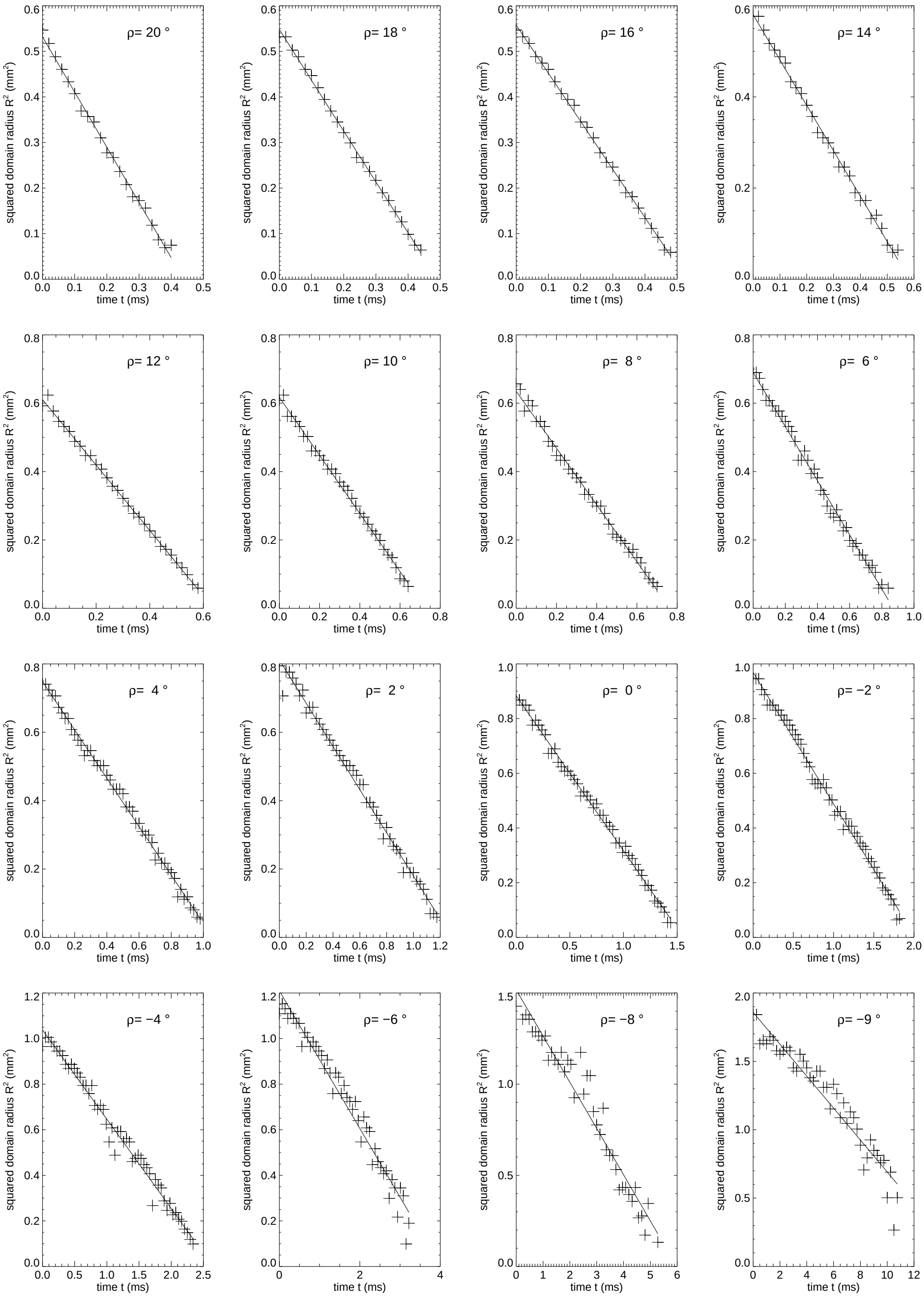

Figure 4.16: Contraction sequences of positive domains under variation of the wave plate rotation angle ρ. Parameters: $d = 110\,\mathrm{mm}$, $\Delta = 15.5\,\mathrm{GHz}$, $T = 340.0\,^{\circ}\mathrm{C}$, $P_{in} = 92\,\mathrm{mW}$.

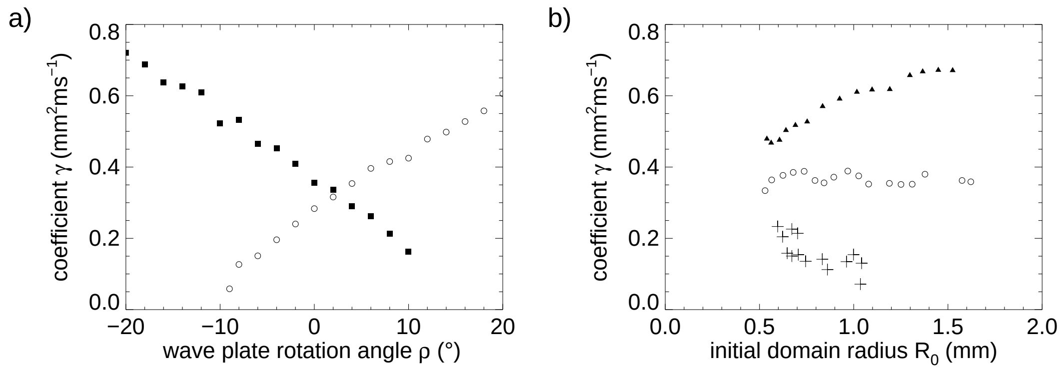

Figure 4.17: a) Coefficient γ_c in dependency on wave plate rotation angle ρ for positive (■) and negative (○) domains. Parameters: see Fig. 4.16. b) Dependency of the contraction coefficient γ on the initial domain radius for $\rho = -7\,°$ (+), $\rho = 0\,°$ (○) and $\rho = 7\,°$ (▲). Parameters: $d = 112\,\text{mm}$, $\Delta = 15.8\,\text{GHz}$, $T = 346.0\,°\text{C}$, $P_{\text{in}} = 90.4\,\text{mW}$.

only give a rough qualitative picture of the dynamics, since both the initial radius of the domain varied and the linear fit seem to be inappropriate in the case where the dynamics is very slow. This is further illustrated by Fig. 4.17b, where γ is shown in dependency on the initial domain radius for three different angles ρ. If the two unstructured states are equivalent ($\rho = 0$, circles), γ does not significantly depend on the initial radius of the domain. Consequently, a description of the dynamics following equation 4.1 seems to be sufficient.

In the case $\rho \neq 0$, γ depends on the initial conditions. Nevertheless, the dynamics can be approximated by equation 4.1 for small $|\rho|$. However, the consideration of a refined model for the dynamics seems to be necessary.

From theoretical considerations, the inclusion of a small imperfection into a system with similar homogeneous states leads to the following equation describing the dynamics of the domain:

$$\frac{dR}{dt} = -\frac{\gamma_c}{R} + \gamma_i \tag{4.2}$$

Here, γ_i describes the front velocity of a straight front. It is induced by favoring one of the homogeneous states over the other one. Hence, γ_i should depend on the degree of imperfection. In the present experiment, it should depend on the wave plate rotation angle ($\gamma_i = \gamma_i(\rho)$). Compared to equation 4.3.2, the above equation allows for a much larger variety of solutions that are discussed in [Cou02, GCOSM04]. In the present experiment, γ_c seems to be positive. In this case, the contraction of the domain can be counteracted by a positive γ_i. The equation has a fixed point $R_{crit} = \frac{\gamma_c}{\gamma_i}$, where curvature-driven contraction and the expansion due to a preference of the domain state compensate. However, the fixed point is not stable. This corresponds nicely to the experimental observations. Separation of variables of equation 4.2 leads to the following equation for contracting domains ($R < R_{crit}$):

$$-\frac{R}{\gamma_i} - \frac{\gamma_c}{{\gamma_i}^2} \ln(\gamma_c - \gamma_i R) + t = c$$

which is transcendent and therefor cannot be resolved to an explicit form R(t). Instead, it is resolved to the inverse function t(R):

$$t(R) = c + \frac{R}{\gamma_i} + \frac{\gamma_c}{{\gamma_i}^2} \ln(\gamma_c - \gamma_i R)$$

Setting $t(0) = t_0$ yields

$$\begin{aligned} t(R) &= t_0 - \frac{\gamma_c \ln \gamma_c}{{\gamma_i}^2} + \frac{R}{\gamma_i} + \frac{\gamma_c}{{\gamma_i}^2} \ln(\gamma_c - \gamma_i R) && (4.3) \\ &= t_0 + \frac{1}{\gamma_i}(R + \frac{\gamma_c}{\gamma_i} \ln(1 - \frac{\gamma_i}{\gamma_c} R)). && (4.4) \end{aligned}$$

This function can, in principle, be fitted to experimental data giving the three parameters γ_c,γ_i and t_0. However, in many cases the experimental data is noisy and limited to a certain range of radii. Thus, γ_i and γ_c can compensate to a ceratin extent and the fit does not give reasonable results. This problem can be circumvented by a multiple measurement of the domain dynamics at equal parameters for varying initial conditions. For a given angle ρ, the dynamics of a positive domain is measured 10-15 times, each time varying the size of the initial domain. The measured array of curves is then fitted to equation 4.4 by means of a nonlinear least-squares fit with shared parameters γ_i and γ_c.

The outcome of such a measurement is shown in Fig. 4.18. It shows the array of curves measured at $\rho = -5°$ (a), $\rho = 0°$ (b) and $\rho = 5°$ (c). The experimental data points of a time series are indicated by squares of a single color. The corresponding line represents the best fit obtained from the shared parameter least squares method. These curves match nicely the experimental data. Obviously the experiment can be described by a dynamics following equation 4.4. The figure shows that the overall dynamics is slowed down with increasing preference of the domain state.

By measuring contraction curves at different angles ρ, the dependency of the coefficients γ_i and γ_c on the imperfection of the pitchfork bifurcation can be analyzed. Figure 4.19a shows the dependency of γ_i on the imperfection of the pitchfork bifurcation. If the domain is disfavored, γ_i is negative, i.e. it enhances the tendency of the domain to contract. This

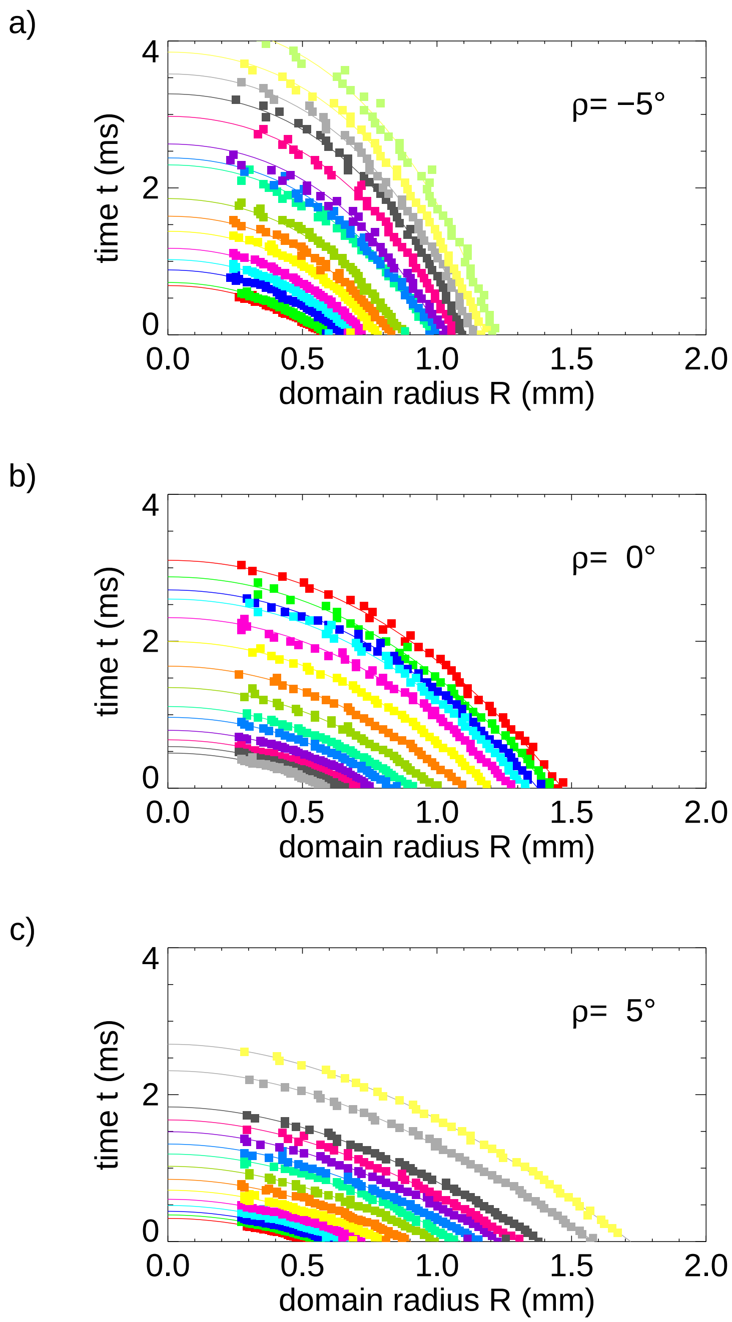

Figure 4.18: Contraction sequences of positive domains under variation of the initial domain radius. Squares indicate data points, line represents best fit. a) $\rho = -5°$, b) $\rho = 0°$, c) $\rho = 5°$. Parameters: see Fig. 4.17b.

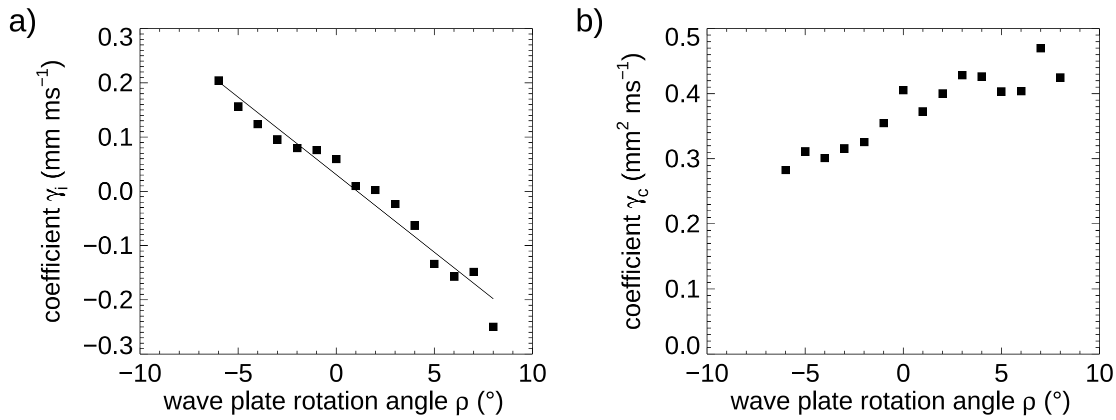

Figure 4.19: Coefficients γ_i (a) and γ_c (b) under variation of wave plate rotation angle ρ. Parameters: see Fig. 4.17b.

tendency is counteracted, if the domain is in the favored state ($\rho < 0$). In the case of equivalent states ($\rho \approx 0$), γ_i vanishes. This is the behavior that is expected from theoretical considerations. In the case of small angles ρ, the dependency of γ_i on ρ can be approximated by a linear interpolation $\gamma_i = \gamma_i'\rho + c$, resulting in a coefficient $\gamma_i' = 0.029\,\frac{mm}{ms^\circ}$ with $c = 0.03\frac{mm}{ms}$.
The coefficient describing the strength of the curvature-driven motion of the front γ_c also seems to depend on the imperfection of the pitchfork bifurcation. In tendency, the dynamics slows down with increasing preference of the domain. However, in the considered range, it always remains positive.

4.3.5 Overview and the transition to stable solitons

The dynamics of a domain is dependent on both input power P_{in} and the imperfection of the underlying bifurcation, which is determined by the wave plate rotation angle ρ. In order to get a full picture of the mechanisms that finally lead to the observation of stable domain configurations, the parameter space spanned by those two parameters is investigated. For a wide range of input powers ($40 - 240\,\mathrm{mW}$) and a wide range of wave plate rotation angles (-15° to 20°) the dynamics of a positive domain having an initial radius $R_0 \approx 0.9\,\mathrm{mm}$ has been recorded. It is analyzed by determining the contraction coefficient γ in a plot, where the squared domain radius is plotted against the time. Due to the appearance of the locking phenomenon at higher input powers, an analysis considering the refined model does not yield reasonable results. In the parameter ranges

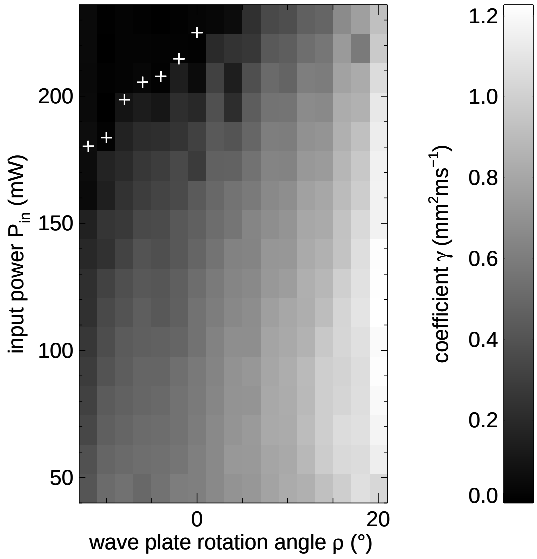

Figure 4.20: Transition from unstable domains to stable solitons. Coefficient γ in dependency on the wave plate rotation ρ and input power P_{in}. White crosses indicate the minimum power for the existence of stable solitons. Parameters: $d = 120\,\text{mm}$, $\Delta = 17.7\,\text{GHz}$, $T = 346.1\,^\circ\text{C}$.

where pronounced locking or large imperfection of the bifurcation is present, the coefficient γ only gives an estimate of a mean timescale of the overall dynamics of the domain. Figure 4.20 shows γ encoded into a greyscale value in dependency on the input power and ρ. White encodes a fast contraction, while black encodes a dynamics that reaches a stable situation at some point in time ($\gamma \approx 0$). For the positive domains considered here, negative (positive) values of ρ indicate that the domain is the favored (disfavored) state. Firstly, the diagram reproduces the phenomena that have been discussed in the previous sections. Making a vertical cut at $\rho = 0$ in the plot, the dynamics of the domain slows down with increasing input power as discussed in section 4.3.3. Apparently this phenomenon also persists in the case of an imperfect bifurcation ($\rho \neq 0$). In tendency, the graph becomes darker with increasing input power at every angle ρ. On the other hand, the dynamics slows down if the domain is in the favored state, while it accelerates if it is in the disfavored state. This behavior already discussed in the previous section apparently applies for all input powers considered here. The graph shows, that both effects seem to apply simultaneously. As a result, domains being in the disfavored state observed at low input powers (lower right corner) exhibit a relatively fast dynamics. The dynamics slows down with increasing input power and increasing preference of the domain state. Accordingly, the diagram becomes darker towards the upper left corner. In addition,

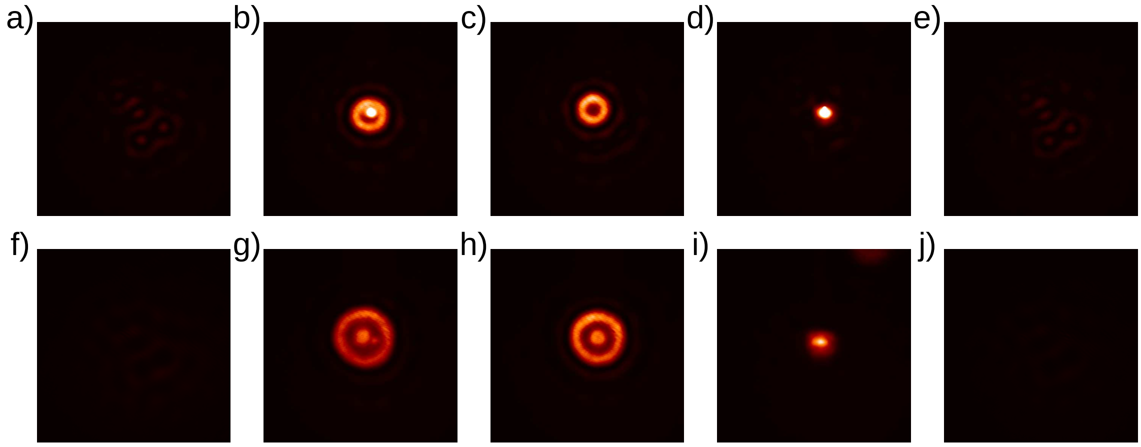

Figure 4.21: Switching sequence of two solitary structures of different order. Polarization analyzer aligned for suppression of the background beam in the detection branch: a) background beam; b) ignition of a soliton with circularly polarized addressing beam; c) stable soliton with addressing beam switched off; d) erasure of soliton with addressing beam of opposite circular polarization; e) background beam. Parameters (first column): $d = 120\,\mathrm{mm}$, a-e) $\Delta = 16.2\,\mathrm{GHz}$; $T = 321.8\,°\mathrm{C}$, $P_{in} = 219\,\mathrm{mW}$, $\rho = 4°30'$ f)-j) $\Delta = 14.6\,\mathrm{GHz}$, $T = 327.3\,°\mathrm{C}$, $P_{\mathrm{in}} = 165\,\mathrm{mW}$, $\rho = 7°00'$.

the locking of domains induced by spatial oscillations leads to a further slowdown of the dynamics at certain domain radii.

As a matter of fact, in the upper left corner, the dynamics completely stops at a certain domain radius, and stable structures that will be interpreted as solitons in the next section are observed. The threshold for the formation of stable structures is indicated by white crosses within the diagram. It will be discussed further in section 4.4.4.

4.4 Discrete family of solitons

In the previous section, the dynamical properties of unstable domains have been characterized, and the mechanisms that modify this dynamics have been identified. In the following section, stable localized structures will be presented which evolve due to an interplay of these mechanisms in adjacent parameter regions.

4.4.1 Preparation of solitons

A fundamental property of spatial solitons is the possibility to ignite and erase them by means of large perturbations, i.e. they exist in bistability with a state where no soliton is present. In many systems, solitons also appear spontaneously, but this behavior is not observed in the present experiment. An ignition and erasure procedure of a soliton is shown in Fig. 4.21a-e. The system is prepared in the state with positive polarization rotation. The $\lambda/8$-plate is oriented to incline a positive angle with the input polarization, therefor this state is the disfavored one. The analyzer is adjusted such that this background is suppressed (Fig. 4.21a). Then the σ_--polarized addressing beam is switched on and induces locally a transition to a state with negative polarization rotation. This results in a high transmission through the analyzer (Fig. 4.21b). If the addressing beam is switched off, a stable solitary structure survives that consists of a bright ring (Fig. 4.21c). Switching on – at the position of the solitary structure – the addressing beam with σ_+-polarization results in an extinction of the solitary structure (Fig. 4.21d). After the erasure procedure the system recovers its initial state (Fig. 4.21e).
If ρ is increased, another stable structure can be ignited in the same manner (see Figs. 4.21f-j). It consist of a central peak surrounded by a ring that is larger than the one described before. These structures resemble the metastable domains in the locking region discussed in the previous section (see Fig.4.15). For the parameters chosen here they are stable.
Similar structures can be ignited by means of a σ_+-polarized beam, if the system is first brought into a state with negative polarization rotation and the sign of ρ is reversed.

4.4.2 Family of solitons

If the diameter of the addressing beam is enlarged, two other types of stable solitary structures can be ignited for the same or similar parameters (see below). This sequence of structures represents the first experimental observation of a discrete family of solitons, which has been predicted in many theoretical works for many years (see chapter 2). An overview of the types of observed solitons concerning their polarization properties is given in Fig.4.22.

Basic properties

The first row shows the solitons with the linear polarizer oriented to suppress the background (as in all pictures before). The solitons differ in size and in the number of radial oscillations. Their order will be denoted by numbering them from 1-4. Depending on the size of the addressing beam, the circular domain, which is initially ignited, will shrink or

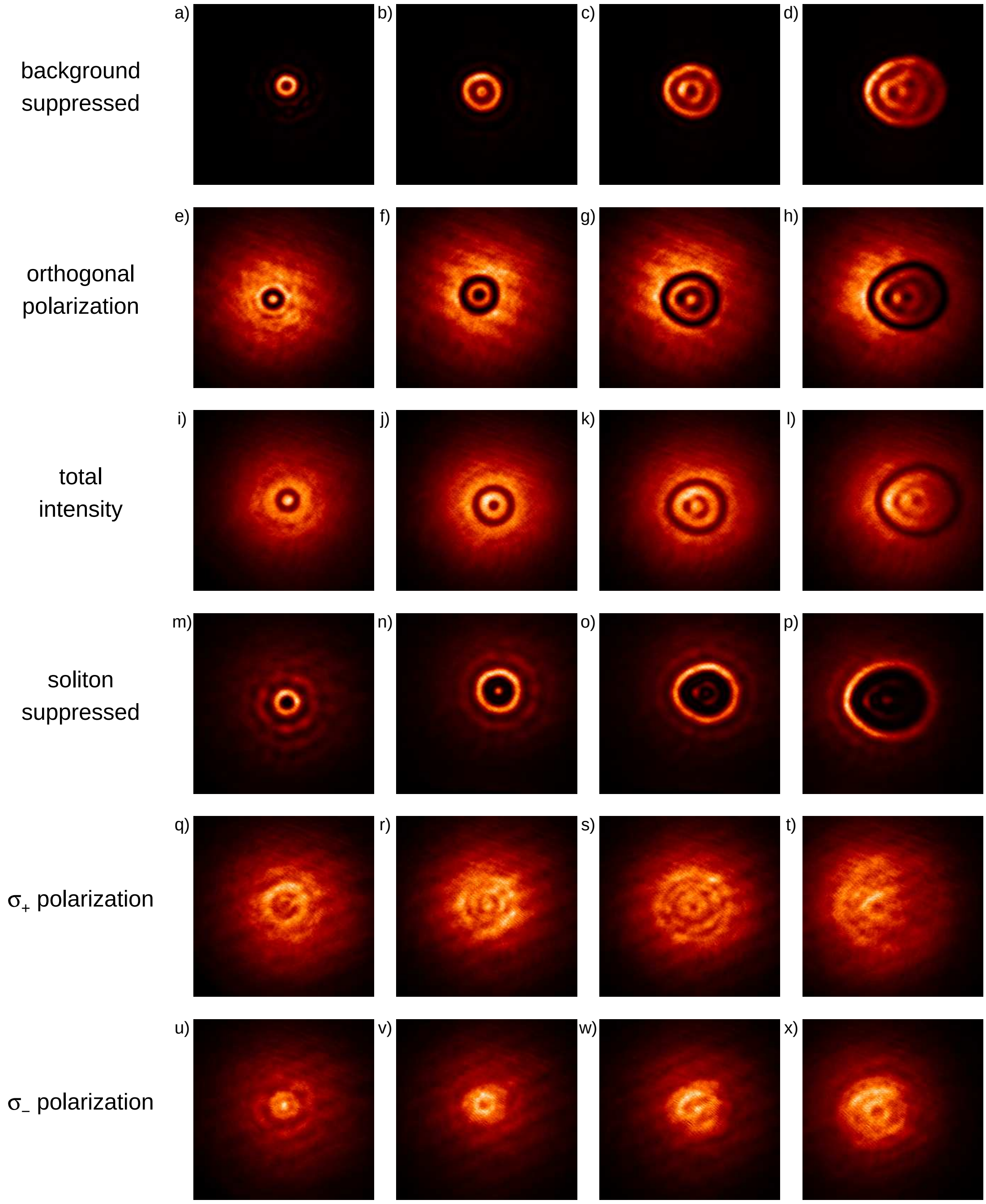

Figure 4.22: Discrete family of solitons. Parameters (first column): see Fig.4.21a-e. Parameters (2nd-4th column): see Fig.4.21f-j.

expand until one of the stable solitary structures is reached. Thus, these stable states are attractors of the dynamics of the system.
Solitons 1-3 persist for time periods of some seconds to minutes depending on the parameters. This is very long compared to the typical timescale of the system being of the order of microseconds. Soliton 4 is much more difficult to prepare and has been rarely observed. It typically persists for some seconds, which is enough to identify it as a stable structure. It has a tendency to drift off the beam center. Frequently, soliton 4 is observed only as a metastable structure that drifts to the boundaries of the beam and then decays or expands.
The second row of Fig. 4.22 shows the situation when the linear polarizer is adjusted orthogonal with respect to the position used in the images in the first row. So it is optimized for the transmission of the background. From these pictures, the size and position of the solitons with respect to the background beam is visible. While the first three solitons are oriented in the beam center, the fourth one is not. Rows one and three are complementary. However, even the total intensity distributions without any polarization analysis elements are modulated (see row four). This is due to the amount of absorption that is still present despite the relatively large detuning of the holding beam. This view of the soliton family resembles the intensity distributions of the solitons that were theoretically predicted to occur in the presence of a pitchfork bifurcation which have been called 'dark ring cavity solitons'. However, in the present system, the orientation is the state variable, and hence the intensity does not vanish within the dark rings.
In row three of Fig.4.22, the linear polarizer is optimized to suppress the state of the pitchfork bifurcation that does not serve as the background state for the solitons. It is obvious that the polarization of the solitons (aside from the oscillations) is near that polarization state. The image of soliton 1 leads to the conjecture that this structure is a single-peaked structure and therewith the fundamental soliton of this family. This will be proven in the next section.
Rows five and six show the components of circular polarization. There is a slight modulation of the Gaussian background, however it is very limited. In tendency, the modulations for σ_+ and σ_- light are complementary. This is expected for a nonzero orientation of the vapor.
From the shown possibilities to display the solitons, the images with suppressed background (row one) have the largest contrast. Therefor they have been chosen as the standard in this work.

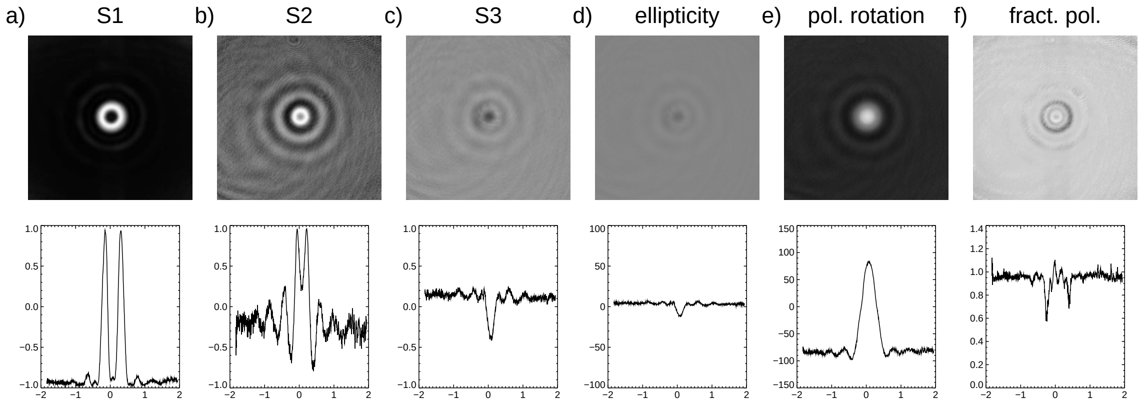

Figure 4.23: Spatially resolved Stokes parameters of a first order soliton. Parameters: $d = 112\,\mathrm{mm}$, $\Delta = 16.7\,\mathrm{GHz}$, $T = 360.4\,°\mathrm{C}$, $P_{in} = 180.7\,\mathrm{mW}$, $\rho = -14°03'$.

Measurement of Stokes parameters

A very powerful method to characterize the polarization of a light field is the spatially resolved measurement of its Stokes parameters. It gives the full information about the polarization state as described in section 3.4.

The measurement of the Stokes parameters can be performed only if the system is very stationary. This is due to to the need to exchange elements in the polarization analysis between taking the four required images. A full measurement takes up to two minutes. So only a subset of structures can be covered by this measurement. This excludes all dynamical structures like the unstable domains discussed in section 4.3. Also pattern formation is excluded, though the patterns are stable in principle. However, they move on a timescale of hundrets of microseconds to milliseconds. This drift is attributed to the noise that is present in the system. The solitons are stable on a much longer timescale. Nevertheless they exhibit a certain jitter, which can be attributed to noise as well. To improve image quality in the measurement, the single images have been shifted by up to 10 pixels in order to perfectly overlay the structures.

The result of a measurement of the spatially resolved Stokes parameters of a first order soliton is given in Fig. 4.23. The Stokes parameter S1 characterizes the tendency of the light field to be linearly polarized in the direction of the input polarization (S1=1) or the orthogonal direction (S1=-1). Figure 4.23a shows the spatially resolved parameter S1 and a vertical cut through the center of the structure. It is a bright ring that looks similar to the pictures with suppressed background discussed in the previous subsection. The absolute value of S1 is close to one in a large region of the image. The light field is obviously linearly polarized to a very high level. As expected, the sodium vapor has a large influence on the input light field, since S1 is close to one only in a very small region. Figure 4.23b shows the parameter S2 that describes a tendency of the light field to be linearly polarized at an angle of 45° (S2=1) or -45° (S2=-1) with respect to the input polarization. It shows nicely the oscillations of the background field. S3 gives the tendency of the light field to be σ_- polarized (S3=1) or σ_+ polarized (S3=-1). The amount of circular polarization is a measure for the strength of nonlinear absorption present in the system. An orientation of the vapor leads to a difference in the absorption coefficients for circularly polarized light of different helicity (see section 5.1). Thus, a linearly polarized input field becomes elliptical. Figure 4.23c shows that the amount of circular polarization is rather small for the parameters used throughout this work. This is also reflected by the ellipticity of the light field that does not exceed |15°| (Fig. 4.23d). It can bee seen, however, that the ellipticity changes its sign at the position of the soliton. This gives a hint that also the orientation of the vapor changes its sign at the position of the soliton.

The dispersive part of the nonlinearity that leads to a rotation of a linearly polarized light field seems to play the dominant role in this experiment. Hence, it seems especially promising to determine the angle of the main axis of polarization with respect to the input polarization. While a direct measurement of the orientation is not possible, the polarization rotation angle is proportional to the orientation of the sodium vapor (see section 5.1). Hence, the spatially resolved measurement of the Stokes parameters of the light field transmitted by the vapor can provide an indirect measure of its orientation and thus to the state variable of the microscopic model.

Fig. 4.23e shows the spatially resolved measurement of the angle of the main axis of polarization with respect to the input polarization. The state serving as the background exhibits a negative polarization rotation angle of $\xi \approx -85°$ It can be identified as one of the two states emerging from the pitchfork bifurcation. In the region of the soliton the polarization state changes drastically. Obviously soliton 1 is a single-peaked structure and can now be identified as the fundamental soliton. The center of the soliton exhibits a polarization rotation angle of $\xi \approx +80°$. This angle corresponds nicely to the second state emerging from the pitchfork bifurcation, which will be called the *target state*. Thus, the soliton is interpreted as a high-amplitude localized excursion from one (nearly) homogeneous state towards the vicinity of the other one and back.

Fig. 4.23f shows the fractional polarization of the light field. In this experiment, only fully polarized light should occur since spontaneous emission is suppressed by the choice of the buffer gas. As a result, the measured fractional polarization is near one in large areas of Fig. 4.23f. Of course some noise is present especially in the outer regions where all measured intensities are low. However, there is a systematic deviation that is connected to the existence of the solitary structure. At some radius around the structure the fractional polarization significantly deviates from one. This is attributed to the jittering of the structure which in the presence of the steep gradients can lead to an apparent breakdown of the fractional polarization.

The spatially resolved measurement of the polarization rotation angle ξ seems to be a promising method to characterize the solitons. Figure 4.24 shows the first three members of the family of solitons together with the two (nearly) homogeneous states that serve as the background and target state. Each subfigure shows a three-dimensional surface plot of ξ. At the front side of the plots of the solitons, two orthogonal cuts through the center of the structure are shown. In order to reduce spatial noise especially in the outer parts of the plot, a two-dimensional adaptive noise-removal filter[1] has been applied to the ξ distribution. Some lighting has been added in order to emphasize small-scale oscillations that cannot be distinguished by the color table gradients in the printout.

The state that serves as the background of the solitons is shown in Fig. 4.24a. It exhibits a mean polarization rotation $\xi = -89.5\,^\circ$ and is nearly homogeneous. Slight modulations are visible in the beam center. The measurement was conducted at an input power near the threshold for pattern formation. The rudiment of the evolving pattern is visible here, because it is pinned due to the boundary conditions of the Gaussian beam. The polarization rotation angle does not change even in the outermost parts of the plot where light intensities are significantly lower. Obviously the large intensity gradient of the light field does not lead to the appearance of large gradients within the orientation distribution. This can be understood from the following aspects: Due to the low threshold of the pitchfork bifurcation orientation can be generated even at low intensities. Furthermore the thermal diffusion of the sodium atoms leads to an orientation even in the areas where there is virtually no light. The only losses in these areas leading to a depolarization of the vapor are the very small ground state relaxation mechanism induced by particle-particle collisions, collisions of sodium atoms with the cell walls at a distance of 6 mm and small magnetic stray fields.

The second state emerging from the pitchfork bifurcation which serves as the target state of the solitons is shown in Fig. 4.24e). Its mean polarization rotation is $\xi = 60.2\,^\circ$ The difference compared to the background state is a result of the imperfection of the pitchfork bifurcation that is introduced by rotation of the wave plate. The target state is the favored state and thus it exhibits a smaller polarization rotation. It also has a slightly lower threshold for pattern formation as can be concluded from the slightly larger amplitude of the oscillations in the beam center.

The 3D plot of the already discussed fundamental soliton is shown in Fig. 4.24b. The

[1] Function `wiener2` from the image processing toolbox of MATLAB 7.0 using a neighborhood of 20x20 pixels to estimate the local image mean and standard deviation

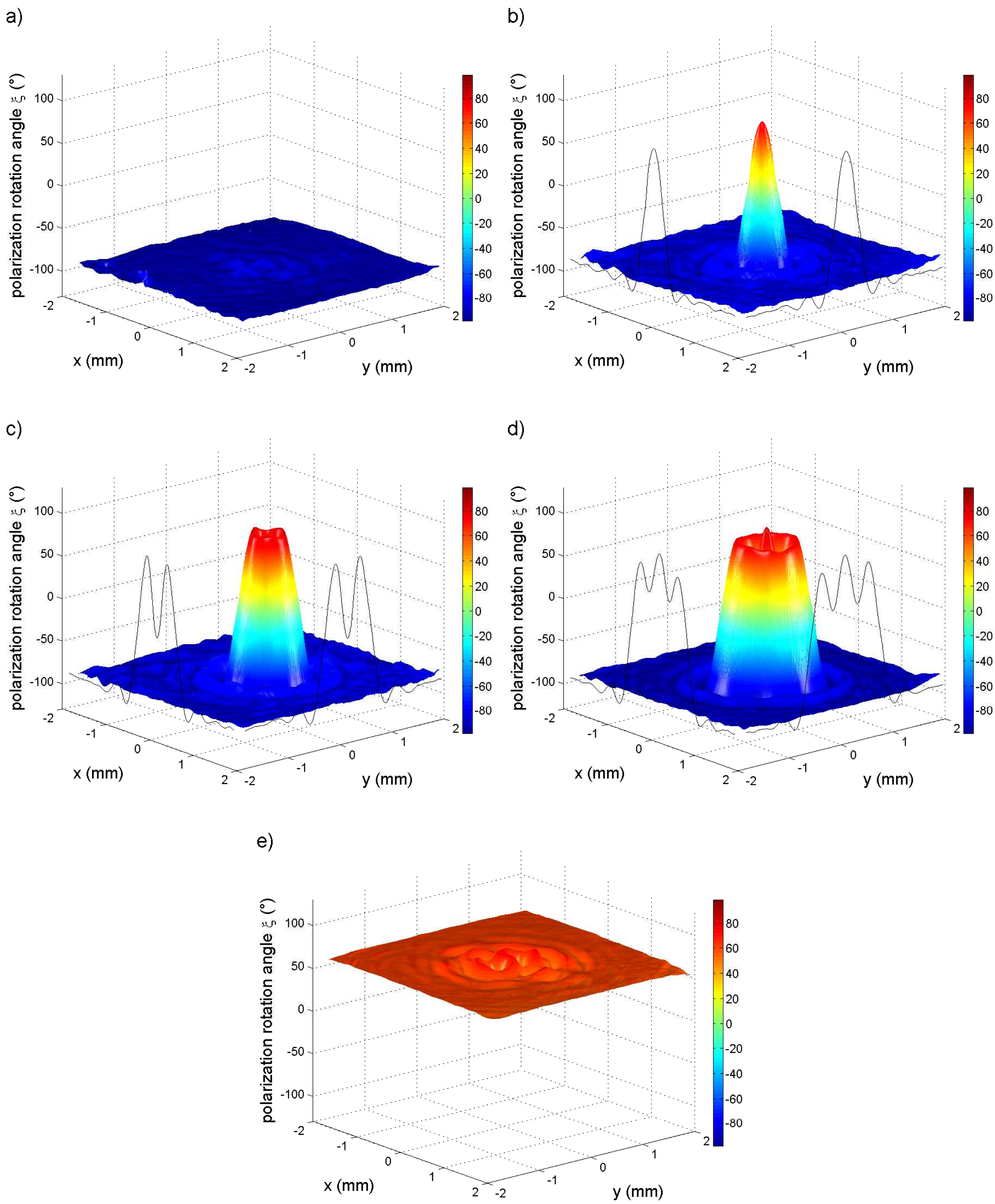

Figure 4.24: First to third order positive solitons (b-d) and corresponding (nearly) unstructured states (a,e). Spatially resolved polarization rotation angle ξ obtained from a measurement of the Stokes parameters of the light field. Parameters: see Fig. 4.23, except: d) $\rho = -15°21'$.

figure illustrates nicely the shape of the single-peaked structure. In the surface plot as well as in the cuts the ring-shaped oscillations of the background around the structure become apparent. At exactly the same parameters, soliton 2 can be ignited which is shown in Fig. 4.24c. The width of the whole structure is larger than the first order soliton. It also has a circular shape, but it has a dip in the center. In a radial cut, the system undergoes one spatial oscillation around the target state before returning to the background state. The structure is surrounded by ring-shape oscillations that have the same appearance as the ones of soliton 1.

If the wave plate rotation angle is slightly decreased, the third member of the soliton family can be ignited (Fig.4.24d). It is a circular structure consisting of a central peak which is surrounded by a ring. Here the system undergoes two spatial oscillation periods before returning to the background. These oscillations are less pronounced than in soliton 2.

All solitons shown in Fig.4.24 are large-amplitude structures that exhibit a positive polarization rotation (and thereby positive orientation) existing on a background of a state with negative polarization rotation (and orientation). Hence, they will be called *positive solitons* in the following.

As an analogon, a soliton exhibiting a negative polarization rotation existing on a background with positive polarization rotation is called *negative soliton*. These structures can be obtained if the wave plate rotation angle is reversed. This interchanges the role of the two (nearly) homogeneous states. Of course, the helicity of the ignition beam has to be changed also. The family of negative solitons together with their background and target states are shown in Fig.4.25.

The family of negative solitons exhibits the same properties already discussed for the family of positive solitons with reversed polarization rotation angles ξ. This is the expected result because of the symmetry properties of the system. It has to be emphasized that the described behaviour is significantly different from the phenomenon of 'bright' and 'dark' solitons that is commonly discussed in systems where background and target state are not (nearly) equivalent.

From the given results, a first interpretation of the nature of the soliton families can be derived. It appears that all members of the soliton family represent a localized excursion from the background state into the vicinity of the target state and back, i.e. the soliton represents a homoclinic connection of the background state with itself (see, e.g., [CRT00b]). In the one-dimensional case this situation is characterized by the existence of two switching fronts which are locked, while in the two-dimensional case a circular front is interacting with itself. Since oscillations around the states that serve as background and target seem to play an important role here, it can be assumed that the locking process

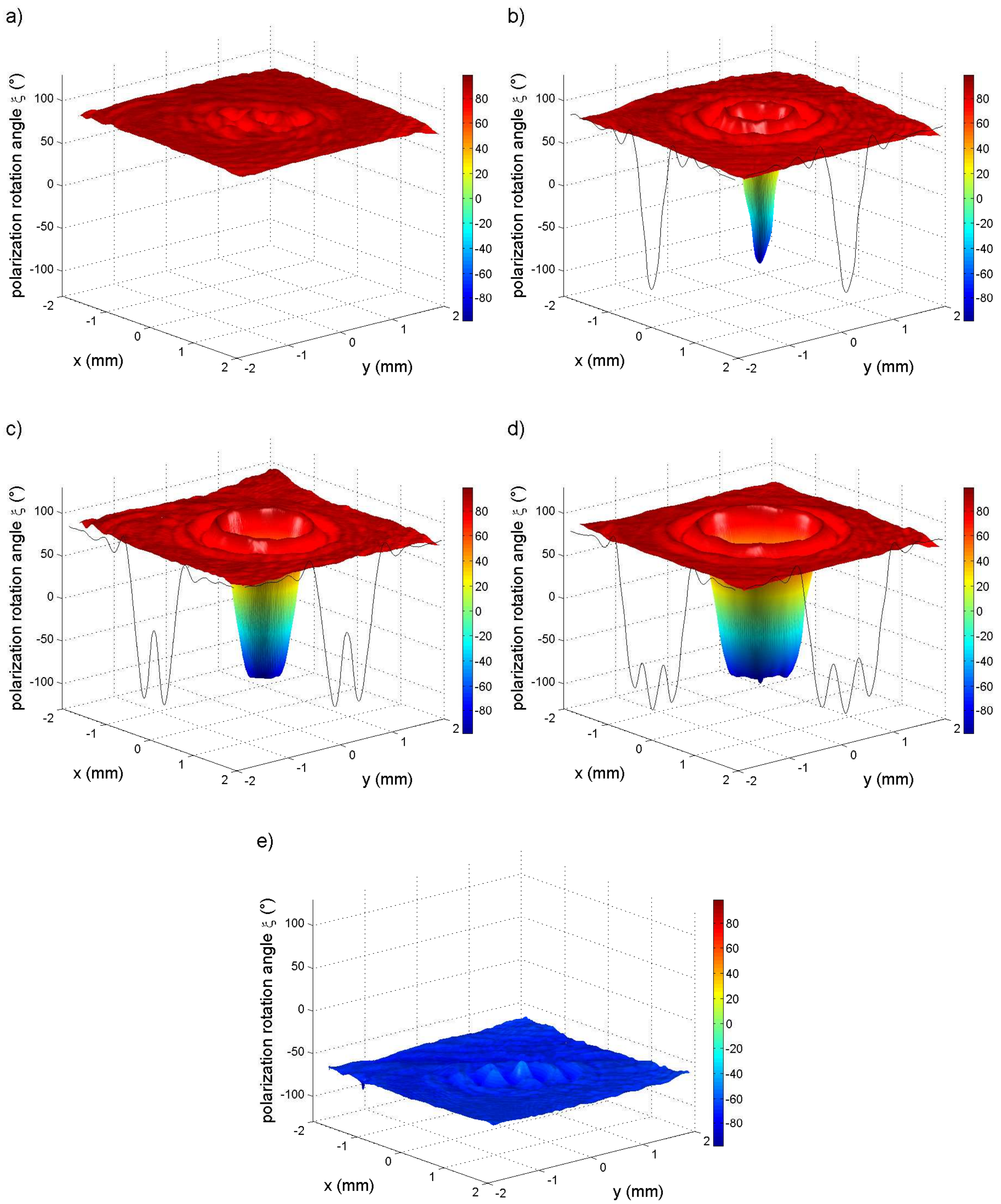

Figure 4.25: First to third order negative solitons (b-d) and corresponding (nearly) unstructured states (a,e). Spatially resolved polarization rotation angle ξ obtained from a measurement of the Stokes parameters of the light field. Parameters: see Fig. 4.23, except: a)-c,e) $\rho = 11°59'$; d) $\rho = 13°39'$.

is heavily supported by the presence of the modulational instability which exists on both branches, i.e. in the states of positive or negative rotation of the polarization. Locking should then be possible at different spatial separations of the fronts due to the periodicity of the modulated states. The existence of a discrete family of solitons appears to be the natural consequence.

4.4.3 Length scales

A quantitative analysis of the sizes and modulation length scales of the solitons gives further insight into the mechanisms leading to the formation of a discrete family of solitons. As discussed in the previous subsection, a radially averaged profile of each soliton can be derived from the measurement of the spatially resolved polarization rotation angle (the ξ distribution without noise filtering has been used here). These radial profiles are shown in Fig. 4.26a. For a better comparison, the profiles of the family of negative solitons have been reversed: Solid lines show the profile of positive solitons, while dashed lines represent the inverse profile of negative solitons.
Firstly, it is noticed that there are virtually no differences between the profiles of positive and of negative solitons of the same order. Once more, this nicely illustrates the symmetry properties of the system. The radial profile of a soliton can be divided into three parts. Starting from the middle, at first there are potentially oscillations around the target state. This, of course, does not apply to the fundamental soliton. In the case of S2, there is a half oscillation leading from a minimum to a maximum at 0.23 mm. In the case of S3, there is a full oscillation period starting from a maximum and leading back to a maximum at 0.43 mm. It can be noticed that the oscillation period is approximately the same. As stated in the description of Figs. 4.24 and 4.25, the experiment was performed near the threshold for pattern formation, where no clear pattern has yet evolved. In order to compare the length scale of the modulational instability with the oscillation period found within the solitons, a hexagonal pattern at higher input powers was observed and analyzed. It is known that the length scale might slightly change with increasing power. However, it can be taken as a good estimate of the length scale. The light grey vertical lines in Fig.4.26a indicate multiples of the half wavelength of the hexagonal pattern ($\Lambda/2 = 0.218\,\mathrm{mm}$). The length scale of the modulational instability matches quite well the oscillation period that is observed within the target state.
The second remarkable feature of the radial profile of the solitons is the polarization front leading from the target state towards the background state, which is characterized by a change of sign of ξ. The polarization rotation angle $\xi = 0$ can serve as a good measure for the width of the structures, as it is similar to the width at half maximum in a good approximation. From any soliton order to the next, the width of the solitons increases

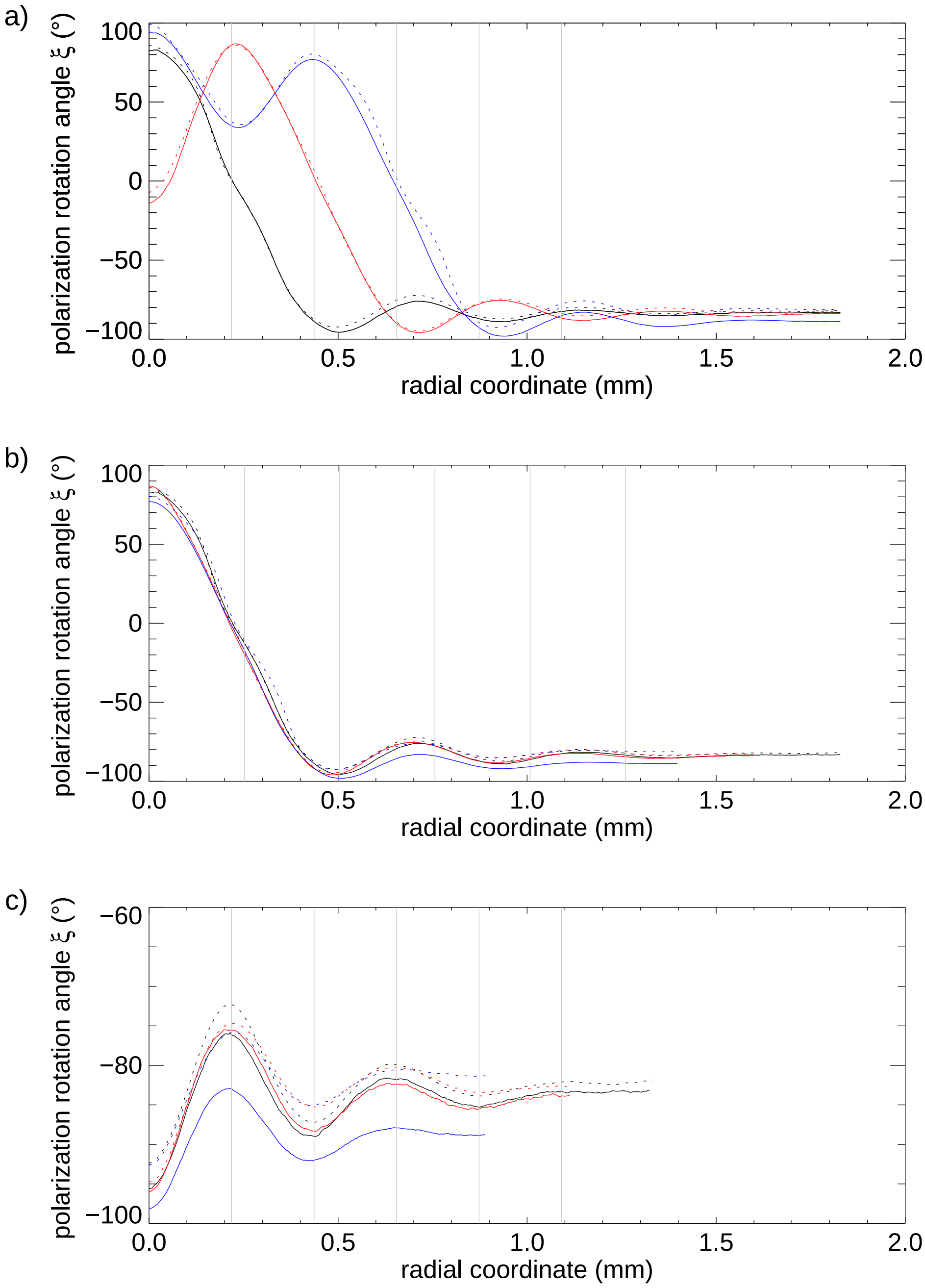

Figure 4.26: Radially averaged profiles of positive (straight lines) and inverted negative (dashed lines) solitons of first (black), second(red) and third (blue) order. a) full profiles; b) polarization front starting from the outermost maximum of each soliton; c) oscillatory tails starting from the first minimum of the solitons. Parameters: see Figs. 4.23, 4.24, 4.25.

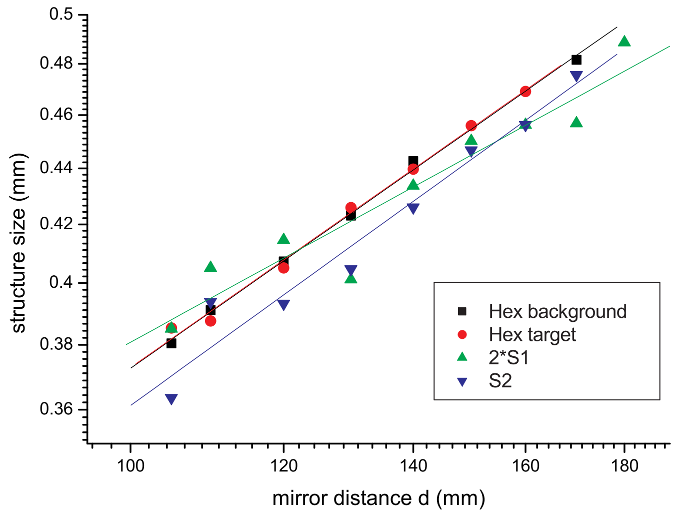

Figure 4.27: Double logarithmic plot of structure sizes against mirror distance d. Parameters: $d = 105\,\mathrm{mm}$, $\Delta = 16.0\,\mathrm{GHz}$, $T = 331.0\,^\circ\mathrm{C}$, $P_{in} = 331\,\mathrm{mW}$, $\rho = 1^\circ$ (105 mm)-11° (180 mm).

in discrete equal steps. These equal steps are well connected to the length scale of the modulational instability (see vertical lines). However, the whole front (leading from the last maximum at positive angles to the first minimum at negative angles), is slightly larger than one oscillation period of the modulational instability. In order to characterize the front further, Fig. 4.26b shows the radial profile of the solitons starting at the last maximum of the respective soliton. It turns out that the shape of the front seems to be fixed and independent from the order of the soliton. Its size amounts to 0.50 mm. This corresponds to the distance between the constituents of a hexagonal pattern, that is connected to the length scale of the pattern by $d_c = \Lambda \cdot \frac{2}{\sqrt{3}} = 0.50\,\mathrm{mm}$.
The third remarkable feature of the solitons is the occurrence of modulations around the background state, which are generally referred to as oscillatory tails. These oscillatory tails, starting from the end of the front, are depicted in Fig. 4.26c. The amplitude of the oscillation decreases significantly with increasing distance from the soliton. Nevertheless, a clear oscillation period is observed in all curves. Just as in the case of the modulations around the target state, it is connected to the length scale of the modulational instability. The above considerations suggest that the length scale of the solitons is connected to the length scale of the modulational instability, which can commonly be derived from the Talbot effect as discussed in section 2.3.2. It is mainly given by the distance of the feedback mirror d. The wavelength of the pattern is expected to scale like $\Lambda_p \propto \sqrt{d}$. A

similar scaling behavior should then be observed for patterns and solitons, if the mirror distance is varied. Fig. 4.27 shows the sizes of solitons S1 and S2 compared to the length scale of the hexagonal patterns that serve as background and target state in a double logarithmic plot. The size of the solitons is determined from images that show the soliton with suppressed background. The radius of the outer ring gives a rough measure of the width at half maximum as indicated in the scheme in Fig. 4.27. The size of S1 has been scaled by a factor 2 in order to show all data in one plot. The length scale of the hexagonal patterns is determined from the distance between the constituents scaled by a factor of $\frac{\sqrt{3}}{2}$. For all structures, an increase in size is observed if the mirror distance is increased. A linear fit in the logarithmic plot reveals the underlying power law. The slope of the linear fit for the hexagonal patterns is given by 0.491 ± 0.012 (background state) and 0.491 ± 0.017 (target state). This is in a good agreement with the expected $\sqrt{d}$ scaling behavior.

In the case of the solitons, growth exponents of 0.384 ± 0.047 (S1) and 0.505 ± 0.043 are observed. At least for S2 a clear connection to scaling of the underlying modulational instability can be verified. The data of S1 shows large fluctuations. However, a similarity of the scaling behavior can be conjectured.

4.4.4 Region of existence

Figure 4.28 shows an overview of the bifurcation scenario and of the regions of existence of positive and negative solitons in dependency on the wave plate rotation angle and input power. The black squares separate the regions where only one homogeneous or patterned solution exists from the one where bistability is observed. Triangles facing up- and downwards indicate the threshold for pattern formation as discussed in section 4.2.3. The regions of existence of the solitons are measured in the following manner: A soliton is ignited for a given input power. Then ρ is increased and decreased until the soliton either decays and disappears or expands and switches the whole beam to the favored state. Typically there are transformations concerning the order of the soliton when ρ is varied, which is disregarded in this measurement and will be discussed below.

The margin of the region of existence of positive solitons is indicated by the blue open circles. All data points in the diagram are connected by straight lines to guide the eye and increase clarity. The region of existence of negative solitons is indicated by red full circles. It can be easily seen from the diagram that the system behaves very symmetric with respect to $\rho = 0$. This has already been shown in the previous sections, and here it becomes clear that the same is true for the region of existence of the solitons. Therefor they will not be individually discussed.

The minimum threshold power $P_c \approx 125\,\mathrm{mW}$ for the existence of solitons occurs, if the

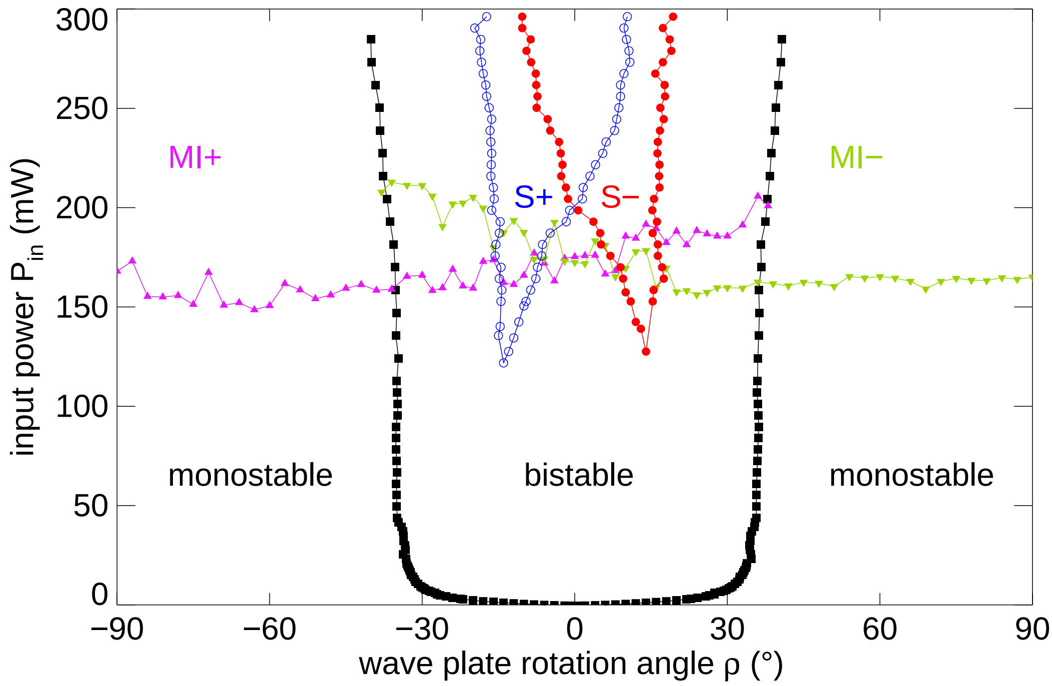

Figure 4.28: Overview of the bifurcation scenario and the region of existence of positive and negative solitons. ■: threshold for bistability; threshold for pattern formation of the positive (▲) and negative (▼) branch of the pitchfork bifurcation; regions of existence of positive (○) and negative (●) solitons. Parameters: see Fig. 4.7.

slow axis of the $\lambda/8$-plate and the input polarization include some finite angle ρ_c which disfavors the polarization state of the background and favors the polarization state of the soliton. About the same threshold is obtained for the angle -ρ_c, of course, with the roles of the two polarization states being interchanged. When the input power is increased above P_c, then there is a finite range of angles ρ, where solitons exist. If $|\rho|$ decreased below a critical angle, the soliton becomes unstable and disappears. If $|\rho|$ is increased beyond the border of the existence region, the soliton becomes unstable and expands and the whole beam switches to the favored branch. In a certain power range, solitons can exist below the threshold for pattern formation. Above a second threshold $P_c' \approx 200\,\mathrm{mW}$, the range of ρ, where solitons exist, includes ρ=0. In that case the two polarization states are completely equivalent. At this power level they are both modulationally unstable. Above this second threshold there is a finite range of angles ρ where positive and negative solitons can exist for the same parameters. For very high input powers, solitons can even be stable if the polarization state of the background is the favored one and the polarization state of the soliton is the disfavored one.

The presented experimental results lead to a first interpretation of the mechanism that leads to the formation of stable solitons. In section 4.3 it was shown that in the case of the existence of two equivalent states circular domains shrink and finally disappear. The edge of the domain, however, may be pinned by spatial modulations, and pinning is more probable, when strong modulations are present, of course. Obviously robust pinning occurs here when the input power P_{in} exceeds P'_c.

If the two homogeneous states are not completely equivalent, i.e. in the case $\rho \neq 0$, the curvature-driven shrinkage of a droplet is counteracted, if the droplet is in the preferred state. For large values of $|\rho|$ the shrinkage can even be overcompensated and then the droplet expands. For a given ρ, there is a critical radius of the droplet where the two effects are in balance. However, this situation is unstable, at least in the absence of spatial oscillations. Nevertheless, front velocities are low near this critical radius. Due to the existence of the modulational instability, spatial modulations become much more pronounced for increased input power. In the case ρ=ρ_c the modulations occurring for $P_{\text{in}} = P_c$ are considered to warrant stabilization, while in the case ρ=0, i.e. without other effects counteracting the curvature-driven dynamics, the modulations corresponding to P'_c are necessary.

To refine this picture, a measurement was conducted that determines the region of existence of the different members of the family of positive solitons. The result is shown in Fig.4.29. For the given set of parameters, positive solitons of first, second and third order are observed. The measurement was conducted similar to the previous one. For a given input power, soliton 1 was ignited by means of the addressing beam. Then ρ was increased until the soliton disappeared. Then ρ was adjusted back to the starting position, the soliton was ignited again and ρ was decreased. At the point where the soliton becomes unstable, it typically either transforms into a soliton of neighboring order or into an elongated bound state of same order (see below in section 4.5.2). Then the measurement is continued with the next order soliton. For the measurement of the minima of the regions, ρ and the laser power have been varied simultaneously. It has been checked that there are no unconnected regions of existence of solitons of same order.

While the outline of all regions together generally reproduces the region of existence discussed in Fig. 4.28, there are some interesting aspects of the single curves. The minimum power necessary for a stable soliton is nearly the same for soliton 2 and 3 ($P_{\text{in}} \approx 130\,\text{mW}$). In the case of soliton 1, it is significantly higher ($P_{\text{in}} \approx 160\,\text{mW}$). It can be conjectured that the stability of soliton 1 requires a larger amount of spatial oscillations.

The absolute values of the critical angles ρ_c depend in a systematic way from the soliton

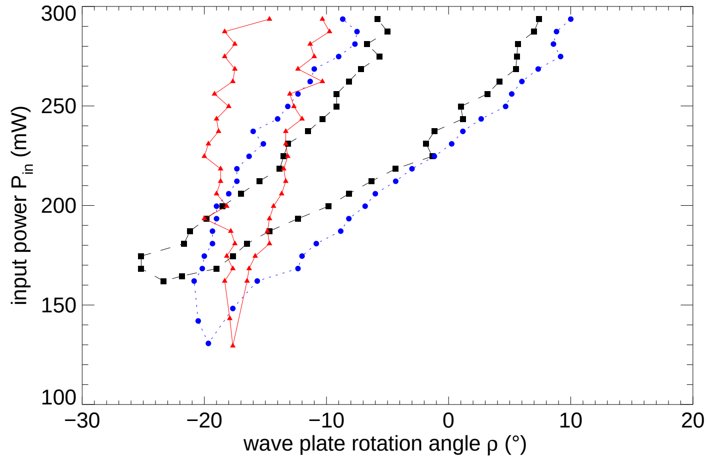

Figure 4.29: Regions of existence of positive solitons of first(■), second (●) and third (▲) order. Parameters: $d = 112\,\mathrm{mm}$, $\Delta = 16.3\,\mathrm{GHz}$, $T = 360.2\,^\circ\mathrm{C}$.

order. For the smallest structure, it is the highest ($|\rho_c| = -23.3°$). For soliton 2 it is $|\rho_c| = -20.5°$, and soliton 3 has the smallest critical angle $|\rho_c| = -17.7°$. This can be understood by looking again at the domain dynamics. Small domains that have a large curvature of the domain wall have a strong drive to contract. Therefor the amount of non-equivalence of the two states needed to compensate this curvature-driven dynamics is high. Hence, a domain of the size of soliton 1 requires larger angles ρ to reach an equilibrium than the higher order solitons. This equilibrium is then stabilized by the modulations.

Above the threshold the regions of existence become broader. This is interpreted to be due to the stronger locking of the domain walls with higher input powers. There are large regions where neighboring orders of solitons can exist simultaneously. For medium input powers there even is an area where all three regions of existence overlap. If the input power is increased further, the situation reverses. Smaller solitons are observed for small angles, while large structures are observed for large angles. Solitons 1 and 2 can be observed beyond $\rho = 0$.

With increasing input power, the modulations in the system due to the modulational instability increase with respect to their amplitude as well as to the size of the patterned area in the Gaussian beam (see section 4.2.1). For high input powers, the patterns exist on both branches of the pitchfork bifurcation. However, their amplitude is still small compared to the amplitude of the solitons. Figure 4.30 shows how these high-amplitude solitons interact with the modulation of the background state at high input powers.

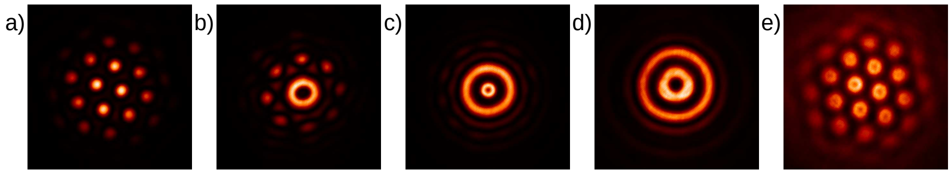

Figure 4.30: Patterns and solitons at high input power. a),e) hexagonal patterns of background and target state, b)-d) S1-S3. Parameters: see Fig. 4.29, $P_{\text{in}} = 261\,\text{mW}$, a)-c),e) $\rho = -5°$, d) $\rho = -15°$.

Image 4.30a shows the hexagonal pattern emerging from the branch of the pitchfork bifurcation that is used as the background state, while Fig. 4.30e shows the hexagonal pattern emerging from the other branch. A clear hexagonal symmetry is observed in both situations. Figs. 4.30b-d show the solitons 1-3 in increasing order for the same input power. Soliton 1 is surrounded by modulations. Its own shape, however, is radially symmetric. The surrounding modulations are interpreted as a highly distorted pattern. Obviously the high-amplitude soliton has a large impact on the background state, while the impact of the pattern on the soliton is negligible. Soliton 2 is larger in size and therefor the area in the Gaussian beam where patterns can exist is mostly occupied by the soliton. No azimuthal modulation of the background is observed anymore. Hence, the existence of the soliton suppresses pattern formation. The same is true for soliton 3, where nearly the whole central area of the beam is occupied.

The interaction of the solitons with the background under variation of the input power is shown in Fig. 4.31. The first row shows images of soliton 1 taken at the center of its region of existence with respect to ρ. At low input powers, the soliton as well as the modulations of the background have a perfect circular shape. With increasing input power, the background modulation becomes more and more azimuthally modulated. The intensity peaks of the background modulation all have the same distance from the soliton, i.e. they are organized on a ring. The size and the shape of the soliton itself does not change significantly. However, a very slight azimuthal modulation of the soliton is observed for high input powers.

Solitons 2 and 3 are also perfectly circular at low input powers (see Fig. 4.31g-r). Soliton 2 slightly changes its appearance with increasing input power. The central peak develops a small dip in its middle. This is interpreted as an increasing modulation depth of the oscillation within the soliton. This leads to the observation of a dip when looking at the soliton with a linear polarizer that suppresses the background. The evolving azimuthal modulation of the background is again interpreted as a strongly distorted pattern. Soliton

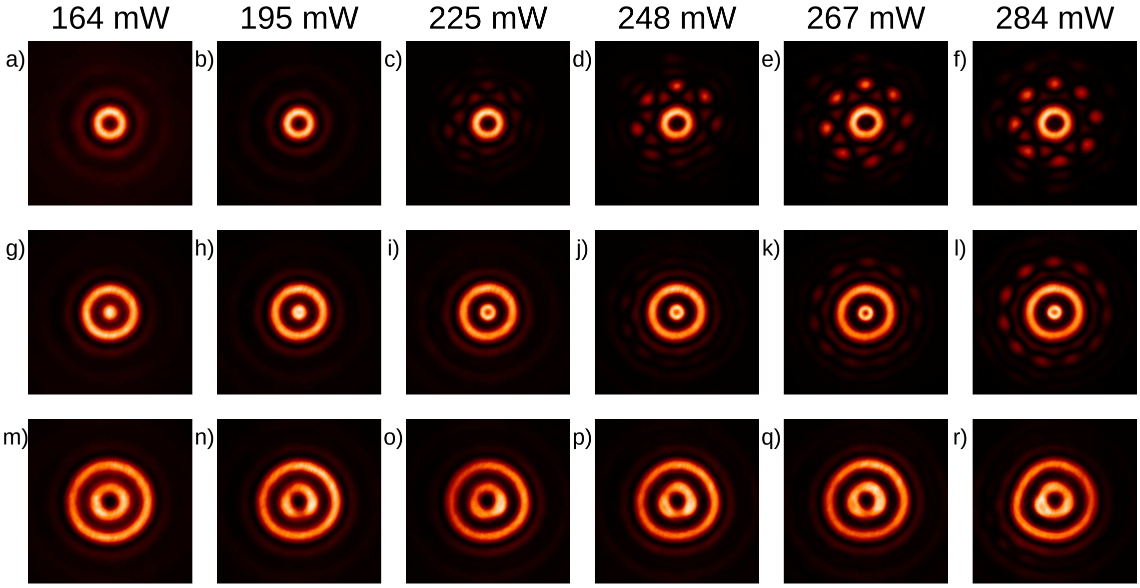

Figure 4.31: Evolution of first (first row), second (second row) and third (third row) order solitons under variation of input power P_{in}. Images were taken at the center of the corresponding existence region (see Fig. 4.29). Parameters: see Fig. 4.29.

3 is large enough to completely suppress pattern formation in the background. However, at high input powers, the inner ring of the soliton becomes slightly modulated. This leads to the conjecture that the modulational instability of the second branch has a growing influence. This influence finally leads to the formation of localized patterns which will be discussed in section 4.6.3.

4.5 Multiple solitons and bound states

Hitherto, in order to characterize the basic properties, the discussion of the solitons has been limited to a single soliton existing at a certain instance of time. Interesting situations arise, if – by means of the addressing beam – one or more additional solitons are ignited. Indeed, the interaction of multiple solitons leads to the formation of a large variety of stable configurations.

4.5.1 Soliton clusters

An important property of dissipative solitons is their individual addressability, which makes them interesting candidates for using them in all-optical memories. Figure 4.32

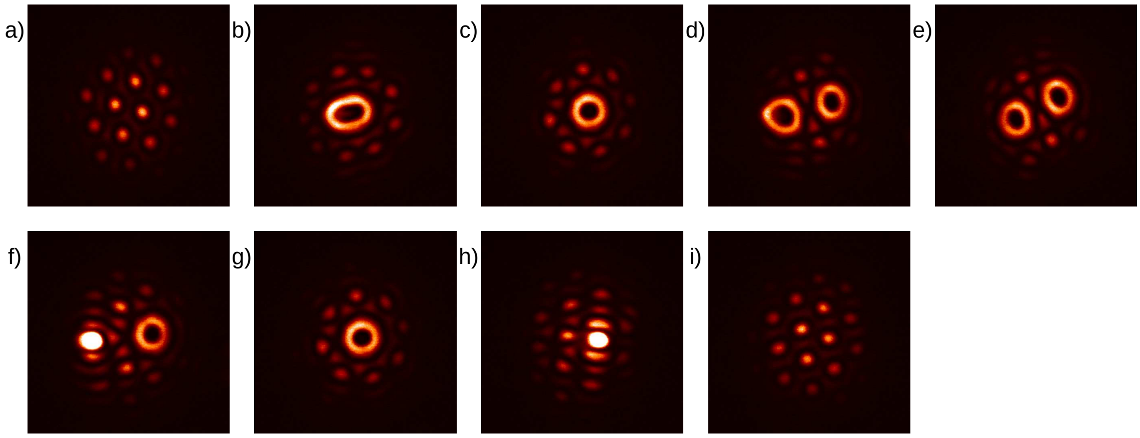

Figure 4.32: Individual ignition and erasure of two solitons. a) background beam; b) ignition of first soliton; c) stable soliton with addressing beam switched off; d) ignition of second soliton; e) two stable solitons with addressing beam switched off; f) erasure of first soliton; g) second soliton with addressing beam switched off; h) erasure of second soliton; i) background beam. Parameters: $d = 112\,\mathrm{mm}$, $\Delta = 15.6\,\mathrm{GHz}$, $T = 346.0\,^\circ\mathrm{C}$, $P_{\mathrm{in}} = 239\,\mathrm{mW}$, $\rho = -3\,^\circ\,40\,'$.

shows a switching sequence where two solitons are individually ignited and erased. The addressing beam is positioned at an off-center position. Starting from a hexagonal pattern (Fig. 4.32a), it is switched on and ignites a domain similar to an S1 soliton (Fig. 4.32b). If the addressing beam is switched off, the domain forms a stable S1 soliton which moves towards the beam center (Fig. 4.32c). If the addressing beam is switched on again, a second soliton is ignited (Fig. 4.32d). After the addressing beam is switched off, the two solitons start to interact and establish a stable configuration (Fig. 4.32e). Such a stable configuration of two or more solitons will be called a *soliton cluster* in the following. If the addressing beam, its polarization now having the opposite helicity, is switched on at the position of the left soliton (Fig. 4.32f), it is erased. The remaining soliton again moves towards the beam center (Fig. 4.32g). It can also be erased by means of the the addressing beam (Fig. 4.32h), restoring the initial situation (Fig. 4.32i).

A measurement of the spatially resolved polarization rotation angle of a cluster of two fundamental solitons is shown in Fig 4.33a. Each soliton persists as a single entity and remains nearly unchanged in its shape. The solitons have a distance of 0.81 mm. This distance seems to be given by a locking mechanism where the opposing fronts of the two solitons enclose their minimum distance. This becomes apparent in the cut through the center of both solitons. The system returns to the vicinity of the background state between the solitons. The soliton cluster is surrounded by peaks that have a significantly smaller

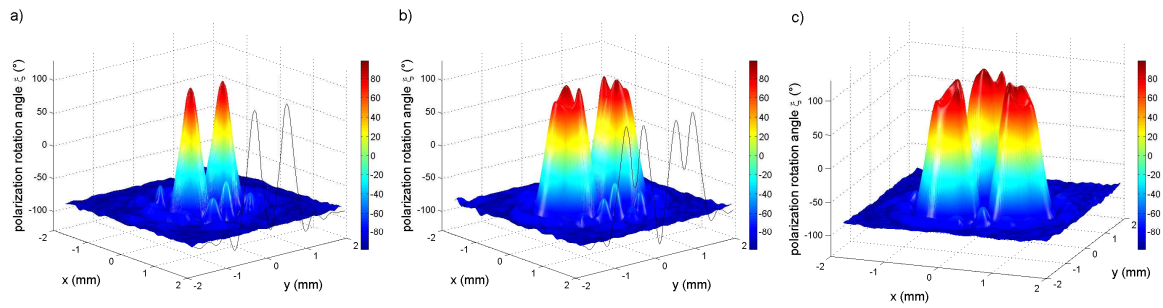

Figure 4.33: Simple soliton clusters. Spatially resolved polarization rotation angle ξ obtained from a measurement of the Stokes parameters of the light field. a) 2 S1 solitons; b) 2 S2 solitons; c) 3 S2 solitons. Parameters: a),b) $d = 112\,\mathrm{mm}$, $\Delta = 17.6\,\mathrm{GHz}$, $T = 357.6\,^\circ\mathrm{C}$, a) $P_{\mathrm{in}} = 224.6\,\mathrm{mW}$, $\rho = -11^\circ\,21'$, b) $P_{\mathrm{in}} = 207.0\,\mathrm{mW}$, $\rho = -12^\circ\,31'$; c) $d = 112\,\mathrm{mm}$, $\Delta = 15.1\,\mathrm{GHz}$, $T = 359.5\,^\circ\mathrm{C}$, $P_{\mathrm{in}} = 252.9\,\mathrm{mW}$, $\rho = -12^\circ\,45'$.

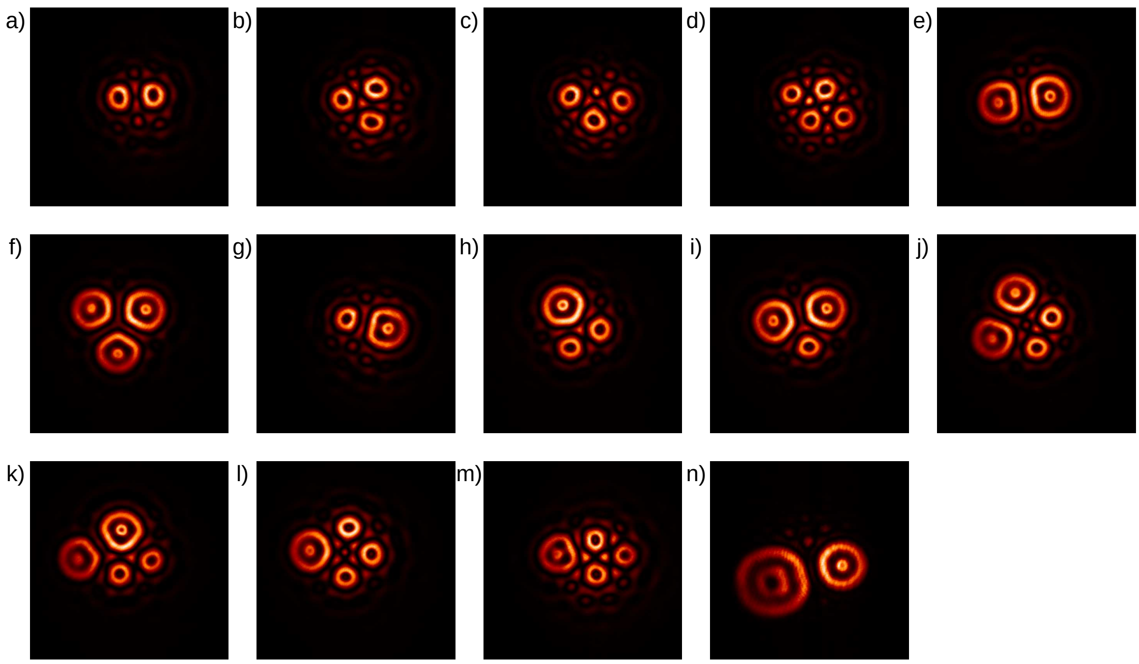

Figure 4.34: Miscellaneous configurations of soliton clusters. a) 2 S1; b),c) 3 S1 in different configurations; d) 4 S1; e) 2 S2; f) 3 S2; g) S1 + S2; h) 2 S1 + 1 S2; i) 1 S1 + 2 S2; j),k) 2 S1 + 2 S2 in different configurations; l),m) 3 S1 + S2 in different configurations; n) S2 + S3.

amplitude than the solitons. These are the remnants of the modulational instability of the background state. In order to ignite more than one soliton the area where solitons can exist in principle has to be increased. In a Gaussian beam this is only possible if the threshold for pattern formation is crossed. As a consequence, the oscillations of the background are not circular but are better described by a strongly distorted pattern as discussed in section 4.4.4. While the pattern itself cannot be covered by a measurement of the Stokes parameters, the distorted pattern is pinned by the large perturbation induced by the solitons and can therefor be seen in the measurement.

A soliton cluster built by two second order solitons is shown in Fig.4.33b. In principle, the same argument applies here. However, the shape of the single solitons is deformed. The circle on top of the soliton becomes azimuthally modulated and exhibits three peaks, two of which are located at the side opposing the other soliton. Nevertheless, the single soliton keeps its status as a single entity. The solitons keep a distance of 1.22 mm, whereas the cut through the centers shows that the system returns to the background state only for a single oscillation similar to the situation in Fig. 4.33a.

If a third second order soliton is ignited, the structures arrange in the shape of an equilateral triangle, where the average distance between the vertices is 1.24 mm. This corresponds nicely to the two-soliton case. Obviously the system always strives for the smallest distance between the solitons, which might be supported by the gradient-induced movement towards the beam center.

Despite the low aspect ratio, a lot of different configurations of soliton clusters can be observed. This repertory of clusters is shown in Fig.4.34. Here the solitons are depicted in the usual way with the linear polarizer aligned for maximum suppression of the background. The configurations corresponding to those that have been discussed up to now are shown in Figs. 4.34a,e,f. Clusters of first order solitons with increasing number of constituents and varying configurations can be seen in Figs. 4.34a-d, while clusters consisting exclusively of S2 solitons are found in Figs. 4.34e,f. Frequently soliton clusters are observed that consist of solitons of different order. Most commonly, clusters consisting of S1 and S2 solitons are found in many configurations (see Figs. 4.34g-m). Due to the limited aspect ratio, clusters of solitons of higher order are very rarely observed. A cluster of an S2 and an S3 soliton is shown in Fig. 4.34n.

From all the images a fixed distance of the outer bounds of two neighboring solitons can be identified. The order of magnitude of this distance seems to be independent of the order of the neighboring solitons. For a detailed analysis of this issue see below.

It can be seen in the pictures that the single soliton slightly changes its shape on the side(s) that is (are) facing other solitons. In tendency, the circular shape flattens which is leading to a slightly larger 'contact area'. This might lead to an increased level of stability

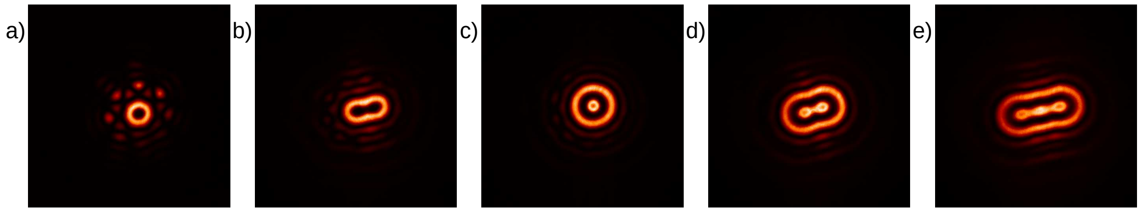

Figure 4.35: Bound states of solitons of first and second order. a) first order soliton; b) bound state of two first order solitons; c) second order soliton; d) bound state of two second order solitons; e) bound state of three second order solitons. Parameters: $d = 112\,\text{mm}$, $\Delta = 16.3\,\text{GHz}$, $T = 360.2\,^\circ\text{C}$, $P_{in} = 247.9\,\text{mW}$, a) $\rho = -7°$, b) $\rho = -9°$, c) $\rho = -10°$, d) $\rho = -15°$, e) $\rho = -18°$.

for the soliton.
Commonly, a single soliton in a cluster can be erased by means of the addressing beam, while the other solitons persist. A reconfiguration of the remaining solitons will take place in this case. Sometimes, however, other solitons disappear if a neighboring soliton is erased. This is interpreted to be a result of the loss of the increased stability that has been induced by the neighboring soliton. It is possible that solitons of a specific order are stable in a cluster for certain parameters where the single soliton is not stable. In those cases, the individuality of the single soliton is limited, which might lead to unwanted crosstalk effects in the framework of using spatial solitons as a medium for all-optical data storage.

4.5.2 Bound states

Typically a single soliton becomes unstable at some point, if the degree of imperfection of the pitchfork bifurcation ($|\rho|$) is increased. After the soliton has become unstable, there are three ways the system can react: The first one is a transformation into another soliton, typically of higher order. The domain expands symmetrically and stops the expansion, if another locking state is reached. If there are no stable larger soliton for the given parameters, the domain will expand until the whole area is switched to the target state of the former soliton.
The third observed behavior of the system is an expansion of the domain where the rotational symmetry is broken. Eventually the system reaches another stable configuration in this case. Figure 4.35a shows a stable first order soliton. If $|\rho|$ is increased, the soliton becomes unstable and a stable structure evolves that is depicted in Fig. 4.35b. This structure is an elongated structure whose shorter diameter is the one of the soliton it has evolved from, while the longer diameter is approximately given by twice the diameter of

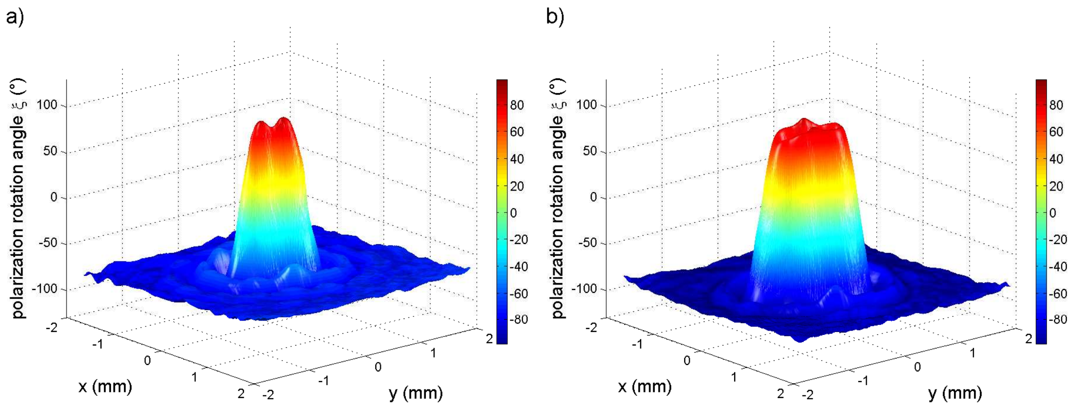

Figure 4.36: Bound states of two a) first and b) second order solitons. Spatially resolved polarization rotation angle ξ obtained from a measurement of the Stokes parameters of the light field. Parameters: a) $d = 112\,\mathrm{mm}$, $\Delta = 17.0\,\mathrm{GHz}$, $T = 359.5\,°\mathrm{C}$, $P_{\mathrm{in}} = 270.7\,\mathrm{mW}$, $\rho = -5°\,58'$; b) $d = 112\,\mathrm{mm}$, $\Delta = 17.0\,\mathrm{GHz}$, $T = 362.8\,°\mathrm{C}$, $P_{\mathrm{in}} = 237.1\,\mathrm{mW}$, $\rho = -16°\,36'$.

the single soliton. Along the long axis the structure is narrowed down in the middle. A similar behavior is observed if, starting from a second order soliton (Fig. 4.35c, $|\rho|$ is increased. Again, an elongated structure evolves that is narrowed in the middle (Fig. 4.35d). In the central part, two peaks similar to the one of the single soliton are observable which are interconnected. If $|\rho|$ is increased even more, the structure expands along its long axis and a third stable situation is reached which is depicted in Fig. 4.35e. It is characterized by three interconnected central peaks.

An interpretation of the nature of these elongated states can be derived from a measurement of the Stokes parameters. A state corresponding to Fig. 4.35b is shown in a 3D plot of the polarization rotation angle in Fig. 4.36a. It shows that the structure is a stable entity that has two peaks. Along its short axis, it has the properties of a first order soliton. It is interpreted as a tightly *bound state* consisting of two first order solitons. Unlike the soliton clusters discussed in the previous section, the two solitons are inseparable, and the system does not return to the background state between the solitons but oscillates around the target state. Figure 4.36b shows a situation corresponding to Fig.4.35d. Similarly this structure is interpreted as a tightly bound state consisting of two solitons of second order.

Bound states can also be created in ways different from those that were described above. In some parameter regions, a single soliton can be expanded to a bound state by switching on the addressing beam at a position very close to the soliton. For some settings of ρ

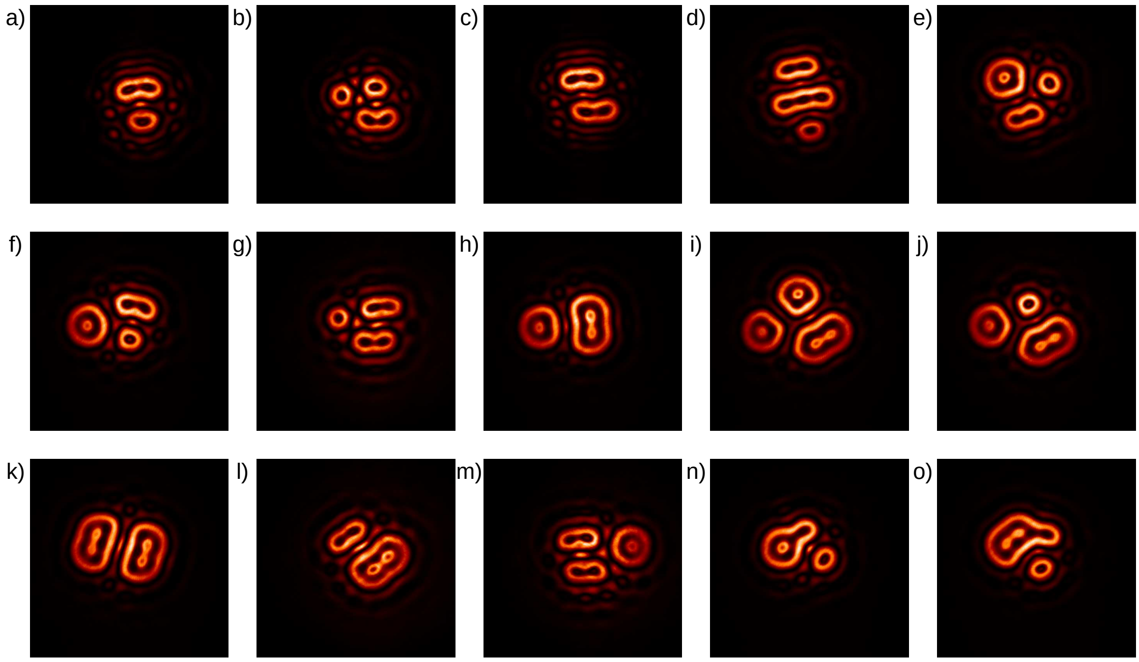

Figure 4.37: Miscellaneous configurations of bound states coexisting with solitons.

it even is the most stable structure and can be addressed by using an addressing beam diameter slightly larger than the size of the single soliton. Probably addressing bound states could be simplified by modifying the shape of the addressing beam.

The bound states behave as a single entity and hence can interact with other solitons and bound states. Many different configurations can be observed even at the given low aspect ratio. Some of them are depicted in Fig. 4.37. The images are roughly ordered in an ascending degree of complexity. Bound soliton states can coexist with each other and with single solitons of the same or of a different order. Typically neighboring bound states align parallel. The mechanism that leads to the observation of a certain distance between neighboring structures as discussed in the previous subsection seems to apply in the same manner for the distances between bound states and other structures.

A very interesting structure is observed in Figs. 4.37n and o. Subfigure n shows a bound state of an S1 with an S2 soliton, while subfigure o shows a bound state consisting of one S1 soliton and two S2 solitons. However, these structures are only observed in the presence of other structures and are therefor interpreted as a metastable configuration. This observation supports the conjecture that the stability properties of single structures

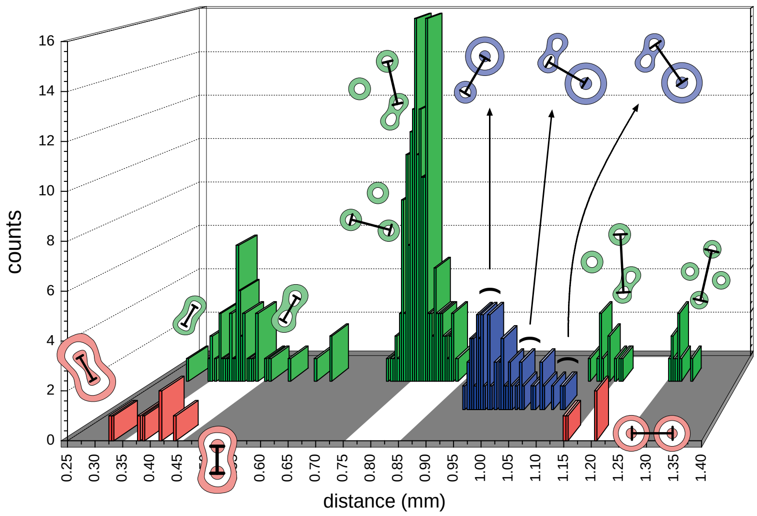

Figure 4.38: Histogram of the preferred distances between solitons and bound states. Parameters: $d = 120\,\mathrm{mm}$, $\Delta = 16.0\,\mathrm{GHz}$, $T = 326.5\,°\mathrm{C}$, $P_{in} = 310\,\mathrm{mW}$.

can be modified under the presence of other structures. Nevertheless the solitons are separately addressable in a wide range of parameters.

4.5.3 Preferred distances between solitons and bound states

Despite the diversity of possible configurations of clusters of solitons and bound states, the distance between the constituents of these clusters does not seem to be an arbitrary quantity. For the purpose of the analysis of the distances involved in the formation of soliton clusters, a series of 250 images of the system taken for similar parameters has been evaluated. A statistical analysis of the cluster configurations is not possible, however, since the solitons do not appear spontaneously but have to be ignited. Accordingly, the observed cluster configurations depend on the parameters of the ignition beam. The ignition beam was positioned at an outer border of the beam having a radius that lies between the ones of S1 and S2. The ignited structures drift towards the center, where already one ore more solitons might be present. With every soliton added, an image was taken. This sequence was then repeated starting from the situation where no soliton is present. Thus, the series of images should represent a typical distribution of structures. However it represents only a subset of all the possible configurations.

Within every soliton cluster, every distance between the constituents is evaluated. A histogram of the observed distances is given in Fig. 4.38. The distances between S1 solitons are indicated by green bars. Distances between S1 and S2 solitons are shown as

blue bars, and distances between S2 solitons are shown in red. Apparently, some distances between the solitons are preferred over others. The configuration associated with the single classes of distances are schematically inserted into the figure. The smallest distance is found around 0.4 mm. It represents the distance of the constituents within a bound state consisting of two solitons. Similar distances are observed for bound states built from S1 and S2 solitons. The next preferred distance represents the next-neighbor distance between S1 solitons. This distance around 0.8 mm is observed very frequently.
A rather broad distribution of distances is found around 1.0 mm. This distribution represents the distances between S1 and S2 solitons and bound states. Larger distances are rarely observed. This is a consequence of the limited area around the beam center. However, soliton clusters consisting of S2 solitons and clusters also yield defined distances. The observed distances seem to be multiples of an elementary unit. It was shown in section 4.4.3 that the sizes of the solitons are connected to the length scale of the modulational instability. Multiples of the length scale of the underlying hexagonal pattern are indicated as white stripes in Fig. 4.38. Apparently the distances between the solitons are also connected to this length scale.

4.6 Complex behaviour

If the input power is increased far beyond the threshold for pattern formation, not only the aspect ratio, i.e. the area where nontrivial structures exist, increases. Also the modulation depth of the oscillations becomes more pronounced. This leads to the observation of even more complex structures than discussed up to now as well as to situations, where the solitons continuously lose their radial symmetry and a transition to states that can be better described in terms of localized patterns takes place.

4.6.1 Solitons and fronts

The existence of stable straight polarization fronts has been discussed in section 4.3.1. They can be observed in the nearly symmetric case ($\rho \approx 0$) at input powers where both branches of the pitchfork bifurcation are modulationally unstable. It has been shown in section 4.4.4 that solitons can be ignited in this parameter region as well. This leads to the conjecture that it should be possible to prepare the system in a way that both types of structure can coexist.
Figure 4.39 shows the result of this experiment in a measurement of the Stokes parameters. At first, the system is prepared to exhibit a straight polarization front (Fig.4.39a). This situation corresponds to the one described in 4.3.1. Thanks to the Stokes parameter

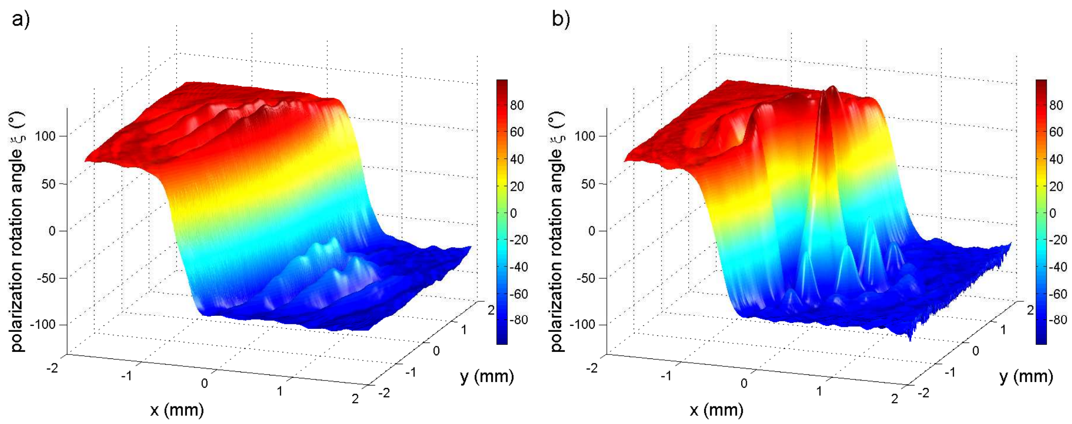

Figure 4.39: Coexistence of a front and a S1 soliton. a) spatially resolved polarization rotation angle ξ of a polarization front. b) stable configuration of front and S1. Parameters: $d = 112\,\mathrm{mm}$, $\Delta = 16.8\,\mathrm{GHz}$, $T = 361.0\,°\mathrm{C}$, $P_{in} = 268.3\,\mathrm{mW}$, a) $\rho = -1°\,40'$, b) $\rho = -1°\,00'$.

technique it can now be analyzed in more detail. In the left part of the plot the polarization rotation angle is positive, while in the right part it is negative. The two states are connected by a continuous steep polarization front. Due to the large amplitude of the front, both states show modulations which are oriented parallel to the front. It should be noted that both states normally exhibit a hexagonal pattern in this parameter region. The modulation of the straight oscillations in the longitudinal direction is interpreted to be a remnant of these hexagonal patterns.

Then a σ_+ polarized addressing beam is switched on and off in the right part of the image. A soliton is ignited that starts to drift towards the beam center. It is then stopped by interaction with the polarization front. The front starts to bend around the soliton and finally a stable situation is achieved (see Fig.4.39b). The soliton is sitting in front of the polarization front which is bent in a way to maintain a certain distance from the soliton, while the soliton itself does not significantly change its shape. This distance is interpreted to be the one with the optimal locking properties. Interestingly the existence of the soliton seems to trigger the formation of a (distorted) pattern where the single constituents are far more pronounced compared to Fig.4.39a. This does not apply for the state with positive polarization.

The described stable configuration is not the only one that has been observed in the experiment. Fig. 4.40 shows that other stable configurations are possible. While subfigures a) and b) show the configurations already discussed in a view where one state is suppressed by the linear polarizer, subfigure c) shows that another distance between soliton and

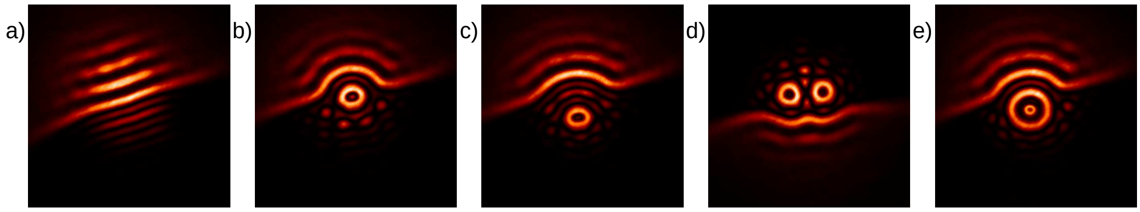

Figure 4.40: Stable configurations of a front and solitons. a) front; b) front and S1 soliton; c) front and S1 soliton with larger distance; d) front and 2 S1 solitons; e) front and S2 soliton. Parameters: $d = 112\,\mathrm{mm}$, $\Delta = 15.5\,\mathrm{GHz}$, $T = 346.0\,^\circ\mathrm{C}$, $P_{in} = 285.3\,\mathrm{mW}$, $\rho = -0^\circ\,15'$.

front is possible, though not very common. It seems to be the distance where there is one oscillation wavelength more between the structures. It is also possible to ignite two fundamental solitons (see Fig. 4.40d) next to the front. In this case, the front bends around both structures, which themselves keep the typical distance discussed in section 4.5.3. If the size of the addressing beam is increased, a second-order soliton can be ignited (Fig. 4.40e). Also here the front will bend around the soliton, while the soliton remains unchanged. The distance between front and soliton is the same as in Fig. 4.40b.

4.6.2 Observation of a ring-shaped solitary structure

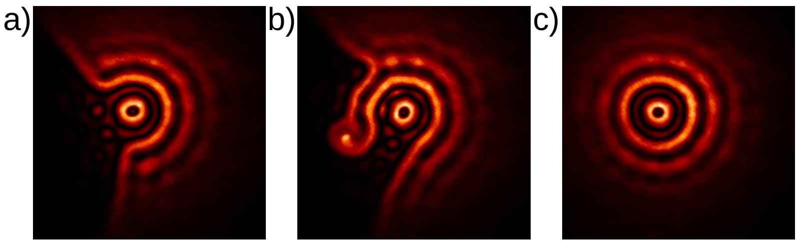

Figure 4.41: Preparation of a ring-shaped soliton. a) soliton 1 in front of a polarization front. b) front is closed around the soliton by means of the addressing beam. c) ring-shaped soliton. Parameters: $d = 120\,\mathrm{mm}$, $\Delta = 16.6\,\mathrm{GHz}$, $T = 326.3\,^\circ\mathrm{C}$, $P_{in} = 311.2\,\mathrm{mW}$, $\rho = -7^\circ\,0'$.

For the same parameters where solitons and fronts can coexist, a new type of solitary structure can be prepared. The process of preparation is illustrated in Fig. 4.41. First, a soliton is ignited in front of a polarization front (Fig. 4.41a). Then, at the position of the upper corner of the front, the ignition beam is switched on again and moved downwards. Doing so, it is possible to 'pull out' an elongated structure (see Fig. 4.41b). This is done

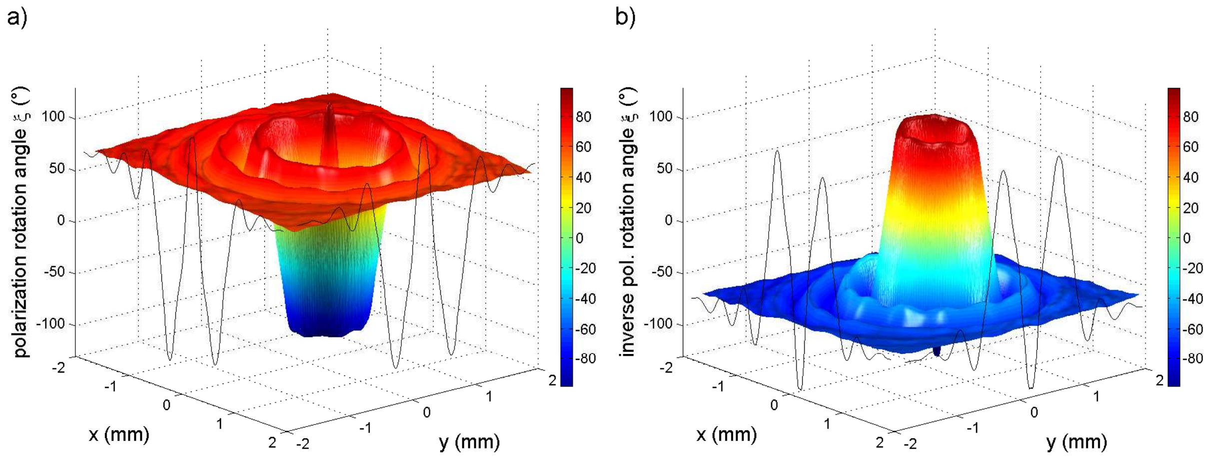

Figure 4.42: Ring-shaped soliton. Spatially resolved polarization rotation angle ξ obtained from a measurement of the Stokes parameters of the light field. a) bottom view; b) top view (ξ inverted). Parameters: $d = 112\,\mathrm{mm}$, $\Delta = 16.2\,\mathrm{GHz}$, $T = 359.5\,°\mathrm{C}$, $P_{\mathrm{in}} = 278.7\,\mathrm{mW}$, $\rho = -2°\,10'$.

keeping a certain distance from the soliton. When the ignition beam approaches the lower corner of the polarization front, the front closes completely around the soliton. Typically at the same time, the elongated structure expands to the left and switches the left part of the beam to the state that is not suppressed by the linear polarizer. The result is a fundamental soliton that is surrounded by a closed polarization front.

However, this very stable structure can be interpreted in a completely different way. This can be seen best in a 3D plot of the polarization rotation angle ξ obtained from a measurement of the Stokes parameters. Figure 4.42a shows the structure in a way that suggests the interpretation discussed up to now. If the structure is turned upside down as it is done in Figure 4.42b, it becomes clear that the structure can also be interpreted as a soliton being of a different type than the ones discussed up to now. This soliton is circular symmetric like the other solitons. In contrast to those, the system returns to the vicinity of the background and beyond in the center of the structure, i.e. the central dip is much deeper. The cuts through the center of the structure show that this structure is built up by four polarization fronts in contrast to the domain-shaped solitons that consist of two polarization fronts locking at different positions. In a one-dimensional picture this structure could be interpreted as a cluster of two single solitons. In a two-dimensional expansion, however, the variety of possibilities is obviously larger. The structure can be considered as a 'ring-shaped' soliton.

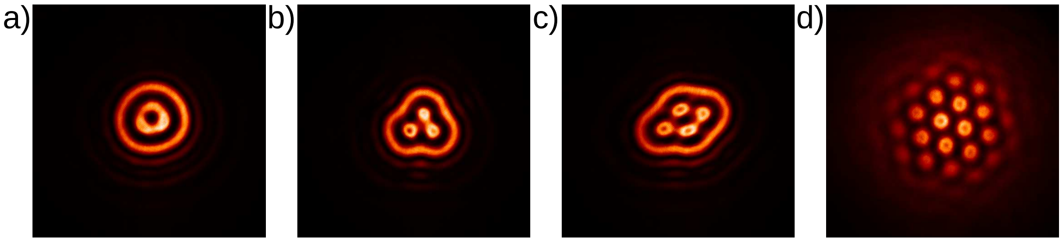

Figure 4.43: Transition to localized patterns. a) S3 soliton; b) triangular localized pattern; c) diamond-shaped localized pattern; d) extended hexagonal pattern. Parameters: $d = 112\,\mathrm{mm}$, $\Delta = 16.23\,\mathrm{GHz}$, $T = 360.2\,°\mathrm{C}$, $P_{\mathrm{in}} = 273.5\,\mathrm{mW}$, $\rho = -18°$.

If one makes the justified assumption that the front locking mechanism involved here is even more pronounced than in the case of the domain-shaped solitons, the described structure could be the first member of a completely new family of solitons. However, the construction of an addressing beam that could be used to ignite one of these solitons should be rather complicated, since a nontrivial shape and nontrivial polarization properties would have to be realized. In case of the described soliton, an alternative but complex preparation scheme is obviously applicable. A first numerical indication of the existence of such a new soliton family will be given in section 5.5.4.

4.6.3 Transition to localized patterns

At the maximum available input power a transition from the (nearly) circular symmetric solitons to states that have an inner structure which is not circularly symmetric takes place. Fig. 4.43 shows a situation in which a soliton 3 exists in a multistability with structures that have a similar size but that do not have a circular symmetry. Instead these structures exhibit three or four intensity peaks in the inner structure that have a defined distance which can be identified to be similar to the distance of the constituents of the hexagonal pattern existing on both branches of the pitchfork bifurcation. Typically one structure is stable at timescales in the order of seconds. Then a rapid transition to one of the other states takes place. Fig. 4.43b shows a structure consisting of three constituents arranged in a triangle, while in Fig. 4.43c a structure consisting of four constituents aligned in a diamond shape is shown. These structures are interpreted as patches of the hexagonal pattern that serves as the target state (Fig. 4.43d) embedded in a background of the hexagonal pattern that serves as the background state, i.e. a *localized pattern*. They could, of course, also be classified as bound states consisting of three or four second order solitons arranged on a hexagonal grid. However, this classification would not be reasonable, if the number of constituents could be increased in an experiment having a larger aspect ratio. Obviously the importance of the locking of fronts discussed up to now becomes less significant compared to the modulational instability of the target state which leads to a broken circular symmetry.

Chapter 5

Theoretical Analysis

Besides the given experimental reasons, a main advantage of choosing sodium vapor as the nonlinear medium is the availability of a good theoretical model. A microscopic model for the interaction of light with sodium atoms can be derived from first principles [MDLM86, Möl92]. It is obtained on the basis of the density matrix formalism from quantum mechanics and has been successfully adapted in many preceding works [Ack96, Aum99, Sch01, GW02, Hun06].
In this chapter, a theoretical analysis based on this established microscopic model of the system is carried out. The aim is to complete the understanding of the mechanisms that lead to the formation of a discrete family of solitons. Besides the systematic reproduction and enhancement of the experimental results, a further understanding of the properties of the system can be obtained from an analysis of the system in situations that are either not or hardly accessible in the experiment.

5.1 Model equations for the $\lambda/8$ system

In this work, the transition belonging to the sodium D_1 line leading from the excited $3^2P_{1/2}$ state to the $3^2S_{1/2}$ ground state is considered. The interaction of the electron angular momentum with the nuclear spin leads to a hyperfine splitting of the excited (190 MHz) and ground (1772 MHz) state [HW87]. The presence of a buffer gas of a sufficiently high pressure leads to a homogeneous pressure broadening that exceeds the hyperfine structure of the ground state as well as the Doppler broadening. Under these conditions, the sodium D_1 line can be treated as a homogeneously broadened ($J = \frac{1}{2} \rightarrow J' = \frac{1}{2}$) transition [MDLM86]. The use of nitrogen as the buffer gas gives rise to an efficient radiationless decay of the excited state [Tam79] and thus suppresses radiation trapping [Ank93]. In this case, the hyperfine splitting can be taken into account by a rescaling and doesn't need do be considered further [ML94, Ack96]. Additionally, the population of the excited state can be neglected under certain conditions [MDLM86, Möl92, Gah96, Ack96] which are fulfilled in the present experiment due to the choice of the preparation of the vapor .

5.1.1 Nonlinear susceptibility of sodium vapor

The result of the given considerations is an equation of motion for a unit vector, whose components are proportional to the expectation values of the cartesian components of the spin. This vector is called Bloch vector $\vec{m}$ and is proportional to a magnetization of the sodium vapor. Taking the quantization axis parallel to the direction of propagation of the forward light field in the z direction, the equation of motion results in

$$\frac{d}{dt}\vec{m} = -\gamma\,\vec{m} + D\Delta\vec{m} + \vec{e}_z\,(P_+ - P_-) - \vec{m}\,(P_+ + P_-) - \vec{m} \times \vec{\Omega}_{eff}. \tag{5.1}$$

The first term in the equation describes the relaxation of the Bloch vector due to collisions with a rate γ. The second term describes the thermal diffusion of the sodium atoms with a diffusion constant D. The optical pumping process with rates P_+ and P_- induced by σ_+ and σ_- light is described by the third term. The impact of the intensities of the circular components of the light field is given by

$$P_\pm = \frac{3}{16}\frac{|\mu|^2}{4\Gamma_2\hbar^2(\bar{\Delta}^2+1)}\,|E_\pm|^2\,, \tag{5.2}$$

where μ_e is the dipole matrix element of the transition, Γ_2 is the half homogeneous linewidth , $\bar{\Delta}$ is the detuning of the light field normalized to Γ_2, ϵ_0 is the vacuum dielectricity constant, and $\hbar$ is Planck's constant . The factor 3/16 accounts for the influence of the hyperfine structure on the optical pumping process [ML94, Ack96].

The saturation of the optical pumping is described by the fourth term of equation 5.1. The last term describes the precession of the magnetization vector in an effective magnetic field $\vec{\Omega}_{\rm eff} = (\Omega_{\rm x}, \Omega_{\rm y}, \Omega_{\rm z,eff})^T$. Here, the Ω_i are the Larmor frequencies corresponding to the cartesian components of the of the external magnetic field, while $\Omega_{\rm z,eff} = \Omega_{\rm z} - \bar{\Delta}(P_+ - P_-)$ describes an effective magnetic field that takes into account the light shift [CT62, She84]. By the choice of a magnetic field whose longitudinal component is large with respect to its transverse components ($|\Omega_{\rm z,eff}| \gg \Omega_{\rm x}, \Omega_{\rm y}$), a reduction of the equation of motion to the z component of the Bloch vector is possible [Aum99].

$$\frac{\partial}{\partial t}w = -\gamma\,w + D\Delta w + (P_+ - P_-) - w\,(P_+ + P_-). \tag{5.3}$$

The z component w of the Bloch vector is proportional to the population difference of the Zeeman substates of the ground state and is called orientation. It determines the optical properties of the sodium vapor for the circular light components $\sigma_\pm$

$$\chi_\pm(w) = \chi_{\mathrm{lin}}(1 \mp w). \tag{5.4}$$

The linear susceptibility χ_{lin} of the vapor is given by

$$\chi_{lin} = -\frac{N|\mu|^2}{2\epsilon_0 \hbar \Gamma_2} \frac{\bar{\Delta} + i}{\bar{\Delta}^2 + 1}, \tag{5.5}$$

where N is the particle density of the vapor.

5.1.2 Single-mirror feedback arrangement

Longitudinal averaging of the orientation

During the propagation of the light field through the medium diffraction is neglected. However, due to absorption, the intensities of the circular polarization components continuously change. The depletion of the pump fields has been taken into account by Le Berre et al. [BLR$^+$95] by introducing a longitudinal averaging of the medium orientation

$$\phi(x, y) = \int_0^L w(x, y, z)dz. \tag{5.6}$$

Neglecting diffusion in the z direction, equation 5.1 is then transformed to [Aum99]

$$\begin{aligned} \frac{\partial \phi(x, y)}{\partial t} &= -\gamma\, \phi(x, y) + D\Delta_\perp \phi(x, y) + \frac{1}{2\alpha_0 L} \cdot \\ &\quad \Big[\Big(P_{+,f}(x, y, 0) - P_{+,f}(x, y, L)\Big) - \Big(P_{-,f}(x, y, 0) - P_{-,f}(x, y, L)\Big) \\ &\quad + \Big(P_{+,b}(x, y, L) - P_{+,b}(x, y, 0)\Big) - \Big(P_{-,b}(x, y, L) - P_{-,b}(x, y, 0)\Big)\Big]. \end{aligned} \tag{5.7}$$

Here, $2\alpha_0$ is the linear absorption coefficient, which is given by the imaginary part of the linear susceptibility, $2\alpha_0 = -\mathrm{Im}(\chi_{lin})k_0$. The pump rates of the σ_+ $(+)$ and σ_- $(-)$ polarized components of the beam propagating forward ($+z$ direction, f) and backwards (-z direction, b) have to be evaluated at the front ($P_{\pm,f/b}(0)$) and exit face $P_{\pm,f/b}(L)$ of the medium.

Description of the optical field

The propagation of the slowly varying amplitudes of the circularly polarized components of the light field through the medium and to the feedback mirror and back is described by the paraxial wave equation [Boy92]

$$2ik_0\frac{\partial}{\partial z}E_{\pm,\mathrm{f}}(\vec{r}_\perp,z,t) = \nabla_\perp^2 E_{\pm,\mathrm{f}}(\vec{r}_\perp,z,t) + k_0^2\chi_\pm E_{\pm,\mathrm{f}}(\vec{r}_\perp,z,t) \tag{5.8}$$

for the light field propagating in $+z$ direction and

$$-2ik_0\frac{\partial}{\partial z}E_{\pm,\mathrm{b}}(\vec{r}_\perp,z,t) = \nabla_\perp^2 E_{\pm,\mathrm{b}}(\vec{r}_\perp,z,t) + k_0^2\chi_\pm E_{\pm,\mathrm{b}}(\vec{r}_\perp,z,t) \tag{5.9}$$

for the light field propagating in -z direction.
Within the medium, diffraction is neglected, and the propagation of the optical field through the medium can be written as

$$\begin{aligned} E_{\pm,f}(L) &= \exp(-\alpha_0 L(1-i\bar{\Delta})(1\mp\phi))E_{\pm,f}(0) && (5.10)\\ E_{\pm,b}(0) &= \exp(-\alpha_0 L(1-i\bar{\Delta})(1\mp\phi))E_{\pm,b}(L). && (5.11)\end{aligned}$$

Equation 5.2 is used for the calculation of the corresponding pump rates from the field amplitudes.
It has been discussed descriptively in section 2.3.4 that a nonvanishing orientation induces a phase shift between the circularly polarized components of the light field. If the input light field is linearly polarized, this phase shift induces a rotation of the polarization axis by an angle ξ. It is described by equation 5.10. Under the assumption of a linearly polarized input field, a transformation on the basis of linear polarizations yields [GWKL+00]

$$\begin{aligned}\begin{pmatrix} E_x^T \\ E_y^T \end{pmatrix} &= e^{-\alpha_0 L(1-i\bar{\Delta})}\begin{bmatrix} \cos(\alpha_0 L\bar{\Delta}\phi) & -\sin(\alpha_0 L\bar{\Delta}\phi) \\ \sin(\alpha_0 L\bar{\Delta}\phi) & \cos(\alpha_0 L\bar{\Delta}\phi)\end{bmatrix} \\ &\quad\times\begin{bmatrix} -i\sinh(\alpha_0 L\phi) \\ \cosh(\alpha_0 L\phi)\end{bmatrix} E^0. \end{aligned} \tag{5.12}$$

The first matrix indicates the rotation of the main polarization axis of the transmitted light field by an angle $\xi = \alpha_0 L\bar{\Delta}\phi$. The rotation angle depends linearly on the orientation ϕ, thereby allowing a direct comparison between theoretical and experimental results.
To describe the vacuum propagation of the light field from the exit face of the medium to the mirror and back, the wave equations are reduced to

$$2ik_0 \frac{\partial}{\partial z} E_{\pm,\mathrm{f}}(\vec{r}_\perp, z, t) = \nabla_\perp^2 E_{\pm,\mathrm{f}}(\vec{r}_\perp, z, t) \tag{5.13}$$

and

$$-2ik_0 \frac{\partial}{\partial z} E_{\pm,\mathrm{b}}(\vec{r}_\perp, z, t) = \nabla_\perp^2 E_{\pm,\mathrm{b}}(\vec{r}_\perp, z, t)\,. \tag{5.14}$$

A formal integration of these equations yields:

$$E_{\pm,b}(\vec{r}_\perp, L, t) = \sqrt{R}\,\mathbf{P}\,E_{\pm,\mathrm{f}}(\vec{r}_\perp, L, t)\,, \tag{5.15}$$

where the propagation operator

$$\mathbf{P} = \exp\left[-i\frac{d\,\nabla_\perp^2}{k_0}\right] \tag{5.16}$$

is defined by the corresponding power series. Delays that are induced by the finite speed of light are neglected, since the slowest timescale corresponding to these delays ($\approx 10^{-9}$ s) are much faster than the fastest time scales in the atomic system ($\approx 10^{-6}$ s).
The action of the $\lambda/8$ plate is taken into account using the Jones matrix formalism. The slow axis of the $\lambda/8$ plate is assumed to be parallel to the y axis for $\rho = 0°$. The circularly polarized components $E_{\pm,b}(\vec{r}_\perp, L, t)$ of the reflected fields are calculated from the transmitted fields $E_{\pm,\mathrm{f}}(\vec{r}_\perp, L, t)$ by

$$\begin{pmatrix} E_{+,b}(\vec{r}_\perp, L, t) \\ E_{-,b}(\vec{r}_\perp, L, t) \end{pmatrix} = \sqrt{R} e^{-i\frac{d}{k_0}\nabla_\perp^2} \underbrace{\frac{1}{\sqrt{2}}\begin{pmatrix} -1 & i \\ 1 & i \end{pmatrix}}_{I} \underbrace{\begin{pmatrix} i & 0 \\ 0 & 1 \end{pmatrix}}_{II} \tag{5.17}$$

$$\cdot \underbrace{\begin{pmatrix} \cos\rho & \sin\rho \\ -\sin\rho & \cos\rho \end{pmatrix}}_{III} \underbrace{\frac{1}{\sqrt{2}}\begin{pmatrix} -1 & 1 \\ -i & i \end{pmatrix}}_{IV} \begin{pmatrix} E_{+,\mathrm{f}}(\vec{r}_\perp, L, t) \\ E_{-,\mathrm{f}}(\vec{r}_\perp, L, t) \end{pmatrix} \tag{5.18}$$

Here, the matrices describe

- I : transformation from the basis of linear polarizations into the basis of circular polarizations
- II : the phase shift induced by the $\lambda/4$ plate (double transmission of a $\lambda/8$ plate)
- III : the rotation angle ρ of the $\lambda/8$ plate
- IV : transformation from the basis of circular polarizations into the basis of linear polarizations

Together with equations 5.5, 5.2, 5.11, and 5.18, equation 5.7 is a closed equation describing the temporal evolution of the longitudinally averaged orientation ϕ; it will be used for the analytical and numerical analysis of the system.

Numerical simulations

The computational area of a size of typically 8mm x 8mm is discretized on a quadratic grid of 256 x 256 points. The integration of equation 5.7 is accomplished using a 4th order Runge Kutta algorithm [PFTV92]. The occurring spatial derivatives (diffusion of orientation and propagation of the light field) are computed in Fourier space [Aum99, GW02, Pes00].
A plane wave input light field is realized by choosing a scalar $2P_0 = P_{+,f}(x, y, 0) = P_{-,f}(x, y, 0)$. The spectral computation of the spatial derivatives results in periodic boundary conditions.
In order to model the experimental situation, the pump rate distribution $P_0(x, y)$ is chosen as a Gaussian distribution with a radius of 1.89 mm. As a boundary condition, the orientation distribution is set to zero at a radius of 4 mm to model the deorientation of the vapor at the cell walls.
The initial condition for the orientation ϕ is chosen depending on the focused problem. Typically, it is started from a homogeneous solution that can be determined analytically (see below). Spatial noise is added at the beginning of the calculations to shorten the transients. The action of the incoherent pumping of the addressing beam in a situation where the system has two homogeneous solutions is realized by choosing a top-hat distribution with one homogeneous solution embedded into the other one as the initial condition.

Newton method

Often it is the main interest of the study of a nonlinear dynamical system to find its stationary solutions. The full calculation of the dynamics of the system via numerical solutions is one possibility to obtain stationary solutions. On the one hand this is often computationally expensive, and on the other hand numerical simulations can only converge towards stable stationary solitons. The knowledge of unstable stationary solutions of the dynamics, however, can help to understand the bifurcation structure of the system. The Newton method [PFTV92] has been proven to be a powerful method to iteratively find stationary solutions of a system (see e.g. [FH98, OSF01, HFOM02, MFOH02]). It has been successfully applied to the single-mirror feedback system with sodium vapor in earlier works [Sch01, Hun06]. The method is efficiently applicable in situations where the system has a rotational symmetry in a good approximation. The rotationally symmetric stationary solutions $\tilde{\phi}(r)$ of the dynamics 5.7

$$\frac{\partial}{\partial t}\tilde{\phi}(r) = 0 = \mathcal{N}(\tilde{\phi}(r)), \tag{5.19}$$

where the nonlinear operator $\mathcal{N}(\phi)$ is defined by the right-hand side of equation 5.7

$\frac{\partial}{\partial t}\phi =: \mathcal{N}(\phi)$, are then obtained iteratively from a suited initial distribution ϕ^0 by

$$\phi^{n+1} = \phi^n - (\nabla\mathcal{N}(\phi^n))^{-1}\mathcal{N}(\phi^n), \tag{5.20}$$

where $\nabla\mathcal{N}$ is the Jacobian of the operator $\mathcal{N}$. In addition to the spatial distribution of the stationary solution the algorithm is also capable of making a statement on its stability against rotationally symmetric perturbations. The details on the implementation of the Newton method have been discussed in [Sch01, Hun06]. They are summarized together with the changes made in order to describe the system under study here in appendix A.

5.2 Basic properties of the system

5.2.1 Stationary homogeneous solutions

The usual first step taken in the theoretical analysis of a system that exhibits dissipative spatial structures is to assume a homogeneous input of energy (in this case a plane wave light field) and to ask for stationary homogeneous solutions of the dynamics of the system. Setting all spatial and temporal derivatives zero in equation 5.7 results in an implicit equation for the stationary homogeneous solutions ϕ_h [GWKL$^+$00][1]:

$$\begin{aligned}\phi^h = {} & \frac{P_0}{\gamma \cdot 2\alpha_0 L} e^{-2\alpha_0 L}[R\sin(2\alpha_0 L\bar{\Delta}\phi^h - 2\rho) - \\ & \sinh(2\alpha_0 L\phi^h) - Re^{-2\alpha_0 L}\cosh(2\alpha_0 L\phi^h) \times \\ & [\sinh(2\alpha_0 L\phi^h) + \sin(2\alpha_0 L\bar{\Delta}\phi^h - 2\rho)]].\end{aligned} \tag{5.21}$$

This equation has the trivial solution $\phi_h = 0$ in the cases where the slow axis of the wave plate is aligned with ($\rho = 0°$) or orthogonal ($\rho = \pm 90°$) to the input polarization. This result is well expected since no net pumping can occur if the wave plate does not alter the linear polarization of the input field. All other solutions are computed numerically.
Figure 5.1a shows the homogeneous solutions for $\rho = 0°$. A pitchfork bifurcation is obtained. At the bifurcation point, the system changes from one fixed point ($\phi = 0$) to three fixed points. It will be shown later that the solution $\phi = 0$ becomes unstable at this point (indicated by a dashed line). The orientation saturates around ± 0.17, the corresponding polarization rotation angle is $\pm 75°$. This is in good agreement with the situation found experimentally.
Figure 5.1b indicates the change in the bifurcation scenario, if the wave plate is rotated by $\rho = -5°$. Equation 5.21 loses its inversion symmetry and a perturbed pitchfork bifurcation

[1] The original publication [GWKL$^+$00] contained a typo that is corrected here

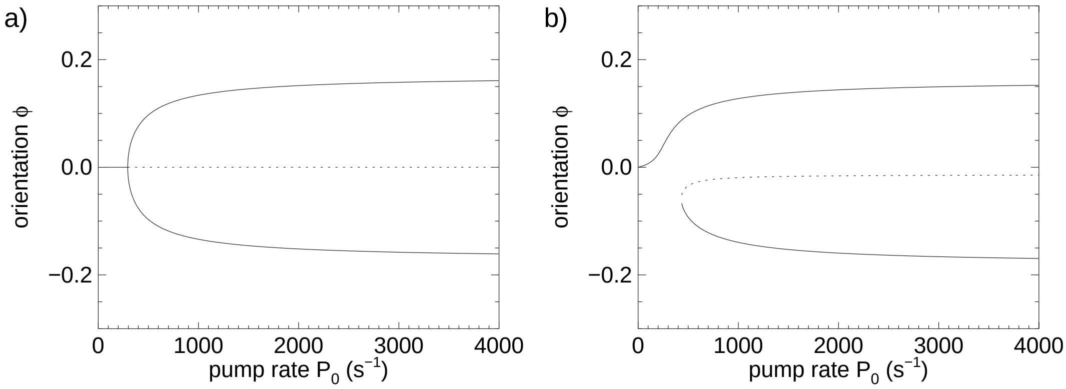

Figure 5.1: Pitchfork bifurcation. a) perfect pitchfork bifurcation; b) perturbed pitchfork bifurcation. Parameters: $d = 120\,\mathrm{mm}$, $\bar{\Delta} = 7.5$, $D = 255\,\mathrm{mm\ s^{-1}}$, $\gamma = 200\,\mathrm{s^{-1}}$, $\Gamma_2 = 9.936 \cdot 10^9\,\mathrm{rad\ s^{-1}}$, $L = 0.015\,\mathrm{m}$, $R = 0.995$, $N = 4.65 \cdot 10^{19}\,\mathrm{m^{-3}}$, a) $\rho = 0\,°$, b) $\rho = -5\,°$.

is observed. Due to the structure of equation 5.21 the orientation in the bifurcation scenario will reverse its sign if the wave plate rotation angle is reversed. While in the experimental measurements both cases (positive and negative wave plate rotation angles) have been discussed in order to check for the symmetry of the experimental system with respect to the case $\rho = 0°$, the discussion in this chapter will mostly only discuss one of the cases.

5.2.2 Linear stability analysis

When the stationary homogeneous solutions of the system have been found, the next step in the analysis is to ask for their stability.
A linear stability analysis with respect to sinusoidal perturbations of the homogeneous solution of the form $\delta\phi \sim e^{\eta t}\cos(q_\perp r_\perp)$ yields a growth exponent[2]

$$\begin{aligned}
\eta \;=\;& -\gamma - Dq_\perp^2 - P_0 e^{-2L\alpha_0}\cos(2L\alpha_0\phi_h) \\
& -\frac{1}{2}P_0 R e^{-4L\alpha_0}\cosh(4L\alpha_0\phi_h)\left[1+\cos\left(\frac{dq_\perp^2}{k_0}\right)+\bar{\Delta}\sin\left(\frac{dq_\perp^2}{k_0}\right)\right] \\
& +P_0 R e^{-2L\alpha_0}\cos(2L\alpha_0\bar{\Delta}\phi_h - 2\rho)\left[\sin\left(\frac{dq_\perp^2}{k_0}\right)-\bar{\Delta}\cos\left(\frac{dq_\perp^2}{k_0}\right)\right](\cosh(2L\alpha_0\phi_h)e^{-2L\alpha_0}-1)
\end{aligned} \tag{5.22}$$

[2] A recalculation of the linear stability analysis yields a growth exponent slightly different from the one published in [GWKL+00]. The qualitative behavior of the system is maintained, while the quantitative deviation is ≈ 10% for the curve of marginal stability at the considered parameters.

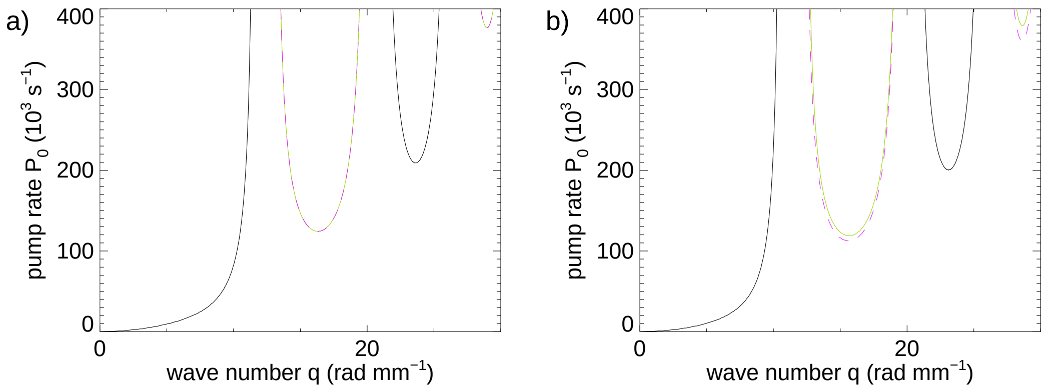

Figure 5.2: Result of a linear stability analysis. – instability regions of the homogeneous state $\phi = 0$, – instability regions of the homogeneous state with positive orientation, – instability regions of the homogeneous state with negative orientation. a) $\rho = 0°$, b) $\rho = -5°$ Parameters: see Fig. 5.1.

$$-P_0 Re{-}4L\alpha_0 \sinh(2L\alpha_0\phi_h)\sin(2L\alpha_0\bar{\Delta}\phi_h - 2\rho)$$
$$+\frac{1}{2}P_0 Re^{-4L\alpha_0}\left[-1 + \bar{\Delta}\sin\left(\frac{dq_\perp^2}{k_0}\right) + \cos\left(\frac{dq_\perp^2}{k_0}\right)\right]$$

The curve of marginal stability of the system is described by the zeros of η. The result of the linear stability analysis for the case $\rho = 0°$ is depicted in Fig. 5.2a [GWKL+00]. The homogeneous solution $\phi = 0$ becomes unstable against a homogeneous perturbation ($q = 0$) at very low pump rates (black lines). This instability represents the pitchfork bifurcation discussed above. At higher input powers, a modulational instability of the state $\phi = 0$ with finite wave number is found. However, it is not observed, since the pitchfork bifurcation occurs first due to the lower threshold. The two homogeneous branches emerging from the pitchfork bifurcation exhibit equal stability properties indicated by colored lines in Fig. 5.2a. A modulational instability is observed at pump rates which are around three orders of magnitude larger than the threshold of the pitchfork bifurcation. The wave number ($q_\perp = 15.7\,\text{rad mm}^{-1}$) corresponds to the wave number of a limiting absorptive instability as it would be expected from the Talbot effect ($q_\perp = \sqrt{\frac{\pi k_0}{d}} = 15.67\,\text{rad mm}^{-1}$) and corresponds quite well to the experimental findings. The linear stability analysis also finds instabilities with higher wave numbers that are typical for single mirror feedback arrangements. They have been discussed as as a possible reason for the occurrence of complex patterns composed of Fourier modes with different fundamental wave numbers [PSA97, VK97, BLRT98]. However, these instabilities have not been found to play a role in the formation of the structures discussed here.

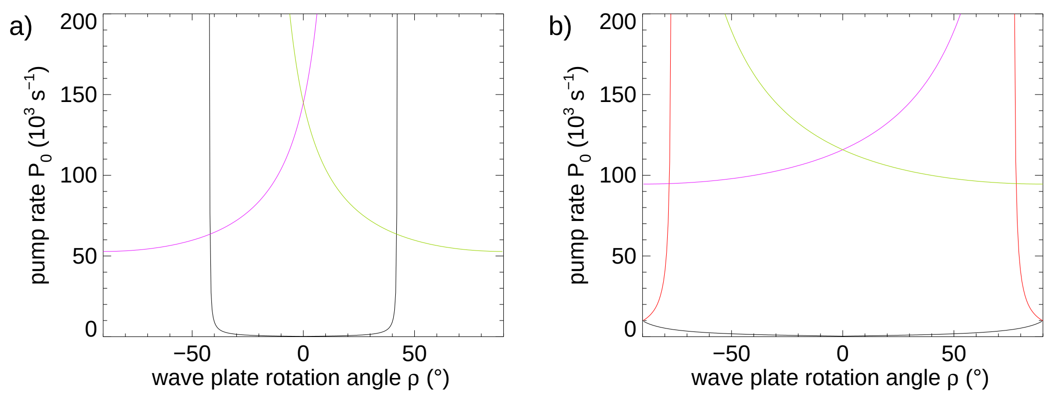

Figure 5.3: Bifurcation scenario. – threshold for bistability, – threshold for tristability, threshold for pattern formation of the homogeneous state with positive (–) and negative(–) orientation a) medium particle density; b) high particle density. Parameters: see Fig. 5.1, except: a) $N = 3.4 \cdot 10^{19}\,\mathrm{m}^{-3}$, $\bar{\Delta} = 12.8$.

If the pitchfork bifurcation is perturbed, the degeneracy of the two branches is abolished. Accordingly the stability properties are changed. Fig. 5.2b shows the result of a linear stability analysis at a wave plate rotation angle $\rho = -5°$. The threshold for pattern formation is lower than for the symmetric case if the favored branch (here: branch with positive orientation) is considered. For the disfavored branch, it is higher (negative orientation).
Figure 5.3 shows an overview of the bifurcation structure in parameter space for medium particle densities N. The full straight line indicates the threshold for bistability. The bistable region broadens quickly with increasing input power and then saturates at a certain level of wave plate rotation angles.
The threshold of the modulational instability occurring on the branch with positive orientation increases monotonically with increasing wave plate rotation angle, i.e. the more favored the state is, the lower is the threshold for pattern formation. The same is obviously true for the threshold for pattern formation of the branch with negative orientation.
The bifurcation diagram qualitatively reproduces the experimental observations (compare to Fig. 4.8). However, the dependency of the threshold of the modulational instability on the wave plate rotation angle ρ is significantly lower in the experiment.
If the particle density is increased, the width of the bistable region increases (Fig. 5.3b). At a certain point, the maximum wave plate rotation angle of $\rho = \pm 90°$ is crossed. In this case, three stable homogeneous solutions are obtained around $\rho = 90°$. This tristable situation has been found already in [GWKL$^+$00]. However, it is not observed in the experiment and for this reason won't be discussed further here. Nevertheless it has proven to be beneficial to assume a high particle density in order to systematically

reproduce the experimental findings around the wave plate rotation angle $\rho = \pm 0°$. For this reason a high particle density has been assumed in the following calculations.

5.2.3 Numerical simulations of patterns

The linear stability analysis can predict the critical wave number of a modulational instability. However, in a system with rotational and translational symmetry, the shape of the observed pattern cannot be predicted due to the degeneracy of all wave vectors with the critical wave number in the two-dimensional plane. This degeneracy is then abolished by the nonlinear interaction of the wave vectors leading to the formation of a (typically) simple, periodic pattern composed of few Fourier modes [CH93].
The patterns that evolve above the threshold of the modulational instability can be obtained via numerical simulations. For the present system, this issue has been discussed in [GWKL+00] and will therefor be discussed only briefly.

Patterns

If the system is considered at wave plate rotation angles $\rho \approx 0°$, two homogeneous solutions exist before the modulational instability occurs. If the threshold for pattern formation is crossed in a system with Gaussian beam input, hexagonal patterns evolve from both homogeneous solutions (see first two rows of Fig. 5.4). Both patterns are completely identical except for the sign of the orientation. In Fourier space, the patterns are represented by six intensity peaks that have an equal wave number ($q = 15.5\,\mathrm{rad\ mm}^{-1}$) and include an angle of 60°. Subfigures c) and g) show the intensity distributions of the light fields that are transmitted by the sodium vapor. This light field is projected onto a state of linear polarization where the background is suppressed. Like in the experiment, the result is a hexagonal pattern of intensity peaks (compare to Fig. 4.6). Infinitely extended hexagonal patterns are observed on both branches of the pitchfork bifurcation, if a plane wave input is assumed. The resulting orientation distributions are given in Figs. 4.6d,h.
The observation of hexagons is expected, since the homogeneous solutions have a non-vanishing orientation, due to which the inversion symmetry of equation 5.7 is strongly broken. In such a situation, general considerations predict the occurrence of hexagonal patterns at threshold [CH93].
If the system is considered at $\rho \approx 90°$, the input polarization is stable. Hence, the homogeneous orientation below threshold is zero, and the inversion symmetry of equation 5.7 is maintained. In this situation, triangular and rhombic patterns can be observed which are depicted in the 3rd and 4th row of Fig. 5.4.
The triangular patterns are characterized by six intensity peaks in Fourier space like the

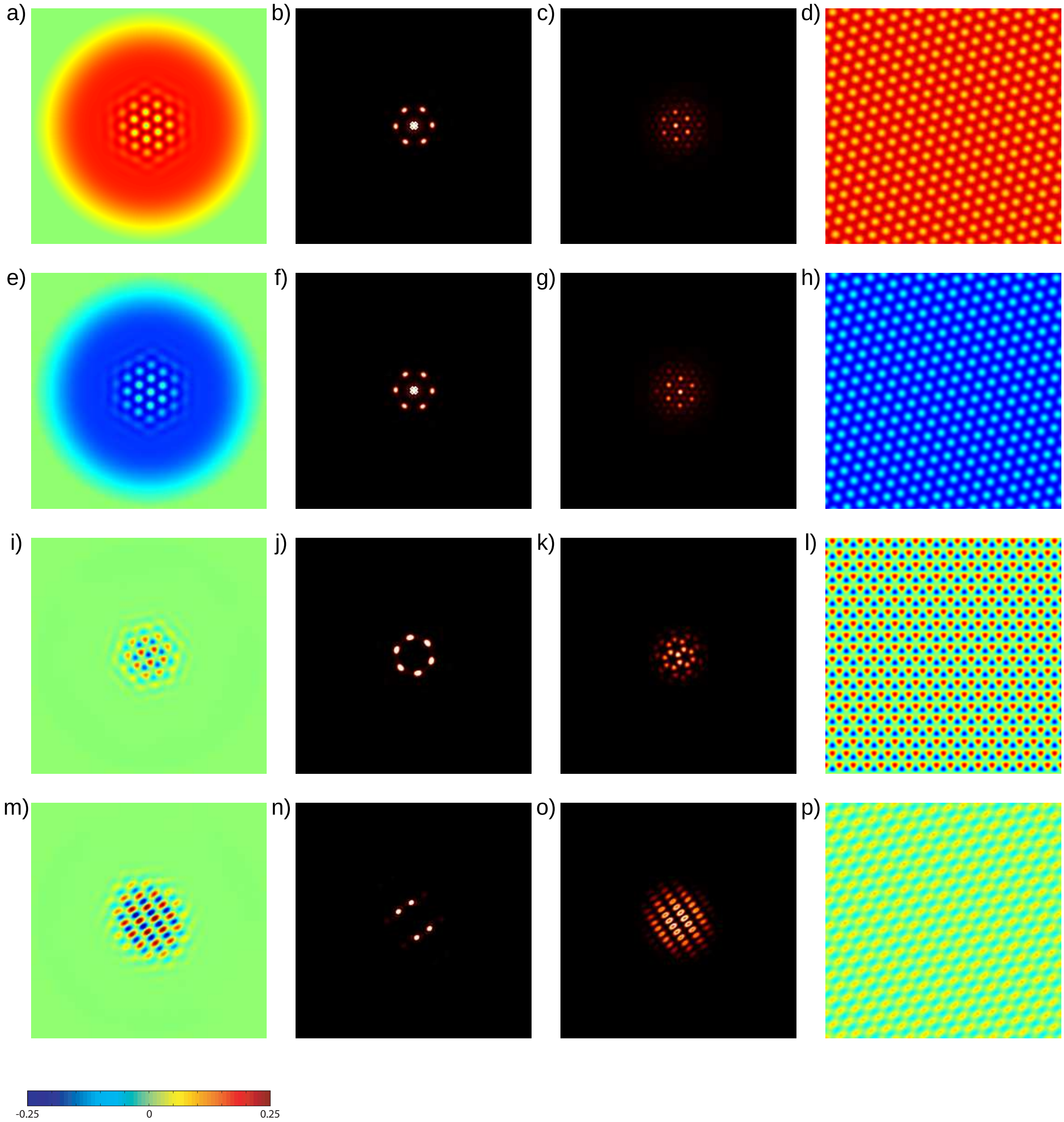

Figure 5.4: Numerical simulation of patterns. 1st row: hexagons with positive orientation, 2nd row: hexagons with negative orientation, 3rd row: triangular patterns, 4th row: rhombic patterns. 1st column: orientation distribution in a Gaussian beam, 2nd column: Fourier transform of 1st row, 3rd column: transmitted light field with background suppressed by linear polarizer, 4th column: orientation distribution in plane wave simulations. Color table applies to 1st and 4th column. Parameters: see Fig. 5.1, first three columns: $w_0 = 1.89\,\mathrm{mm}$, a)-h) $\rho = 0\,°$, i)-p) $\rho = 90\,°$, a)-c) $P_0 = 200000\,\mathrm{s}^{-1}$, d) $P_0 = 130000\,\mathrm{s}^{-1}$, e)-g) $P_0 = 200000\,\mathrm{s}^{-1}$, h) $P_0 = 130000\,\mathrm{s}^{-1}$, i)-k) $P_0 = 150000\,\mathrm{s}^{-1}$, l) $P_0 = 120000\,\mathrm{s}^{-1}$, m)-o) $P_0 = 280000\,\mathrm{s}^{-1}$, p) $P_0 = 100000\,\mathrm{s}^{-1}$.

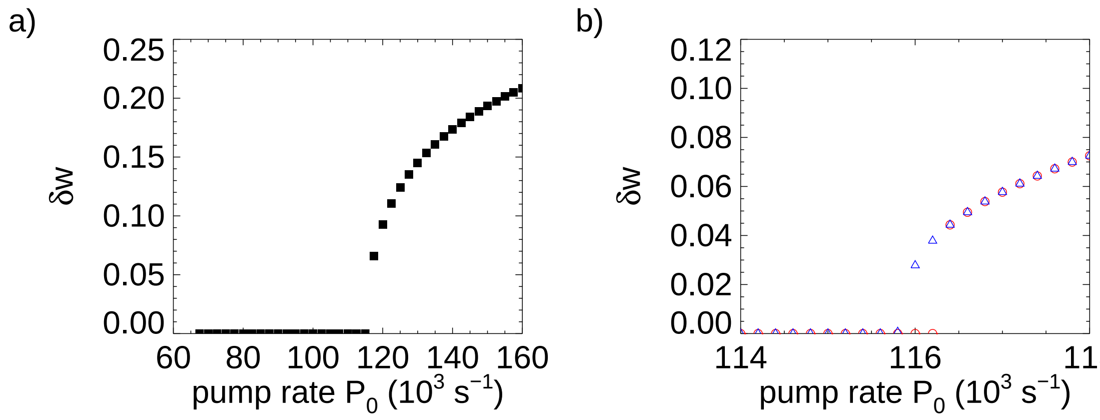

Figure 5.5: Numerical simulation of the threshold behavior of the modulational instability. a) scan over a wide rage of pump rates P_0. b) increase (○) and decrease (△) of pump rate P_0 around the threshold point. Parameters: see Fig. 5.1, $\rho = 0\,°$.

hexagons. However, in the triangular pattern, the phase difference between the three Fourier modes is $\pi/2$. This is in contrast to hexagonal patterns, where the phase sum of the three modes amounts to zero (positive hexagons) or π (negative hexagons).
The rhombic patterns are composed of four Fourier components (subfigure n) enclosing angles of 54° and 126°, the wave number being $q = 15.1\,\mathrm{rad\,mm}^{-1}$. Triangular patterns are the dominant pattern for $\rho = 90°$. In order to obtain rhombic patterns, they were seeded in the simulations. Triangles as well as rhombic patterns exist also if the inversion symmetry is not exactly maintained. Nevertheless they have never been observed in the parameter range that will be considered in the following.

Threshold behavior

A linear stability analysis can only give the threshold pump rate, at which the homogeneous state becomes unstable against a perturbation with a certain wave number. However, if a pattern has evolved and the pump rate is reduced again, the threshold at which the pattern disappears is generally not equal to the switch-on threshold.
In this work, the modulational instability leading to hexagonal patterns around $\rho = 0°$ is considered. Typically a bifurcation to a hexagonal pattern is subcritical, the switch-off threshold of the pattern being lower than the switch-on threshold. However, this behavior is not observed in the experiment.
The result of a simulation scanning the pump rate across the threshold for pattern formation is shown in Fig. 5.5. It shows the modulation depth of the orientation distribution

(minimum to maximum) in dependency on the pump rate. If the pump rate is scanned over a wide rage (Fig. 5.5a), the modulation depth jumps from zero to a certain finite value at a pump rate of $P_0 = 116500\,\mathrm{s}^{-1}$. This pump rates coincides with the minimum of the instability balloon from the linear stability analysis within the considered resolution. After the threshold is crossed, the pattern amplitude increases with increasing pump rate. Figure 5.5b shows a finer scan around the threshold for pattern formation. Red circles indicate the data points of a scan where the pump rate is increased, while the blue triangles indicate the result of a simulation where the pump rate is stepwise reduced. A small region of bistability is observed, hence the bifurcation is subcritical. However, the bistable range is very small ($\Delta P \approx 500\,\mathrm{s}^{-1}$). A similar bistability range is found if a Gaussian beam input is considered. It can be concluded that this small range of bistability cannot be resolved in the experiment due to the omnipresent fluctuations. The subcriticality of the bifurcation can in a good approximation be neglected in the further description of the system.

5.3 Fronts, circular domains and the stabilization of solitons

Up to now the analysis was restricted to small-amplitude structures that develop spontaneously from an unstructured orientation distribution. The basic properties of such structures can be understood by means of a linear or weakly nonlinear analysis.
The main focus of this work, however, lies on large-amplitude structures that do not develop spontaneously but have to be ignited by means of a large-amplitude perturbation for the system. Hence, these structures are inherently strongly nonlinear and are not accessible via linear approximations of the nonlinear system.
At first, the properties of fronts and circular domains that incorporate two homogeneous solutions of the system will be studied in analogy to the experimental analysis.

5.3.1 Straight fronts

Basic properties

In numerical simulations with a plane wave input, a stable resting straight front is found above the threshold for bistability for the case of equivalent homogeneous states ($\rho = 0°$). It connects the two equivalent homogeneous states (Fig. 5.6) and is surrounded by small spatial oscillations oriented parallel to the front axis that decay with increasing distance to the front.

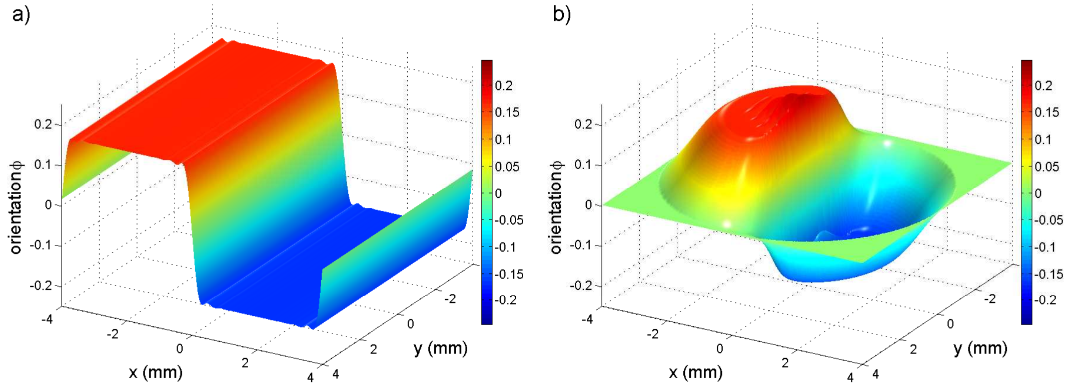

Figure 5.6: Straight orientation front in simulations with a) plane wave and b) Gaussian beam input. Parameters: see Fig. 5.1, $\rho = 0\,°$, a) $P_0 = 50000\,\mathrm{s}^{-1}$, b) $P_0 = 170000\,\mathrm{s}^{-1}$, $w_0 = 1.89\,\mathrm{mm}$.

A classification of the observed front with respect to the Ising and Bloch types of fronts (see section 2.2.2) is easily obtainable. The front is fully described by the real-valued magnitude orientation and it connects two equivalent states thereby crossing the zero. This excludes a handedness of the front. Furthermore the front is resting and a symmetry operation Z exists, that transforms the front into itself ($Z : \phi \to -\phi, x \to -x$). Following the argumentation in [MPL+01], the front can thereby be classified as an Ising front.
Straight fronts can also be observed in simulations using a Gaussian input beam (see Fig. 5.6b). In contrast to the simulations with a plane wave input it is not stable at low input powers that are beyond the threshold for bistability. The front will start to move and switch the whole area to one of the two equivalent states. Stable fronts are observed only for higher input powers. In this situation the spatial oscillations surrounding the front are quite pronounced in the beam center. They might stabilize the front in this situation, where the finite size of the system normally would introduce an instability of the front. As described in section 4.3.1, straight fronts are observed experimentally only at high input powers. The simulations confirm this observation.

Front dynamics

If the equivalence of the two homogeneous states connected by the front is omitted ($\rho \neq 0°$), the straight front starts to move. A systematic analysis of this motion of straight fronts by means of the video sampling method is not possible in the experiment. Nevertheless, an analysis of this dynamics in simulations can support the experimental findings made concerning circular domains.

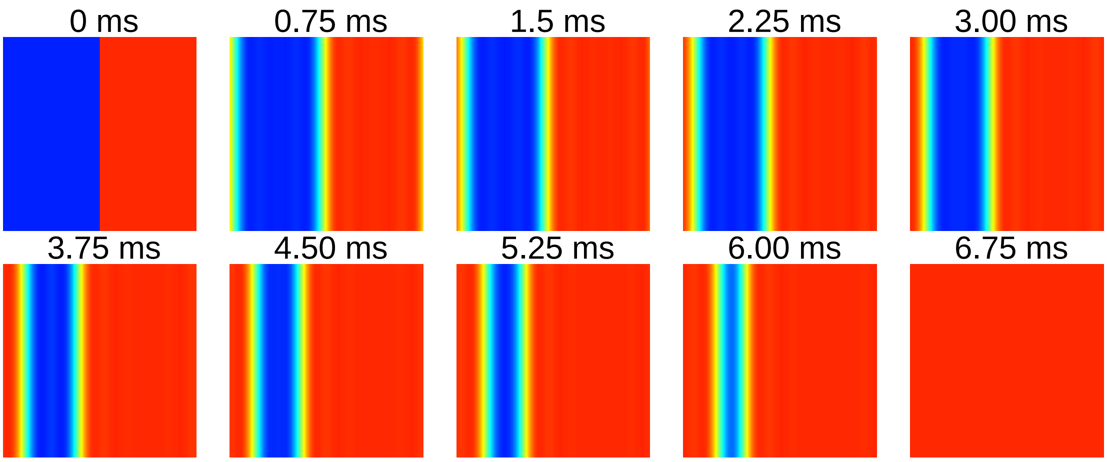

Figure 5.7: Motion of a straight front due to the inequality of the homogeneous bistable states. Parameters: see Fig. 5.1, $\rho = -5\,°$, $P_0 = 50000\,\mathrm{s}^{-1}$. Color table: see Fig. 5.6.

Due to the periodic boundary conditions, there are always two fronts in numerical simulations. As the initial condition, one front is located at the outer left and right border, while the other one is located in the center (see Fig. 5.7a). When the simulation is started, the shape of the fronts rapidly smoothes out due to the spatial coupling mechanisms and the front starts to move. The motion leads to an expansion of the favored homogeneous state (in this case the one with positive orientation). The front stays straight while moving, hence no modulational instability of the front is observed. After 7 ms, the whole area is switched to the preferred state.
The front velocity as well as the direction of motion of the front depends on the inequality of the two states, which is in accordance with general expectations (see section 2.2.1). Fig. 5.8a shows the position of the front in dependency on time for different wave plate rotation angles. The curves describe a uniform motion of the front that can very well be described by a linear fit, thereby assuming a constant velocity of the front. For positive wave plate rotation angles, the state with negative orientation expands and vice versa. The velocity of the front in dependency on the wave plate rotation angle is plotted in Fig. 5.8b. The graph shows, that the front velocity depends linearly on the wave plate rotation angle ρ. The slope is given by $\gamma_i' = 0.022\,\frac{mm}{ms°}$. Though the motion of a straight front cannot be directly measured in the experiment, it has been determined indirectly (see section 4.3.4) by fitting the dynamics of circular domains to the theoretical prediction

$$\frac{dR}{dt} = -\frac{\gamma_c}{R} + \gamma_i\,. \tag{5.23}$$

The coefficient γ_i describes the motion of a straight front due to the inequality of the

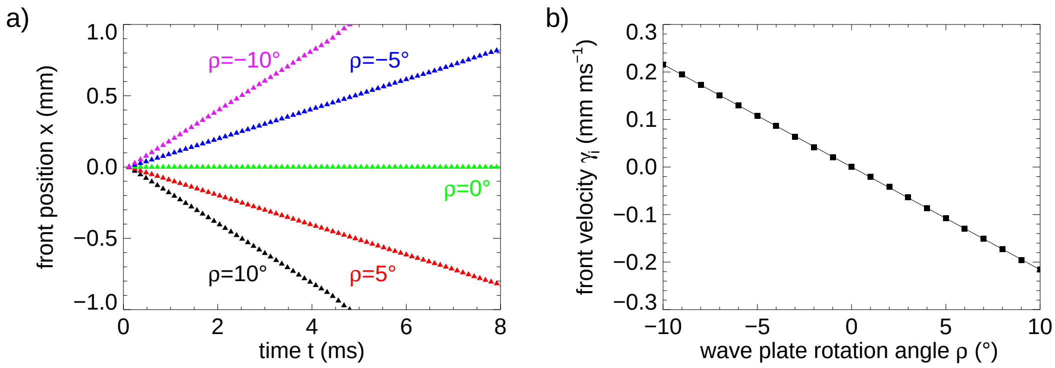

Figure 5.8: Motion of a straight front due to the inequality of the homogeneous bistable states. a) front position in dependency on time; b) coefficients γ_i resulting from a linear fit of the front dynamics. Parameters: see Fig. 5.1, $P_0 = 50000\,\mathrm{s}^{-1}$.

two homogeneous states and was determined in dependency on ρ in Fig. 4.19a. These results match nicely the numerical observations. The coefficient γ_i can now be refined to $\gamma_i = \gamma_i' \rho$.

Oscillatory tails and quasi one-dimensional solitons

The observed fronts are always surrounded by spatial oscillations that decay with increasing distance from the front. The modulation depth of these oscillatory tails increases with increasing input power. Figure 5.9a shows cuts made perpendicular to a straight front under variation of the input power. The grey level encodes the pump rate, where the brightness of the line increases with increasing pump rate. The pump rates range from $P_0 = 50000\,\mathrm{s}^{-1}$ to $P_0 = 110000\,\mathrm{s}^{-1}$, the threshold for pattern formation being at $P_0 = 117000\,\mathrm{s}^{-1}$. Even far below the threshold for pattern formation there are pronounced spatial oscillations with a well-defined spatial frequency ($q \approx 16\,\mathrm{rad\,mm}^{-1}$) that corresponds well to the critical wave number of the modulational instability occurring at higher pump rates. With increasing pump rate, their amplitude increases. Due to the periodic boundaries, at a certain point the oscillatory tails of the two fronts will start to interact.

The interaction of the oscillatory tails of two fronts will be stronger, if the fronts are close to each other and if the modulation depth of the tails is large. In the previous subsection, the pump rate was chosen to be far from the threshold for pattern formation and only the dynamics of fronts that have a large distance from each other was considered.

If now high pump rates are considered, the motion of the two fronts approaching each other

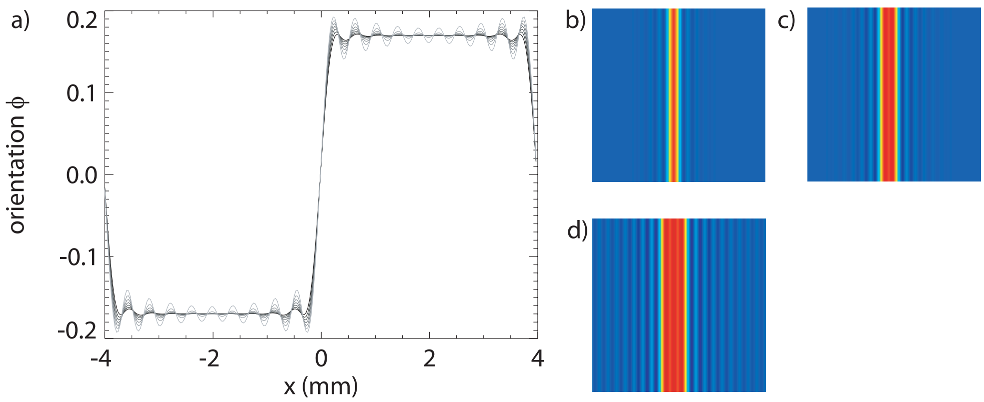

Figure 5.9: a) Emergence of oscillatory tails with increasing pump rate P_0. Gray levels encode pump rate from $P_0 = 50000\,\mathrm{s}^{-1}$ (black) to $P_0 = 110000\,\mathrm{s}^{-1}$ (light gray). Quasi one-dimensional solitons of b) first, c) second and d) third order. Color table: see Fig. 5.6. Parameters: see Fig. 5.1; a) $\rho = 0\,°$; b)-d) $\rho = 5\,°$; b) $P_0 = 80000\,\mathrm{s}^{-1}$; c) $P_0 = 95000\,\mathrm{s}^{-1}$; d) $P_0 = 110000\,\mathrm{s}^{-1}$.

might be completely stopped at a certain distance. Since the oscillatory tails incorporate multiple oscillation periods, this locking can occur at different discrete distances. The situations incorporating the smallest three distances are shown in Fig. 5.9b-d. These stable configurations of two opposing straight fronts can be interpreted as the one-dimensional equivalent to the circular solitons that will be discussed in the following sections. The motion of fronts due to their curvature is not present here, and stable quasi-1D solitons are observed for small angles $|\rho|$, enclosing the angle $\rho = 0°$. As in many other systems, the locking of oscillatory tails obviously is a sufficient mechanism for the stabilization of one-dimensional solitons. The situation becomes more complex, if two-dimensional effects are considered.

5.3.2 Domain dynamics

In bistable systems, circular domains of one homogeneous solution that are embedded into a background of the other stable homogeneous solution are generally not stable due to the curvature of the domain interface. Nevertheless the analysis of the dynamics of unstable domains will give further insight into the system itself and it will provide the key mechanisms that finally lead to the observation of stable solitary structures.

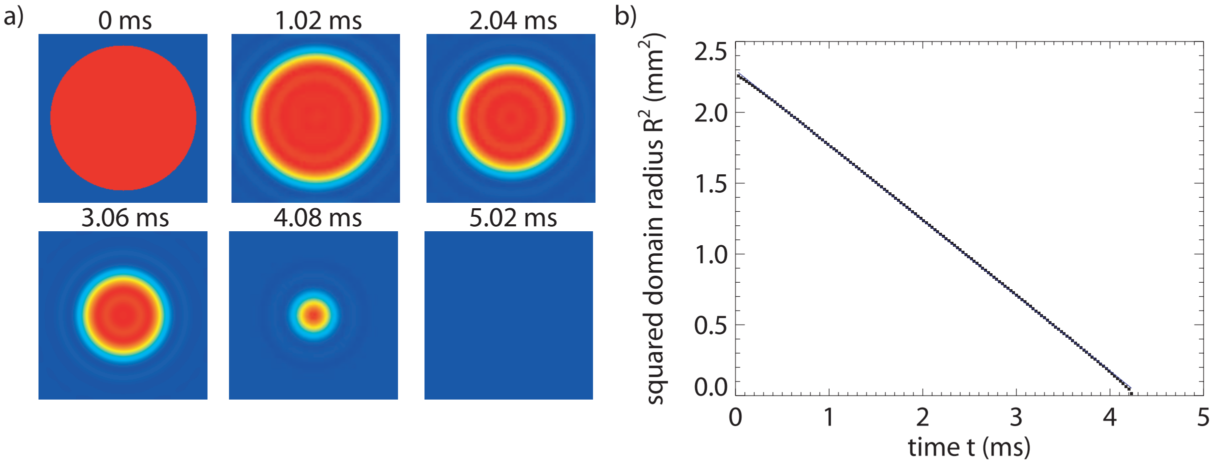

Figure 5.10: Contraction sequence of a circular domain. a) Images of the orientation distributions. b) squared domain radius plotted against time. ▪ data points, – linear interpolation. Parameters: see Fig. 5.1, $\rho = 0\,°$, $P_0 = 50000\,\mathrm{s}^{-1}$. Color table: see Fig. 5.6.

Basic observation

The system is considered in a situation where two equivalent homogeneous solutions exist ($\rho = 0°$). The pump rate is chosen to be far below the threshold for pattern formation. In order to study the pure domain dynamics the pump field is chosen to be a plane wave. The initial domain is given as an orientation distribution. It is realized as a top-hat distribution having the homogeneous solution with a positive orientation as the central domain of radius R_0 surrounded by the homogeneous solution with negative orientation.

The temporal evolution of a domain having an initial radius of $R_0 = 1.5\,\mathrm{mm}$ is shown in Fig. 5.10a. The domain contracts maintaining its circular shape and disappears after 4.2 ms. Some slight radial oscillations are present. However, at the given pump rate ($P_0 = 50000\,\mathrm{s}^{-1}$), they do not significantly influence the dynamics. The squared domain radius R^2 in dependency on time is plotted in Fig.5.10b. The data points lie on a straight line in a very good approximation. Only at the very beginning of the sequence, where the front has an rectangular shape and first relaxes to a smooth shape, and at the end, where strong interaction of the approaching fronts is present, a slight deviation from the interpolation line is detectable. Thereby the $\sqrt{t}$ power law expected from theory and observed experimentally is confirmed by the simulations.

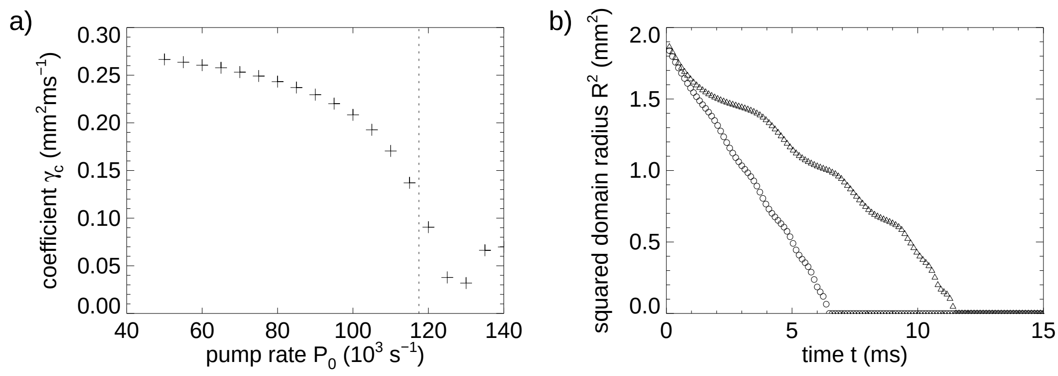

Figure 5.11: a) Coefficient γ_c in dependency on the pump rate P_0. Dashed line indicates threshold for pattern formation ($P_{crit} = 117500\,\mathrm{s}^{-1}$). b) Locking of contracting domains slightly below ($P_0 = 115000\,\mathrm{s}^{-1}$, $\circ$) and above ($P_0 = 125000\,\mathrm{s}^{-1}$, $\triangle$) the threshold for pattern formation. Parameters: see Fig. 5.1, $\rho = 0\,°$.

Variation of pump rate

In the experiment, a slowdown of the dynamics of contracting circular domains with increasing input power is observed (see section 4.3.3). This dependency is also found in numerical simulations. Figure 5.11a shows the coefficient γ_c in dependency on the pump rate. The obtained curve nicely matches the experimental observations qualitatively and in the order of magnitude of γ_c (cf. Fig. 4.12). For low and medium pump rates, the $\sqrt{t}$ law is nicely confirmed.

Near the threshold for pattern formation the dynamics is modified. The contraction of a domain slightly below and above the threshold for pattern formation is shown in Fig. 5.11b. Below the threshold, the contraction curve becomes slightly modulated. This suggests the influence of a locking process due to the oscillatory tails of the circular front. The influence of locking is heavily increased if the threshold for pattern formation is crossed. The contraction is slowed down further and the the curve becomes more and more horizontal within the locking regions. At a certain point, the dynamics is completely stopped and, depending on the initial conditions and the pump rate, solitons (see section 5.4) or localized patterns (see section 5.5.5) are observed.

Variation of wave plate rotation angle

The dynamics of circular domains is modified, if the more general case of nonequivalent homogeneous states is considered, i.e. the wave plate rotation being $\rho \neq 0°$. It has been shown in section 5.3.1 that in this case a straight front will start to move, leading to an

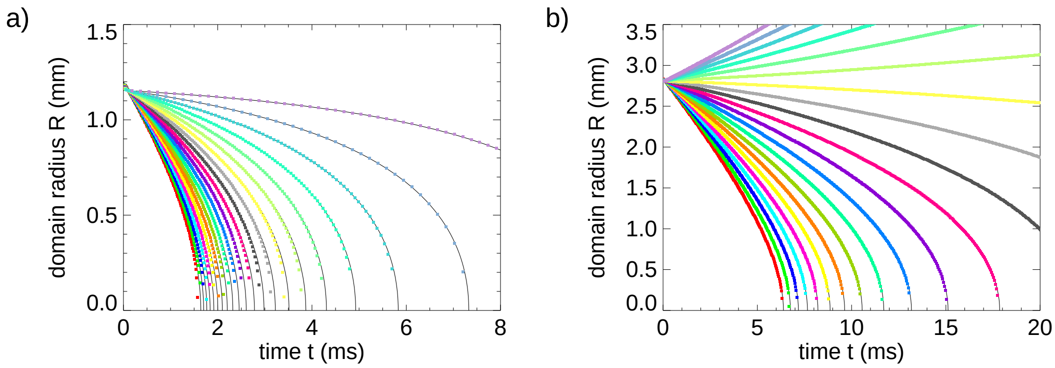

Figure 5.12: Dynamics of a) small ($R_0 = 1.17\,\mathrm{mm}$) and b) large ($R_0 = 2.81\,\mathrm{mm}$) circular domains in dependency on the wave plate rotation angle ρ. Colored data points: numerical result; black curves: results of a shared parameter fit. Parameters: see Fig. 5.1, $P_0 = 50000\,\mathrm{s}^{-1}$.

expansion of the favored state. This motion due to the nonequivalence of the two states occurs also if circular domains are considered. While the motion due to the curvature of the front always leads to a contraction and disappearance of circular domains for the parameters considered here, this motion can be either accelerated or slowed down by the motion due to the nonequivalence of the two homogeneous states.

The dynamics of domains under variation of the wave plate rotation angle ρ is shown in Fig. 5.12. ρ is varied from $-10°$ (domain state is favored) to $10°$ (background is favored). If a small domain is considered (initial domain radius $R_0 = 1.17\,\mathrm{mm}$, Fig. 5.12a), it always contracts and disappears for the given range of ρ. If the domain is disfavored, the contraction takes place faster than for equivalent states because both effects leading to a motion of the domain wall tend to reduce the domain radius. If the domain is favored, the motion due to the nonequivalence of the states counteracts the motion induced by the curvature of the front. Thus, the dynamics is significantly slowed down.

The contraction of the domain can even be overcompensated, leading to an expansion of the domain until the whole area is switched to the domain state. This can be observed, if the initial domain size is increased to $R_0 = 2.81\,\mathrm{mm}$ (see Fig. 5.12b). Below an angle of $\rho = -4°$, the domain expands. However, a stable domain is not observed for the given parameters.

The described dynamics is well described by the theoretical expectation already discussed (equation 5.23). A shared parameter fit for the two given curve arrays yields the parameters γ_i and γ_c as described in section 4.3.4. The fitted curves are given as a straight black line below the data points in Fig. 5.12.

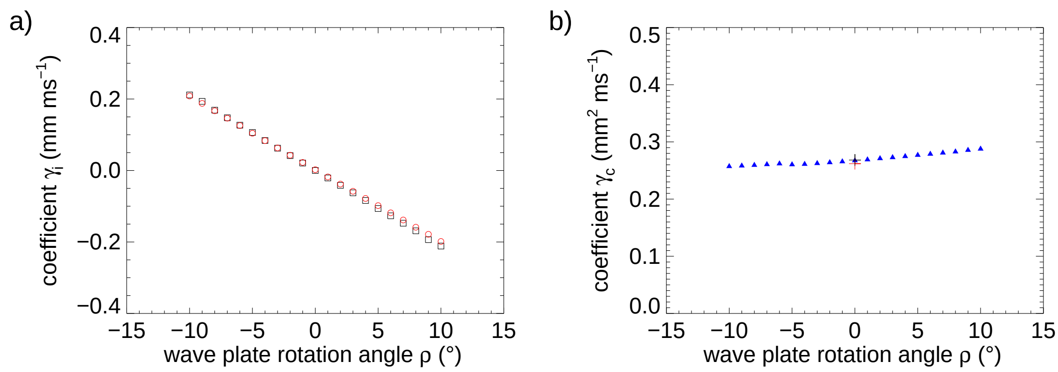

Figure 5.13: Coefficients γ_i (a) and γ_c (b) in dependency on the wave plate rotation angle ρ. a) □: linear motion of a straight front cf. Fig. 5.8; ○: result from a shared parameter fit of the dynamics of circular domains. b) ▲: result from a shared parameter fit of the dynamics of circular domains. Crosses: result from a linear fit for the squared domain radius in dependency on time with $R_0 = 1.17\,\mathrm{mm}$ (+) and $R_0 = 2.81\,\mathrm{mm}$ (+). Parameters: see Fig. 5.1, $P_0 = 50000\,\mathrm{s}^{-1}$.

The resulting coefficients of the fitting procedure are given in Fig. 5.13. The motion of the front induced by the nonequivalence of the two states described by γ_i is plotted as red circles in Fig. 5.13a. The data points lie on a straight line with vanishing γ_i at $\rho = 0°$ in a good approximation. The values for γ_i obtained independently from the analysis of the motion of straight fronts (section 5.3.1) are given as black squares. Both curves show a good agreement and support the validity of equation 5.23.
The coefficient γ_c depends only weakly on ρ (Fig. 5.13b). It tends to decrease with increasing preference for the domain state. At $\rho = 0°$, the values for γ_c obtained for a linear fit of the squared domain radius versus time as described in section 5.3.2 are reproduced (black ($R_0 = 1.17\,\mathrm{mm}$) and red ($R_0 = 2.81\,\mathrm{mm}$) crosses).
The numerical results match the experimental observations nicely (compare Fig. 5.13 to Fig. 4.19). However, in the experiment, a larger dependency of γ_c on ρ is observed. This is possibly due to the gradients induced by the Gaussian beam.

5.3.3 Stationary domains

The described domain dynamics has a stationary domain solution that is not stable. Due to this instability it cannot be calculated by numerical simulations performing a time integration of the microscopic model. However, stationary solutions of the dynamics can be calculated directly by means of the Newton method. As an initial condition for the algorithm, a domain which has a very long transient in the simulations is taken. It is

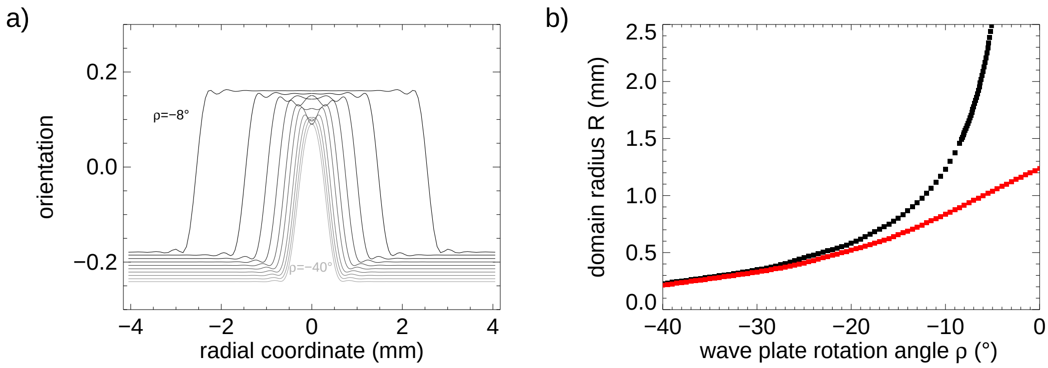

Figure 5.14: Unstable stationary domains in a radially symmetric system. a) Unstable domains in a plane wave under variation of the wave plate rotation angle ρ (grayscale encodes ρ); b) Radii of the unstable domains in a plane wave (■) and a Gaussian beam (■, $w_0 = 1.89\,\mathrm{mm}$). Parameters: see Fig. 5.1, $P_0 = 50000\,\mathrm{s}^{-1}$.

expected to be close to the unstable stationary domain.

The stationary domain solutions that are obtained for different wave plate rotation angles ρ are plotted in Fig. 5.14a. The brightness of the curve increases with $|\rho|$, ranging from $\rho = -8°$ to $\rho = -40°$. The domain radius decreases with increasing inequality of the two homogeneous states. This is expected, since the stationary domain should be given by $R_{crit} = \frac{\gamma_c}{\gamma_i}$, and it has been shown experimentally and numerically, that γ_i increases linearly with ρ and that γ_c is positive and only weakly dependent of ρ. At the given pump rate far below the threshold for pattern formation, pronounced oscillations surrounding the front are observed.

The radius R_{crit} of the stationary unstable domain in dependency on ρ is shown in Fig. 5.14b. The curve shows the hyperbolic-type behavior expected from the theoretical considerations. If a Gaussian input light field is considered, the radius of the stationary unstable domain is not diverging at small angles $|\rho|$. The inhomogeneous pumping and the assumption of a vanishing orientation ϕ seems to introduce a pinning of the stationary front at a radius, where the gradients of the light field are large. However, the domain radius still decreases monotonically with increasing $|\rho|$.

5.4 Solitons

The combination of all effects discussed in the preceding sections can lead to the formation of stable solitons in a certain range of parameters. At first, the existence of a discrete family of solitons will be presented with the help of numerical simulations of the full microscopic model. The basic properties of the solitons will be discussed with respect to the experimental findings. Subsequently, the variation of the most important parameters pump rate P_0 and wave plate rotation angle ρ will be considered using the Newton method, which will give further insight into the bifurcation structure.

5.4.1 Numerical simulations

Gaussian beam input

As an initial condition for the simulations, a domain having the orientation of the positive homogeneous solution that is embedded in the background of the homogeneous solution with negative orientation is used. For simulation with a Gaussian beam input, the homogeneous solutions in the beam center have been considered.
Depending on the size of the initial domain, four types of solitons are obtained in simulations with a Gaussian beam input. The center parts (4x4 mm, original grid size 8x8 mm) of the stable orientation distributions of these solitons are depicted in a three-dimensional plot in Fig. 5.15. They show the typical discrete series of solitons that differ in size and the number of radial oscillations around the target state. The different solitons are shown for parameters that lie in the minimum of their respective region of existence (see below). Thus, the amount of radial oscillations that is present around the target and background states is the minimum necessary to provide a stable structure.
The orientation distributions show a very good agreement with the experimental observations, where the spatially resolved polarization rotation angle ξ was measured (compare Fig. 5.15 to Fig. 4.24). Hence, the experimental method of analyzing the Stokes parameters of the light field transmitted by the sodium cell is suitable for an indirect measurement of the orientation distribution of the vapor. In analogy to the experimental findings, the solitons are interpreted as a homoclinic connection of the background state with itself that travels around the vicinity of the target state for a discrete number of oscillations. Of course, a family of negative solitons is observed if the wave plate rotation angle ρ is reversed.
The measurement of the Stokes parameters of the light field is not always applicable in the experiment. Instead, often the light field that is transmitted by the sodium cell has been considered in a projection onto a linearly polarized state, where the background is suppressed. The respective light fields that are transmitted by the orientation distributions

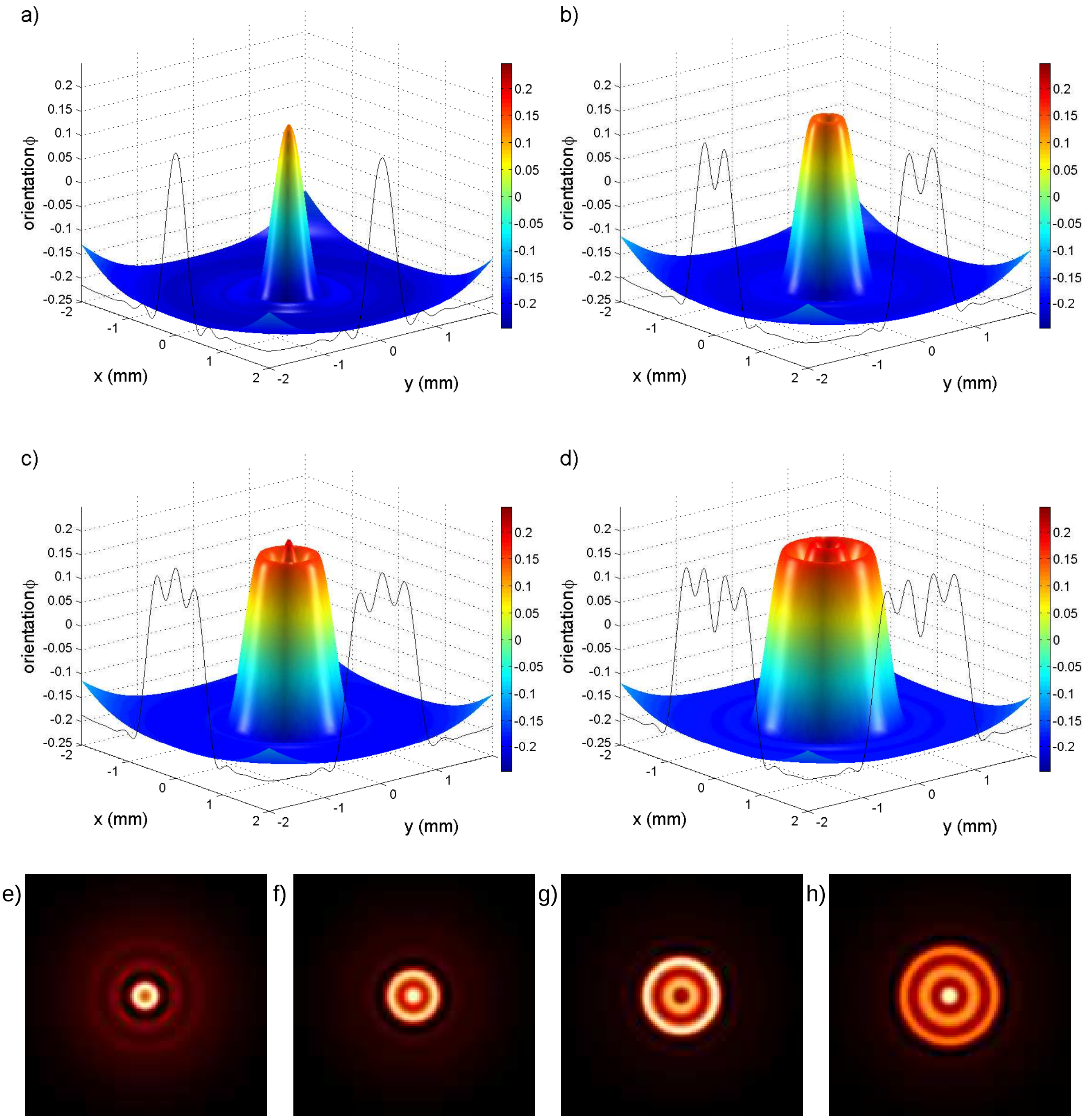

Figure 5.15: Stable solitons in numerical simulations assuming a Gaussian beam input. a)-d) Orientation distributions. e)-h) Projection of the transmitted light field onto a linear polarization state with suppressed background. a),e) S1; b),f) S2; c),g) S3; d),h) S4. Parameters: see Fig. 5.1; a),e) $\rho = -28\,^\circ$, $P_0 = 138000\,\mathrm{s}^{-1}$; b),f) $\rho = -20\,^\circ$, $P_0 = 90000\,\mathrm{s}^{-1}$; c),g) $\rho = -13\,^\circ$, $P_0 = 102000\,\mathrm{s}^{-1}$; d),h) $\rho = -10\,^\circ$, $P_0 = 123000\,\mathrm{s}^{-1}$.

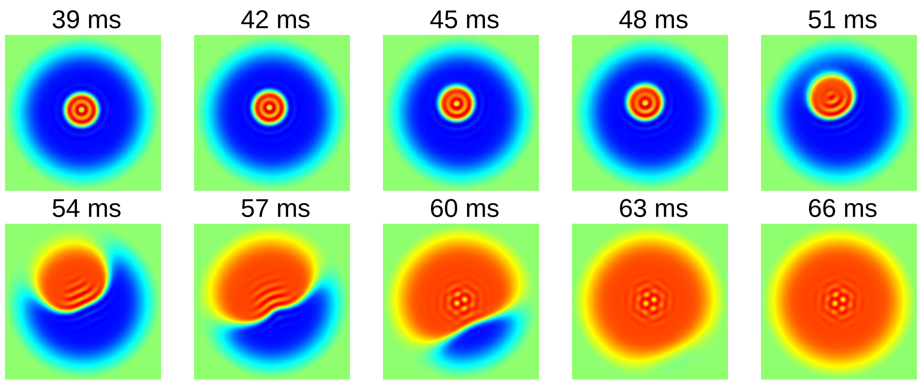

Figure 5.16: Metastable S4 soliton moving towards the beam boundaries. Soliton is at rest for 39 ms before. Parameters: see Fig. 5.1, $\rho = -12\,°$, $P_0 = 150000\,\mathrm{s}^{-1}$. Color table: see Fig. 5.18.

from Fig. 5.15a-d are shown in Fig. 5.15e-h. The number of radial oscillations of the solitons is increased by one with respect to the orientation distributions. The experimental findings are well reproduced (compare Figs. 5.15e-h to the first row of Fig. 4.22).

In contrast to the experimental findings, the outer parts of the background show a slight gradient that is induced by the inhomogeneous pumping and the Dirichlet boundary condition. It is interpreted to be more pronounced due to the position of the cell walls at a radius of 4 mm in contrast to the experiment (6 mm). In [PGWAL05], an even smaller grid was used, which lead to the instability of S4. For the parameters in Fig. 5.15 it is stable in the beam center. However, at higher pump rates, it is only metastable (Fig. 5.16). After having rested at the beam center for 39 ms, the soliton starts to move towards the beam boundaries and switches the whole beam to the target state, in accordance with the experiment. Solitons of an order above S4 have not been found stable due to this mechanism.

The mechanism that is typically observed for low order solitons whose size is small compared to the size of the beam is a motion towards the beam center. If a S2 soliton is ignited off-center, it will start to move until it reaches a stable final position that is given by the beam center (see Fig. 5.17). This is in accordance with the experimental observation.

Plane wave input

If a plane wave input field is considered, the existence of a soliton family is preserved. Figure 5.18 shows the first five members of the soliton family near the lowest stable pump rate. While all the higher order solitons exist also for parameters below the thresholds for pattern formation of background and target state, the fundamental soliton is only observed

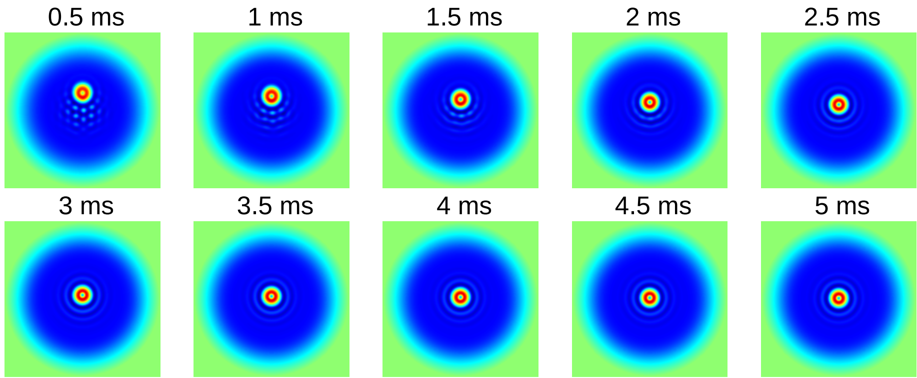

Figure 5.17: Motion towards the beam center of a S2 soliton that was ignited off-center. Parameters: see Fig. 5.1, $\rho = -15\,^\circ$, $P_0 = 190000\,\mathrm{s}^{-1}$. Color table: see Fig. 5.18.

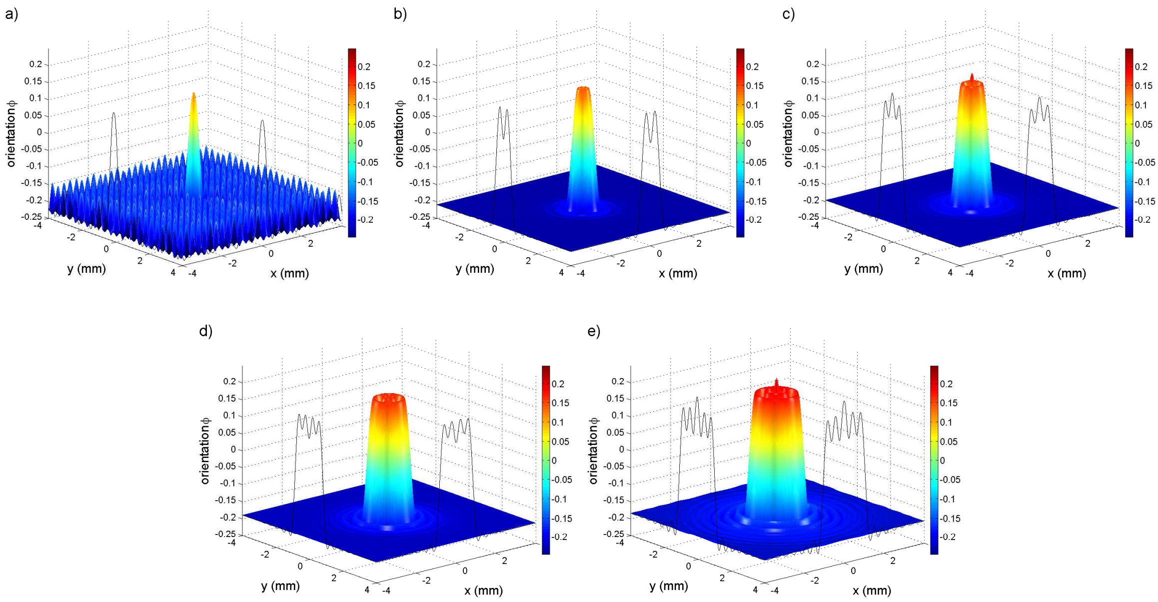

Figure 5.18: Stable solitons in numerical simulations assuming a plane wave input. a) S1; b) S2; c) S3; d) S4; e) S5. Parameters: see Fig. 5.1, a) $\rho = -22\,^\circ\,30\,'$, $P_0 = 142000\,\mathrm{s}^{-1}$, b) $\rho = -21\,^\circ\,30\,'$, $P_0 = 80000\,\mathrm{s}^{-1}$, c) $\rho = -14\,^\circ\,18\,'$, $P_0 = 84000\,\mathrm{s}^{-1}$, d) $\rho = -10\,^\circ\,36\,'$, $P_0 = 89000\,\mathrm{s}^{-1}$, e) $\rho = -7\,^\circ\,30\,'$, $P_0 = 110000\,\mathrm{s}^{-1}$.

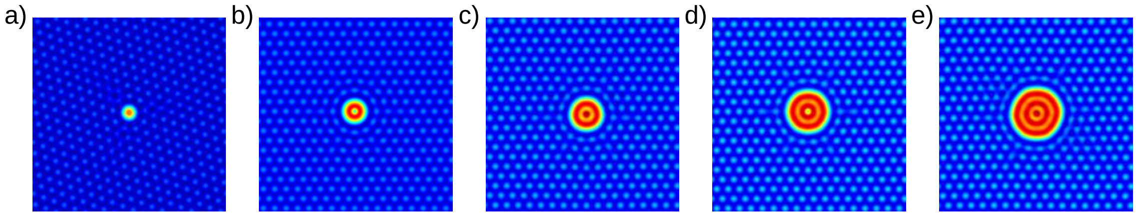

Figure 5.19: Soliton family above the threshold for pattern formation. a) S1; b) S2; c) S3; d) S4; e) S5. Parameters: see Fig. 5.1, a) $\rho = -22^\circ 30'$, $P_0 = 143000\,\mathrm{s}^{-1}$, b) $\rho = -13^\circ 00'$, $P_0 = 130000\,\mathrm{s}^{-1}$, c) $\rho = -8^\circ 00'$, $P_0 = 130000\,\mathrm{s}^{-1}$, d) $\rho = -5^\circ 00'$, $P_0 = 130000\,\mathrm{s}^{-1}$, e) $\rho = -5^\circ 00'$, $P_0 = 130000\,\mathrm{s}^{-1}$. Color table: see Fig. 5.18

for parameters above that threshold. However, the amplitude as well as the size of the constituents of the underlying pattern are considerably smaller than the fundamental soliton. The necessity of an increased amount of spatial oscillations for the stability has already been conjectured in the discussion of the existence regions in the experimental part (section 4.4.4), now it has manifested in the numerical simulations.
If the soliton families with a Gaussian beam input and plane wave input are compared, it turns out that the shape of the solitons does not significantly depend on the boundary conditions.
Higher order solitons also exist on a patterned background, i.e. at pump rates where the threshold for pattern formation is crossed (see Fig. 5.19). The circular shape of the solitons is mostly maintained, though the interaction with the symmetry-broken background will of course modify their appearance[3]. If the pump rate is increased further and the amplitude of the pattern becomes larger, the solitons lose their (approximately) radial symmetry and are transformed into localized patterns that will be discussed in section 5.5.5.

5.4.2 Solitons in a radially symmetric system

By means of full numerical simulations of the microscopic model, stable states of the dynamics can be determined. However, full simulations of the system are computationally expensive. For this reason, numerical simulations are not well suited for the systematic analysis of parameter dependencies. Especially near bifurcation points, the dynamics

[3] Occasionally, a slight drift (order of magnitude mm/s) of the pattern together with the soliton was observed. The drift velocity, however, depends on the discretization of the computational area. The drift motion is directed along the asymmetry axis of the hexagonal pattern, which, as a matter of principle, on a quadratic grid cannot have exactly equal wave numbers of the corresponding Fourier modes. Though a drift motion, in principle, cannot be excluded, it is considered a numerical artifact for the given reasons.

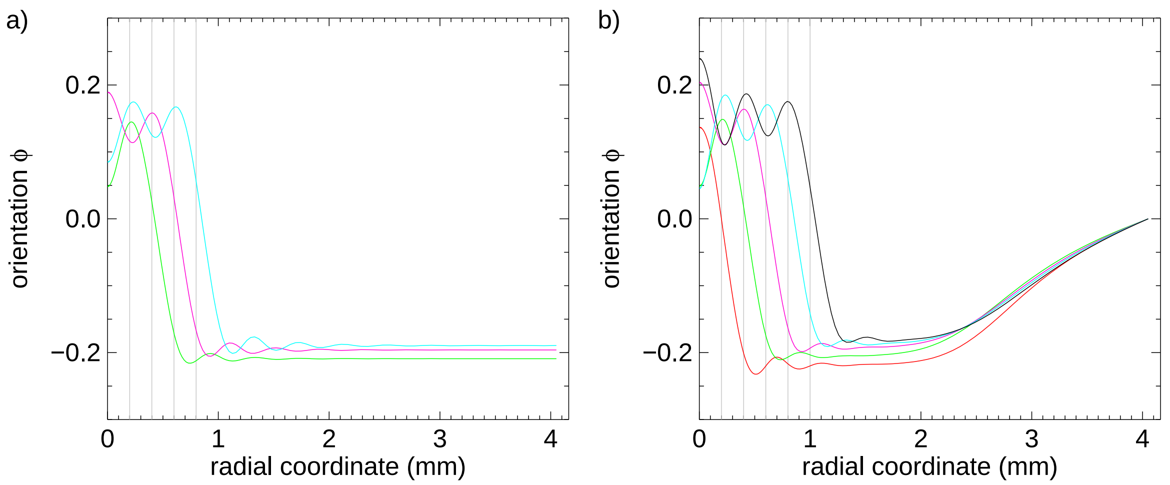

Figure 5.20: Soliton family obtained in a radially symmetric system. a) plane wave input. b) Gaussian beam input and Dirichlet boundary conditions. – S1, – S2, – S3, – S4, – S5. Parameters: see Fig. 5.1; a) S2: $\rho = -21^\circ 30'$, $P_0 = 80000\,\mathrm{s}^{-1}$; S3: $\rho = -14^\circ 12'$, $P_0 = 84000\,\mathrm{s}^{-1}$; S4: $\rho = -10^\circ 36'$, $P_0 = 89000\,\mathrm{s}^{-1}$; b) $w_0 = 1.89\,\mathrm{mm}$; S1: $\rho = -27^\circ 0'$, $P_0 = 144000\,\mathrm{s}^{-1}$; S2: $\rho = -20^\circ 0'$, $P_0 = 91000\,\mathrm{s}^{-1}$; S3: $\rho = -13^\circ 0'$, $P_0 = 105000\,\mathrm{s}^{-1}$; S4: $\rho = -10^\circ 0'$, $P_0 = 120000\,\mathrm{s}^{-1}$; S5: $\rho = -7^\circ 30'$, $P_0 = 140000\,\mathrm{s}^{-1}$.

becomes very slow, and numerical simulations take very long to converge. On the other hand, numerical simulations are not capable of determining unstable stationary solutions of the system, which often shed a light on the bifurcation structure of a nonlinear system. Hence, an analysis of the bifurcation structure leading to the formation of stable solitons will be conducted using the Newton method which allows for the calculation of stable and unstable domain solutions.

Solitons are observed slightly below and above the threshold for pattern formation in the numerical simulations. This implicates a large amount of spatial oscillations extending over a wide range below the threshold for pattern formation and infinitely extended oscillations above the pattern formation threshold. Due to the boundary conditions of the Newton method, spatial oscillations extending to the border of the computational grid will cause the method to fail to converge. An analysis with a plane wave input is restricted to parameters below the threshold for pattern formation. For this reason, the analysis of the bifurcation structure is conducted with a Gaussian beam input and the assumption of a vanishing orientation at a radius of 4 mm (like in the numerical simulations). This Dirichlet type boundary condition enables an analysis even above the threshold for pattern formation.

Of course, the assumption of a radial symmetry of the system is a restriction that is not strictly fulfilled above the threshold of a modulational instability leading to hexagonal patterns. But as the domain solutions that will be considered here are high-amplitude structures compared to the small amplitude of the patterns near the threshold, the obtained results can still be considered valid above but near that threshold. This is confirmed by spot sample full numerical simulations.

The discrete family of stable solitons can be easily reproduced by taking the results of the full numerical simulations as the initial condition for the Newton algorithm. Figure 5.20a shows solitons S2, S3, and S4 with a plane wave input, while Figure 5.20b reproduces the full soliton family S1-S5 with a Gaussian beam input. Both figures show the discreteness of the sizes and the number of radial oscillations of the solitons as it has been discussed before. The half wavelength of the modulational instability is indicated by light gray stripes. The sizes of the solitons are correlated to this length scale, however they do not match exactly. This issue will be discussed below. The Newton method even converges to solitons of higher orders than 5. However, as those structures have not been observed to be stable neither in the full simulations with a Gaussian beam input nor in the experiment, they will not be considered here.

5.4.3 Region of existence

Starting from a stable soliton, the parameters ρ and P_0 are varied in small steps, using the soliton obtained from the last step as the initial condition of the next one. In this manner, the soliton solution can be tracked and the region of existence of a soliton can be determined.

The borders of the existence regions of the first five members of the soliton family are shown in Fig. 5.21. The solitons are stable in the area enclosed by the respective data points. Near the threshold for the existence of every single soliton, the curve has a needle-like appearance, starting at a descent point with a certain angle ρ and minimal pump rate. Above this threshold, a finite width of the regions is observed that expands with increasing pump rate.

The threshold point of Soliton 1 is at the highest pump rate and the largest angle ρ. With increasing pump rate, the region of existence is shifted towards smaller angles ρ. Soliton 2 has the lowest threshold of all solitons and a large threshold angle of $\rho = 20.5°$. The region of existence is the largest one and extends over the symmetry point $\rho = 0°$ within the considered range of pump rates. The threshold points of the larger solitons increase in power and decrease in the angle $|\rho|$. In contrast to the smaller solitons the regions expand towards larger angles $|\rho|$ with increasing input power.

The numerical simulations have shown that solitons can exist below and above the thresh-

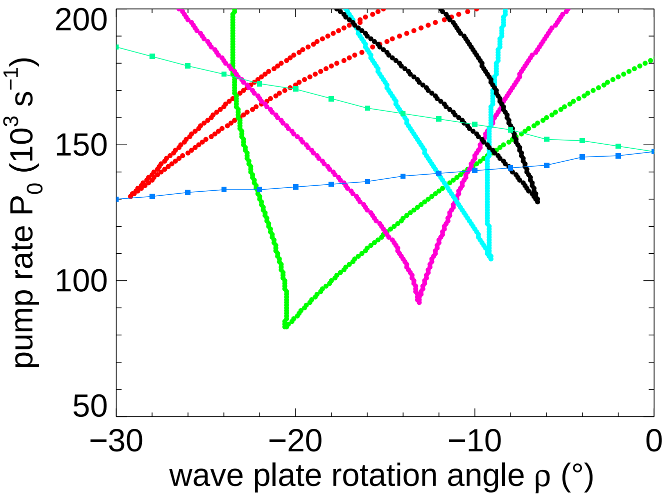

Figure 5.21: Regions of existence of solitons in a radially symmetric system. • S1, • S2, • S3, • S4, • S5. Threshold for pattern formation of the ▪ background and ▪ target state obtained from full numerical simulations. Parameters: see Fig. 5.1, $w_0 = 1.89\,\mathrm{mm}$.

old for pattern formation. In order to put the obtained existence regions of solitons in relation to that threshold, it has been computed in full numerical simulations. The threshold of the disfavored state with negative orientation is indicated by light green squares. The line between the data points has been added to guide the eye. It can be conjectured that a modulational instability of the state serving as the background of the solitons is not necessary for the existence of solitons. The threshold for pattern formation of the favored state with positive orientation that is serving as the target state of the solitons is indicated by blue squares. Higher order solitons can exist even below this threshold. However, the stability of the fundamental soliton seems to require a modulational instability of the target state, as the two thresholds coincide quite accurately.

The regions of existence have a large overlap at higher pump rates. Typically adjacent orders of solitons have the largest overlap, but multistability is also possible.

In the experiment, the regions of existence of the first three solitons have been measured (see Fig. 4.29). The numerical results match these experimental results qualitatively. Of course, in the experiment the threshold of the existence of a solitons cannot be determined as accurately, but the needle-type narrowing of the region of existence at that point can be anticipated.

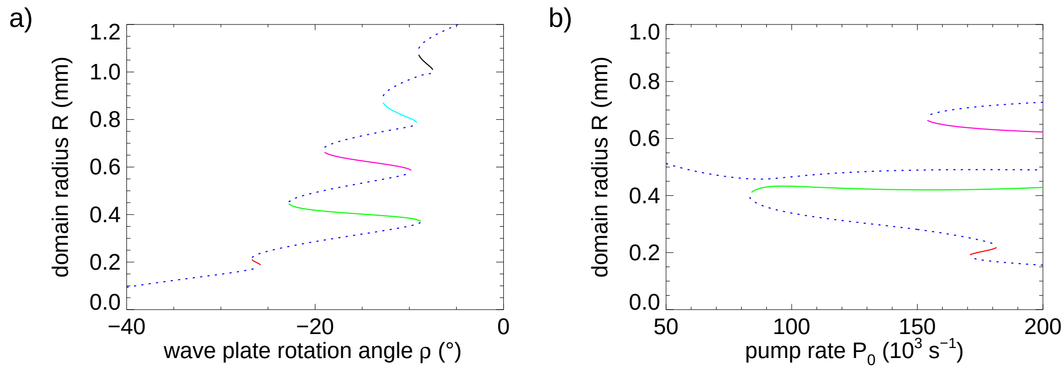

Figure 5.22: Bifurcation scenario under variation of a) ρ and b) P_0. – S1, – S2, – S3, – S4, – S5, - - unstable domain. Parameters: see Fig. 5.1, $w_0 = 1.89\,\mathrm{mm}$, a) $P_0 = 148000\,\mathrm{s}^{-1}$, b) $\rho = -20\,^\circ\,24\,'$.

5.4.4 Stable and unstable domains

In the preceding section, only stable soliton solutions have been considered. However, also the unstable stationary domain solutions can be determined by means of the Newton method. For low pump rates, these unstable domains have been characterized in section 5.3.3. For a given set of parameters, one stable domain solution is obtained.

If the pump rate is increased beyond the threshold for the existence of solitons, the variety of solutions increases. As an example, a pump rate of $P_0 = 148000\,\mathrm{s}^{-1}$ is considered. The radii of the stable and unstable domain solutions are plotted as a function of the wave plate rotation angle ρ in Fig. 5.22a. Stable solitons are indicated by a full colored line. For the given parameter range, five stable solitons are observed. They exist over a finite range of angles ρ, being multistable at certain angles. Over the range of stability they slightly change their size. However, the discrete steps between solitons of different order are maintained.

Unstable solutions are shown as a dashed blue line. Starting from very large angles $|\rho|$, the size of the unstable domain is small and increases with decreasing angle $|\rho|$. This has already been discussed in section 5.3.3. But at a certain point, the unstable solution is transformed into a stable solution, i.e. the fundamental soliton. A method for finding the stable branch is to take the unstable solution, add a small perturbation and use the perturbed solution as the initial condition for the algorithm. From this point, $|\rho|$ has to be increased to track down this stable solution. It reaches the border of the respective region of existence again, being connected to a new unstable solution. Again, the direction of motion has to be reversed to track down the unstable solution. This process is then repeated to find the other stable and unstable solutions. Obviously the stable solitons are interconnected by unstable branches, where the appearance of the soliton is transformed from one stable configuration to another one.

Of course, the unstable domains are not observed in the experiment. However, figure 5.22 nicely illustrates the observation that typically a soliton of adjacent order is observed if the border of the region of existence is passed. At that point, the system becomes unstable and is attracted by the nearest stable configuration, often being another soliton.

If the wave plate rotation angle ρ is kept constant and instead the pump rate P_0 is increased from a value where no stable soliton is present, the bifurcation structure appears to be quite different. As an example, an angle $\rho = 20.4°$ is considered in Fig. 5.22b. At low pump rates, the equilibrium between curvature-driven motion and expansion due to the inequality of the unstructured states emerging from the pitchfork bifurcation results in the existence of an unstable domain of a certain radius, cf. section 5.3.3. The radius of that domain decreases slowly with increasing pump rate, which can be interpreted as a result of the decrease of the coefficient γ_c with increasing pump rate (see section 5.3.2). At a certain point ($P_0 \approx 90000\,\mathrm{s}^{-1}$), the unstable domain increases again. At the same point, a saddle-node bifurcation is observed that leads to the appearance of a stable soliton (here a S2 soliton) and another unstable domain. This bifurcation can also be interpreted as a strongly disturbed pitchfork bifurcation, see below. If the pump rate is increased further, solitons of different orders appear by a cascade of saddle-node bifurcations. Here, the stable soliton branch S1 is connected to two unstable branches within the considered parameter range.

A full picture of the bifurcation structure leading to the appearance of stable solitons is obtained if the two-dimensional parameter space spanned by ρ and P_0 is analyzed with respect to stable and unstable domain solutions. The obtained domain solutions of such an analysis are then depicted in a three-dimensional diagram, the radius of the domain being the z axis value.

The result of this analysis is a surface built up by the stationary domain solutions of the system. An oblique view of this surface is shown in Fig. 5.23. Unstable domains are shown as blue dots in the diagram. Stable solitons are represented by red (S1), green (S2), magenta (S3), cyan (S4), and black (S5) dots.

At low pump rates, only unstable domains are observed. The lowest considered pump rate reproduces the result of Fig. 5.14, i.e. a curve monotonically increasing with increasing angle ρ. If the pump rate is increased, the curve becomes more and more modulated, which is interpreted to be due to an increasing amount of radial oscillations. At a certain set of parameters ρ and P_0, the tangent of this curve becomes vertical for the first time. This is the point where the soliton S2 is emerging. The surface becomes folded at that

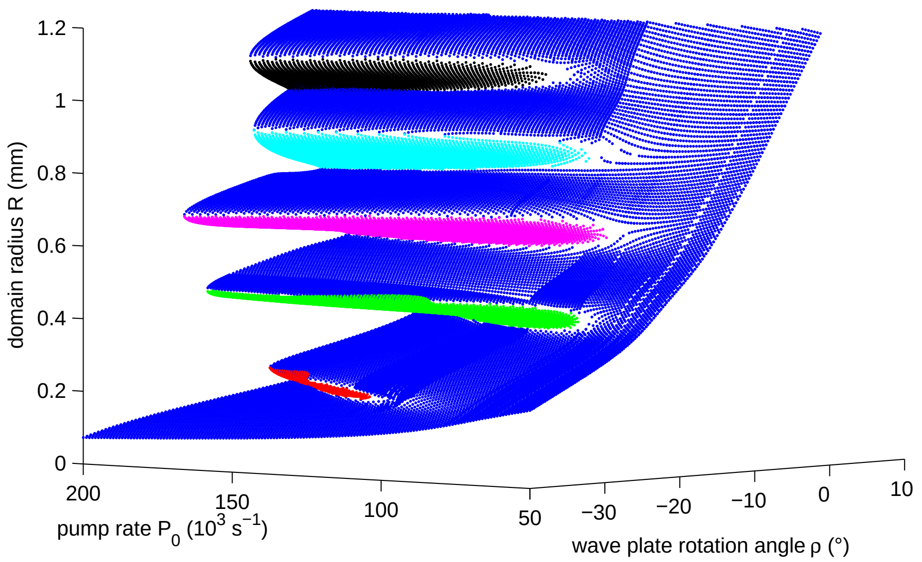

Figure 5.23: Oblique view of the bifurcation structure. • S1, • S2, • S3, • S4, • S5, • unstable domain. Parameters: see Fig. 5.1, $w_0 = 1.89\,\mathrm{mm}$.

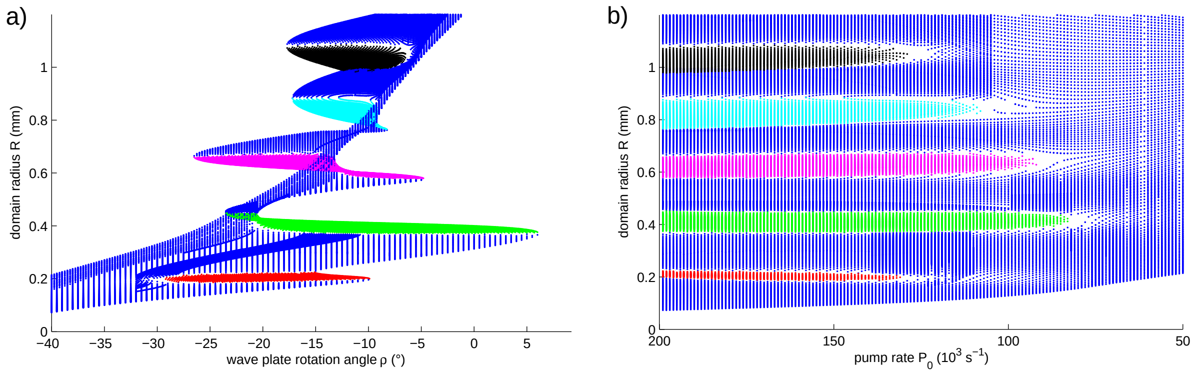

Figure 5.24: Front (a) and side (b) view of the bifurcation structure. • S1, • S2, • S3, • S4, • S5, • unstable domain. Parameters: see Fig. 5.1, $w_0 = 1.89\,\mathrm{mm}$.

point. If the angle ρ is fixed at that point and the pump rate is increased, the unstable domain passes through a bifurcation where two unstable branches and a stable branch, i.e. the stable soliton, emerge from the unstable branch in a pitchfork-type way. If the angle ρ is not exactly adjusted, the stable soliton and the other unstable domain appear in a disturbed pitchfork-type bifurcation cf. Fig. 5.22b. Such a bifurcation is described as a codimension 2 bifurcation and has been discussed widely in terms of the cusp catastrophe. It explains the needle-type appearance of the regions of existence around that bifurcation point discussed in Fig. 5.21. At different combinations of the parameters ρ and P_0 the same type of bifurcation is observed that leads to the appearance of solitons of different orders. Stable solitons are represented by surfaces whose normal vector is facing downwards, while unstable domains have a normal vector pointing upwards.

Two other views, each omitting one of the two parameters, illustrate the features of the bifurcation structure. If P_0 is omitted, a front view on the surface is generated (Fig. 5.24a). It shows a generalization of Fig. 5.22a. Wide oscillations of the stationary solutions around the hyperbolic shape of the solutions obtained at low pump rates are observed, leading to large regions of existence and multistability of solitons of different orders.

The radii of the solitons in increasing order are multiples of around 0.2 mm. This corresponds to the half length scale of the modulational instability ($\lambda_c = 0.40\,\text{mm}$). However, the size of the solitons is not fixed to a certain value, but there is a finite range of sizes for each soliton. The size of the solitons is influenced by the angle ρ. The locking of radial oscillations seems to provide an efficient stabilization of the domain, even if the counteracting effects of curvature-driven contraction and motion due to the inequality of the homogeneous solutions are not completely balanced.

However, the finite ranges of soliton radii do not have an overlap, which can be seen from Fig. 5.24b. The discreteness of the steps determining the size of the solitons is still maintained. Obviously the size of the solitons does not significantly depend on the pump rate.

5.4.5 Modified model for front dynamics

Up to now a model for the dynamics of circular domains has been considered that does not take into account spatial oscillations. It has been proven to be valid for low input powers. This model, however, does not allow for stable domain solutions for the situation present here. At high input powers, the dynamics has been shown to be modified by a locking mechanism that has been attributed to the appearance of spatial oscillations.

Stable soliton solutions can also be obtained in the model, if the impact of radial oscillations around the domain boundary is included. Such an oscillatory term has been discussed in the literature [CER87, BSC88, BP95, CEK05, BCF$^+$06] and will be included

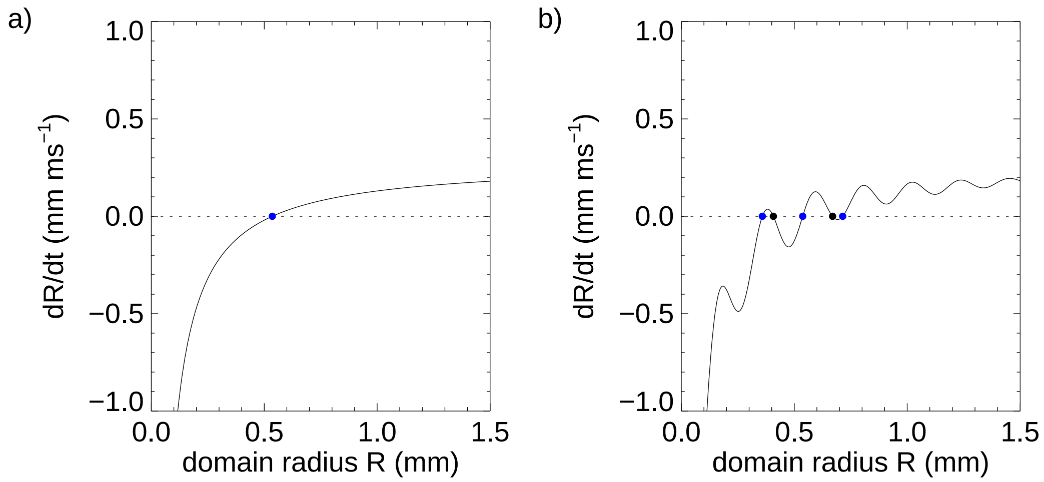

Figure 5.25: Domain dynamics without (a) and with (b) oscillatory term. • stable fixed points, • unstable fixed points. Parameters: $\gamma_c = 0.15\,\mathrm{mm}^2\mathrm{ms}^{-1}$, $\gamma_i' = 0.02\,\frac{\mathrm{mm}}{\mathrm{ms}^{-1}\,{}^\circ}$, $P_{crit} = 120000\,\mathrm{s}^{-1}$, $\lambda = 0.43\,\mathrm{mm}$, $c_2 = 2\,\mathrm{mm}^{-1}$, $P_0 = 190000\,\mathrm{s}^{-1}$, $\rho = 14\,^\circ$, a) $c_1 = 0$, b) $c_1 = 0.15$.

here in a quite simple way:

$$\frac{dR}{dt} = -\frac{\gamma_c}{R} + \gamma_i'\,\rho - c_1\left(\frac{2P_0}{P_{crit}} - 1\right)\sin\left(\frac{4\pi}{\lambda}R\right)e^{-c_2 R} \tag{5.24}$$

It describes an oscillation with a spatial period of $\lambda/2$, where λ is the spatial period of the modulational instability. It has been shown in section 4.4.3 and in the previous subsection that stable soliton radii are approximately given as discrete multiples of $\lambda/2$. The amplitude of the oscillation is modelled to increase linearly with increasing pump rate starting at $P_{crit}/2$, where P_{crit} is the threshold pump rate of the modulational instability. For pump rates lower than $P_{crit}/2$ spatial oscillations are assumed to vanish. Furthermore the spatial oscillations are assumed to decay exponentially with increasing domain radius R in order to model the vanishing interaction of the domain boundaries at large distances. All coefficients and parameters apart from P_0 and ρ are assumed to be constant, which is a very rough approximation. Nevertheless this model is sufficient to reproduce the main characteristics of the bifurcation structure discussed in the previous section. The influence of the oscillatory term is depicted in Fig. 5.25. Without spatial oscillations (Fig. 5.25a), one stationary solution is obtained for $\rho < 0°$. However, it is not stable, since the smallest fluctuations will lead to an expansion or contraction of the domain. If spatial oscillations are introduced, more than one stationary solution can be obtained (Fig. 5.25b). Some of them are still unstable (indicated by blue dots), but stable solutions are also observed

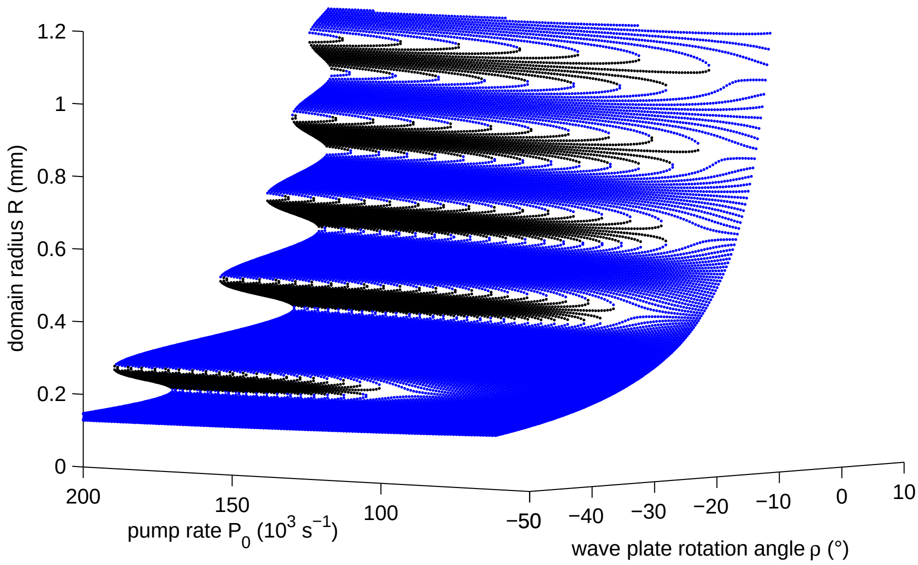

Figure 5.26: Oblique view of the bifurcation structure. • stable fixed points, • unstable fixed points. Parameters: $\gamma_c = 0.15\,\mathrm{mm^2ms^{-1}}$, $\gamma_i' = 0.02\,\frac{\mathrm{mm}}{\mathrm{ms^{-1}\,{}^\circ}}$, $c_1 = 0.15$, $P_{crit} = 120000\,\mathrm{s^{-1}}$, $\lambda = 0.43\,\mathrm{mm}$, $c_2 = 2\,\mathrm{mm^{-1}}$.

(black dots). The latter are characterized by a negative slope of the curve, which makes them an attractor. Those stable domain solutions are interpreted as solitons.

Figure 5.26 shows a three-dimensional plot, where stable and unstable stationary solutions of the dynamics described by equation 5.24 are plotted for parameters similar to those obtained from the numerical simulations. The resulting surface depicts five areas where stable soliton solutions are found. Similar to Fig. 5.23, these stable solutions emerge from a certain point, where the surface becomes folded. Despite of the simplicity of the given model, it can qualitatively reproduce the bifurcation structure obtained from applying the Newton method. The exact shape of the surface is, of course, dependent on all parameters that are assumed to be constant here.

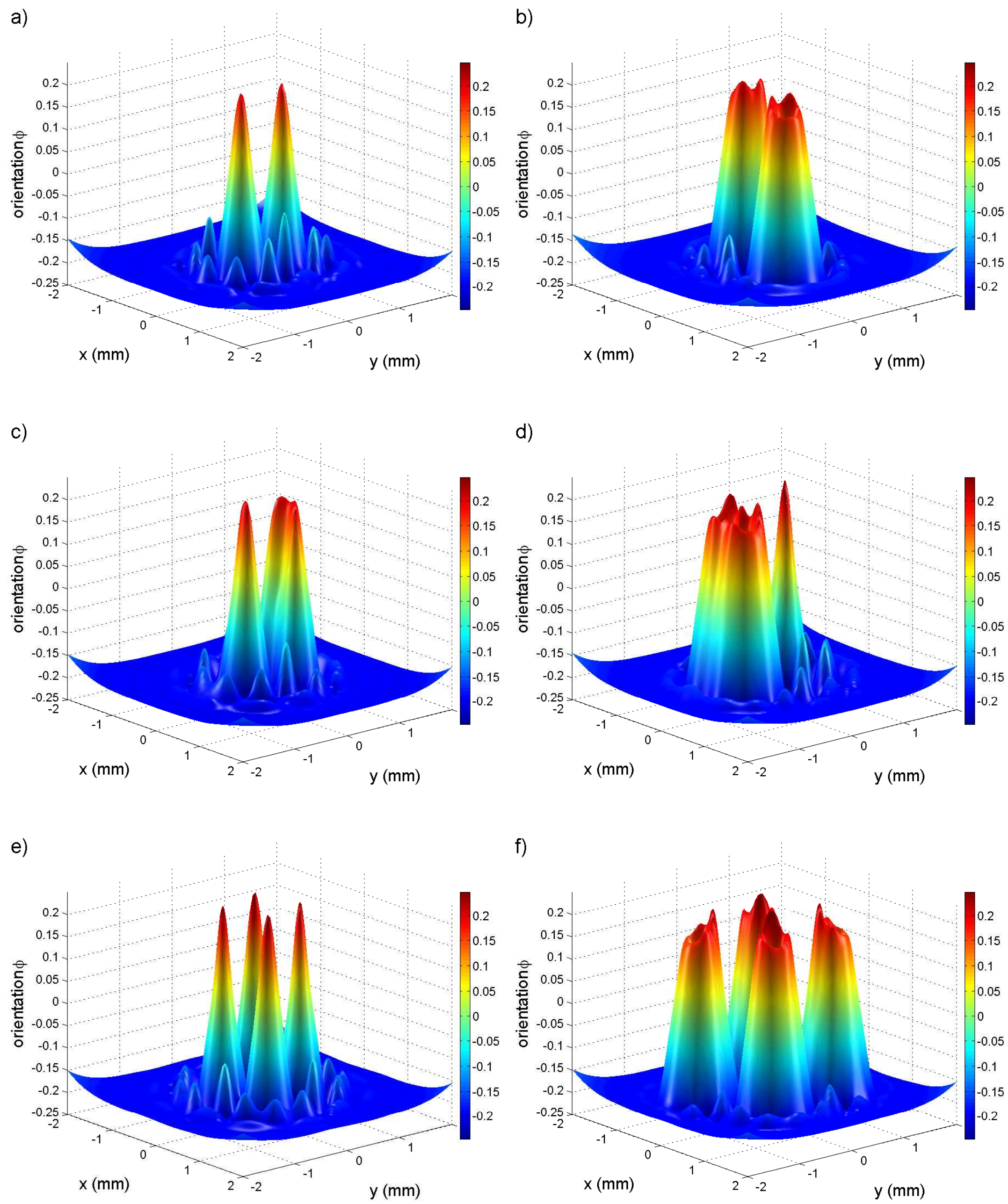

Figure 5.27: Basic configurations of clusters of solitons and bound states. a) 2 S1 solitons, b) 2 S2 solitons, c) S1 soliton and S1 bound state, d) S1 soliton and S2 bound state, e) 4 S1 solitons, f) 4 S2 solitons. Parameters: see Fig. 5.1, $w_0 = 1.89\,\mathrm{mm}$; a) $\rho = -14^\circ\,30'$, $P_0 = 240000\,\mathrm{s}^{-1}$; b) $\rho = -12^\circ\,0'$, $P_0 = 190000\,\mathrm{s}^{-1}$; c) $\rho = -16^\circ\,30'$, $P_0 = 240000\,\mathrm{s}^{-1}$; d) $\rho = -13^\circ\,30'$, $P_0 = 240000\,\mathrm{s}^{-1}$; e) $\rho = -14^\circ\,30'$, $P_0 = 280000\,\mathrm{s}^{-1}$; f) $\rho = -14^\circ\,0'$, $P_0 = 260000\,\mathrm{s}^{-1}$.

5.5 Interaction of solitons and complex structures

5.5.1 Interaction of solitons

Basic configurations

In numerical simulations, many configurations of soliton clusters and bound states are obtained. Some of the basic configurations are shown in Fig. 5.27. The first row shows clusters of two solitons of order one (a) and two (b). The orientation distributions match nicely the measurements of the Stokes parameters in the experiment (compare to Figs. 4.33 a,b). The soliton clusters are surrounded by small peaks that are interpreted to be the remains of the hexagonal pattern that exists as the background state for the given parameters. The patterned area is limited by the Gaussian beam input. While the shape of S1 is essentially maintained, S2 experiences a modulation that slightly breaks the circular symmetry. It is interpreted to be due to the interaction of the solitons and possibly to a small interaction of the solitons with the underlying pattern.
Tightly bound states of solitons are also observed in the simulations. A bound state of two S1 solitons interacting with another S1 soliton is shown in Fig. 4.33c. This bound state matches the experimental observation. However, it has not been observed stable as a single structure in the simulations, though it is observed frequently in the experiment. This might be related to the choice of the numerical parameters as well as to small inhomogeneities in the experiment that favor the stability of bound states. In contrast, bound states of solitons of higher order can be easily obtained. Figure 4.33d shows a bound state of two S2 solitons in a cluster with a S1 soliton.
As in the experiment, the maximum number of coexisting solitons is limited due to the Gaussian pump profile. For the parameters considered here, a maximum of four solitons is observed. Figures 4.33e,f show configurations of four S1 and four S2 solitons. While the S1 solitons are arranged in a square configuration, the S2 cluster has a diamond shape.

Analysis of two-soliton clusters

In order to obtain a systematic analysis of the interaction of solitons, two solitons are considered in the following. A plane wave input is used, and the parameters are chosen in a way that the state serving as the background is homogeneous.
As the initial condition, two solitons are positioned at a certain (center-to-center) distance. When the simulation is started, the two solitons generally start to move. After a certain time the soliton cluster typically reaches a stable configuration with a different soliton distance.
Clusters consisting of two S2, S3 and S4 solitons as well as clusters of one S2 and one

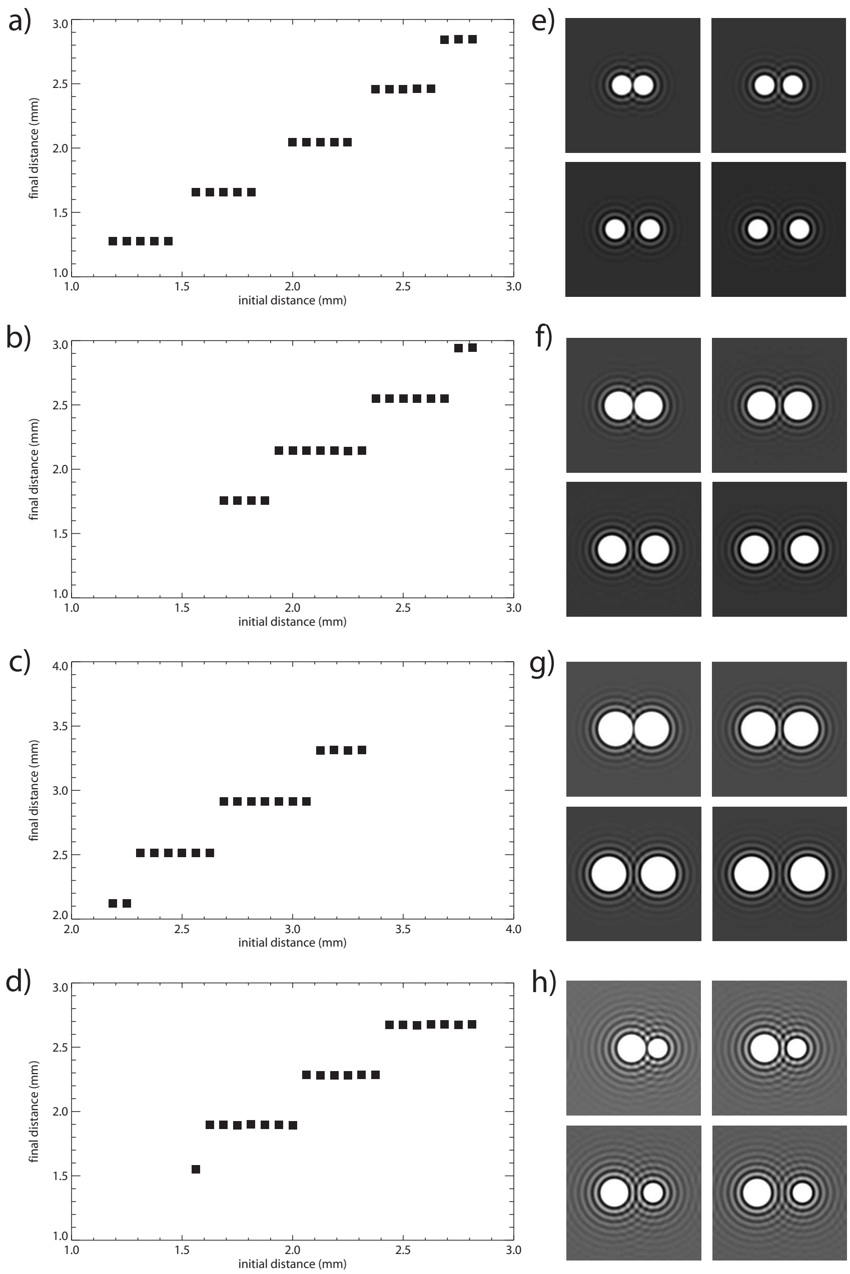

Figure 5.28: a)-d) Stable distances between two solitons as a function of the initial distance. a) S2 clusters; b) S3 clusters; c) S4 clusters; d) S2 + S3 clusters. e)-h) Stable soliton clusters with different distances. e) S2 clusters; f) S3 clusters; g) S4 clusters; h) S2 + S3 clusters. Images are linearly scaled in order to highlight the oscillatory tails, solitons are clipped.Parameters: see Fig. 5.1; a),e) $\rho = -19\,^\circ\,0\,'$, $P_0 = 90000\,\mathrm{s}^{-1}$; b),f) $\rho = -14\,^\circ\,0\,'$, $P_0 = 90000\,\mathrm{s}^{-1}$; c),g) $\rho = -10\,^\circ\,36\,'$, $P_0 = 90000\,\mathrm{s}^{-1}$; d),h) $\rho = -12\,^\circ\,0\,'$, $P_0 = 115000\,\mathrm{s}^{-1}$.

S3 soliton have been considered. The stable distances of the solitons in dependency on their initial distances are shown in Fig. 5.28a-d. The interaction of the solitons leads to the observation of several discrete distances. Within the considered range of initial distances, five stable configurations of S2 soliton clusters are observed (Fig. 5.28a). Four stable configurations are found for S3 (b), S4 (c) and S2+S3 (d) clusters. The cluster with the smallest distance of the S2+S3 configuration is stable as a cluster but it moves with a constant velocity $v \approx 5\,\mathrm{mm\,s^{-1}}$. This is interpreted to be due to the asymmetry of the cluster and was predicted by Rosanov [RK90, Ros02]. The cluster corresponding to the next stable distance has a velocity below $v \approx 0.5\,\mathrm{mm\,s^{-1}}$, and the motion of clusters with larger distances cannot be resolved within the numerical resolution.
The absolute distance between the solitons within the stable clusters is dependent on the order of the considered solitons. However, the step between the discrete distances of the solitons is of the same order of magnitude for all cluster types. The step sizes Δx_i that lead from one to the next stable configuration are compiled in table 5.1.

Table 5.1: Distances between different solitons Δx_i

Configuration	Δx_1 [mm]	Δx_2 [mm]	Δx_3 [mm]	Δx_4 [mm]	average Δx [mm]
S2 + S2	0.381	0.387	0.414	0.387	0.392
S3 + S3	0.387	0.405	0.395	–	0.395
S4 + S4	0.392	0.400	0.398	–	0.397
S2 + S3	0.345	0.387	0.391	–	0.374

The steps slightly vary around an average value of $\Delta_x \approx 0.39\,\mathrm{mm}$. This is very close to the wavelength of the modulational instability appearing at slightly higher input powers ($\lambda = 0.40\,\mathrm{mm}$). It has been widely discussed in the literature that the interaction of solitons is often mediated by the oscillatory tails of the single solitons which is leading to a locking process and to the appearance of discrete distances. This mechanism seems to apply here as well. The oscillatory tails have a spatial period that is connected to the modulational instability. Though no interaction potential of the solitons can be derived here, it is evident that in an one-dimensional picture the interaction of two solitons exhibiting spatial oscillations with a certain spatial period will lead to a discrete set of stable configurations that is characterized by a similar spatial period. Obviously this mechanism is not qualitatively different if two spatial dimensions are considered. Figure 5.28e-h shows images of the stable cluster configurations, where the intensity levels have been scaled in order to display the small range of orientation that includes the oscillatory tails. Obviously the system establishes soliton distances that are nearly characterized by a maximum-on-maximum configuration of the oscillatory tails on the connecting line between the solitons. The two-dimensional interaction apparently modifies this simple picture. The oscillation circles are flattened between the solitons, leading to slightly smaller soliton distances than expected from the simple one-dimensional model.

5.5.2 Soliton patterns

In many systems, solitons are observed in a situation where a subcritical bifurcation leading from a homogeneous to a patterned state takes place (see section 2.2.1). Within the subcritical range, solitons are interpreted as an independent single constituents of the pattern on a homogeneous background. If several solitons are considered, they typically arrange to form a cutout of the extended pattern.

This mechanism obviously does not apply for the system considered here. The solitons can not be interpreted as a constituent of a spontaneously appearing pattern. However, solitons can be arranged to form a different type of extended patterns here. In the previous section the interaction of two solitons has been considered, which lead to the observation of several discrete distances. If many solitons are arranged on a hexagonal grid with a next-neighbor distance given by one of these discrete distances, these solitons can form a stable pattern. Hexagonal patterns consisting of S2 solitons with a next-neighbor distance corresponding to the first three stable distances (cf. table 5.1) are shown in Figs. 5.29a-c. The size of the numerical grid has been adjusted in each simulation to match the periodic boundary conditions. These patterns obviously connect the two homogeneous states emerging from the pitchfork bifurcation. Though both branches are stable with respect to the modulational instability discussed previously, a large-amplitude pattern connecting the two states seems to be a stable configuration. The patterns inherently possess two spatial frequencies, one being the distance between the solitons and the other being the oscillation frequency within the single soliton. From this point of view they can be interpreted as superlattices [Dah87, DSS97].

Structures that have a large amplitude and exhibit more than one spatial frequency are generally not accessible via the standard linear stability analysis. In the experiment they are not observed spontaneously. However, with a larger aspect ratio they could be constructed from single solitons. Though patterns are generally not decomposable into their single constituents, the presented patterns are. This is illustrated by the fact that single constituents of the pattern can be left out (Fig. 5.29d).

Such patterns can also be constructed from solitons of order 3 (e) and 4 (f). Of course the distance between the constituents have to be adjusted to match the stable distances obtained in the preceding section. Even other configurations like square patterns are

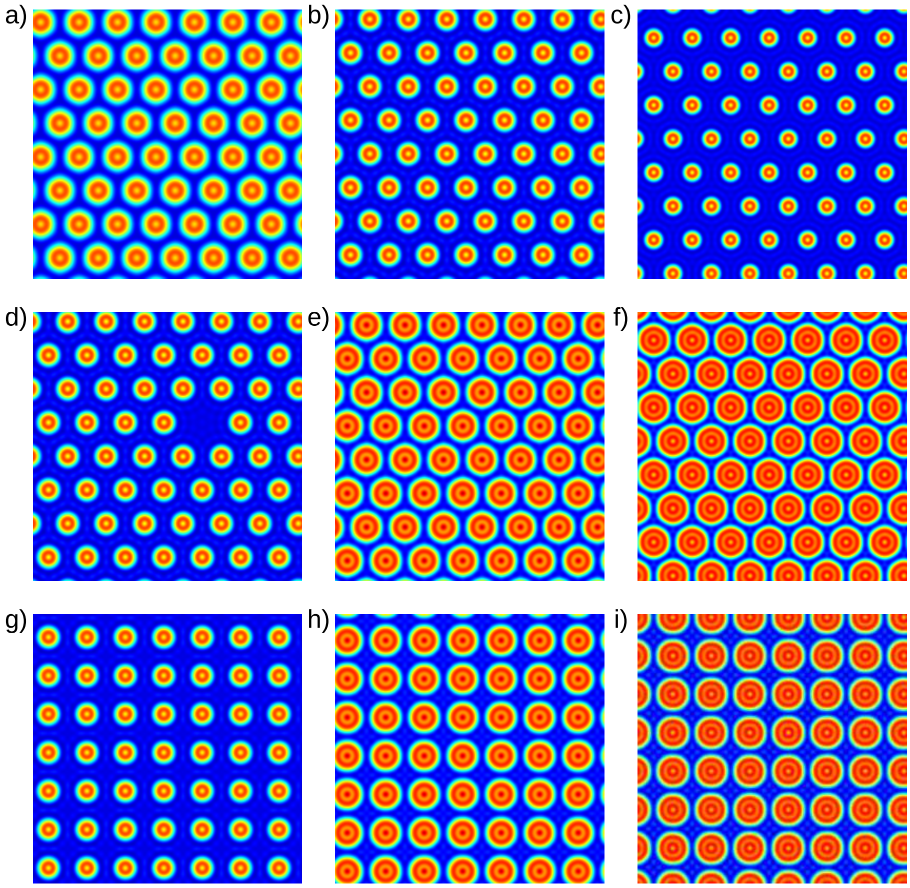

Figure 5.29: Patterns generated from single solitons of different order. a)-c) S2 hexagons with different next-neighbor distances; d) S2 hexagon with void; e) S3 hexagon; f) S4 hexagon; g) S2 square; h) S3 square; i) S4 square. Parameters: see Fig. 5.1, $P_0 = 90000\,\mathrm{s}^{-1}$; a)-d),g) $\rho = -19^\circ\,0'$; e),h) $\rho = -14^\circ\,0'$; f),i) $\rho = -10^\circ\,36'$. Color table: see Fig. 5.30.

stable (Figs. g-i).

Due to the limited aspect ratio in the Gaussian beam, extended soliton patterns cannot be observed in the experiment. Nevertheless, the soliton clusters presented in Fig. 4.34 can of course be interpreted as cutouts from soliton patterns.

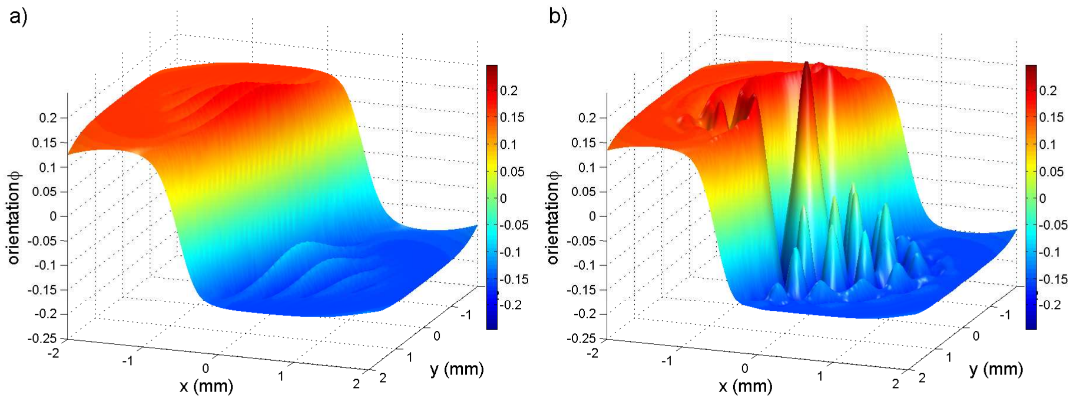

Figure 5.30: Interaction of a soliton with a straight front. a) Stable straight front; b) stable configuration of a front and a S1 soliton. Parameters: $d = 112\,\text{mm}$, $\bar{\Delta} = 10.8$, $D = 268\,\text{mm s}^{-1}$, $\gamma = 1.5\,\text{s}^{-1}$, $\Gamma_2 = 9.72 \cdot 10^9\,\text{rad s}^{-1}$, $L = 0.015\,\text{m}$, $R = 0.995$, $N = 7.21 \cdot 10^{19}\,\text{m}^{-3}$, $\rho = 0\,°$, $w_0 = 1.89\,\text{mm}$, a) $P_0 = 80000\,\text{s}^{-1}$, b) $P_0 = 120000\,\text{s}^{-1}$.

5.5.3 Solitons and fronts

In the experiment, a stable configuration of a soliton interacting with a polarization front is observed. This situation can be easily reproduced by calculating the corresponding orientation distribution from the measurement of the polarization rotation angle for a certain set of parameters. The calculated orientation distribution is then used as an initial condition for the numerical simulations and converges to a stable configuration shown in Fig.5.30. This configuration agrees very well with the experimental one, thereby confirming the interpretation of the polarization rotation angle as a measure for the orientation.

5.5.4 New type of solitary structures

If the experiment is performed at very high input powers, a new type of solitary structure is observed (see section 4.6.2). This ring-shaped soliton can be reproduced in numerical simulations (see Fig.5.31a). But also other stable configurations are found that do not have a disc shape but incorporate more than two domain walls in a cut through the center. Figure 5.31b shows a wider stable localized structure that exhibits one more oscillation around the background state in its central part. It could be interpreted as the second member of a soliton family. At different parameters, the central oscillation even leads back to the target state and beyond (see Fig. 5.31c), leading to an even more complex

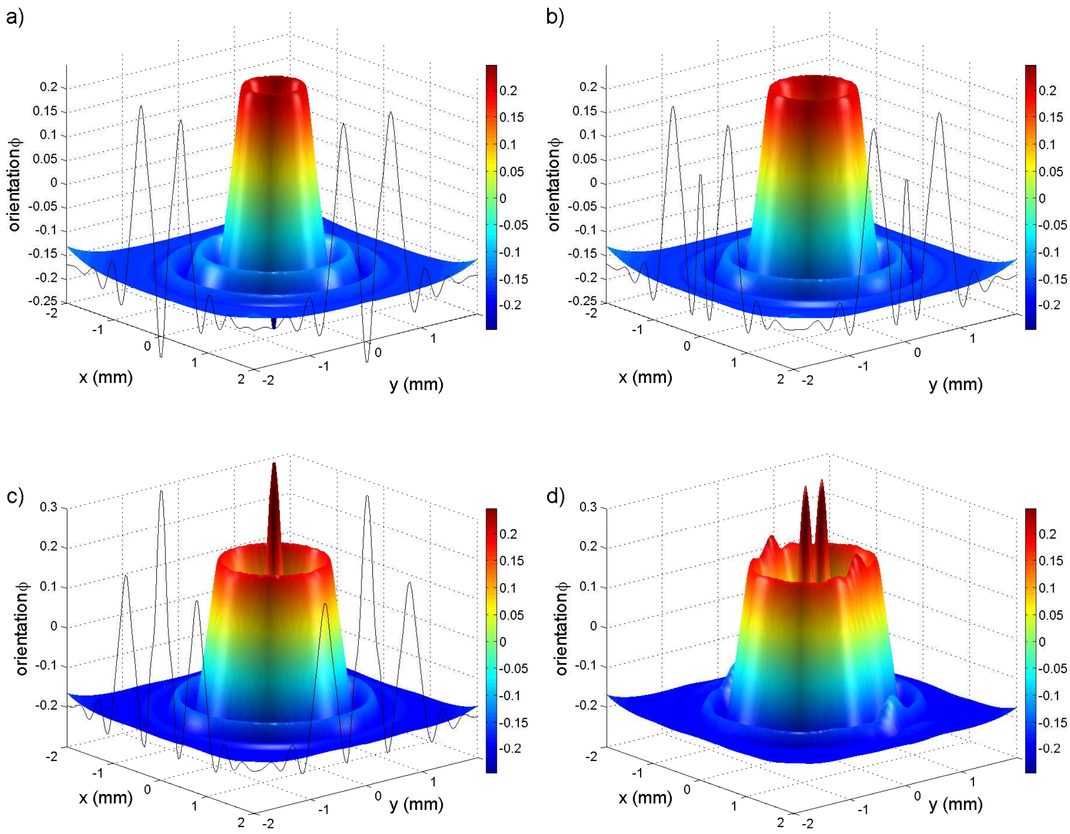

Figure 5.31: New types of solitary structures. Parameters: $w_0 = 1.89\,\mathrm{mm}$, a),b) see Fig. 5.1, $P_0 = 230000\,\mathrm{s}^{-1}$, $\rho = 0^\circ\,0'$; c),d) see Fig. 5.30, except c) $P_0 = 150000\,\mathrm{s}^{-1}$, $\rho = -19^\circ\,30'$, d) $P_0 = 160000\,\mathrm{s}^{-1}$, $\rho = -21^\circ\,30'$.

appearance. This configuration consists of six domain walls in the cut through the center. These solitary structures can even be observed in a stable bound state consisting of two sstructures sharing the outer ring (Fig. 5.31d).

Apparently there are many stable structures that can be described in the framework of localized structures. From the given examples, it can be conjectured that more discrete families of solitons exist. Since they cannot be observed in the present experiment due to the limited aspect ratio and input power, an in-depth study of the properties of these localized states is beyond the scope of this work. However, the (presumably more complex) bifurcation behavior of these structures, their systematic classification and interaction as well as the question of the generalizability to a plane wave input could be interesting tasks in future work.

5.5.5 Localized patterns

If the pump rate is increased far beyond the threshold for pattern formation, the amplitude of the patterns grows and becomes of the order of magnitude of the solitons, though still being smaller. If in such a situation a higher-order soliton is present, the soliton loses its (nearly) circular symmetry and complies with the hexagonal symmetry of the patterns existing as the background and target state. The result is a localized pattern existing on the background of the other pattern with inverse orientation.

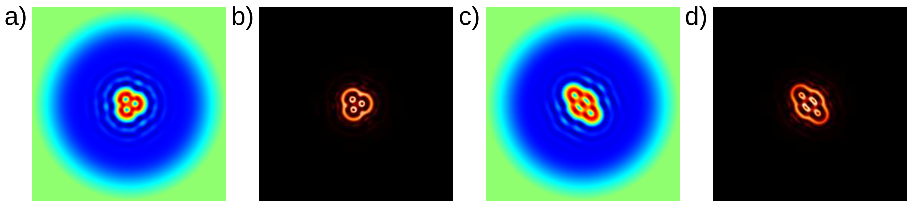

Figure 5.32: Localized patterns in a Gaussian beam. a),b) triangular localized pattern; c),d) diamond-shaped localized pattern. a),c) orientation distributions; b),d) transmitted light field projected on to a linear polarization state with suppressed background. Parameters: see Fig. 5.1, $w_0 = 1.89\,\mathrm{mm}$, $P_0 = 280000\,\mathrm{s}^{-1}$; a),b) $\rho = -14^\circ\,30'$; c),d) $\rho = -16^\circ\,30'$. a),c) Color table: see Fig. 5.31.

Typical localized patterns that result from the instability of (nearly) circular solitons are shown in Fig. 5.32. In the orientation distribution (a,c), they consist of three or four (distorted) elementary cells of the pattern arranged in a triangular and diamond configuration. The corresponding intensity distributions of the transmitted light field with suppressed background (subfigs. b,d) reproduce the experimental findings (compare to Fig. 4.43b,c).

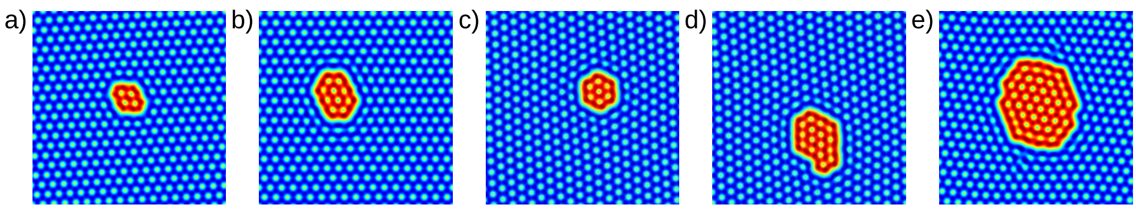

Figure 5.33: Orientation distributions of localized patterns in plane wave simulations. Parameters: see Fig. 5.1, $P_0 = 200000\,\mathrm{s}^{-1}$, $\rho = 0^\circ$. Color table: see Fig. 5.31.

The size of such a localized pattern is of course limited in a Gaussian beam. Larger

localized patterns can be observed, if a plane wave input is considered and the simulation is started with a circular domain as the initial condition. At the beginning of each simulation, strong noise is added to the system which is then reduced to zero. The domain will first start to contract. However, then the interaction with the patterns existing on both branches of the pitchfork bifurcation takes place. As a result, different configurations of localized patterns are found (see Fig. 5.33). These structures are stable for the given parameters, i.e. the motion of the fronts connecting the different patterned branches is completely stopped by the modulations within the patterns.
However, recent experimental and numerical results show that front motion can set in again if even higher pump rates are considered. In this case, the coefficient γ_c changes its sign, which results in an expansion of domains and leads to the formation of labyrinthine patterns, which will be the issue of future investigations [Sch06].

Chapter 6

Discussion of the results

6.1 Basic properties of the system

The observation of a symmetry-breaking pitchfork bifurcation is at the basis of this work. This polarization instability has been observed by Yabuzaki et al. [YOKO84], neglecting the transverse spatial degrees of freedom, and by Große Westhoff et al. [GWKL+00] in an experiment that takes those degrees of freedom into account. At the bifurcation point, the linear input polarization becomes unstable. As a result, two elliptically polarized spatially homogeneous states evolve, whose main axis of polarization is rotated into opposite directions with respect to the input polarization. Correspondingly, the orientation of the vapor, that is zero below the bifurcation point, reaches a nonzero value with positive and negative sign for the two stable bifurcation branches.

A broken symmetry can be introduced by rotating the slow axis of the wave plate with respect to the input polarization. As a result, a perturbed pitchfork bifurcation is observed. The degree of asymmetry is determined by the rotation angle of the wave plate. If the rotation angle is taken as the control parameter for an input power above the bifurcation threshold, an s-shaped bifurcation is observed as theoretically predicted in [YOKO84]. In the two dimensional parameter plane spanned by the input power and the wave plate rotation angle, the whole bifurcation scenario can be interpreted in terms of a cusp catastrophe [YOKO84]. For the considered parameters, a large region within this two-dimensional parameter space is characterized by optical bistability.

At input powers that are at least two orders of magnitude larger than the threshold power of the pitchfork bifurcation, a modulational instability is observed on both branches of the pitchfork bifurcation. Since the emergence of patterns is always connected with a change of the polarization of the light field, these instabilities are interpreted as polarization instabilities. The hexagonal, rhombic and triangular patterns that were reported in [GWKL+00] are reproduced with a larger aspect ratio, which is due to an increased beam diameter. Within the region where optical bistability is present, hexagonal patterns are observed. The modulational instability is slightly subcritical. However, the range of bistability between the homogeneous state and the pattern is not resolvable within the experimental resolution. Therefor, it can be neglected in the further discussion. The threshold for pattern formation depends on the rotation angle of the wave plate, i.e. the degree of imperfection of the pitchfork bifurcation. If the homogeneous state under consideration is favored by the imperfection, the threshold is low, and it increases with decreasing preference.

Comparison to other experimental systems

The results of Yabuzaki and Große Westhoff are well reproduced in the present experiment. The aspects of the bifurcation scenario that were of special interest in the scope of this work have been analyzed in more detail. Compared to the previous works, the symmetry of the system has been improved further in the present work.
Only one other optical experiment with the aim of observing transverse structures in a system that exhibits a symmetry-breaking pitchfork bifurcation is reported in the literature. It is a degenerate four-wave mixing experiment using a photorefractive crystal as the nonlinear medium [TSW98, LPEM+04, EMTG+05]. The two states that emerge from the pitchfork bifurcation are shifted by π in the phase of the subharmonic field. From an experimental point of view, this complicates the discrimination of the two states, since interferometric techniques need to be applied. In the experiment considered in this work, the two states can easily be discriminated by the use of a linear polarizer. The possibility of preparing a disturbed bifurcation as well as the symmetry properties of the bifurcation in general have not been discussed in the literature. It turns out that these aspects play a major role in the work presented here.

6.2 Front dynamics

Within the region of optical bistability, fronts that connect the two states emerging from the pitchfork bifurcation are observed. These fronts are heteroclinic connections and are classified as Ising fronts [MPL+01]. In the experiment, a stable front is occasionally created in the situation of a perfect pitchfork bifurcation, if the input power is switched from a level below the threshold of the pitchfork bifurcation to a level where the modulational instability is present [GWKL+00]. In numerical simulations assuming a plane wave input, the straight front is always stable in the case of a perfect pitchfork bifurcation. Hence, the instability of the front that is observed in the experiment below the threshold for pattern formation is attributed to the finite size of the experimental system.

Circular domains of one homogeneous state emerging from the pitchfork bifurcation embedded into the other one can be prepared using a circularly polarized addressing beam. The dynamics of these circular domains has been studied using a video sampling technique in a power region far from the modulational instability. For the case of two equivalent homogeneous states, the domains contract and disappear. The motion of the front was identified to be curvature-driven. A power law for the temporal evolution of circular domains is obtained that is valid over a wide range of input powers.

The dynamics of domains is modified if an asymmetry of the pitchfork bifurcation is introduced by a rotation of the retardation plate in the feedback loop of the system. The contraction is accelerated if the domain state is disfavored. The dynamics is slowed down, however, if the domain is the favored state. The curvature-driven contraction can even be overcompensated by the expansive motion that is introduced by the imbalance of the two homogeneous states. In this situation, the domain expands and switches the whole area to the domain state. A stationary domain, where the two effects exactly compensate is not observed in the experiment. Using numerical methods, it is shown to be stationary, but unstable. For small imperfections, the curvature-independent part of the front velocity is found to depend linearly on the wave plate rotation angle. This is confirmed by numerical simulations of the motion of straight fronts with a plane wave input.

If the input power is increased, the domain dynamics is to an increasing degree modified by a locking phenomenon. While the curvature-driven motion becomes less pronounced with increasing input power, spatial oscillations that surround the domain boundaries occur. These spatial oscillations have a defined wave number that can be associated with the one of the modulational instability that is observed at higher input powers. The interaction of these weakly damped spatial oscillations leads to a further slow-down of the domain dynamics at certain domain radii. These radii are similar to the ones of stable solitons that appear at higher input powers. Locking becomes very pronounced in the presence of a modulational instability.

Comparison to theoretical predictions and to other experiments

Theoretical predictions for systems with pitchfork bifurcation

Domain dynamics in a situation with two equivalent homogeneous states has been studied extensively in theoretical models of nonlinear optical systems. These numerical studies indicate the occurrence of curvature-driven motion (e.g. [OSF99, GMT00, GCOM01]). Analytic results show that the growth law describing curvature-driven dynamics is given

by a $t^{\frac{1}{2}}$ scaling [GCOM01].
In different systems, a qualitative change in the behavior of the system is observed when a control parameter is varied. This change is related to a change of sign of the coefficient describing the curvature driven motion [GMT00, GCOM01]. For large positive coefficients, domain coarsening is observed, which describes the contraction of circular domains and shortening of fronts. Near the zero, the dynamics becomes slow, and dark-ring cavity solitons in coexistence with domain walls are observed. If the coefficient becomes negative, a flat front is modulationally unstable and domains expand until the whole area is filled with a labyrinthine pattern [GMT00, GAGW+03].
The predicted $t^{\frac{1}{2}}$ growth law is confirmed by the present experiments and is observed over a wide parameter range. For low input powers, the coefficient describing the strength of the curvature-driven motion is large. Hence, domains contract and disappear. With increasing input power, the dynamics slows down and together with an increased amount of spatial oscillations, this results in the observation of solitons. A change of sign of the coefficient at even higher input powers was not observed, since the front dynamics is then dominated by locking due to the modulational instability. However, labyrinthine patterns have been observed in a very similar experiment and are under current investigation [Sch06].
In [GCOSM04], the analytical results considering domain dynamics are extended to situations where the symmetry of the pitchfork bifurcation is slightly perturbed. The analysis predicts an additional component in the velocity of the front that is curvature independent and that depends on the asymmetry parameter. This characteristic is confirmed by the experimental and numerical results. The obtained results also indicate a dependence of the curvature-driven dynamics on the asymmetry parameter that is not predicted by the analytical results. The instability of the stationary domain, which is observed in an asymmetric situation before robust locking due to the appearance of pronounced spatial oscillations occurs, is in agreement with the theoretical expectations [GCOSM04, Cou02].

Experiments in a quasi one-dimensional setup

In previous experiments, the quantitative study of front motion in nonlinear optics has been restricted to quasi one-dimensional systems where curvature effects are suppressed by the design of the experiment. Detailed experiments have been conducted for the situation where an Ising-Bloch transition is observed [EMTRV05, EMTG+05]. Such a bifurcation cannot occur in the present experiment, since the state variable is one-dimensional. In principle, the introduction of a transverse magnetic field could enable an Ising-Bloch transition, since in such a situation the state variable becomes three-dimensional. However, preliminary theoretical studies have almost ruled out the occurrence of an Ising-Bloch

transition for experimentally feasible parameters [Bab05].
In a system where the two states connected by the front are not equivalent [CNP+04], the velocity of quasi one-dimensional fronts has been determined, and the existence of a Maxwell point was clearly demonstrated despite the fact that front motion is modified due to inhomogeneities of the LCLV. At higher input powers a so-called Freedericksz transition is observed, leading to a front motion where the front velocity in a transient stage is not given by the energy difference of the two states it connects. In a two dimensional experimental arrangement, curvature-driven motion was qualitatively demonstrated.

Experiments in two-dimensional setups

In two-dimensional systems with pitchfork bifurcation, the characterization of front dynamics had been limited to a qualitative description. The contraction of arbitrarily shaped domains as well as the reduction of the length of an ondulated front towards a straight front was demonstrated in the four-wave mixing experiment [TSW98, TZWW99, WVS+99]. In a transient stage, an arbitrarily shaped large domain reduces the domain length faster than a small one [TZWW99]. A rough measurement shows that the front velocity of an arbitrary front increases with its curvature [LPEM+04], which is in accordance with the observations in this work.
The dynamics of fronts that exist as a result of random initial conditions cannot be characterized in the present experiment due to its fast timescales in the order of microseconds. The slow timescale in the order of seconds of a photorefractive crystal is more appropriate for such a study. However, by the introduction of defined initial conditions and the use of a video sampling method, a quantitative characterization of the domain dynamics becomes possible in the present experiment. The possibility to prepare a circular domain in a defined way by means of the addressing beam enables a refined study of curvature-driven motion, yielding a growth law.

6.3 Discrete family of solitons

The core issue of this work is the observation of a discrete family of dissipative solitons. The solitons differ in the number of radial oscillations. Solitons are not observed to occur spontaneously, but they can be robustly switched on and off by means of an incoherent addressing beam. Within the regions of multistability of solitons of different order, the width of the addressing beam can be used to ignite a desired soliton order. Equivalent familes of positive and negative solitons are observed.
A direct connection of the optical field that is transmitted by the vapor to the state variable of the microscopic model, being its orientation, was enabled by the spatially resolved

measurement of the Stokes parameters of that light field. These measurements and the numerically obtained solitons show a very good agreement and support the interpretation of the solitons as a localized excursion from a spatially extended state to the vicinity of another spatially extended state and back, i.e. a homoclinic connection of the background with itself. The spatial oscillations around the target state as well as the oscillatory tails around the background state are characterized by a defined wave number that can be identified as the wave number of the modulational instability. Hence, also the sizes of the solitons differ in discrete steps that are roughly given by the half wavelength of that instability. In a Gaussian beam, solitons typically drift towards the beam center. However, higher-order solitons whose size approaches the dimensions of the beam often become unstable towards a drift that is directed outwardly and destroys the soliton.

The formation of the soliton family is strongly connected to the described domain dynamics. The existence of stable solitons is promoted by low front velocities and by a large amount of spatial oscillations. Low front velocities are observed in situations where the omnipresent curvature-driven motion is compensated for by the introduction of a preference of the domain which can be induced by an asymmetry of the pitchfork bifurcation. The amplitude of spatial oscillations is determined by the input power and thus the distance to the modulational instability. Even far below the threshold for pattern formation, spatial oscillations with the wave number corresponding to the modulational instability are only weakly damped. Hence, the threshold for the existence of stable solitons is lowest in a situation, where an imperfection of the underlying pitchfork bifurcation reduces the front velocities and robust pinning can occur. A numerical analysis shows that at this point a codimension 2 bifurcation, where two unstable and a stable domain solutions emerge from an unstable one, takes place. Above this point, a broad region of existence of solitons is observed. The existence regions of solitons of neighboring order typically show a large overlap in parameter space. These results can be qualitatively reproduced by a heuristic extension of the simple front motion model which accounts for the occurrence of spatial oscillations.

Except for the fundamental one, solitons can be observed below the threshold for pattern formation, i.e. in a parameter region where spatial oscillations are weakly damped. Above the threshold for pattern formation, the modulation of background and target state is still small compared to the amplitude of the solitons. However, robust pinning occurs in this situation. At a certain power above threshold, solitons are even observed in in the situation of equivalent states, where locking is the only mechanism that counteracts the curvature-driven motion. Over a wide range of input powers above the threshold of the modulational instability the solitons maintain their circular symmetry to a very good approximation. Not until the maximum input power available in the experiment is reached, a transition to localized patterns that obey the hexagonal symmetry of the patterns takes place.

Comparison to theoretical predictions and other experiments

Discrete families of solitons in theoretical works

The occurrence of a discrete family of localized states is a quite general phenomenon in various theoretical models that describe nonlinear optical systems. Its interpretation is always connected to locking of fronts that connect two spatially extended states. This includes systems with two nonequivalent [RK90, Ros91, Ros02] or equivalent [SSM98a, PMEL98, OSF99, OSF01, GAGW$^+$03] homogeneous states as well as systems where one [MPL97] or two [BCF$^+$06] of the extended states are patterned.

In one-dimensional models [RK90, Ros91], low front velocities are observed around the Maxwell point. Hence, it is this region where solitons occur in the presence of oscillatory tails. If curvature effects are taken into account, the point where fronts do not move is shifted towards an asymmetric situation [GCOSM04, Cou02]. In a symmetric situation, the curvature dynamics can only be overcome by a pronounced locking phenomenon [OSF01, OSF99] or a change of sign of the coefficient describing the curvature-driven motion [GMT00].

The mechanisms that are predicted to play a key role in the formation of a soliton family, being front dynamics and locking, have been demonstrated experimentally and numerically. Hence, the well-accepted models formulated in literature apply well to the present experiment. A smooth transition between a situation where solitons exist on a homogeneous background and solitons sitting on top of a (weakly) modulated background indicates that these cases are based on similar mechanisms.

Due to the locking process of fronts in the presence of oscillations, solitons of different order [Ros91, Ros02] or multi-peaked solitons [CRT00b, MFOH02, BCF$^+$06] appear in a cascade of saddle-node bifurcations with the stable domain solutions being connected by unstable domains when a control parameter is varied. This behavior is also found in the present system. In a two-dimensional parameter space, these bifurcations are found to be folds in the surface of stationary solutions. The corresponding regions of existence of solitons of different order show some similarities to the ones of n-peaked solitons states in [MFOH02], indicating that locking is a key element in the stabilization of solitons. Also the (one-dimensional) interaction law of fronts that connect two different patterned states [BCF$^+$06] resembles some of the obtained results. However, finding a direct connection between the two cases is not straight-forward.

Degenerate four-wave mixing

The only experimental observation of a (fundamental) dark-ring cavity soliton in the presence of a pitchfork bifurcation is reported in the four-wave mixing experiment [TSW98, TZWW99, WVS+99]. These solitons appear as a result of the shrinkage of arbitrarily shaped large domains due to curvature-driven motion. The stability of the soliton is interpreted to be due to the locking of oscillatory tails. Since labyrinthine patterns are observed in nearby parameter regions (indicating a dynamics where domains expand), curvature-driven dynamics does not seem to be very pronounced, which enables locking of fronts, even if the oscillatory tails are also not very pronounced. Higher-order solitons were predicted [SSM98a] but not observed in the experiment yet. A controlled ignition of solitons or domains is not demonstrated in two dimensions, but a recent publication shows that the ignition and positioning of a domain wall is possible in quasi one-dimensional systems [EMTRV05].
In the present experiment, solitons are only observed beyond the threshold for pattern formation in the case of a perfect pitchfork bifurcation. This is interpreted to be due to relatively strong curvature-driven dynamics which requires pronounced spatial oscillations to provide robust locking. The stabilization of a whole family of solitons is significantly simplified by the controlled introduction of an asymmetry to the system.

LCLV systems

In a single mirror-feedback experiment using an LCLV the bistability of two different localized structures is reported [BPR+04]. The coexistence of the structures with different symmetries (circular and triangular) is attributed to the coexistence of two different pattern-forming instabilities. Hence, the quite general mechanism of fronts locking at different positions, which leads to the formation of a consecutive family of solitons differing in size and the number of radial oscillations like it has been demonstrated in this work, does not seem to apply to this very special situation. Similarly, the spontaneous nucleation of localized peaks with two different amplitudes over another pattern has been interpreted to be due to a coexistence of three patterned solutions [BRR05].

The experiment of Schäpers et al.

Schäpers et al. have experimentally and theoretically analyzed solitons in a single-mirror feedback arrangement using sodium vapor as the nonlinear medium [SFAL00, SAL01, SAL02, SAL03]. Hence, the experimental setup is very similar to the one described in this work. Nonetheless, the solitons described in the two experiments are entirely different, which is a result of the versatility of the nonlinear properties of sodium vapor.

The experiment of Schäpers is conducted with a circularly polarized input beam, and no polarization-changing elements are inserted into the feedback loop. Hence, the light field can be treated as a scalar. As a result, the inversion symmetry of the system is always broken in the presence of a light field. The sodium vapor is exposed to an oblique magnetic field, which makes a vectorial description of the magnetization necessary. For the experimental parameters used by Schäpers, a light shift-induced level crossing is observed, which results in a nonmonotonic, resonance-like characteristic curve [AHLL97, SAL02] for the orientation. Solitons are observed in a situation of nascent bistability, where the characteristic curve exhibits a nearly infinite slope. Slightly below this point, a variety of subcritical modulational instabilities leading to hexagonal patterns with different wave numbers is observed. Within the region of bistability between a homogeneous state and these patterns, solitons are observed. The shape of the solitons corresponds very well to the one of a single constituent of the coexisting pattern. Depending on the parameters, solitons are either spontaneously created or can be switched by means of a circularly polarized addressing beam. The robust incoherent switching method is one of the few similarities of the two systems. Concluding, the two experiments with sodium vapor can be considered as prime examples for the two different mechanisms leading to the formation of solitons. The experiment of Schäpers corresponds well with the picture of a soliton being an excerpt of an extended pattern, whereas the observation of solitons presented in this work is closely related to the locking of fronts.

6.4 Interaction of solitons and complex structures

Multiple solitons can be individually ignited and erased by means of the addressing beam. Many different configurations of solitons clusters are observed, including clusters of solitons of different orders. However, the number of solitons that can coexist at a time is limited due to the small aspect ratio. In the experiment, soliton clusters arrange in the center of the beam and display discrete preferred distances between the single constituents. Typically, the smallest possible distance is observed. However, numerical simulations assuming a plane wave indicate that several discrete stable distances are possible. They are connected to the length scale of the oscillatory tails, hence the length scale of the (weakly damped) modulational instability.

Consequently, superlattice patterns that consist of higher order solitons with a next-neighbor distance that corresponds to these discrete distances can be constructed. Hexagonal and square arrangements are stable, and even local defects do not perturb the stability of the pattern significantly.

Besides the solitons clusters, where the solitons interact only weakly, elongated structures are observed which are interpreted as tightly bound states of two or more single solitons of the same order. Bound states of differerent soliton orders have been observed. The interaction of these bound states with other structures is mediated by oscillatory tails similarly to the solitons.

In a parameter region where straight polarization fronts as well as solitons are stable for themselves, they can also coexist. Due to the interaction of the two structures, the straight front becomes bended. This is interpreted in a way that the system tries to keep the preferred distance between fronts to the maximum possible degree.

At high input powers, near the symmetry point of the pitchfork bifurcation, a ring-shaped soliton is observed. In its central part, the system returns to the vicinity of the state that serves as the background. It is interpreted to be stable due to pronounced locking and is a demonstration of a structure that is essentially based on the existence of two spatial dimensions. Numerical simulations indicate the existence of a whole new family of solitons of this type.

Comparison with theoretical and experimental results

Clusters of fundamental solitons that display one or several discrete preferred distances are a very general result that has been widely discussed in theory as well as in experiments [RK90, BLS96, TSB$^+$99a, SFAL00, GNKT03, BRB05]. It is always connected to the occurrence of oscillatory tails. Since these oscillatory tails are also present around higher order solitons, the general mechanisms are expected to apply (with small changes) also to these structures. The prediction that asymmetric clusters move slowly [RK90] was verified for an exemplary case in numerical simulations. However, the predicted slow motion is not observed in the experiment due to the inhomogeneous pumping.

Bound states of solitons have been obtained in numerical simulations of a DOPO [SSM98a] as a stationary structure and in a laser with saturable absorber [FRS$^+$03] as a rotating structure. The rotation is attributed to an asymmetry of the bound state. In both cases, bound states of fundamental solitons are reported. In the present experiment, also bound states of higher order solitons have been observed.

The possibility to compose a superlattice pattern from single higher-order solitons has been previously reported in a model of a semiconductor resonator [MPL97]. The hexagonal pattern composed of second-order solitons is interpreted to be stable due to the interaction of the single solitons through oscillating tails. This approach has been extended in this work to different geometries and next-neighbor distances. An analytical treatment of this type of superlattice patterns is presently not available.

The coexistence of fronts and fundamental solitons has been demonstrated in different theoretical models [TSW98, GMT00, GAGW$^+$03] and in the four-wave mixing experiment

[TSW98]. However, statements on the interaction of those structures were not made.
In theoretical works where two-dimensional systems are considered, the existence of solitons that are different from the standard soliton family has been demonstrated. One example is the stable droplet, which is a very large stable circular domain whose stability is entirely based on curvature effects [GCOM01, GAGW$^+$03, GCOSM04]. An even more complicated structure is observed, if the stable droplet is combined with a central dark-ring cavity soliton in the region of coexistence of these structures [GAGW$^+$03]. Another type of soliton is described in [OSF01] as a fundamental soliton having a small dip in the center. Hence, solitons in two dimensions seem to exhibit a larger variety of possible realizations than the one-dimensional ones and require further investigations. The observed ring-shaped soliton belongs to this class.

Chapter 7

Conclusion

The existence of a discrete family of higher-order solitons that accompanies the fundamental single-peaked soliton has been predicted in a large number of theoretical works [SSM98a, PMEL98, OSF99, OSF01, GAGW$^+$03]. In this work, such a soliton family was observed experimentally for the first time, and the mechanisms that lead to the formation of the solitons have been identified and characterized.

The system under consideration is a conceptually simple optical structure forming system. It can be interpreted as a realization of the well-known single-mirror feedback arrangement [Fir90, DF91, DF92]. Sodium vapor is used as the nonlinear medium, and a $\lambda/8$ retardation plate is placed in the feedback loop as a modification. This system displays a symmetry-breaking pitchfork bifurcation leading to two equivalent homogeneous states that differ in their polarization properties [YOKO84, GWKL$^+$00].

Solitons that occur in the presence of a pitchfork bifurcation have been widely discussed in literature [Lon97, SSM98a, PMEL98, GMT00, TSW98]. Only in one case, however, the (fundamental) soliton was also observed experimentally [TSW98]. In the present experiment, the solitons correspond to localized excursions that lead from one polarization state emerging from the pitchfork bifurcation to the vicinity of the other one. The members of the soliton family differ in size and in their inner structure, i.e. the number of radial oscillations. They can be robustly ignited and erased with an incoherent addressing beam. By means of a novel technique to measure the spatially resolved Stokes parameters of the transmitted light field, the experimental observations could be directly compared to numerical simulations of the microscopic model of the system. A good agreement between the experimental findings and numerical simulations has been achieved.

It turns out that the stability properties of the soliton family are strongly connected to the dynamics of curved fronts. In general, a circular domain that is ignited by means of the addressing beam is unstable in the presence of a perfect pitchfork bifurcation.

It will contract and disappear due to curvature of the domain boundaries. For the first time, this curvature-driven motion was captured in a controlled experiment, and a growth exponent for the domain size has been determined that is in good accordance with general theoretical expectations [GCOM01] as long as the two states that are connected by the domain boundary can be described as nearly homogeneous.

It was demonstrated that the dynamics of domains can be modified by the introduction of a nonequivalence of the two homogeneous states which can be easily prepared by a controlled perturbation of the pitchfork bifurcation. In accordance with general expectations [GCOSM04], the favored state shows a tendency to expand. If the ignited domain is prepared to be in the favored state, the tendency to expand can compensate for the curvature-driven motion. A stationary equilibrium exists for a unique domain radius. However, it is not stable, and the domain will either contract or expand.

Stabilization of domains is provided by the occurrence of nonmonotonic spatial oscillations around the domain boundary. The interaction of these oscillations provides a locking mechanism that can stop the contraction of domains at certain discrete domain radii. The occurrence of spatial oscillations is related to the existence of a near modulational instability. The resulting stable domains, whose sizes increase roughly in steps of the wavelength of the modulational instability are identified as the members of the discrete family of solitons.

The regions of existence of the solitons have been determined experimentally and numerically and show a good qualitative agreement. As a result of the interplay of the described mechanisms, solitons of all orders are preferably found in a situation of an imperfect pitchfork bifurcation, where the velocity of a curved front is low. This is in contradiction to many one-dimensional models, where curvature-driven motion does not exist and where the regions of existence of solitons are located around the Maxwell point, which in the present system is given by the situation of a perfect pitchfork bifurcation. Furthermore, the existence of solitons is promoted by a large amount of spatial oscillations. Broad regions of existence in parameter space are found that show a large overlap between neighboring orders of solitons. A numerical analysis of the stable and unstable stationary domains of the system shows, that stable soliton solutions are connected by unstable domains and that each soliton order originates from an individual codimension 2 bifurcation. Higher order solitons are observed below and above the threshold for pattern formation, while the fundamental one appears slightly above the threshold for pattern formation. Even far above that threshold, the solitons essentially maintain their shape. At the highest available input powers, the structures lose their circular symmetry, and localized patterns are observed.

Multiple solitons can be ignited at a certain instance of time. A large variety of soliton

clusters of same and of different order is observed, where the constituents essentially maintain their shape. The number of solitons is limited by the finite size of the Gaussian beam in the experiment. Different discrete distances between the solitons are observed, and numerical simulations indicate that these distances originate from the interaction of the oscillatory tails, as it is observed in many systems. Furthermore, elongated structures are observed that are interpreted as tightly bound solitons of same order. These bound states are also found in clusters with solitons, and the interaction behavior was found to be similar to the soliton-soliton interaction.
Even more complex situations have been described. In numerical simulations, higher-order solitons can be arranged on regular grids and form stable superlattice patterns. These patterns are high-amplitude and are interpreted to be strongly nonlinear, hence they cannot be understood in terms of perturbative techniques. Solitons can coexist with fronts, and their interaction leads to a stable configuration, where the soliton is embedded into the front. At high input powers, a ring-shaped solitary structure has been observed experimentally that is essentially different from the solitons described before. Numerical simulations indicate the existence of a whole family of this intrinsically two-dimensional type of solitons, which might be the issue of future work.

Appendix A

Details on the Newton method

The use of a Newton method in order to obtain stationary solutions of a system has proven successful in many systems [FH98, Sch01, Hun06]. The calculation of the stationary solutions in this work follows the approach in [Sch01, Hun06], where rotationally symmetric solutions were computed. The algorithm has been adapted to the present model described in section 5.1.2. The rotationally symmetric stationary solutions $\tilde{\phi}(r)$ of the dynamics 5.7

$$\frac{\partial}{\partial t}\tilde{\phi}(r) = 0 = \mathcal{N}(\tilde{\phi}(r)), \tag{A.1}$$

where the nonlinear operator $\mathcal{N}(\phi)$ is defined by the right-hand side of equation 5.7 $\frac{\partial}{\partial t}\phi =: \mathcal{N}(\phi)$, are then obtained iteratively from a suited initial distribution ϕ^0 by

$$\phi^{n+1} = \phi^n - (\nabla\mathcal{N}(\phi^n))^{-1}\mathcal{N}(\phi^n), \tag{A.2}$$

where $\nabla\mathcal{N}$ is the Jacobian of the operator $\mathcal{N}$. $\nabla\mathcal{N}$ can be computed via finite differences [Sch01].

Propagation of the light field

The calculation of the reflected field components is accomplished using a spectral algorithm in polar coordinates. It is based on the fact, that the propagation of a light field that has a rotational symmetry can be easily calculated in Hankel space by the multiplication of a phase factor. The (scalar) paraxial wave equation in polar coordinates is given by

$$\frac{\partial E}{\partial z} = -\frac{i}{2k}\Delta_\perp E = -\frac{i}{2k}\left(\frac{1}{r}\frac{\partial E}{\partial r} + \frac{\partial^2 E}{\partial r^2}\right). \tag{A.3}$$

The Hankel transform is defined by

$$\hat{f}(\rho) = 2\pi \int_0^\infty r f(r) J_0(2\pi r \rho) dr \tag{A.4}$$

with the symmetric back transformation

$$f(r) = 2\pi \int_0^\infty \rho \hat{f}(\rho) J_0(2\pi r \rho) d\rho, \tag{A.5}$$

where J_0 is the zero-order Bessel function. The representation of $E(r)$ by means of Hankel transforms is given by:

$$E(r) = 2\pi \int_0^\infty \rho \hat{E}(\rho) J_0(2\pi \rho r) d\rho \tag{A.6}$$

$$\frac{1}{r}\frac{\partial E}{\partial r} = 2\pi \int_0^\infty \rho \hat{E}(\rho) \frac{2\pi\rho}{r} J_0'(2\pi \rho r) d\rho \tag{A.7}$$

$$\frac{\partial^2 E}{\partial r^2} = 2\pi \int_0^\infty \rho \hat{E}(\rho) (2\pi\rho)^2 J_0''(2\pi \rho r) d\rho\,. \tag{A.8}$$

Under consideration of the relation $x^2 J_0''(x) + x J_0'(x) + x^2 J_0(x) = 0$, it follows:

$$\Delta_\perp E(r) = 2\pi \int_0^\infty \rho \hat{E}(\rho)(-4\pi^2\rho^2) J_0(2\pi \rho r) d\rho\,. \tag{A.9}$$

In order to solve the paraxial wave equation (A.3), the equation

$$\frac{\partial \hat{E}(\rho, z)}{\partial z} = \frac{i4\pi^2\rho^2}{2k} \hat{E}(\rho, z) \tag{A.10}$$

needs to be solved in Fourier space. Thus,

$$\hat{E}(\rho, z = 2d) = \exp\left\{\frac{i4\pi^2\rho^2 d}{k}\right\} \hat{E}(\rho, z = 0)\,. \tag{A.11}$$

The transformations of the light field into Hankel space and back are numerically accomplished using the ‘Quasi Fast Hankel Transform’ (QFHT) [Sie77] with a correcting term [AL81]. The use of the QFHT requires a discretization of the spatial coordinates on a radial grid with exponentially increasing steps in real and Hankel space:

$$r_l = r_0 e^{\alpha l} \quad \rho_m = \rho_0 e^{\alpha m} \quad l, m = 0, 1, ..., N-1\,. \tag{A.12}$$

where r is the discrete radial coordinate in real space, while ρ represents the radial component in Hankel space. The choice of α determines the increase of distances within the exponential grid. The calculations were conducted with the discretization parameters

$N = 280$, $r_0 = 2.05\,\mu$m, $\rho_0 = 3.4\,\mathrm{mrad\,mm}^{-1}$ and $\alpha = 0.0272$. The maximum coordinates in real and Hankel space for this discretization are given by $r_{max} = 4.05\,$mm and $\rho_{max} = 42.2\,\mathrm{rad\,mm}^{-1}$, respectively. In analogy to [Hun06], the options to have a Gaussian beam input and Dirichlet boundary conditions at r_{max} have been included. In this work, a vectorial description of the light field is necessary. Hence, a second polarization component has been added.

Calculation of the diffusion term

The diffusion term in equation is calculated as a Laplacian that is reduced to its radial component. It is computed by means of finite differences [Sch01]:

$$\begin{aligned}\Delta_\perp \phi &= \frac{1}{r}\frac{\partial \phi}{\partial r} + \frac{\partial^2 \phi}{\partial r^2} \\ &= \frac{1}{r_j}\frac{\phi(r_{j+1}) - \phi(r_{j-1})}{r_{j+1} - r_{j-1}} \\ &\quad + \frac{2}{r_{j-1} + r_{j+1}}\left(\frac{\phi(r_{j-1})}{r_j - r_{j-1}} + \frac{\phi(r_{j+1})}{r_{j+1} - r_j} - \phi(r_j)\left(\frac{1}{r_j - r_{j-1}} + \frac{1}{r_{j+1} - r_j}\right)\right)\end{aligned} \tag{A.13}$$

Stability of the obtained stationary solutions

A statement on the stability of the solutions obtained from the Newton method against small perturbation can easily be made. Be $\phi_s(r)$ a stationary solution. Then consider small perturbations of the form

$$\phi(r) = \phi_s(r) + e^{\eta t}\delta\phi(r)\,. \tag{A.14}$$

Inserting this ansatz into the equation of motion $\dot{\phi} = \mathcal{N}(\phi)$ leads to

$$\dot{\phi} + \eta\delta\phi e^{\eta t} = \mathcal{N}(\phi_s) + \nabla\mathcal{N}\left(\phi_s\right)\delta\phi e^{\eta t}\,, \tag{A.15}$$

and hence

$$\eta\delta\phi = \nabla\mathcal{N}\left(\phi_s\right)\delta\phi\,. \tag{A.16}$$

The growth exponent η is an eigenvalue of $\nabla\mathcal{N}(\phi_s)$ corresponding to the eigenmode $\delta\phi$. The matrix $\nabla\mathcal{N}(\phi_s)$ is already computed within the Newton method. For a stability analysis, its eigenvalues and eigenvectors are determined by means of a library function.

Bibliography

[AA05] N. Akhmediev and A. Ankiewicz. *Dissipative Solitons*, Volume **661** of *Lecture Notes in Physics*. Springer, Berlin, Heidelberg, New York, 2005.

[AAGWL02] A. Aumann, T. Ackemann, E. Große Westhoff, and W. Lange. *Eight-fold quasipatterns in an optical pattern-forming system*. Phys. Rev. E **66**, 046220, 2002.

[ABL+97] A. Aumann, E. Büthe, Yu. A. Logvin, T. Ackemann, and W. Lange. *Polarized patterns in sodium vapor with single mirror feedback*. Phys. Rev. A **56**, R1709, 1997.

[Ack96] T. Ackemann. *Spontane Musterbildung in einem atomaren Dampf mit optischer Rückkopplung*. Dissertation, Westfälische Wilhelms-Universität Münster, 1996.

[Ack06] T. Ackemann. Personal communication, 2006.

[AHLL97] T. Ackemann, A. Heuer, Yu. A. Logvin, and W. Lange. *Light-shift induced level crossing and resonatorless optical bistability in sodium vapor*. Phys. Rev. A **56**, 2321, 1997.

[AL81] G. P. Agrawal and M. Lax. *End-correction in the quasi-fast Hankel transform for optical-propagation problems*. Opt. Lett. **6**, 171, 1981.

[AL94] T. Ackemann and W. Lange. *Non- and nearly hexagonal patterns in sodium vapor generated by single-mirror feedback*. Phys. Rev. A **50**, R4468, 1994.

[AL01] T. Ackemann and W. Lange. *Optical pattern formation in alkali metal vapors: Mechanisms, phenomena and use*. Appl. Phys. B **72**, 21, 2001.

[ALHL95] T. Ackemann, Y. Logvin, A. Heuer, and W. Lange. *Transition between positive and negative hexagons in optical pattern formation*. Phys. Rev. Lett. **75**, 3450, 1995.

[Ank93] G. Ankerhold. *Strahlungsdiffusion bei Laseranregung von Natriumdampf: Einfluß auf die räumliche Verteilung und die zeitliche Entwicklung von Anregung und Spinorientierung.* Dissertation, Westfälische Wilhelms-Universität Münster, 1993.

[Aum99] A. Aumann. *Optical patterns and quasipatterns in an alkali metal vapor with feedback.* Dissertation, Westfälische Wilhelms-Universität Münster, 1999.

[BA74] J. E. Bjorkholm and A. Ashkin. *Cw self-focusing and self-trapping of light in sodium vapor.* Phys. Rev. Lett. **32**, 129, 1974.

[Bab05] I. V. Babushkin. Personal communication, 2005.

[BCF+06] U. Bortolozzo, M. G. Clerc, C. Falcon, S. Residori, and R. Rojas. *Localized states in bistable pattern-forming-systems.* Phys. Rev. Lett. **96**, 214501, 2006.

[BLP+97] M. Brambilla, L. A. Lugiato, F. Prati, L. Spinelli, and W. J. Firth. *Spatial soliton pixels in semiconductor devices.* Phys. Rev. Lett. **79**, 2042, 1997.

[BLR+95] M. Le Berre, D. Leduc, E. Ressayre, A. Tallet, and A. Maître. *Simulation and analysis of the flower-like instability in the single-feedback mirror experiment with rubidium vapor.* Opt. Commun. **118**, 447, 1995.

[BLRT98] M. Le Berre, D. Leduc, E. Ressayre, and A. Tallet. *Optical quasipatterns and multicriticality.* Asian J. Phys. **7**, 483, 1998.

[BLS96] M. Brambilla, L. A. Lugiato, and M. Stefani. *Interaction and control of optical localized structures.* Europhys. Lett. **34**, 109, 1996.

[Boy92] R. W. Boyd. *Nonlinear Optics.* Academic Press, Boston, 1992.

[BP95] M. Bode and H. G. Purwins. *Pattern formation in reaction-diffusion systems - dissipative solitons in physical systems.* Physica D **86**, 53, 1995.

[BPR+04] U. Bortolozzo, L. Pastur, P. L. Ramazza, M. Tlidi, and G. Kozyreff. *Bistability between different localized structures in nonlinear optics.* Phys. Rev. Lett. **93**, 253901, 2004.

[BRB05] U. Bortolozzo, P. L. Ramazza, and S. Boccaletti. *Dissipative solitons driving and bound state control via parameter gradients.* Chaos **15**, 013501, 2005.

[BRR05] U. Bortolozzo, R. Rojas, and S. Residori. *Spontaneous nucleation of localized peaks in a multistable nonlinear system.* Phys. Rev. E **72**, 045201, 2005.

[BRT00] M. Le Berre, E. Ressayre, and A. Tallet. *Kinetics of domain walls in the degenerate optical parametric oscillator.* J. Opt. B: Quantum Semiclass. Opt. **2**, 347, 2000.

[Bru94] H.-J. Bruns. *Das Video-Sampling Verfahren.* Diplomarbeit, Westfälische Wilhelms-Universität Münster, 1994.

[BSC88] D. Bensimon, B. I. Shraiman, and V. Croquette. *Nonadiabatic effects in convection.* Phys. Rev. A **38**, 5461, 1988.

[BTB+02] S. Barland, J. R. Tredicce, M. Brambilla, L. A. Lugiato, S. Balle, M. Giudici, T. Maggipinto, L. Spinelli, G. Tissoni, T. Knödel, M. Miller, and R. Jäger. *Cavity solitons as pixels in semiconductors.* Nature **419**, 699, 2002.

[BTV92] V. Yu. Bazhenov, V. B. Taranenko, and M. V. Vasnetsov. *Transverse optical effects in bistable active cavity with nonlinear absorber on bacteriorhodopsin.* Proc. SPIE **1840**, 183, 1992.

[CEK05] M. Clerc, D. Escaff, and V.M. Kenkre. *Patterns and localized structures in population dynamics.* Phys. Rev. E **72**, 056217, 2005.

[CER87] P. Coullet, C. Elphick, and D. Repaux. *Nature of spatial chaos.* Phys. Rev. Lett. **58**, 431, 1987.

[CH93] M. C. Cross and P. C. Hohenberg. *Pattern formation outside of equilibrium.* Rev. Mod. Phys. **65**, 851, 1993.

[CLHL90] P. Coullet, J. Lega, B. Houchmanzadeh, and J. Lajzerowics. *Breaking chirality in nonequilibrium systems.* Phys. Rev. Lett. **65**, 1352, 1990.

[CM95] M. C. Cross and D.I. Meiron. *Domain coarsening in systems far from equilibrium.* Phys. Rev. Lett. **75**, 2152, 1995.

[CNP+04] M. G. Clerc, T. Nagaya, A. Petrossian, S. Residori, and C. S. Riera. *First-order Fredericksz transition and front propagation in a liquid crystal light valve with feedback.* Eur. Phys. J. D **28**, 435, 2004.

[Cou02] P. Coullet. *Localized patterns and fronts in nonequilibrium systems.* Int. J. Bif. Chaos **12**(11), 2445, 2002.

[CRT00a] P. Coullet, C. Riera, and C. Tresser. *Qualitative theory of stable stationary localized structures in one dimension.* Prog. Theor. Phys. Suppl. **139**, 46, 2000.

[CRT00b] P. Coullet, C. Riera, and C. Tresser. *Stable static localized structures in one dimension.* Phys. Rev. Lett. **84**, 3069, 2000.

[CRT04] P. Coullet, C. Riera, and C. Tresser. *A new approach to data storage using localized structures.* Chaos **14**, 193, 2004.

[CT62] C. Cohen-Tannoudji. *Théorie quantique du cycle de pompage optique.* Ann. Phys. (N.Y.) **7**, 423, 1962.

[Dah87] U. Dahmen. *Encyclopedia of physical science and technology* **10**, 319, 1987.

[DF91] G. D'Alessandro and W. J. Firth. *Spontaneous hexagon formation in a nonlinear optical medium with feedback mirror.* Phys. Rev. Lett. **66**, 2597, 1991.

[DF92] G. D'Alessandro and W. J. Firth. *Hexagonal spatial pattern for a Kerr slice with a feedback mirror.* Phys. Rev. A **46**, 537, 1992.

[DHV04] P. D. Drummond, M. Haelterman, and R. Vilaseca. *Optical solitons.* Journal of Optics B-Quatntum and Semiclassical Optics **6**, 159, 2004.

[DJ96] P. G. Drazin and R. S. Johnson. *Solitons: an introduction.* Cambridge University Press, Cambridge, 1996.

[DSS97] B. Dionne, M. Silber, and A. C. Skeldon. *Stability results for steady, spatially periodic planforms.* Nonlinearity **10**, 321, 1997.

[DSS+98] C. Denz, M. Schwab, M. Sedlatschek, T. Tschudi, and T. Honda. *Pattern dynamics and competition in a photorefractive feedback system.* J. Opt. Soc. Am. B **15**, 2057, 1998.

[EMTG+05] A. Esteban-Martín, V. B. Taranenko, J. Garcia, G. J. Valcárcel, and E. Roldán. *Controlled observation of a nonequilibrium Ising-Bloch transition in a nonlinear optical cavity.* Phys. Rev. Lett. **94**, 223903, 2005.

[EMTRV05] A. Esteban-Martín, V. B. Taranenko, E. Roldán, and G. J. de Valcárcel. *Control and steering of phase domain walls.* Opt. Express **13**, 3631, 2005.

[FH98] W. J. Firth and G. K. Harkness. *Cavity solitons.* Asian J. Phys. **7**, 665, 1998.

[Fir90] W. J. Firth. *Spatial instabilities in a Kerr medium with single feedback mirror.* J. Mod. Opt. **37**, 151, 1990.

[FRS+03] S. V. Fedorov, N. N. Rosanov, A. N. Shatsev, N.A. Veretenov, and A. G. Vladimirov. *Topologically multicharged and multihumped rotating solitons in wide-aperture lasers with a saturable absorber.* IEEE J. Quantum Electron. **39**, 197, 2003.

[FS96] W. J. Firth and A. J. Scroggie. *Optical bullet holes: robust controllable localized states of a nonlinear cavity.* Phys. Rev. Lett. **76**, 1623, 1996.

[FT90] S. Fauve and O. Thual. *Solitary waves generated by subcritical instabilities in dissipative systems.* Phys. Rev. Lett. **64**, 282, 1990.

[FW02] W. J. Firth and C. O. Weiss. *Cavity and feedback solitons.* Opt. Photon. News **13**, 54, 2002.

[GAGW+03] D. Gomila, T. Ackemann, E. Große Westhoff, P. Colet, and W. Lange. *Secondary bifurcations of hexagonal patterns in a nonlinear optical system: alkali metal vapor in a single-mirror arrangement.* Phys. Rev. E **69**, 036205, 2004.

[Gah96] A. Gahl. *Räumliche Vektorinstabilitäten in der nichtlinearen Optik: Die magneto-optisch induzierte Aufspaltung eines Laserstrahles in atomaren Dämpfen.* Dissertation, Westfälische Wilhelms-Universität Münster, 1996.

[GCOM01] D. Gomila, P. Colet, G. L. Oppo, and M. San Miguel. *Stable Droplets and Growth Laws Close to the Modulational Instability of a Domain Wall.* Phys. Rev. Lett. **87**, 194101, 2001.

[GCOSM04] D. Gomila, P. Colet, G. L. Oppo, and M. San Miguel. *Stable droplets and nucleation in asymmetric bistable nonlinear optical systems.* J. Opt. B: Quantum Semiclass. Opt. **6**, 265, 2004.

[GCSM+03] D. Gomila, P. Colet, M. San Miguel, A. Scroggie, and G. L. Oppo. *Stable droplets and dark-ring cavity solitons in nonlinear optical devices.* IEEE J. Quantum Electron. **39**, 238, 2003.

[GKNT02] B. Gütlich, M. Kreuzer, R. Neubecker, and T. Tschudi. *Manipulation of solitary structures in a nonlinear optical single feedback experiment.* Mol. Cryst. Liq. Cryst. **375**, 281, 2002.

[GMP94] G. Grynberg, A. Maître, and A. Petrossian. *Flowerlike patterns generated by a laser beam transmitted through a rubidium cell with a single feedback mirror.* Phys. Rev. Lett. **72**, 2379, 1994.

[GMS83] J. D. Gunton, M. San Miguel, and P. S. Sahni. In C. Domb and J. Lebowitz (Hrsg.), *Phase transitions and critical phenomena*, pages 269–466. Academic Press, London, 1983.

[GMT00] R. Gallego, M. San Miguel, and R. Toral. *Self-similar domain growth, localized structures, and labyrinthine patterns in vectorial Kerr resonators.* Phys. Rev. E **61**, 2241, 2000.

[GNKT03] B. Gütlich, R. Neubecker, M. Kreuzer, and T. Tschudi. *Control and manipulation of solitary structures in a nonlinear optical single feedback experiment.* Chaos **13**, 239, 2003.

[Gom03] D. Gomila. *Dynamics of spatial structures in nonlinear optics.* PhD thesis, Universitat de les Illes Balears, Spain, 2003.

[GSMT98] R. Gallego, M. San Miguel, and R. Toral. *Fronts, domain growth, and dynamical scaling in a d=1 nonpotential system.* Phys. Rev. E **58**, 3125, 1998.

[GW02] E. Große Westhoff. *Quasimuster und Überstrukturen in einem optisch getriebenen atomaren Dampf.* Dissertation, Westfälische Wilhelms-Universität Münster, 2002.

[GW03] E. Große Westhoff. Internal report, 2003.

[GWHAL03] E. Große Westhoff, R. Herrero, T. Ackemann, and W. Lange. *Self-organized superlattice patterns with two slightly differing wave numbers.* Phys. Rev. E **67**, 025293, 2003.

[GWKL$^+$00] E. Große Westhoff, V. Kneisel, Yu. A. Logvin, T. Ackemann, and W. Lange. *Pattern formation in the presence of an intrinsic polarization instability.* J. Opt. B: Quantum Semiclass. Opt. **2**, 386, 2000.

[GZD+05] B. Gütlich, H. Zimmermann, C. Denz, R. Neubecker, M. Kreuzer, and T. Tschudi. *Forcing and control of localized states in optical single feedback systems.* Appl. Phys. B **81**, 927, 2005.

[HAL04] F. Huneus, T. Ackemann, and W. Lange. *Self-organized intensity spirals and target patterns in a single-mirror feedback scheme.* Ukr. J. Phys. **49**, 358, 2004.

[HBF+04] X. Hachair, S. Barland, L. Furfaro, M. Giudici, S. Balle, J. Tredicce, M. Brambilla, T. Maggipinto, I. M. Perrini, G. Tissoni, and L. Lugiato. *Cavity solitons in broad-area vertical-cavity surface-emitting lasers below threshold.* Phys. Rev. A **69**, 043817, 2004.

[HFOM02] G. K. Harkness, W. J. Firth, G. L. Oppo, and J. M. McSloy. *Computationally Determined Existence and Stability of Transverse Structures: I. Periodic Optical Patterns.* Phys. Rev. E **66**, 046605, 2002.

[HGWA+99] R. Herrero, E. Große Westhoff, A. Aumann, T. Ackemann, Yu. A. Logvin, and W. Lange. *Twelvefold quasiperiodic patterns in a nonlinear optical system with continuous rotational symmetry.* Phys. Rev. Lett. **82**, 4627, 1999.

[Hon93] T. Honda. *Hexagonal pattern formation due to counterpropagation in* $KNbO_3$. Opt. Lett. **18**, 598, 1993.

[Hun06] F. Huneus. *Dynamische Targetmuster und Spiralen in einem optischen Experiment zur Selbstorganisation.* Dissertation, Westfälische Wilhelms-Universität Münster, 2006.

[HW87] H. Haken and H. C. Wolf. *Atom- und Quantenphysik.* Springer, Berlin, 1987.

[JR97] C. Josserand and S. Rica. *Coalescence and droplets in the subcritical nonlinear Schrödinger equation.* Phys. Rev. Lett. **78**, 1215, 1997.

[KA03] Y. S. Kivshar and G. P. Agrawal. *Optical solitons.* Academic Press, Amsterdam, 2003.

[Kas50] A. Kastler. *Quelques suggetions concernant la production optique et la détection optique dúne inégalité de population des niveaux de quantification spatiale des atomes. Application a l'expérience de stern et gerlach et a la résonance magnétique.* J. Phys. et Rad.J. Phys. et Rad. **6**, 255, 1950.

[KO94] B. S. Kerner and V. V. Osipov. *Autosolitons.* Kluwer Academic Publishers, Dordrecht, 1994

[KST96] M. Kreuzer, A. Schreiber, and B. Thüring. *Evolution and switching dynamics of solitary spots in nonlinear optical feedback systems.* Mol. Cryst. Liq. Cryst. **282**, 91, 1996.

[KTT98] M. Kreuzer, B. Thüring, and T. Tschudi. *Creation, dynamics and stability of localized states in a nonlinear optical single feedback system.* Asian J. Phys. **7**, 678, 1998.

[LA98] W. Lange and T. Ackemann. *Alkaline vapors with single-mirror feedback - a model system for pattern formation.* Asian J. Phys. **7**, 439, 1998.

[LAA+99] W. Lange, T. Ackemann, A. Aumann, E. Büthe, and Yu. A. Logvin. *Atomic vapors – a versatile tool in studies of optical pattern formation.* Chaos, Solitons & Fractals **10**, 617, 1999.

[LAAB98] W. Lange, A. Aumann, T. Ackemann, and E. Büthe. *Polarization patterns in alkaline vapors.* Quantum Semiclass. Opt. **10**, R23, 1998.

[LAF96] O. Lioubashevski, H. Arbell, and J. Fineberg. *Dissipative solitary states in driven surface waves.* Phys. Rev. Lett. **76**, 3959, 1996.

[Lef80] H. C. Lefevre. *Single-mode fibre fractional wave devices and polarization controllers.* Electron. Lett. **16**, 778, 1980.

[Lon97] S. Longhi. *Localized structures in optical parametric oscillation.* Physica Scripta **56**, 611, 1997.

[LPEM+04] Y. Larionova, U. Peschel, A. Esteban-Martín, J. Garcia Monreal, and C. O. Weiss. *Ising and Bloch walls of phase domains in two-dimensional parametric wave mixing.* Phys. Rev. A **69**, 033803, 2004.

[Lug03] L. A. Lugiato. *Introduction to the feature section on cavity solitons: An overview.* IEEE J. Quantum Electron. **39**, 193, 2003.

[MB95] M. Möller and H. J. Bruns. *Video sampling: A new low-cost method of capturing fast repetitive processes.* Rev. Sci. Instrum. **66**, 4535, 1995.

[MDLM86] F. Mitschke, R. Deserno, W. Lange, and J. Mlynek. *Magnetically induced optical self-pulsing in a nonlinear resonator.* Phys. Rev. A **33**, 3219, 1986.

[Mer92] E. Meron. *Pattern formation in excitable media.* Phys. Rep. **218**, 1, 1992.

[MFOH02] J. M. McSloy, W. J. Firth, G. L. Oppo, and G. K. Harkness. *Computationally Determined Existence and Stability of Transverse Structures: II. Multi-Peaked Cavity Solitons.* Phys. Rev. E **66**, 046606, 2002.

[ML94] M. Möller and W. Lange. *Radiation trapping: a new mechanism for chaos in a nonlinear optical resonator.* Phys. Rev. A **49**, 4161, 1994.

[Möl92] M. Möller. *Verallgemeinerte optische Bistabilität und Chaos: ein nichtlineares Szenario in einem natriumdampfgefüllten Fabry-Pérot-Resonator.* Dissertation, Westfälische Wilhelms-Universität Münster, 1992.

[MPL97] D. Michaelis, U. Peschel, and F. Lederer. *Multistable localized structures and superlattices in semiconductor optical resonators.* Phys. Rev. A **56**, R3366–R3369, 1997.

[MPL$^+$01] D. Michaelis, U. Peschel, F. Lederer, D. V. Skryabin, and W. J. Firth. *Universal criterion and amplitude equation for a nonequilibrium Ising-Bloch transition.* Phys. Rev. E **63**, 066602, 2001.

[MSA$^+$99] M. Möller, J. P. Seipenbusch, T. Ackemann, B. Schäpers, A. Aumann, A. Gahl, H.-J. Bruns, and W. Lange. *Observing pattern dynamics in nonlinear optical systems using the video-sampling method.* Chaos, Solitons & Fractals **10**, 675, 1999.

[MT04] P. Mandel and M. Tlidi. *Transverse dynamics in cavity nonlinear optics (2000–2003).* J. Opt. B: Quantum Semiclass. Opt. **6**, R60, 2004.

[Nic95] G. Nicolis. *Introduction to Nonlinear Science.* Cambridge University Press, Cambridge, 1995.

[NOTT95] R. Neubecker, G. L. Oppo, B. Thüring, and T. Tschudi. *Pattern formation in a liquid crystal light valve with feedback, including polarization, saturation, and internal threshold effects.* Phys. Rev. A **52**, 791, 1995.

[OF96] K. Ouchi and H. Fujisaka. *Phase ordering kinetics in the Swift-Hohenberg equation.* Phys. Rev. E **54**, 3895, 1996.

[Ohl87] J. Ohlenbusch. *Entwicklung eines kostengünstigen, Mikroprozessor gesteuerten Wavemeters.* Diplomarbeit, Hannover, 1987.

[OSF99] G.-L. Oppo, A. J. Scroggie, and W. J. Firth. *From domain walls to localized structures in degenerate optical parametric oscillators.* J. Opt. B: Quantum Semiclass. Opt. **1**, 133, 1999.

[OSF01] G. L. Oppo, A. J. Scroggie, and W. J. Firth. *Characterization, dynamics and stabilization of diffractive domain walls and dark ring cavity solitons in parametric oscillators.* Phys. Rev. E **63**, 066209, 2001.

[OSSB00] G. L. Oppo, A. J. Scroggie, S. Sinclair, and M. Brambilla. *Complex spatio-temporal dynamics of optical parametric oscillators close to threshold.* J. Mod. Opt. **47**, 2005, 2000.

[PASRV04] I. Pérez-Arjona, F. Silva, E. Roldán, and G. J. Valcárcel. *Stabilizing and controlling domain walls and dark-ring cavity solitons.* Opt. Express **12**, 2130, 2004.

[Pes00] M. Pesch. *Untersuchungen zur numerischen Behandlung von Laplaceoperatoren am Beispiel einer Einspiegelanordnung.* Semesterarbeit, Münster, 2000.

[PFTV92] W. H. Press, B. Flannery, S. Teukolsky, and W. Vettering. *Numerical recipes: the art of scientific computing.* Cambridge University Press, Cambridge, 1992.

[PGWAL05] M. Pesch, E. Große Westhoff, T. Ackemann, and W. Lange. *Observation of a Discrete Family of Dissipative Solitons in a Nonlinear Optical System.* Phys. Rev. Lett. **95**, 143906, 2005.

[PMEL98] U. Peschel, D. Michaelis, C. Etrich, and F. Lederer. *Formation, motion, and decay of vectorial cavity solitons.* Phys. Rev. E **58**, R2745, 1998.

[PMW03] U. Peschel, D. Michaelis, and C. O. Weiss. *Spatial solitons in optical cavities.* IEEE J. Quantum Electron. **39**, 51, 2003.

[Pom86] Y. Pomeau. *Front motion, metastability and subcritical bifurcations in hydrodynamics.* Physica D **23**, 3, 1986.

[PRA93] E. Pampaloni, S. Residori, and F. T. Arecchi. *Roll-hexagon transition in a Kerr-like experiment.* Europhys. Lett. **24**, 647, 1993.

[PSA97] E. Pampaloni, S. Soria, and F. T. Arecchi. *Phase locking in nonlinear optical patterns.* Phys. Rev. Lett. **78**, 1042, 1997.

[RBB+02] P. L. Ramazza, E. Benkler, U. Bortolozzo, S. Boccaletti, S. Ducci, and F. T. Arecchi. *Tailoring the profile and interactions of optical localized structures.* Phys. Rev. E **65**, 066204, 2002.

[RDBA00] P. L. Ramazza, S. Ducci, S. Boccaletti, and F. T. Arecchi. *Localized versus delocalized patterns in a nonlinear optical interferometer.* J. Opt. B: Quantum Semiclass. Opt. **2**, 399, 2000.

[Rem99] M. Remoissenet. *Waves called solitons: Concepts and Experiments.* Springer, Berlin, Heidelberg, New York, 1999.

[Res05] S. Residori. *Patterns, fronts and structures in a Liquid-Crystal-Light-Valve with optical feedback.* Physics Reports - Review Section of Physics Letters **416**, 201, 2005.

[Rie99] H. Riecke. Localized structures in pattern-forming systems. In: *Pattern Formation in Continuous and Coupled Systems*, Volume **115** of *The IMA volumes in mathematics and its applications*, pages 215–228. Springer, New York, 1999.

[RK90] N. N. Rosanov and G. V. Khodova. *Diffractive autosolitons in nonlinear interferometers.* J. Opt. Soc. Am. B **7**, 1057, 1990.

[Ros91] N. N. Rosanov. *Switching waves, autosolitons, and parallel digital-analogous optical computing.* Proc. SPIE **1840**, 130, 1991.

[Ros02] N. N. Rosanov. *Spatial hysteresis and optical patterns.* Springer Series in Synergetics. Springer, Berlin, 2002.

[SAL01] B. Schäpers, T. Ackemann, and W. Lange. *Characteristics and possible applications of localized structures in an optical pattern–forming system.* Proc. SPIE **4271**, 130, 2001.

[SAL02] B. Schäpers, T. Ackemann, and W. Lange. *Robust control of switching of localized structures and its dynamics in a single-mirror feedback scheme.* J. Opt. Soc. Am. B **19**, 707, 2002.

[SAL03] B. Schäpers, T. Ackemann, and W. Lange. *Properties of feedback solitons in a single-mirror experiment.* IEEE J. Quantum Electron. **39**, 227, 2003.

[Sch01] B. Schäpers. *Lokalisierte Strukturen in einem atomaren Dampf mit optischer Rückkopplung.* Dissertation, Westfälische Wilhelms-Universität Münster, 2001.

[Sch06] J. Schüttler. Personal communication, 2006.

[SFAL00] B. Schäpers, M. Feldmann, T. Ackemann, and W. Lange. *Interaction of localized structures in an optical pattern forming system.* Phys. Rev. Lett. **85**, 748, 2000.

[SFM+94] A. J. Scroggie, W. J. Firth, G. S. McDonald, M. Tlidi, R. Lefever, and L. A. Lugiato. *Pattern formation in a passive Kerr cavity.* Chaos, Solitons & Fractals **4**, 1323, 1994.

[She84] Y. R. Shen. *The Principles of Nonlinear Optics.* Wiley, New York, Chichester, Brisbane, Toronto, Singapore, 1984.

[Sie77] A. E. Siegman. *Quasi fast Hankel transform.* Opt. Lett. **1**, 13, 1977.

[SJMO05] A. J. Scroggie, J. Jeffers, G. McCartney, and G.-L. Oppo. *Reversible soliton motion.* Phys. Rev. E **71**, 046602, 2005.

[SKTT97] A. Schreiber, M. Kreuzer, B. Thüring, and T. Tschudi. *Experimental investigation of solitary structures in a nonlinear optical feedback system.* Opt. Commun. **136**, 415, 1997.

[SMS97] V. J. Sánchez-Morcillo and K. Staliunas. *Stability of localized structures in the Swift-Hohenberg equation.* Phys. Rev. E **60**, 6153, 1997.

[SSBP98] C. P. Schenk, P. Schütz, M. Bode, and H.-G. Purwins. *Interaction of self-organized quasiparticles in a two-dimensional reaction-diffusion system: The formation of molecules.* Phys. Rev. E **57**, 6480, 1998.

[SSM97] K. Staliunas and V. J. Sánchez-Morcillo. *Localized structures in degenerate optical parametric oscillators.* Opt. Commun. **139**, 306, 1997.

[SSM98a] K. Staliunas and V. J. Sánchez-Morcillo. *Spatial-localized structures in degenerate optical parametric oscillators.* Phys. Rev. A **57**, 1454, 1998.

[SSM98b] K. Staliunas and V. J. Sánchez-Morcillo. *Dynamics of phase domains in the Swift-Hohenberg equation.* Phys. Lett. A **241**, 28, 1998.

[STB+98] L. Spinelli, G. Tissoni, M. Brambilla, F. Prati, and L. A. Lugiato. *Spatial solitons in semiconductor microcavities.* Phys. Rev. A **58**, 2542, 1998.

[Str94] S. H. Strogatz. *Nonlinear dynamics and chaos.* Addison-Wesley, Reading, 1994.

[Tal36] W. H. F. Talbot. *Facts relating to optical science. No. IV.* Philos. Mag. **9** (Third series), 401, 1836.

[Tam79] A. C. Tam. *Optical pumping of a dense Na+He+N_2 system: Application as an rf spectrum analyser.* J. Appl. Phys. **50**, 1171, 1979.

[TBWS93] M. Tamburrini, M. Bonavita, S. Wabnitz, and E. Santamato. *Hexagonally patterned beam filamentation in a thin liquid-crystal film with a single-feedback mirror.* Opt. Lett. **18**, 855, 1993.

[TF88] O. Thual and S. Fauve. *Localized structures generated by subcritical instabilities.* J. Phys. France **49**, 1829, 1988.

[TGKW00] V. B. Taranenko, I. Ganne, R. J. Kuszelewicz, and C. O. Weiss. *Patterns and localized structures in bistable semiconductor resonators.* Phys. Rev. A **61**, 063818, 2000.

[TGKW01] V. B. Taranenko, I. Ganne, R. J. Kuszelewicz, and C. O. Weiss. *Spatial solitons in a semiconductor microresonator.* Appl. Phys. B **72**, 377, 2001.

[THS97] S. Trillo, M. Haelterman, and A. Sheppard. *Stable topological spatial solitons in optical parametric oscillators.* Opt. Lett. **22**, 970, 1997.

[TM98] M. Tlidi and P. Mandel. *Scaling laws for localized pattern formation in optical bistability.* Europhys. Lett. **44**, 449, 1998.

[TM99] M. Tlidi and P. Mandel. *Space-time localized structures in the degenerate optical parametric oscillator.* Phys. Rev. A **59**, R2575, 1999.

[TML94] M. Tlidi, P. Mandel, and R. Lefever. *Localized structures and localized patterns in optical bistability.* Phys. Rev. Lett. **73**, 640, 1994.

[TMLB$^+$00] M. Tlidi, P. Mandel, M. Le Berre, E. Ressayre, A. Tallet, and L. Di Menza. *Phase-separation dynamics of circular domain walls in the degenerate optical parametric oscillator.* Opt. Lett. **25**, 487, 2000.

[TNT93] B. Thüring, R. Neubecker, and T. Tschudi. *Transverse pattern formation in liquid crystal light valve feedback system.* Opt. Commun. **102**, 111, 1993.

[TSB$^+$99a] G. Tissoni, L. Spinelli, M. Brambilla, I. Perrini, T. Maggipinto, and L. A. Lugiato. *Cavity solitons in bulk semiconductor microcavities: dynamical properties and control.* J. Opt. Soc. Am. B **16**, 2095, 1999.

[TSB+99b] G. Tissoni, L. Spinelli, M. Brambilla, I. Perrini, T. Maggipinto, and L. A. Lugiato. *Cavity solitons in bulk semiconductor microcavities: microscopic model and modulational instabilities.* J. Opt. Soc. Am. B **16**, 2083, 1999.

[TSW97] V. B. Taranenko, K. Staliunas, and C. O. Weiss. *Spatial soliton laser: localized structures in a laser with a saturable absorber in a self-imaging resonator.* Phys. Rev. A **56**, 1582, 1997.

[TSW98] V. B. Taranenko, K. Staliunas, and C. O. Weiss. *Pattern formation and localized structures in degenerate optical parametric mixing.* Phys. Rev. Lett. **81**, 2236, 1998.

[TW02] V. B. Taranenko and C. O. Weiss. *Spatial solitons in semiconductor micro-cavitities.* IEEE J. Selected Topics Quantum Electron. **8**, 488, 2002.

[TZWW99] V. B. Taranenko, M. Zander, P. Wobben, and C. O. Weiss. *Stability of localized structures in degenerate wave mixing.* Appl. Phys. B **69**, 337, 1999.

[UMS96] P. B. Umbanhowar, F. Melo, and H. L. Swinney. *Localized excitations in a vertically vibrated granular layer.* Nature **382**, 793, 1996.

[URE80] R. Ulrich, S. C. Rashleigh, and W. Eickhoff. *Bending-induced birefringence in single-mode fibers.* Opt. Lett. **5**, 273, 1980.

[VK97] M. A. Vorontsov and A. Yu. Karpov. *Pattern formation due to interballoon spatial mode coupling.* J. Opt. Soc. Am. B **14**, 34, 1997.

[VPAR02] G. J. de Valcárcel, I. Pérez-Arjona, and E. Roldán. *Domain walls and Ising-Bloch transitions in parametrically driven systems.* Phys. Rev. Lett. **89**, 164101, 2002.

[vS03] W. van Saarloos. *Front propagation into unstable states.* Phys. Rep. **386**, 29, 2003.

[WVS+99] C. O. Weiss, M. Vaupel, K. Staliunas, G. Slekys, and V. B. Taranenko. *Solitons and Vortices in lasers.* Appl. Phys. B **68**, 151, 1999.

[YOKO84] T. Yabuzaki, T. Okamoto, M. Kitano, and T. Ogawa. *Optical bistability with symmetry breaking.* Phys. Rev. A **29**, 1964, 1984.

Danksagung

Mein erster Dank gilt Herrn Prof. Dr. Wulfhard Lange für die Möglichkeit, diese Arbeit anzufertigen, für die Gewährung von Mitteln sowie für die zahlreichen Hinweise und Diskussionen.

Herrn Dr. Thorsten Ackemann danke ich für viele wertvolle Anregungen, Gespräche und Hinweise, die sehr zum Gelingen dieser Arbeit beigetragen haben.

Ich danke Herrn Dr. Edgar Große Westhoff für die Einführung in das Gebiet der Strukturbildung und in das Experiment im Allgemeinen sowie im Speziellen für die Vermittlung der Grundlagen des $\lambda/8$-Systems. I thank Dr. Damià Gomila for many valuable discussions and suggestions. Herrn Dipl.-Phys. Jens-Uwe Schurek danke ich für die Beiträge zu dieser Arbeit, die er im Rahmen seiner Diplomarbeit geleistet hat.

Den Herren Dipl.-Phys. Malte Schulz-Ruhtenberg, Dipl.-Phys. Karl Jentsch, Dr. Markus Sondermann und insbesondere Herrn Dr. Florian Huneus und Herrn Dipl.-Phys. Jens Schüttler danke ich für viele wertvolle und hilfreiche Diskussionen, die gute Zusammenarbeit und die fachliche wie moralische Unterstützung.

Ich danke allen Mitgliedern der Arbeitsgruppe für die ständige Gespächsbereitschaft und die gute Arbeitsatmosphäre. Mein Dank gilt außerdem allen Mitgliedern des Instituts für Angewandte Physik für die vielfältige Unterstützung und das gute Arbeitsklima.

Meiner Familie danke ich für ihre stete Unterstützung während des Studiums und der Promotion. Nicht zuletzt danke ich meinem Freundeskreis für die grandiose Zeit in Münster.